TESIS DE LA UNIVERSIDAD DE ZARAGOZA

2021 308

Sergio Martínez Aranda

Efficient Simulation Tools (EST) for sediment transport in geomorphological shallow flows

Director/es
García Navarro, Pilar

ISSN 2254-7606

Prensas de la Universidad
Universidad Zaragoza

ISSN 2254-7606

Universidad Zaragoza
1542

Tesis Doctoral

EFFICIENT SIMULATION TOOLS (EST) FOR SEDIMENT TRANSPORT IN GEOMORPHOLOGICAL SHALLOW FLOWS

Autor

Sergio Martínez Aranda

Director/es

García Navarro, Pilar

UNIVERSIDAD DE ZARAGOZA
Escuela de Doctorado

2021

Universidad Zaragoza
1542

Efficient Simulation Tools (EST) for sediment transport in geomorphological shallow flows

PhD thesis by:

Sergio Martínez-Aranda

Supervised by:

Pilar García-Navarro

A thesis submitted in fulfilment of the requirements for the degree of

***PhD* in Fluid Mechanics**

June 2021

Universidad Zaragoza

DOCTORAL THESIS

Efficient Simulation Tools (EST) for sediment transport in geomorphological shallow flows

Author:
Sergio Martínez Aranda

Supervisor:
Dr. Pilar García Navarro

A thesis submitted in fulfilment of the requirements for the degree of PhD in the

Fluid Mechanics doctoral program

UNIVERSITY OF ZARAGOZA

June 2021

Abstract

**Efficient Simulation Tools (EST)
for sediment transport in
geomorphological shallow flows**

by Sergio Martínez Aranda

Among the geophysical and environmental surface phenomena, rapid flows of water and sediment mixtures are probably the most challenging and unknown gravity-driven processes. Sediment transport is ubiquitous in environmental water bodies such as rivers, floods, coasts and estuaries, but also is the main process in wet landslides, debris flows and muddy slurries. In this kind of flows, the fluidized material in motion consists of a mixture of water and multiple solid phases which might be of different nature, such as different sediment size-classes, organic materials, chemical solutes or heavy metals in mine tailings. Modeling sediment transport involves an increasing complexity due to the variable bulk properties in the sediment-water mixture, the coupling of physical processes and the presence of multiple layers phenomena. Two-dimensional shallow-type mathematical models are built in the context of free surface flows and are applicable to a large number of these geophysical surface processes involving sediment transport. Their numerical solution in the Finite Volume (FV) framework is governed by the particular set of equations chosen, by the dynamical properties of the system, by the coupling between flow variables and by the computational grid choice. Moreover, the estimation of the mass and momentum source terms can also affect the robustness and accuracy of the solution. The complexity of the numerical resolution and the computational cost of simulation tools increase considerably with the number of equations involved. Furthermore, most of these highly unsteady flows usually occur along very steep and irregular terrains which require to use a refined non-structured spatial discretization in order to capture the terrain complexity, increasing exponentially the computational times. So that, the computational effort required is one of the biggest challenges for the application of depth-averaged 2D models to realistic large-scale long-term flows. Throughout this thesis, proper 2D shallow-type mathematical models, robust and accurate FV numerical algorithms and efficient high-performance computational codes are combined to develop Efficient Simulation Tools (EST's) for environmental surface processes involving sediment transport with realistic temporal and spatial scales. New EST's able to deal with structured and unstructured meshes are proposed for variable-density mud/debris flows, passive suspended transport and generalized bedload transport. Special attention is paid to the coupling between system variables and to the integration of mass and momentum source terms. The features of each EST have been carefully analyzed and their capabilities have been demonstrated using analytical and experimental benchmark tests, as well as observations in real events.

Resumen

**Herramientas Eficientes de Simulación (HES)
para transporte de sedimentos en
flujos superficiales geomorfológicos**

por Sergio Martínez Aranda

Entre los fenómenos superficiales geofísicos y medioambientales, los flujos rápidos de mezclas de agua y sedimentos son probablemente los más exigentes y desconocidos de los procesos movidos por gravedad. El transporte de sedimentos es ubicuo en los cuerpos de agua naturales, como ríos, crecidas, costas o estuarios, además de ser el principal proceso en deslizamientos, flujos de detritos y coladas barro. En este tipo de flujos, el material fluidificado en movimiento consiste en una mezcla de agua y múltiples fases sólidas, que pueden ser de distinta naturaleza como diferentes clases de sedimento, materiales orgánicos, solutos químicos o metales pesados en lodos mineros. El modelado del transporte de sedimentos involucra una alta complejidad debido a las propiedades variables de la mezcla agua-sólidos, el acoplamiento de procesos físicos y la presencia de fenómenos multicapa. Los modelos matemáticos bidimensionales promediados en la vertical ('shallow-type') se construyen en el contexto de flujos superficiales y son aplicables a un amplio rango de estos procesos geofísicos que involucran transporte de sedimentos. Su resolución numérica en el marco de los métodos de Volúmenes Finitos (VF) está controlada por el conjunto de ecuaciones escogido, las propiedades dinámicas del sistema, el acoplamiento entre las variables del flujo y la malla computacional seleccionada. Además, la estimación de los términos fuente de masa y momento puede también afectar la robustez y precisión de la solución. La complejidad de la resolución numérica y el coste computacional de simulación crecen considerablemente con el número de ecuaciones involucradas. Además, la mayor parte de estos flujos son altamente transitorios y ocurren en terrenos irregulares con altas pendientes, requiriendo el uso de una discretización espacial no-estructurada refinada para capturar la complejidad del terreno e incrementando exponencialmente el tiempo computacional. Por tanto, el esfuerzo computacional es uno de los grandes retos para la aplicación de modelos promediados 2D en flujos realistas con grandes escalas espaciales y largas duraciones de evento. En esta tesis, modelos matemáticos superficiales 2D apropiados, algoritmos numéricos de VF robustos y precisos, y códigos eficientes de computación de alto rendimiento son combinados para desarrollar Herramientas Eficientes de Simulación (HES) para procesos medioambientales superficiales involucrando transporte de sedimentos con escalas temporales y espaciales realistas. Nuevas HES capaces de trabajar en mallas estructuradas y no-estructuradas son propuestas para el flujos de lodo/detritos con densidad variable, transporte pasivo en suspensión y transporte de fondo generalizado. Una atención especial es puesta en el acoplamiento entre las variables del sistema y en la integración de los términos fuente de masa y momento. Las propiedades de cada HES han sido cuidadosamente analizadas y sus capacidades demostradas usando tests de validación analíticos y experimentales, así como mediciones en eventos reales.

Acknowledgements

Es larga la lista de personas con las que me siento agradecido. Especialmente, me gustaría agradecer a mi directora de tesis, Pilar, su apoyo y orientación a lo largo de todo este camino, así como sus intentos de evitar mis innumerables divagaciones, no siempre fue posible. También a todos los miembros del Grupo de Hidráulica Computacional presentes y pasados, Goevanny, Adrian, Raul, Mario, JFP, Isabel, Pablo, Javier y Cuca. Su trabajo constante y muchas veces a contra reloj siempre ha sido un ejemplo. Me guardo una dedicatoria especial para Victor, por las distracciones 'necesarias' durante estos cuatro años. También para mis amigos de montaña, Miguel, Zafra, Hugo y Guillermo, por todos los buenos ratos 'allí arriba'. Por supuesto, a Juanma y Rafa por ser incondicionales. Este trabajo no habría sido posible sin el apoyo de mi madre Luisa y hermana Cari, su comprensión y ayuda en los momentos más difíciles. Gran parte de lo que hay aquí escrito se lo debo a ellas, aunque les suene a chino. Por último, pero quizás más importante, gracias Marta por compartir este tiempo conmigo y apoyarme en todo momento.

Contents

List of Figures

List of Tables

Abbreviations

EST	Efficient Simulation Tool
1D	one-dimensional
2D	two-dimensional
FV	Finite Volume
RP	Riemann problem
ARoe	Augmented Roe
HPC	High Performance Computing
vdMD	Variable-density mud/debris flow model
udPST	Uniform-density passive suspended transport model
vdPST	Variable-density passive suspended transport model
FCM	Fully-coupled method for bedload transport
ACM	Approximate-coupled method for bedload transport
R-Cap	Fully-coupled capacity model for bedload transport
R-NCap	Fully-coupled non-capacity model for bedload transport

Nomenclature

Symbol	Name or description
$\partial_t a \equiv \dfrac{\partial a}{\partial t}$	Partial time derivative of a
$\partial_i a \equiv \dfrac{\partial a}{\partial i}$	Partial spatial derivatives of a with $i = x, y, z$
$(a)_s$	Variable a evaluated at the flow free surface z_s
$(a)_b$	Variable a evaluated at the bed surface z_b
$(a)_e$	Variable a evaluated at the static-moving bed interface z_e
$\mathrm{tr}(\mathbf{A})$	Traze of the tensor $\mathbf{A}$
∇a	Gradient of the scalar a
$\nabla \cdot \mathbf{A}$	Divergence of the vector/tensor $\mathbf{A}$
$\mathrm{sgn}(a)$	Sign of the scalar a

Chapter 1

Introduction

Among the environmental and geophysical surface phenomena, rapid water-sediment flows are probably the most challenging and unknown gravity-driven processes. In this kind of flows, the fluidized material in motion consists of a mixture of water and multiple solid phases which might be of different nature, such as different sediment size-classes, organic materials, chemical solutes or heavy metals in mine tailings [118]. Sediment transport is ubiquitous in environmental water bodies such as rivers, floods, coasts and estuaries, but also is the main process in wet landslides, debris flows and muddy slurries (Figure 1.1). Furthermore, these flows usually move rapidly downstream steep channels and involve complex topography.

Shallow-type mathematical models are built in the context of free surface flows under the main hypothesis that both the flow layer depth and characteristic wave celerity are smaller than a relevant horizontal length scale. They represent a simplified formulation, derived from the general 3D Navier-Stokes equations, which is applicable to a large number of these geophysical surface processes involving sediment transport. Their numerical solution in the Finite Volume (FV) framework is governed by the dynamical properties of the flow, by the particular set of equations chosen to represent them, by the uneven distribution of the bed level and also by the computational grid choice. The unified discretization of spatial flux derivatives and source terms has proven useful to ensure the properties of monotonicity, stability and conservation in the numerical solution [104].

Figure 1.1: Geophysical surface flows involving sediment transport

Furthermore, surface shallow-type flows that occur in catchments and coasts usually require large space resolution over long periods of time. The increasing complexity of the mathematical models and the advance on numerical methods, as well as the increasing power of computation, are making possible the physically based simulation of these phenomena. The necessity of spatial resolution involves the use of a large number of elements hence increasing the computational time when simulating realistic scenarios for a long time period.

The resulting approach of combining proper mathematical models, robust and accurate numerical algorithms and efficient high-performance computational codes allows the development of Efficient Simulation Tools (EST) [89] for environmental surface processes involving sediment transport with realistic temporal and spatial scales.

Highly sediment-laden flows

Natural ladslides, debris flows, muddy slurries or mining tailings are considered highly solid-laden fluids, where the density of the water-solid mixture can be more than twice or three times the water density and the bulk solid phase represents about 40–80% of the flow volume [55]. Furthermore, the characteristic size of the different transported solids might vary from about a couple of meters (boulders, trees stumps, etc) to very fine materials, as fine clay or heavy metal particles. The presence of the solid phases, especially the fine material as silt or clay, affects the rheological behavior of the mixture. Therefore, different states can be distinguished in highly solid-laden shallow flows. A clear-water flow transitions into a hyperconcentrated flow when particles on the bed begin to move together and coarse sediment becomes suspended in the flow. The water-sediment mixture rheology begins to be affected by fine solid particle transported in the flow when the volumetric concentration of fine sediment particles reaches about 4% by volume [118], creating a slight shear strength within the fluid. For higher concentrations, the mixture shows a marked non-Newtonian rheology. Mud and debris flows lie between hyperconcentrated flows and dry avalanches [54]. High concentrations of solids generate a critical yield stress which allows that coarse particles can be suspended indefinitely in the mixture flow [14]. Mud/debris flows are characterized by high sediment volume concentrations, often greater than 60%. In debris flows, sand/gravel and coarser sediment fractions predominate in the solid phase whereas dominant fine fractions (silt and clay) are typical for mud flows. Also the plasticity of the fine transported materials has been used to difference debris flows (plasticity index lower than 5%) from muddy slurries with plasticity index larger than 5% in the sand and finer fractions [54]. Nevertheless, these transitional processes in the flow behavior are extremely complex and continue to be debated up to now.

The mathematical modeling of solid-liquid mixture flows and their numerical resolution is still a challenging topic, especially when dealing with realistic applications. When liquid and solid phases are well-mixed, assuming that the solid phase is distributed uniformly over the flow column allows the use of depth-averaged models derived from the vertical integration of the Navier-Stokes equations [144]. The simplest models, used

in river and coastal dynamics, assume small enough sediment concentrations throughout the flow to consider the bulk density constant and uniform, hence it can be extracted from the conservative terms of the depth-averaged equations. However, most of the numerical models reported for highly solid-laden flows use this one-single-phase approach, neglecting the bulk density in the shallow-flow mass and momentum equations [12, 64, 81, 102]. Other approaches manipulate the depth-averaged equations to decouple the flow density and depth, leading to a modified form of the shallow-water equations where the mixture density spatial gradients only contribute within the momentum equation as a source term [20, 42, 79, 111, 112]. This simplification has been widely used since it allows to compute the numerical fluxes at the intercell edges using the numerical schemes implemented for plain shallow-water models. Nevertheless, even small density gradients influence importantly the mixing dynamics in flow confluences [47, 75, 123] and larger gradients can also generate numerical oscillations and instabilities throughout mixing interfaces, since the density variation does not participate in the characteristic-waves celerity.

More complicated models consider the separated transport of the liquid and solid phases presented in the mixture. Some distinctions can be made here between two-phase and mixing-phase models. On the one hand, two-phase approaches consider the depth-averaged mass and momentum equations for the liquid and solid phases separately [43, 46, 51, 79, 95]. Theoretically, the two-phase mathematical framework describes properly the complex interaction between fluid and solid particles within the mixture but the high uncertainty involved in the equations and the difficulty to implement efficient and robust numerical schemes have hindered its application to realistic geophysical problems. Two-phase depth-averaged systems are known to lose hyperbolicity since the eigenvalues of the coupled Jacobian matrix of the liquid and solid convective fluxes become complex under certain configurations [62, 121]. This drawback can cause numerical models based on the complete eigenstructure of the Jacobian (Roe-type approach) to become unstable [117] and the loss of hyperbolicity must be prevented numerically. Although system reformulations have been proposed to overcome the loss of hyperbolicity [79], the computational effort demanded by two-phase numerical models is much larger than that required by one-single-phase or mixing-phase models.

On the other hand, an alternative approach consists of encapsulating solid-fluid phase velocities into the depth-averaged bulk velocity of the mixture by accounting for the effects of solid-fluid particle interactions in the mixture stresses. This leads to the mixing-phase approach, which considers separately the mass and momentum conservation for the mixture and the mass conservation for the solid phase. Many versions of this approach have been reported in last years. Denlinger & Iverson [29] and Iverson & Denlinger [56] adopted a constant-density one phase approach but including the solid-liquid phase interaction effects in the mixture basal resistance by using the Terzaghi's effective stress principle, i.e. normal stresses at grain contacts are proportional to bulk normal stresses minus the pore-fluid pressure. The pore-fluid pressure was estimated as a fraction of the basal normal stress, indicating the liquefaction state of the flow. Lancaster *et al.* [74] assumed the same hypothesis but estimating the pore-fluid pressure at the basal surface as an excess of pressure over the hydrostatic

value. George & Iverson [42] proposed a constant-density mixture model but adding a vertical dissipation term for the pore-fluid pressure and advecting this pressure with the bulk mixture velocity. The solid-liquid phases interaction was included into the momentum equations by the evolution of the granular dilatancy, which was determined by the evolution of the pore-fluid pressure excess and solid volume fraction. Kowalski & McElwaine [69] derived a one-dimensional mixing-phase model where changes on the flow density were included into the homogeneous fluxes and the pore-fluid pressure component of the bulk mixture stress was algebraically coupled to the volume fraction, based on whether there is net solid phase settling or resuspension. The mixing-phase mathematical approach requires important simplifications of the multi-grain mixture physics but its unconditional hyperbolic character represents a decisive advantage in order to develop efficient numerical models able to deal with realistic large-scale mud/debris events.

Other important aspect of highly sediment-laden flows is the entrainment of materials from the underlying erodible bed layers. The mass exchange between mud/debris mixtures and erodible beds involves complicated physical processes and the understanding of its theoretical basis remains unclear. Experiments in large-scale channel [31, 60, 125] and field observations in real debris events [5, 94, 142] indicate that the entrainment volume in steep beds can be in the same order of magnitude as the initial volume mobilized. Debris and mud flows gain much of their mass and momentum as they move over steep slopes as a consequence of the material entrainment from the erodible bed, before deposition begins on flatter terrain downstream. Armanini *et al.* [2] proposed a 2D mixing-phase model including the mixture density into the homogeneous part of the system and taking into account the bulk bed entrainment. Ouyang *et al.* [111, 112] also included the bulk bed entrainment in their 2D single-phase models but considering additional momentum terms due to entrainment and deposition of the solid phase Iverson & Ouyang [58]. Moreover, natural beds are composed by a mixing of different size sediment particles which participate directly in the bulk solid phase volume when they are incorporated into the moving mixture. Each sediment size-class can be considered as an independent solid phase, with its own entrainment and settling processes, leading to multi-grain mixture models. Both Li *et al.* [79] and Xia *et al.* [147] obtained promising results using a 1D two-phase and a 1D mixing-phase model, respectively, including entrainment of different sediment classes into the multi-grain mixture.

Suspended and bedload transport in natural surface currents

In the context of natural surface moving water bodies, such as river or coasts, the sediment concentration is much lower than in sediment-laden flows. In these processes, the usual assumption is that the sediment particles can be transported by two basic mechanisms: suspended load, which is composed by the particles moving inside the flow with the same velocity as the fluid, and bedload which involves the particles moving in a relatively thin layer over the static bed. In this bedload layer or transport layer, the sediment particles remain in contact with the bed and their velocity is generally much lower than the fluid velocity [149]. Although the

total load transported by suspension can be much larger than the sediment weight moving in the active bed layer [144], the bedload mechanism plays an important role and it can cause marked and rapid changes in the bed bathymetry. Relevant investigations have been carried out by means of laboratory experiments or field measurements [11, 36, 120, 133, 135, 143, 150], but they are mostly limited by the small scale of the laboratory flumes or the fact that field measurements are very time-consuming, expensive and extremely difficult to perform. Therefore, numerical modelling is an attractive tool to understand and predict the morphodynamical evolution of rivers and reservoirs. However, uncertainties arise in computational simulations due to simplifications, assumptions and empirical relationships introduced into the mathematical models used for sediment transport prediction [149].

The solid particles can be transported under equilibrium (capacity or saturated) conditions or non-capacity (non-equilibrium or unsaturated) conditions. The classical equilibrium approach assumes that the actual sediment transport rates for suspended and bedload are equal to the capacity of the flow to carry solid weight. They are only determined by instantaneous local flow features and can be formulated by different empirical closure relations found in literature [149]. Models based on this assumption are commonly called equilibrium or capacity transport models [15, 22, 45, 48, 52, 65, 83, 86, 103, 137]. On the other hand, in non-capacity models, the actual transport rates are computed through advection and mass exchange with the static erodible bed. Non-equilibrium (i.e. non-capacity) sediment transport models have been proposed [1, 4, 10, 16, 33, 37, 41, 80, 145, 152] for both suspended and bedload transport. Natural morphodynamical systems such as alluvial rivers are always changing in time and space and hence absolute equilibrium states rarely exist in natural conditions. Therefore, intuitively non-capacity approaches are more suitable than models based on the equilibrium assumption since they account for the temporal and spatial delay of the actual sediment transport rate with respect to its potential capacity. However, if this adaptation delay is sufficiently small, equilibrium models can be also applied at least in theory [144].

Unlike purely suspended load models, where it has been demonstrated that the non-capacity assumption is necessary to compute correctly the solid suspended concentration and the bed evolution [16, 99], the importance of assuming non-equilibrium conditions in bedload numerical models remains uncertain. Van-Rijn [140] suggested that the actual bedload transport rate in unsteady flows can be assumed equal to the bedload capacity because the adjustment of the transported sediment particles to the new flow conditions proceeds rapidly close to the bed surface. This assumption was conceptual and without a theoretical or numerical justification. Cao *et al.* [16] and Cao *et al.* [19] analysed numerically the multiple time scales involved in bedload transport for fluvial processes. They found that, at least for flood cases, the bedload transport rate was able to rapidly adapt to the local flow features, which justifies the widespread application of the equilibrium models [19]. However, a comparative analysis of both capacity and non-capacity bedload models in highly erosive unsteady flows, as dam-break waves or overtopping dyke-collapses, remains unperformed, especially including experimental benchmarking cases and accurate numerical schemes.

The assumption of non-equilibrium conditions leads to the requirement

of computing the temporal evolution of the transport layer thickness and the velocity of the bedload particles in order to predict the actual transport rate, as well as the net exchange flux between static and moving bed layers. This requirement introduces a high uncertainty in non-capacity models due to the necessity of calibration parameters associated to solid particles velocity, transport layer thickness and bedload erosion-deposition rates for transient flows. The calibration process for non-capacity models can be an annoying task with few empirical supporting data. Different strategies have been proposed in order to overcome this uncertainty. Wu [144] and El Kadi Abderrezzak *et al.* [34] proposed to approximate the net exchange flux through the static-moving bed layers interface by the difference between the actual and capacity transport rates affected by an adaptation length and to assume a non-storage mass condition for the active bed layer, leading to the quasi-steady solid flux relaxation models. A more complex approach was also proposed by [134, 145, 152], based on the same adaptation length parameter to determine the net exchange flux through the interface but accounting now for the mass storage in the active bed layer. This approach leads to the direct computation of the actual transport rate as one of the unknown conserved variables, assuming that the velocity in the active layer can be evaluated by one of the empirical closure relations for capacity conditions found in literature [39, 76, 139].

Recently, new and more complex approaches to the non-equilibrium bedload transport phenomenon have been derived based on a pioneering work [25]. The physical interaction between flow and sediment particles at the static-moving bed layer interface was studied at a grain scale. Zech *et al.* [150] modelled the net exchange flux through the interface as a function of the shear stress at the moving layer and at the upper boundary of the static layer. Fernández-Nieto *et al.* [37] and Fernández-Nieto *et al.* [38] proposed new empirical formulae for the erosion and deposition rates at the interface, as well as a new closure relation for the actual sediment transport rate which reduces to the classical one under equilibrium conditions. Bohorquez & Ancey [10] also analysed erosion and deposition rates at the static-moving interface including a new diffusion term in the bedload conservation equations.

Furthermore, the presence of bedrock strata underlying the erodible alluvial layers is ubiquitous in natural rivers and estuaries. When a non-erodible layer is reached by erosion, the actual bedload transport rate becomes different from the transport capacity of the flow, leading to a non-capacity transport state even under nearly uniform flow regimes. Some recent approaches to this topic consist of small adaptations of the classical capacity bedload transport theory or of simple numerical fixes. Struiksma [136] proposed to reduce the capacity transport rate in regions where the sediment becomes partially unavailable using a parameter based on the actual sediment thickness over the non-erodible layer and the theoretical active layer thickness for the capacity transport state. Rulot *et al.* [130] proposed an iterative method to correct the over-eroded cells by affecting the sediment distribution after each time step computation. Caviedes-Voullième *et al.* [24] implemented a numerical fix based on the limitation

of the numerical solid flux at the intercell edges as a function of the available sediment volume at the involved cells. Although these simplified approaches to the finite-depth erodible layer problem seem to work reasonably well in some conditions, they offer a limited modelling ability of the real physical phenomenon and require a more detailed analysis.

High-performance computing

Modelling sediment transport involves an increasing complexity with respect to rigid-bed shallow water models [27, 131] due to the presence of variable sediment-fluid mixture properties, coupling of physical processes and multiple layers phenomena [30]. One of the biggest challenges for the application of depth-averaged models to realistic large-scale long-term flows is the computational effort required. Most of these highly unsteady flows usually occur along very steep and irregular terrains which require to use a refined non-structured spatial discretization in order to capture the terrain complexity, increasing exponentially the computational times. Furthermore, the complexity of the numerical resolution and the computational cost of the solvers also increase considerably with the number of equations involved and the coupling between flow variables adds special features to the mathematical model.

Most of the 2D numerical algorithms applied to sediment transport are adaptations of simplified shallow clear-water models. There exists a lack of efficient and robust two-dimensional numerical models specifically designed for highly sediment-laden flows and able to work with non-structured triangular meshes. New strategies to reduce the computational effort have been developed in the last decade through the use of parallelization techniques based on Multiprocessing (OpenMP) or Message Passing Interface (MPI), which allow to run simulations on multi-CPU clusters. Their main drawback is the associated hardware cost and energy requirements, which are directly proportional to the number of CPU-cores available and limit their efficiency. In the last 5 years, the usage of Graphics Processing Units (GPU) hardware accelerators for sequential computation has demonstrated to be an efficient and low cost alternative to the traditional multi-CPU strategies [70]. GPU-accelerated algorithms have been developed for real-time floods forecasting [71, 72, 98], real-scale bedload erosive shallow-flows [67] or tsunami prediction [28, 84].

GPU devices are oriented to perform arithmetical operations on vector-based information. Unlike the conventional shared-memory multi-CPU implementations, the GPU solution must be designed taking into account the fact that the GPU is an independent device with its own RAM memory. This means that the memory transfer between the conventional RAM memory and the GPU device memory plays a key role in the performance of GPU-accelerated software. The most common way of performing this memory transfer is by means of explicit memory copy operations in the code. In any case, if the algorithm requires a large number of transfers, the performance of the GPU solution may be dramatically reduced due to this separate memory space.

1.1 Main goals

This thesis aims the combination of properly derived 2D shallow-type mathematical models with both the development of robust and accurate Finite Volume (FV) numerical algorithms and the implementation of efficient HPC codes. This comprehensive approach allows to develop Efficient Simulation Tools (EST's) for environmental surface processes involving sediment transport with realistic temporal and spatial scales. New EST's able to deal with structured and unstructured meshes are proposed for variable-density mud/debris flows over movable beds, passive suspended transport and generalized bedload transport. GPU-based algorithms are implemented for the proposed models using C++ and the NVIDIA CUDA Toolkit. Similarly, a CPU-based version of the numerical algorithms using shared-memory OMP parallelization with C++ are also developed for code debugging and efficiency comparison.

1.2 Outline

The text organizes as follows:

Chapters

- Chapter 2: The shallow-type mathematical formulation for generalized surface sediment-laden flows is derived from the 3D Navier-Stokes equations. The foundations of the simplified mathematical models used throughout this thesis are analyzed here.
- Chapter 3: A new ETS for highly sediment-laden flows , such as debris flows or muddy slurries, is derived and assessed in this chapter.
- Chapter 4: In this section, simplified numerical models for suspended sediment transport have been derived and analyzed.
- Chapter 5: This chapter is devoted to the numerical modeling of the bedload transport. New approaches for the capacity and non-capacity transport have been assessed.
- Chapter 6: The main conclusions and the relevant contribution are finally summarized in the last chapter.

Appendices

- Appendix A: Is devoted to the explanation of the high-performance computational algorithms implemented throughout this thesis.
- Appendix B: A complete list of the relevant publications and communications carried out in relation with this thesis con be found here.

Chapter 2

Governing equations for sediment-laden erosive flows

The main goals for this chapter are:

- Derivation of the depth-averaged conservation laws for environmental surface flows of water-sediment mixtures from the 3D compressible Navier-Stokes equations.
- Definition of effects of the solid phase dilation and the pore-fluid pressure in the transport of the solid particles within the mixture flow.
- Analysis of the mathematical model for the bed exchange processes considering both capacity and non-capacity conditions for the solid transport.

2.1 Depth-integrated equations for shallow flows

2.1.1 Mass and linear momentum conservation

The flow of a water-sediment mixture can be mathematically described assuming the movement of the solid particles as a diffusion phenomenon into the liquid phase. Then, the continuity and momentum conservation for the mixture, supplemented with the transport equation for the solid phase, can be established for modelling these two-phase flows. Although both solid and liquid phases are incompressible when considered independently, the bulk behaviour of the solid-liquid mixture is the same as that of a compressible material depending on the local solid phase volumetric concentration. Therefore, the 3D time-averaged Navier-Stokes equations for mass and momentum conservation of a two-phase mixture can be written in the Cartesian coordinate system $\mathbf{X} = (x, y, z)$ as

$$\frac{\partial \rho}{\partial t}+\frac{\partial}{\partial x}(u_x\rho)+\frac{\partial}{\partial y}(u_y\rho)+\frac{\partial}{\partial z}(u_z\rho)=0 \tag{2.1a}$$

$$\frac{\partial(\rho u_x)}{\partial t}+\frac{\partial}{\partial x}(u_x\rho u_x)+\frac{\partial}{\partial y}(u_y\rho u_x)+\frac{\partial}{\partial z}(u_z\rho u_x)= F_x-\frac{\partial p}{\partial x}+\frac{\partial \tau_{xx}}{\partial x}+\frac{\partial \tau_{xy}}{\partial y}+\frac{\partial \tau_{xz}}{\partial z} \tag{2.1b}$$

$$\frac{\partial(\rho u_y)}{\partial t}+\frac{\partial}{\partial x}(u_x\rho u_y)+\frac{\partial}{\partial y}(u_y\rho u_y)+\frac{\partial}{\partial z}(u_z\rho u_y)= F_y-\frac{\partial p}{\partial y}+\frac{\partial \tau_{yx}}{\partial x}+\frac{\partial \tau_{yy}}{\partial y}+\frac{\partial \tau_{yz}}{\partial z} \tag{2.1c}$$

$$\frac{\partial(\rho u_z)}{\partial t}+\frac{\partial}{\partial x}(u_x\rho u_z)+\frac{\partial}{\partial y}(u_y\rho u_z)+\frac{\partial}{\partial z}(u_z\rho u_z)= F_z-\frac{\partial p}{\partial z}+\frac{\partial \tau_{zx}}{\partial x}+\frac{\partial \tau_{zy}}{\partial y}+\frac{\partial \tau_{zz}}{\partial z} \tag{2.1d}$$

where (u_x, u_y, u_z) are the components of the bulk mixture velocity $\mathbf{u}$ in any point of the fluidized material, (F_x, F_y, F_z) are the external forces, such as gravity, p denotes the pressure of the mixture and ρ accounts for the bulk density of the mixture. This bulk mixture is usually expressed as a weighted combination of the solid and liquid phase densities depending on the volumetric solid concentration.

Terms τ_{ij} $(i, j = x, y, z)$ are the components of the deviatoric stress tensor $\boldsymbol{\tau}$. With low solid-phase concentrations, the water-sediment mixture behaves as a Newtonian fluid, with a constitutive relation given by the Navier-Poisson law [144]. Nevertheless, for high sediment concentrations the mixture becomes a kind of non-Newtonian fluid with a complex constitutive law, which depends on mulplite factors, relating stresses and deformation rates.

in order to develop a shallow-type depth-averaged mathematical model, the Navier-Stokes system (2.1) is integrated between the free surface $z_s = z_s(t, x, y)$ and the bottom surface of the flow column $z_b = z_b(t, x, y)$, which is also considered a movable interface. The kinematic conditions at these boundaries can be expressed as

$$\frac{\partial z_s}{\partial t}+(u_x)_s\frac{\partial z_s}{\partial x}+(u_y)_s\frac{\partial z_s}{\partial y}=(u_z)_s \tag{2.2}$$

$$\frac{\partial z_b}{\partial t}+(u_x)_b\frac{\partial z_b}{\partial x}+(u_y)_b\frac{\partial z_b}{\partial y}=(u_z)_b+N_b \tag{2.3}$$

being N_b the net volumetric flux through the bed interface along the $z-$coordinate. The subscripts $(\cdot)_s$ and $(\cdot)_b$ indicate the value of the corresponding variable at the flow free surface and the bottom bed interface respectively.

The mass conservation equation (2.1a) is integrated along the water column as

$$\int_{z_b}^{z_s} \partial_t(\rho)\,\mathrm{d}z + \int_{z_b}^{z_s} \partial_x(u_x\rho)\,\mathrm{d}z + \int_{z_b}^{z_s} \partial_y(u_y\rho)\,\mathrm{d}z + \int_{z_b}^{z_s} \partial_z(u_z\rho)\,\mathrm{d}z = 0 \tag{2.4}$$

Applying Leibnitz's rule to each term on the left hand side of (2.4) leads to

$$\int_{z_b}^{z_s} \partial_t(\rho)\,\mathrm{d}z = \frac{\partial}{\partial t}\int_{z_b}^{z_s} \rho\,\mathrm{d}z - (\rho)_s\frac{\partial z_s}{\partial t} + (\rho)_b\frac{\partial z_b}{\partial t} \tag{2.5a}$$

$$\int_{z_b}^{z_s} \partial_x(u_x\rho)\,\mathrm{d}z = \frac{\partial}{\partial x}\int_{z_b}^{z_s} u_x\rho\,\mathrm{d}z - (u_x\rho)_s\frac{\partial z_s}{\partial x} + (u_x\rho)_b\frac{\partial z_b}{\partial x} \tag{2.5b}$$

$$\int_{z_b}^{z_s} \partial_y(u_y\rho)\,\mathrm{d}z = \frac{\partial}{\partial y}\int_{z_b}^{z_s} u_y\rho\,\mathrm{d}z - (u_y\rho)_s\frac{\partial z_s}{\partial y} + (u_y\rho)_b\frac{\partial z_b}{\partial y} \tag{2.5c}$$

$$\int_{z_b}^{z_s} \partial_z(u_z\rho)\,\mathrm{d}z = (u_z\rho)_s - (u_z\rho)_b \tag{2.5d}$$

It is now convenient to introduce the depth-averaged value $\overline{\rho}$ of the mixture bulk density as

$$\overline{\rho}h = \int_{z_b}^{z_s} \rho\,\mathrm{d}z \tag{2.6}$$

being $h = z_s - z_b$ the flow depth so that the depth-averaged velocities are expressed as

$$\overline{u} = \frac{1}{\overline{\rho}h}\int_{z_b}^{z_s} u_x\rho\,\mathrm{d}z \qquad \overline{v} = \frac{1}{\overline{\rho}h}\int_{z_b}^{z_s} u_y\rho\,\mathrm{d}z \tag{2.7}$$

Considering the boundary conditions (2.3) and (2.2), it possible to express the depth-averaged mass conservation equation as

$$\frac{\partial(\overline{\rho}h)}{\partial t} + \frac{\partial}{\partial x}(\overline{\rho}h\overline{u}) + \frac{\partial}{\partial y}(\overline{\rho}h\overline{v}) = -(\rho)_b N_b \tag{2.8}$$

where $(\rho)_b$ is the mixture bulk density at the bed interface z_b. Hence, the term on the right hand side of (2.8) accounts for the mass exchange between the flow and the bed layers, being positive for net entrainment conditions and negative for net deposition fluxes.

Regarding the momentum depth integration, the volumetric force (F_x, F_y, F_z) in (2.1) is considered for the sake of simplicity as

$$F_x = F_y = 0; \qquad F_z = -\rho g \tag{2.9}$$

Moreover, the z-momentum equation (2.1d) can be simplified to the hydrostatic pressure equation for variable density along the mixture column by neglecting temporal, convective and stress terms, leading to

$$\frac{\partial p}{\partial z} = -\rho g \quad \Longrightarrow \quad p(z) = \int_{z}^{z_s} \rho g \, \mathrm{d}z \tag{2.10}$$

assuming the atmospheric pressure at the flow free surface as reference value.

The x-momentum (2.1b) is integrated throughout the flow depth in the following way

$$\int_{z_b}^{z_s} \partial_t(\rho u_x) \, \mathrm{d}z + \int_{z_b}^{z_s} \partial_x(u_x \rho u_x) \, \mathrm{d}z + \int_{z_b}^{z_s} \partial_y(u_y \rho u_x) \, \mathrm{d}z + \int_{z_b}^{z_s} \partial_z(u_z \rho u_x) \, \mathrm{d}z = - \int_{z_b}^{z_s} \partial_x(p) \, \mathrm{d}z + \int_{z_b}^{z_s} \left(\partial_x \tau_{xx} + \partial_y \tau_{xy} + \partial_z \tau_{xz} \right) \mathrm{d}z \tag{2.11}$$

Applying Leibnitz's rule to each term on the left hand side of (2.11) leads to

$$\int_{z_b}^{z_s} \partial_t(\rho u_x) \, \mathrm{d}z = \frac{\partial}{\partial t} \int_{z_b}^{z_s} \rho u_x \, \mathrm{d}z - (\rho u_x)_s \frac{\partial z_s}{\partial t} + (\rho u_x)_b \frac{\partial z_b}{\partial t} \tag{2.12a}$$

$$\int_{z_b}^{z_s} \partial_x(u_x \rho u_x) \, \mathrm{d}z = \frac{\partial}{\partial x} \int_{z_b}^{z_s} u_x \rho u_x \, \mathrm{d}z - (u_x \rho u_x)_s \frac{\partial z_s}{\partial x} + (u_x \rho u_x)_b \frac{\partial z_b}{\partial x} \tag{2.12b}$$

$$\int_{z_b}^{z_s} \partial_y(u_y \rho u_x) \, \mathrm{d}z = \frac{\partial}{\partial y} \int_{z_b}^{z_s} u_y \rho u_x \, \mathrm{d}z - (u_y \rho u_x)_s \frac{\partial z_s}{\partial y} + (u_y \rho u_x)_b \frac{\partial z_b}{\partial y} \tag{2.12c}$$

$$\int_{z_b}^{z_s} \partial_z(u_z \rho u_x) \, \mathrm{d}z = (u_z \rho u_x)_s - (u_z \rho u_x)_b \tag{2.12d}$$

where, assuming (2.6) and (2.7), the spatial derivatives of the momentum integrals can be rewritten as

$$\int_{z_b}^{z_s} u_x \rho u_x \, \mathrm{d}z = \overline{\rho} h \overline{u}^2 + \int_{z_b}^{z_s} \rho (u_x - \overline{u})^2 \, \mathrm{d}z = \overline{\rho} h \overline{u}^2 - \overline{\rho} h D_{xx} \tag{2.13a}$$

$$\int_{z_b}^{z_s} u_y \rho u_x \, \mathrm{d}z = \overline{\rho} h \overline{u}\overline{v} + \int_{z_b}^{z_s} \rho (u_x - \overline{u})(u_y - \overline{v}) \, \mathrm{d}z = \overline{\rho} h \overline{u}\overline{v} - \overline{\rho} h D_{xy} \tag{2.13b}$$

with (D_{xx}, D_{xy}) accounting for the depth-averaged dispersion momentum transport due to the non-uniformity of the vertical velocity profile, and defined as

$$D_{xx} = -\frac{1}{\overline{\rho} h} \int_{z_b}^{z_s} \rho (u_x - \overline{u})^2 \, \mathrm{d}z \tag{2.14a}$$

$$D_{xy} = -\frac{1}{\overline{\rho} h} \int_{z_b}^{z_s} \rho (u_x - \overline{u})(u_y - \overline{v}) \, \mathrm{d}z \tag{2.14b}$$

Therefore, replacing (2.13) into (2.12), and considering the kinematic boundary conditions at both the bed interface (2.3) and free surface (2.2), the left hand side of (2.11) can be expressed as

$$\frac{\partial (\overline{\rho} h \overline{u})}{\partial t} + \frac{\partial}{\partial x}(\overline{\rho} h \overline{u}^2 - \overline{\rho} h D_{xx}) + \frac{\partial}{\partial y}(\overline{\rho} h \overline{uv} - \overline{\rho} h D_{xy}) + (\rho u_x)_b N_b \tag{2.15}$$

On the right hand side of (2.11), using (2.10), the integral of the pressure gradient along the $x-$coordinate can be expressed as

$$-\int_{z_b}^{z_s} \partial_x(p) \, \mathrm{d}z = -g \int_{z_b}^{z_s} \Big(\frac{\partial}{\partial x} \int_{z}^{z_s} \rho \, \mathrm{d}z \Big) \, \mathrm{d}z \tag{2.16}$$

Then, assuming that the vertical density gradient is negligible compared with those along the horizontal plane, as occurs in natural debris and mud slurry flows, it can be stated that

$$\int_{z}^{z_s} \rho \, \mathrm{d}z \approx \overline{\rho}(z_s - z)$$

and, applying Leibnitz's rule, (2.16) can be expressed as

$$\begin{aligned} &-g \int_{z_b}^{z_s} \Big(\frac{\partial}{\partial x} \int_{z}^{z_s} \rho \, \mathrm{d}z \Big) \, \mathrm{d}z = -g \int_{z_b}^{z_s} \frac{\partial}{\partial x} \big(\overline{\rho}(z_s - z) \big) \, \mathrm{d}z = \\ &-g \frac{\partial}{\partial x} \int_{z_b}^{z_s} \overline{\rho}(z_s - z) \, \mathrm{d}z + g \big(\overline{\rho}(z_s - z) \big)_s \frac{\partial z_s}{\partial x} - g \big(\overline{\rho}(z_s - z) \big)_b \frac{\partial z_b}{\partial x} = \\ &\underbrace{-\frac{\partial}{\partial x} \big(\frac{1}{2} g \overline{\rho} h^2 \big)}_{\text{Conservative term}} \quad \underbrace{-g \overline{\rho} h \frac{\partial z_b}{\partial x}}_{\text{Bed-pressure term}} \end{aligned} \tag{2.17}$$

separating the pressure gradient term (2.16) into a conservative component plus a bed-pressure component.

The stress terms on the right hand side of (2.11) are integrated along the flow column as follows

$$\int_{z_b}^{z_s} \partial_x(\tau_{xx})\,\mathrm{d}z = \frac{\partial}{\partial x}\int_{z_b}^{z_s} \tau_{xx}\,\mathrm{d}z - (\tau_{xx})_s\frac{\partial z_s}{\partial x} + (\tau_{xx})_b\frac{\partial z_b}{\partial x} \tag{2.18a}$$

$$\int_{z_b}^{z_s} \partial_y(\tau_{xy})\,\mathrm{d}z = \frac{\partial}{\partial y}\int_{z_b}^{z_s} \tau_{xy}\,\mathrm{d}z - (\tau_{xy})_s\frac{\partial z_s}{\partial y} + (\tau_{xy})_b\frac{\partial z_b}{\partial y} \tag{2.18b}$$

$$\int_{z_b}^{z_s} \partial_z(\tau_{xz})\,\mathrm{d}z = (\tau_{xz})_s - (\tau_{xz})_b \tag{2.18c}$$

It is worth noting that, at the free surface and the bed interface, the boundary conditions for the stress term can be expressed as

$$(\tau_{xz})_s - (\tau_{xx})_s\partial_x(z_s) - (\tau_{xy})_s\partial_y(z_s) = \tau_{sx} \tag{2.19a}$$

$$-(\tau_{xz})_b + (\tau_{xx})_b\partial_x(z_b) + (\tau_{xy})_b\partial_y(z_b) = -\tau_{bx} \tag{2.19b}$$

where τ_{sx} denotes the $x-$coordinate component of the wind action at the free surface, which often is not taken into account in surface flow models, whereas τ_{bx} represents the $x-$coordinate component of the boundary shear stress at the bed interface, opposing to the flow movement. Furthermore, the depth-averaged turbulent stresses along the flow column (T_{xx}, T_{xy}) are defined as

$$T_{xx} = \frac{1}{\overline{\rho}h}\int_{z_b}^{z_s} \tau_{xx}\,\mathrm{d}z \qquad T_{xy} = \frac{1}{\overline{\rho}h}\int_{z_b}^{z_s} \tau_{xy}\,\mathrm{d}z \tag{2.20}$$

allowing to rewrite the stress integral in (2.18) as

$$\int_{z_b}^{z_s} \left(\partial_x\tau_{xx} + \partial_y\tau_{xy} + \partial_z\tau_{xz}\right)\mathrm{d}z = \frac{\partial}{\partial x}(\overline{\rho}hT_{xx}) + \frac{\partial}{\partial y}(\overline{\rho}hT_{xy}) - \tau_{bx} \tag{2.21}$$

Replacing (2.15), (2.17) and (2.21) into (2.11) and reordering terms, the final expression for the depth-integrated momentum equation along the $x-$coordinate for variable-density surface flows over movable beds can be written as

$$\begin{aligned}\frac{\partial(\overline{\rho}h\overline{u})}{\partial t} + \frac{\partial}{\partial x}(\overline{\rho}h\overline{u}^2 + \frac{1}{2}g\overline{\rho}h^2) + \frac{\partial}{\partial y}(\overline{\rho}h\overline{u}\overline{v}) &= -g\overline{\rho}h\frac{\partial z_b}{\partial x} - \tau_{bx} \\ &+ \frac{\partial}{\partial x}\left(\overline{\rho}h(T_{xx} + D_{xx})\right) + \frac{\partial}{\partial y}\left(\overline{\rho}h(T_{xy} + D_{xy})\right) \\ &- (\rho u_x)_b N_b\end{aligned} \tag{2.22}$$

Following the same procedure to integrate (2.1c), the depth-averaged

momentum equation along the $y-$coordinate can be written straightforward as

$$\begin{aligned}\frac{\partial(\overline{\rho}h\overline{v})}{\partial t}+\frac{\partial}{\partial x}(\overline{\rho}h\overline{uv})+\frac{\partial}{\partial y}(\overline{\rho}h\overline{v}^2+\frac{1}{2}g\overline{\rho}h^2)=-g\overline{\rho}h\frac{\partial z_b}{\partial y}-\tau_{by}\\ +\frac{\partial}{\partial x}\big(\overline{\rho}h(T_{yx}+D_{yx})\big)+\frac{\partial}{\partial y}\big(\overline{\rho}h(T_{yy}+D_{yy})\big)\\ -(\rho u_y)_b N_b\end{aligned} \tag{2.23}$$

2.1.2 Constitutive models for complex-rheology flows

So far, there is not a universal closure relation for representing the viscous terms in complex non-Newtonian flows. Stresses in fluid-solid two-phase flows include distinct contributions from pore-fluid shear stress, intergranular collisonal and frictional stress and solid-fluid phases interactions [63]. Constitutive formulations used for environmental sediment-water mixtures are mainly derived from 3D general rheological models which, assuming isotropic material and isochoric flow, allow to express the stress tensor $\boldsymbol{\sigma}=\sigma_{ij}$ $(i,j=x,y,z)$ as

$$\boldsymbol{\sigma}=-p\mathbf{I}+\boldsymbol{\tau}=-p\mathbf{I}+\Phi_1(I_{2D})\mathbf{D} \tag{2.24}$$

where p is the pressure, $\mathbf{I}$ is identity tensor, $\mathbf{D}\equiv D_{ij}=\frac{1}{2}(\partial_j u_i+\partial_i u_j)$ $(i,j=x,y,z)$ is the rate of deformation tensor and ϕ_1 is a scalar function of the second invariant $I_{2D}=\frac{1}{2}\mathrm{tr}(\mathbf{D}^2)$ of the rate of deformation tensor $\mathbf{D}$ [116]. Therefore, the tensor

$$\boldsymbol{\tau}=\Phi_1(I_{2D})\mathbf{D} \tag{2.25}$$

accounts for the deviatoric component of the stress tensor $\boldsymbol{\sigma}$ in the material. The function Φ_1 depends on multiple factor, such as cohesive stress, pore-fluid pressure or flow initial regime. The generalized viscoplastic model, also called Herschel-Bulkley model, assumes dependence of Φ_1 on the three parameters: τ_0 the cohesive-frictional strength, K a viscosity-type coefficient and m a parameter characterizing the rheological response of the mixture [30, 122]. It is worth mentioning that the dimensions of viscosity-type coefficient K depends on the m behaviour parameter. Therefore, the function Φ_1 is expressed as

$$\Phi_1(I_{2D})=\frac{\tau_0}{\sqrt{I_{2D}}}+2K\left(4I_{2D}\right)^{\frac{m-1}{2}} \tag{2.26}$$

Considering simple shear state along the flow direction, the velocity vector $\mathbf{u}$ throughout the flow column is expressed as

$$u_x=U(z)\,n_{ux}\qquad u_y=U(z)\,n_{uy}\qquad u_z=0 \tag{2.27}$$

where $U(z)$ is the modulus of the bulk mixture velocity $\mathbf{u}$ and (n_{ux},n_{uy}) are the components of the velocity unit vector $\mathbf{n_u}$. Therefore, the rate of deformation tensor $\mathbf{D}$ and its second invariant I_{2D} for simple shear states can be expressed as

$$\mathbf{D} = \begin{pmatrix} 0 & 0 & \frac{1}{2}\frac{\mathrm{d}U}{\mathrm{d}z} n_{ux} \\ 0 & 0 & \frac{1}{2}\frac{\mathrm{d}U}{\mathrm{d}z} n_{uy} \\ \frac{1}{2}\frac{\mathrm{d}U}{\mathrm{d}z} n_{ux} & \frac{1}{2}\frac{\mathrm{d}U}{\mathrm{d}z} n_{uy} & 0 \end{pmatrix} \tag{2.28a}$$

$$I_{2D} = \frac{1}{4}\left(\frac{\mathrm{d}U}{\mathrm{d}z}\right)^2 \tag{2.28b}$$

Replacing the simple-shear rate of deformation tensor (2.28a) into (2.25) allows to define the deviatoric stress tensor as

$$\boldsymbol{\tau} = \begin{pmatrix} 0 & 0 & \tau(z)\, n_{ux} \\ 0 & 0 & \tau(z)\, n_{uy} \\ \tau(z)\, n_{ux} & \tau(z)\, n_{uy} & 0 \end{pmatrix} \tag{2.29}$$

being $\tau(z)$ the shear stress along the flow direction, which depends on the fluid rheology (2.26).

Newtonian fluids: For the Newtonian constitutive model, the cohesive-frictional strength τ_0 is null, $K\ [Pa \cdot s]$ is set to the dynamic viscosity of the fluid μ and a behaviour parameter $m = 1$ is considered. The generalized model (2.26) reduces to

$$\Phi_1(I_{2D}) = 2\mu \tag{2.30}$$

and hence the shear stress along the flow direction in (2.29) for the Newtonian viscous model can be expressed as

$$\tau(z) = \mu \frac{\mathrm{d}U}{\mathrm{d}z} \tag{2.31}$$

Linear viscoplastic fluids: A widespread non-Newtonian constitutive relation for geophysical surface flows in laminar regime is the Bingham model, which considers a pure cohesive yield stress $\tau_0 = \tau_y$ for the flow initiation, $K = \mu_B\ [Pa \cdot s]$ the Bingham viscosity and a behaviour parameter $m = 1$. The generalized model (2.26) reduces to

$$\Phi_1(I_{2D}) = \frac{\tau_y}{\frac{1}{2}\frac{\mathrm{d}U}{\mathrm{d}z}} + 2\mu_B \tag{2.32}$$

and the shear stress along the flow direction in (2.29) for the Bingham model is

$$\tau(z) = \tau_y + \mu_B \frac{\mathrm{d}U}{\mathrm{d}z} \tag{2.33}$$

Frictional non-linear viscoplastic fluids: The frictional Herschel-Bulkley viscoplastic model neglects the cohesive effects on the yield stress τ_0 and considers a Coulomb-type linear relation between the effective normal stress $\sigma_e(z)$ and the shear stress, hence

$$\tau_0 = \sigma_e(z)\, \tan\delta_f = \left[\rho g(z_s - z) - \mathcal{P}(z)\right] \tan\delta_f \tag{2.34}$$

where $\mathcal{P}(z)$ denotes de pore-fluid pressure and δ_f accounts for the effective friction angle bewteen solid particles [63].

Estimation of the pore pressure distribution $\mathcal{P}(z)$ is a challenging task for modeling multi-phase fluid-solid flows [55, 59, 63], although its effects on the reduction of the intergranular shear stress seem to be demonstrated [7, 8, 60, 85, 93]. The pore fluid pressure can be divided into a hydrostatic component $p_h(z)$ plus a pore pressure excess $p_e(z)$, hence

$$\mathcal{P}(z) = p_h(z) + p_e(z) \tag{2.35}$$

where the hydrostatic component is calculated as $p_h(z) = \rho_f g(z_s - z)$, being ρ_f the density of the pore-liquid. Following [29, 74, 112], the pressure excess can be idealized as a fraction of the hydrostatic pore pressure $p_h(z)$ and expressed as

$$p_e(z) = \mathcal{E}\rho_f g(z_s - z) \tag{2.36}$$

being $\mathcal{E}$ a tunning coefficient which usually takes values from about 0.4 to 0.8 [61, 74].

Using (2.34) and considering a plastic viscosity $K = \mu_P\ [Pa \cdot s^m]$, the generalized model (2.26) reduces to

$$\Phi_1(I_{2D}) = \frac{\sigma_e(z)\ \tan\delta_f}{\frac{1}{2}\frac{\mathrm{d}U}{\mathrm{d}z}} + 2\mu_P \left(\frac{\mathrm{d}U}{\mathrm{d}z}\right)^{m-1} \tag{2.37}$$

and the shear stress along the flow direction in (2.29) for the frictional Herschel-Bulkley model is

$$\tau(z) = \sigma_e(z)\ \tan\delta_f + \mu_P \left(\frac{\mathrm{d}U}{\mathrm{d}z}\right)^{m} \tag{2.38}$$

2.1.3 Closure formulations for the depth-averaged flow resistance

The stress terms plays a key role in geophysical surface flow modelling, specially when non-Newtonian behaviour is presented. This section is focused on the derivation of depth-integrated models for the flow resistance which incorporate the bulk rheological behaviour of the mixture in motion into the linear momentum conservation equations (2.22) and (2.23). Formulation of depth-averaged models for the shear stress requires to integrate the deviatoric stress tensor (2.25) throughout the flow column. This is not a trivial problem since the structure of the flow along the vertical direction is lost and only the averaged quantities are available.

From the above sections, assuming simple shear along the flow direction implies the deviatoric stress tensor (2.29) depending on the flow behaviour. Note that all the depth-averaged stress terms (T_{xx}, T_{xy}) and (T_{yx}, T_{yy}) (2.20) are null, and the basal resistance term $\boldsymbol{\tau_b} = (\tau_{bx}, \tau_{by})$ (2.19b) as

$$\tau_{bx} = (\tau_{xz})_b - (\tau_{xx})_b \frac{\partial z_b}{\partial x} - (\tau_{xy})_b \frac{\partial z_b}{\partial y} = \tau_b\, n_{ux} \tag{2.39a}$$

$$\tau_{by} = (\tau_{yz})_b - (\tau_{yx})_b \frac{\partial z_b}{\partial x} - (\tau_{yy})_b \frac{\partial z_b}{\partial y} = \tau_b\, n_{uy} \tag{2.39b}$$

where $\tau_b = \tau(z_b)$ is the shear stress at the basal interface along the flow direction. In order to obtain a depth-averaged formulation for the basal shear stress τ_b, the distributed shear stress function $\tau(z)$ must be integrated along the flow column imposing linearity. This allows to obtain a velocity distribution along the vertical direction which depends on the material rheology. The basal resistance τ_b must be expressed as a function of the depth-averaged flow variables.

Turbulent Newtonian flows: Surface flows involving water or granular mixtures with low solid concentrations usually show a Newtonian behaviour and most of the times occur in turbulent regime. Depth-averaged turbulent formulations are expressed as a quadratic relation on the depth-averaged velocity $\overline{U} = \sqrt{\overline{u}^2 + \overline{v}^2}$ as

$$\tau_b = \rho g h C_f \overline{U}^2 \tag{2.40}$$

where C_f $[L^{-2}T^2]$ is a friction coefficient which takes the form

$$C_f = \frac{n_b^2}{h^{4/3}} \tag{2.41}$$

for the Manning relationship, being n_b $[L^{-1/3}T]$ the Manning roughness parameter, and

$$C_f = \frac{1}{hC_z^2} \tag{2.42}$$

for the Chezy equation, where C_z $[L^{1/2}T]$ is the Chezy coeffcient.

Figure 2.1 shows the value of the basal resistance τ_b along the low direction using the Manning's turbulent model, and its normalized value $\tau_b/\rho gh$, for commom values of depth h and velocity $\overline{U}$ in environmental flows. The material density is set to $2000\, kg/m^3$ and the Manning's roughness parameter is $n_b = 0.040\, sm^{-1/3}$.

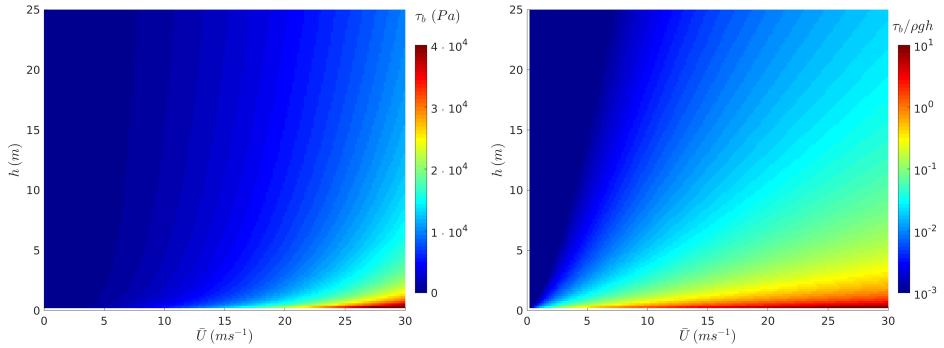

Figure 2.1: Basal resistance map in the $h - \overline{U}$ space for the Manning turbulent Newtonian model.

Cohesive viscoplastic flows: The linear viscoplastic relation, also called Bingham model, can be used to modelling laminar flows of cohesive materials. Assuming simple shear stress, the flow structure consists of the two separate regions depicted in Figure 2.2. For $z_0 < z \leq z_s$, the induced shear stress along the flow direction $\tau(z)$ is lower than the yield strength τ_y, hence

the velocity is constant throughout the plug region. In the lower region ($z_b < z \leq z_0$), the induced shear stress is larger than τ_y and the material is sheared.

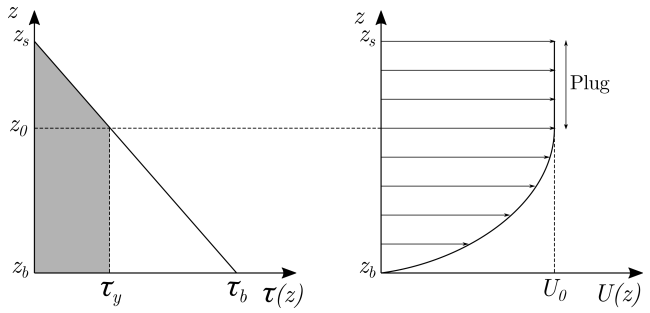

Figure 2.2: Velocity and stress distribution for the cohesive viscoplastic model.

The induced shear stress can be expressed as

$$\tau(z) = \tau_b \left(1 - \frac{z - z_b}{h}\right) \tag{2.43}$$

and, using (2.33), the velocity derivative in the shearing region reads

$$\frac{\mathrm{d}U}{\mathrm{d}z} = \frac{1}{\mu_B}\left(\tau(z) - \tau_y\right) \tag{2.44}$$

Replacing (2.43) into (2.44) and integrating throughout the shearing region $z_b < z \leq z_0$ allows to obtain the velocity profile for the entire flow column as

$$U(z) = \begin{cases} \dfrac{\tau_b - \tau_y}{\mu_B}(z - z_b) - \dfrac{\tau_b}{2\mu_B h}(z - z_b)^2 & \text{if} \quad z_b < z \leq z_0 \\ U_0 & \text{if} \quad z_0 < z \leq z_s \end{cases} \tag{2.45}$$

being z_0 the elevation of the shearing region and U_0 the velocity of the plug region, expressed as

$$z_0 = z_b + h\left(1 - \frac{\tau_y}{\tau_b}\right) \qquad U_0 = \frac{\tau_b h}{2\mu_B}\left(1 - \frac{\tau_y}{\tau_b}\right)^2 \tag{2.46}$$

Integrating (2.45) throughout the flow column leads to a cubic equation

$$\left(\frac{\tau_y}{\tau_b}\right)^3 - \left(3 + \frac{6\mu_B \overline{U}}{\tau_y h}\right)\frac{\tau_y}{\tau_b} + 2 = 0 \tag{2.47}$$

which relates the basal shear stress τ_b, the yield strength τ_y and the averaged flow velocity $\overline{U}$. Note that (2.47) can be rewritten as

$$2\tau_b^3 - 3\left(\tau_y + 2\mu_B \frac{\overline{U}}{h}\right)\tau_b^2 + \tau_y^3 = 0 \tag{2.48}$$

which can be analytically solved to obtain the basal resistance τ_b.

Figure 2.3 shows the value of the basal resistance τ_b along the low direction using the cohesive linear Bingham model for commom values of depth h and velocity $\overline{U}$ in viscoplastic surface flows. The material density is set to

$2000\,kg/m^3$ and the yield strength τ_y and Bingham viscosity μ_B are $2000\,Pa$ and $100\,Pa\cdot s$ respectively.

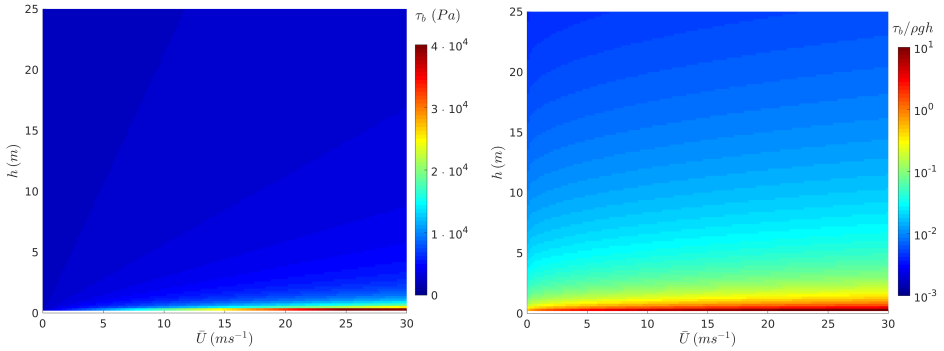

Figure 2.3: Basal resistance map in the $h-\overline{U}$ space for the cohesive Bingham model.

Frictional dilatant/pseudoplastic flows: The non-linear viscoplastic model with a Coulomb-type yield stress can be used to modelling liquid-solid mixture flows where the intergranular frictional stresses are important. If the pore-pressure excess in (2.34) is considered linear, the yield stress distribution can be estimated as

$$\sigma_e(z)\,\tan\delta_f = \left[\rho g h\left(1-\frac{z-z_b}{h}\right)-\mathcal{P}_b\left(1-\frac{z-z_b}{h}\right)\right]\tan\delta_f \tag{2.49}$$

where $\mathcal{P}_b$ is the pore-pressure at the bed surface, and hence the constitutive equation (2.38) can be rewritten as

$$\tau(z)=\tau_f\left(1-\frac{z-z_b}{h}\right)+\mu_P\left(\frac{\mathrm{d}U}{\mathrm{d}z}\right)^m \tag{2.50}$$

being

$$\tau_f=\left(\rho g h-\mathcal{P}_b\right)\tan\delta_f \tag{2.51}$$

the value of the frictional yield stress at the basal surface (Figure 2.4).

Assuming the induced shear distribution (2.43), the velocity derivative along the vertical direction can expressed as

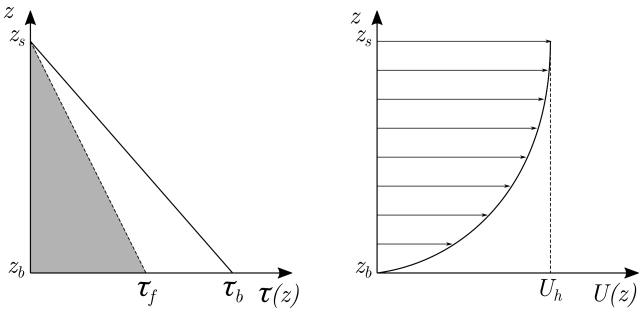

Figure 2.4: Velocity and stress distribution for the generalized non-linear frictional model.

$$\frac{\mathrm{d}U}{\mathrm{d}z} = \left[\frac{\tau_b - \tau_f}{\mu_P}\left(1 - \frac{z - z_b}{h}\right)\right]^{1/m} \tag{2.52}$$

and integrating (2.52) leads to the velocity vertical distribution

$$U(z) = \frac{m}{m+1}\left(\frac{\tau_b - \tau_f}{\mu_P}\right)^{1/m} h\left[1 - \left(1 - \frac{z - z_b}{h}\right)^{\frac{m+1}{m}}\right] \tag{2.53}$$

for the non-linear viscoplastic model. Note that the velocity at the free surface can be expressed as

$$U(z_s) \equiv U_h = \frac{m}{m+1}\left(\frac{\tau_b - \tau_f}{\mu_P}\right)^{1/m} h \tag{2.54}$$

Integrating (2.53) throughout the flow column leads to the depth averaged velocity

$$\overline{U} = \frac{m+1}{2m+1}U_h \tag{2.55}$$

which allows to obtain the basal shear stress τ_b as

$$\tau_b = \tau_f + \left(\frac{2m+1}{m}\right)^m \mu_P \left(\frac{\overline{U}}{h}\right)^m \tag{2.56}$$

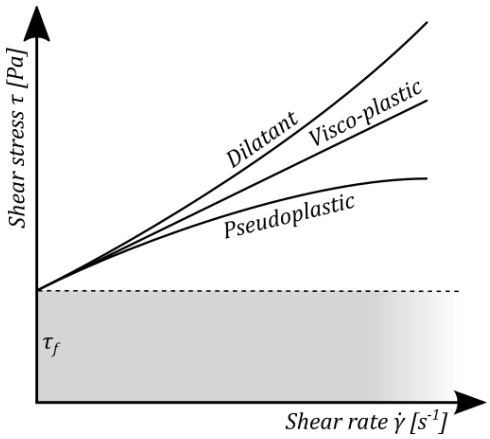

Figure 2.5: Basal resistance behaviour for the generalized non-linear frictional model (2.56).

It is worth mentioning that (2.56) represents a generalized depth-integrated formulation for viscoplastic flows (Figure 2.5) which encompasses:

- Pseudoplastic behaviour for $m < 1$, reducing the apparent viscosity as the induced shear rate increases. Taking $m = 0.5$ leads to

$$\tau_b = \tau_f + \left(\sqrt{2}\mu_P \dot{\gamma}^{-1/2}\right)\dot{\gamma} \tag{2.57}$$

  being $\dot{\gamma} = 2\overline{U}/h$ the macroscopic shear rate.

- Linear viscoplastic behaviour for $m = 1$, with a linear relation between shear stress and shear rate following

$$\tau_b = \tau_f + \left(\frac{3}{2}\mu_P\right)\dot{\gamma} \tag{2.58}$$

- Dilatant behaviour for $m > 1$, increasing the apparent viscosity as the induced shear rate grows. Taking $m = 2$ leads to

$$\tau_b = \tau_f + \left(\frac{25}{16}\mu_P\,\dot{\gamma}\right)\dot{\gamma} \tag{2.59}$$

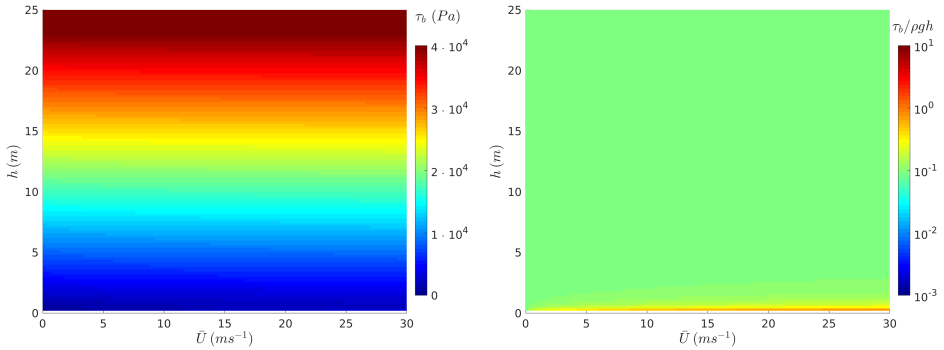

(a) Frictional pseudoplastic model $m = 0.5$ (2.57).

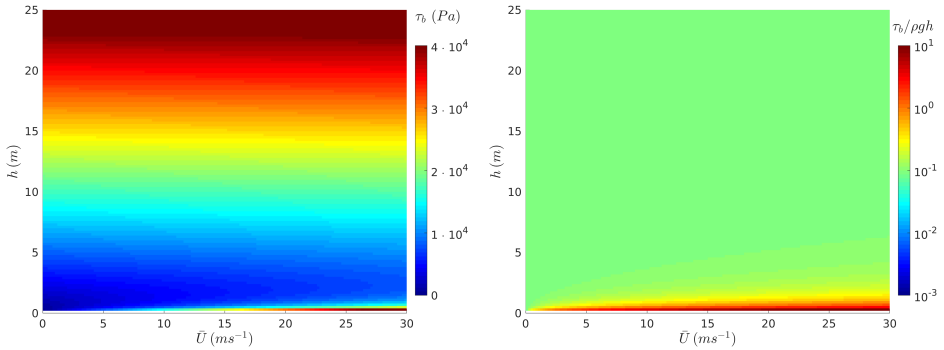

(b) Frictional viscoplastic model $m = 1.0$ (2.58).

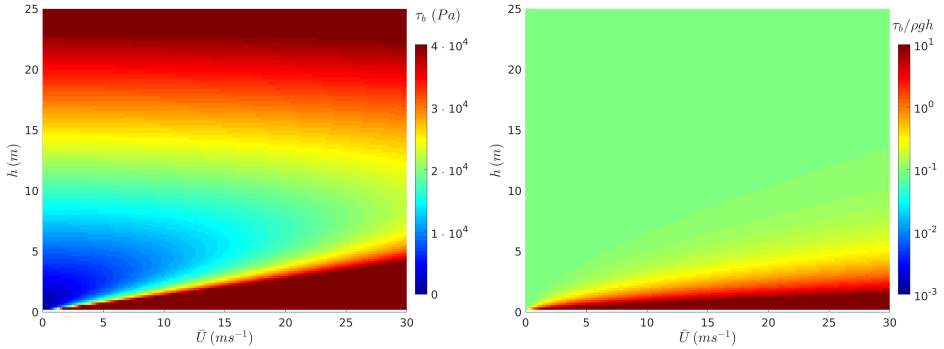

(c) Frictional dilatant model $m = 2.0$ (2.59).

Figure 2.6: Basal resistance map in the $h - \overline{U}$ space for the frictional non-linear Herschel-Bulkley model.

Figure 2.6 shows the value of the basal resistance τ_b along the flow direction using the frictional non-linear Herschel-Bulkley model for common

values of depth h and velocity $\overline{U}$ in surface flows, and using different values of the behavior exponent m. In this example, the material density is set to $2000\,kg/m^3$ and the plastic viscosity is $\mu_P = 100\,Pa \cdot s^m$. To estimate the frictional yield stress, the basal intergranular friction angle is $\delta_f = 10°$, the pore-fluid density is $\rho_f = 1000\,kg/m^3$ and the pore pressure is considered hydrostatic.

Frictional turbulent flows: Different hybrid formulations have been proposed for granular turbulent flows where grain shearing dominate at low shear rate. Based on (2.59), where the basal resistance increases proportionally to $\overline{U}^2$, the Turbulent & Coulomb relationship uses the Manning approach (2.41) to include the turbulent stresses into the basal resistance estimation as

$$\tau_b = \tau_f + \rho g \frac{n_b^2 \overline{U}^2}{h^{1/3}} \tag{2.60}$$

Also, based on the same quadratic relation with the velocity, the Voellmy model considers a Chezy-type relation (2.42) for including the turbulent stresses in the basal resistance as

$$\tau_b = \tau_f + \rho g \frac{\overline{U}^2}{C_z^2} \tag{2.61}$$

The value of the basal resistance τ_b along the flow direction using the Turbulent & Coulomb model is depicted in Figure 2.7 for common values of depth h and velocity $\overline{U}$ in surface flows. In this case, the material density is set to $2000\,kg/m^3$ and the Manning's roughness parameter is $n_b = 0.040\,sm^{-1/3}$. To estimate the frictional yield stress, the basal intergranular friction angle is $\delta_f = 10°$, the pore-fluid density is $\rho_f = 1000\,kg/m^3$ and the pore pressure for the frictional yield stress τ_f estimation (2.51) is considered hydrostatic.

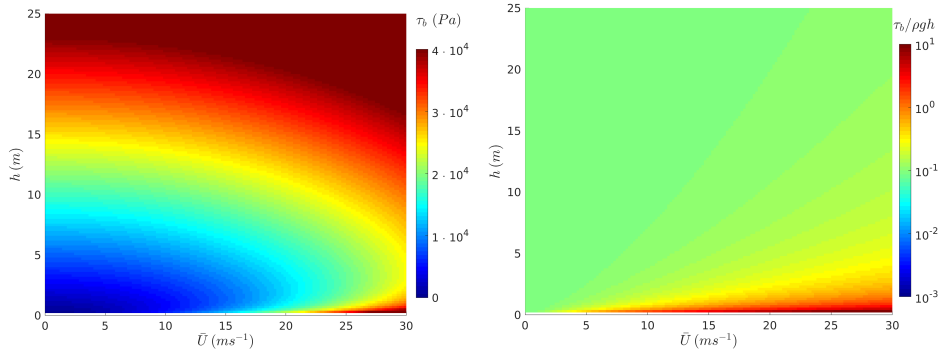

Figure 2.7: Basal resistance map in the $h - \overline{U}$ space for the Turbulent & Coulomb model.

Frictional viscoplastic flows: An alternative formulation for laminar flows of viscoplastic fluids with dominant grain shearing consists of replacing the

cohesive yield stress τ_y in the Bingham formulation (2.48) with a Coulomb-type term τ_f [107], leading to the Coulomb–viscous cubic equation

$$2\tau_b^3 - 3\left(\tau_f + 2\mu_B\frac{\overline{U}}{h}\right)\tau_b^2 + \tau_f^3 = 0 \tag{2.62}$$

for the basal resistance τ_b. Figure 2.8 shows the value of the basal resistance τ_b along the flow direction using the frictional viscoplastic model for common values of depth h and velocity $\overline{U}$ in viscoplastic surface flows. The material density is set to $2000\,kg/m^3$ with a plastic viscosity $\mu_B = 100\,Pa\cdot s$. To estimate the frictional yield stress, the basal intergranular friction angle is $\delta_f = 10°$, the pore-fluid density is $\rho_f = 1000\,kg/m^3$ and the pore pressure is considered hydrostatic.

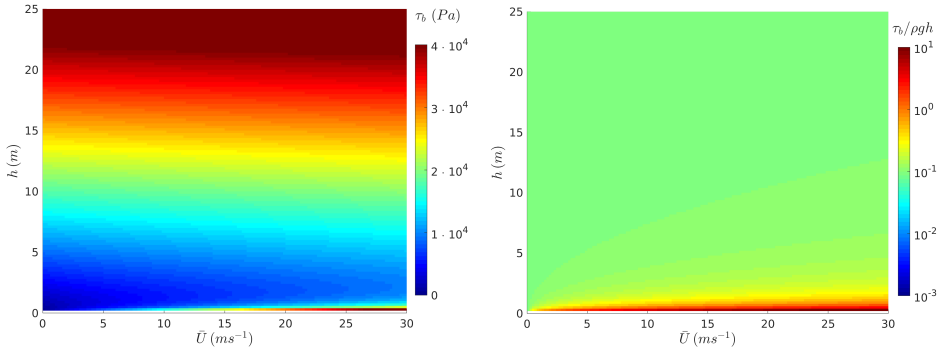

Figure 2.8: Basal resistance map in the $h-\overline{U}$ space for the Coulomb–viscous model.

Cohesive turbulent flows: Combining yield strength, viscous term and turbulent stresses leads to the quadratic formulation [68] for turbulent hyperconcentrated flows with dominant cohesive stress at low shear rates. For this additive model, the basal resistance can be expressed as

$$\tau_b = \tau_y + \frac{k_0}{8}\mu_B\frac{\overline{U}}{h} + \rho g\frac{n_b^2\overline{U}^2}{h^{1/3}} \tag{2.63}$$

where μ is the plastic viscosity of the material and k_0 is a resistance parameter. In the particular case of laminar flow in smooth, rectangular, wide channels, $k_0 = 24$ is usually suitable but it increases with roughness and irregular channel geometry [109].

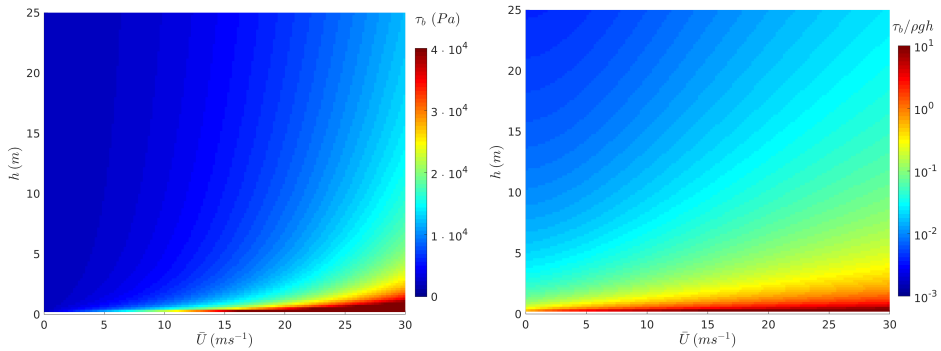

Figure 2.9: Basal resistance map in the $h-\overline{U}$ space for the cohesive–turbulent model.

The value of τ_b using the cohesive–turbulent model is depicted in Figure 2.9 for common values of depth h and velocity $\overline{U}$ in surface flows. The material density is set to $2000\,kg/m^3$, the yield strength is $\tau_y = 2000\,Pa$, the plastic viscosity is $\mu_B = 100\,Pa \cdot s$ and the Manning's roughness parameter is $n_b = 0.040\,sm^{-1/3}$.

Table 2.1 summarizes the different formulations for the basal resistance term $\boldsymbol{\tau_b}$ in the depth-averaged momentum equations.

Formulation	**Basal resistance**
Turbulent Newtonian	$\tau_b = \rho g h C_f \overline{U}^2$ Manning $C_f = \frac{n_b^2}{h^{4/3}}$ Chezy $C_f = \frac{1}{hC_z^2}$
Cohesive Bingham	$2\tau_b^3 - 3\left(\tau_y + 2\mu_B\frac{\overline{U}}{h}\right)\tau_b^2 + \tau_y^3 = 0$
Frictional dilatant/pseudoplastic	$\tau_b = \tau_f + \left(\frac{2m+1}{m}\right)^m \mu_P \left(\frac{\overline{U}}{h}\right)^m$ with $\tau_f = \left(\rho g h - \mathcal{P}_b\right)\tan\delta_f$
Frictional turbulent	$\tau_b = \tau_f + \rho g h C_f \overline{U}^2$
Frictional viscoplastic	$\tau_b^3 - 3\left(\tau_f + 2\mu_B\frac{\overline{U}}{h}\right)\tau_b^2 + \tau_f^3 = 0$
Cohesive turbulent	$\tau_b = \tau_y + \frac{k_0}{8}\mu_B\frac{\overline{U}}{h} + +\rho g\frac{n_b^2\overline{U}^2}{h^{1/3}}$

Table 2.1: Depth-averaged basal resistance formulations.

2.1.4 Local projection of the gravity force

Local coordinate systems are used for mathematical modelling of surface flows over steep slopes. Using the local bed-normal projection of the gravity vector along the direction $\mathbf{n}$ [64], the volumetric force (2.9) in the plane local coordinate system (x', z') (Figure 2.10) can be defined as

$$F_x' = -\rho g \sin\varphi_b \tag{2.64a}$$
$$F_z' = -\rho g \cos\varphi_b \tag{2.64b}$$

where φ_b is the bed-normal angle with the vertical, defined as

$$\tan\varphi_b = \nabla z_b \cdot \mathbf{n} = \cos\theta\frac{\partial z_b}{\partial x} + \sin\theta\frac{\partial z_b}{\partial y} \tag{2.65}$$

and $\mathbf{n} = (\cos\theta, \sin\theta)^T$ is the unit directional vector.

On one hand, assuming hydrostatic pressure along the bed-normal $z'-$coordinate, the corresponding momentum equation allows to define the bed-normal pressure distribution as

$$\frac{\partial p}{\partial z'} = -\rho g\cos\varphi_b \quad \Longrightarrow \quad p(z') \approx \overline{\rho} g\cos\varphi_b\,(z_s' - z') \tag{2.66}$$

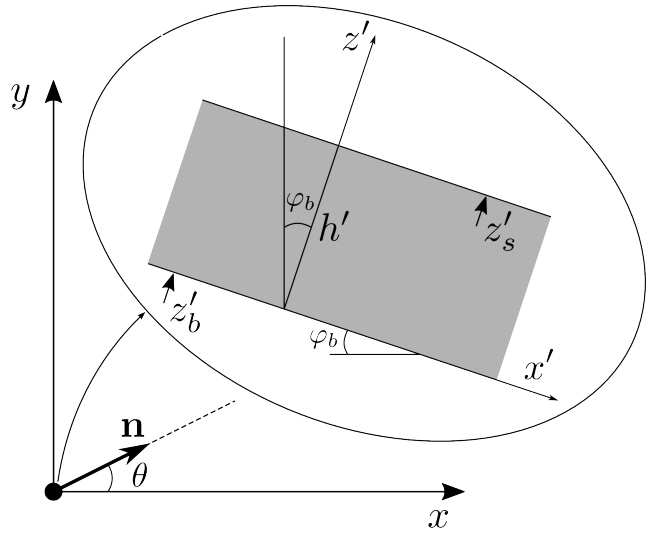

Figure 2.10: Local bed-normal projection of the gravity vector along the direction $\mathbf{n}$.

and, using $z'_s = z_s \cos\varphi_b$ and $z' = z\cos\varphi_b$, leads to

$$p(z) = \overline{\rho} g \cos^2\varphi_b \,(z_s - z) \tag{2.67}$$

which expresses the bed-normal pressure distribution in terms of global coordinates $\mathbf{X} = (x, y, z)$. Therefore, the integral of the pressure gradient along the global $x-$coordinate (2.16) can be expressed as

$$-\int_{z_b}^{z_s} \frac{\partial p(z)}{\partial x}\,\mathrm{d}z = -\frac{\partial}{\partial x}\big(\frac{1}{2} g\cos^2\varphi_b\,\overline{\rho} h^2\big) \tag{2.68}$$

and similarly for the global $y-$coordinate.

On the other hand, the integrals of the volumetric forces along the global $x-$ and $y-$coordinates are approximated as

$$\int_{z_b}^{z_s} F_x\,\mathrm{d}z \approx \int_{z'_b}^{z'_s} F'_x\,\mathrm{d}z'\cos\theta \approx -\overline{\rho} g\sin\varphi_b\, h'\cos\theta \tag{2.69a}$$

$$\int_{z_b}^{z_s} F_y\,\mathrm{d}z \approx \int_{z'_b}^{z'_s} F'_x\,\mathrm{d}z'\sin\theta \approx -\overline{\rho} g\sin\varphi_b\, h'\sin\theta \tag{2.69b}$$

and, using (2.65) and $h' = h\cos\varphi_b$, are expressed as

$$\int_{z_b}^{z_s} F_x\,\mathrm{d}z = -\overline{\rho} g\cos^2\varphi_b\, h\,(\nabla z_b\cdot\mathbf{n})\cos\theta \tag{2.70a}$$

$$\int_{z_b}^{z_s} F_y\,\mathrm{d}z = -\overline{\rho} g\cos^2\varphi_b\, h\,(\nabla z_b\cdot\mathbf{n})\sin\theta \tag{2.70b}$$

Note that, along $x-$coordinate, the directional vector takes the value $\mathbf{n} = (1, 0)^T$ and (2.70a) reduces to

$$\int_{z_b}^{z_s} F_x \, \mathrm{d}z = -g \cos^2 \varphi_b \, \overline{\rho} h \, \frac{\partial z_b}{\partial x} \tag{2.71}$$

Similarly, the directional vector is $\mathbf{n} = (0, 1)^T$ along $y-$coordinate and (2.70b) reads

$$\int_{z_b}^{z_s} F_y \, \mathrm{d}z = -g \cos^2 \varphi_b \, \overline{\rho} h \, \frac{\partial z_b}{\partial y} \tag{2.72}$$

Therefore, using a locally-projected gravity vector, the depth-integrated terms for the pressure and the external forces in the momentum equations along the $x-$ and $y-$coordinates, (2.1b) and (2.1c) respectively, can be expressed as

$$\int_{z_b}^{z_s} F_x \, \mathrm{d}z - \int_{z_b}^{z_s} \frac{\partial p(z)}{\partial x} \, \mathrm{d}z = -\frac{\partial}{\partial x}\left(\frac{1}{2} g_n \overline{\rho} h^2\right) - g_n \overline{\rho} h \, \frac{\partial z_b}{\partial x} \tag{2.73a}$$

$$\int_{z_b}^{z_s} F_y \, \mathrm{d}z - \int_{z_b}^{z_s} \frac{\partial p(z)}{\partial y} \, \mathrm{d}z = -\frac{\partial}{\partial y}\left(\frac{1}{2} g_n \overline{\rho} h^2\right) - g_n \overline{\rho} h \, \frac{\partial z_b}{\partial y} \tag{2.73b}$$

where $g_n = g \cos^2 \varphi_b$ denotes a reduced gravity value depending on the bed slope [64].

2.2 Solid transport in the flow column

2.2.1 Depth-integrated solid transport equation

The bulk density of the mixture can be decomposed into the solid and liquid fractions contributions as

$$\rho = \rho_f n + \rho_s \phi \tag{2.74}$$

being ρ_f and ρ_s the density of the fluid and solid phases, respectively, ϕ the volumetric solid-phase concentration and $n = 1 - \phi$ the volumetric fluid-phase fraction or mixture porosity. The mixture linear momentum is defined as $\rho \mathbf{u} = \rho_f n \mathbf{u_f} + \rho_s \phi \mathbf{u_s}$, being $\mathbf{u_f}$ the velocity of the pore-fluid and $\mathbf{u_s}$ the advective sediment particle velocity. Therefore, the bulk velocity of the mixture can be estimated as

$$\mathbf{u} = \frac{\rho_f n \mathbf{u_f} + \rho_s \phi \mathbf{u_s}}{\rho} \tag{2.75}$$

The solid-phase transport process is governed by the following 3D time-averaged mass-balance equation

$$\frac{\partial(\rho_s \phi)}{\partial t} + \frac{\partial}{\partial x}(u_{sx} \rho_s \phi) + \frac{\partial}{\partial y}(u_{sy} \rho_s \phi) + \frac{\partial}{\partial z}(u_{sz} \rho_s \phi) = 0 \tag{2.76}$$

where (u_{sx}, u_{sy}, u_{sz}) are the components of $\mathbf{u_s}$.

Because the solid-phase velocity is not included in the dependent variables of the fluid dynamic system, and assuming that the sediment particles are incompressible and non-porous, (2.76) is rewritten as

$$\frac{\partial \phi}{\partial t} + \frac{\partial}{\partial x}(u_x \phi) + \frac{\partial}{\partial y}(u_y \phi) + \frac{\partial}{\partial z}(u_z \phi) = \nabla \cdot \left[(\mathbf{u} - \mathbf{u_s})\phi\right] \tag{2.77}$$

Furthermore, one can use (2.74) and (2.75) to rewrite the term on the right hand side of (2.77) as

$$(\mathbf{u} - \mathbf{u_s}) = \frac{\rho_f}{\rho}(\mathbf{u_f} - \mathbf{u_s})(1 - \phi) = \frac{\rho_f}{\rho}\mathbf{q_w} \tag{2.78}$$

being $\mathbf{q_w} = (\mathbf{u_f} - \mathbf{u_s})(1-\phi)$ the volumetric flux of pore-fluid per unit area of mixture, also termed specific discharge or Darcy's velocity in porous media theory. Replacing (2.78) into (2.77) leads to

$$\frac{\partial \phi}{\partial t} + \frac{\partial}{\partial x}(u_x \phi) + \frac{\partial}{\partial y}(u_y \phi) + \frac{\partial}{\partial z}(u_z \phi) = \nabla \cdot \left(\frac{\rho_f}{\rho}\mathbf{q_w}\,\phi\right) \tag{2.79}$$

where the term on the right hand side accounts for the drag effects caused by the liquid phase on the advective solid flux.

The transport equation (2.79) must also be integrated throughout the entire flow column as

$$\begin{aligned}\int_{z_b}^{z_s} \partial_t(\phi)\,\mathrm{d}z + \int_{z_b}^{z_s} \partial_x(u_x\phi)\,\mathrm{d}z + \int_{z_b}^{z_s} \partial_y(u_y\phi)\,\mathrm{d}z + \int_{z_b}^{z_s} \partial_z(u_z\phi)\,\mathrm{d}z = \\ \int_{z_b}^{z_s} \nabla \cdot \left(\frac{\rho_f}{\rho}\mathbf{q_w}\,\phi\right)\mathrm{d}z\end{aligned} \tag{2.80}$$

and the Leibnitz's rule is applied to each term on the left hand side as follows

$$\int_{z_b}^{z_s} \partial_t(\phi)\,\mathrm{d}z = \frac{\partial}{\partial t}\int_{z_b}^{z_s} \phi\,\mathrm{d}z - (\phi)_s\frac{\partial z_s}{\partial t} + (\phi)_b\frac{\partial z_b}{\partial t} \tag{2.81a}$$

$$\int_{z_b}^{z_s} \partial_x(u_x\phi)\,\mathrm{d}z = \frac{\partial}{\partial x}\int_{z_b}^{z_s} u_x\phi\,\mathrm{d}z - (u_x\phi)_s\frac{\partial z_s}{\partial x} + (u_x\phi)_b\frac{\partial z_b}{\partial x} \tag{2.81b}$$

$$\int_{z_b}^{z_s} \partial_y(u_y\phi)\,\mathrm{d}z = \frac{\partial}{\partial y}\int_{z_b}^{z_s} u_y\phi\,\mathrm{d}z - (u_y\phi)_s\frac{\partial z_s}{\partial y} + (u_y\phi)_b\frac{\partial z_b}{\partial y} \tag{2.81c}$$

$$\int_{z_b}^{z_s} \partial_z(u_z\phi)\,\mathrm{d}z = (u_z\phi)_s - (u_z\phi)_b \tag{2.81d}$$

The total solid phase being transported in the flow column is expressed as

$$\overline{\phi}h = \int_{z_b}^{z_s} \phi \, \mathrm{d}z \tag{2.82}$$

defining $\overline{\phi}$ as the dept-averaged volumetric solid concentration. Using (2.6), (2.7) and (2.82), the solid phase flux integrals in (2.81) can be rewritten as

$$\int_{z_b}^{z_s} u_x \phi \, \mathrm{d}z = \overline{\phi} h \overline{u} + \int_{z_b}^{z_s} \rho (u_x - \overline{u}) \Big(\frac{\phi}{\rho} - \frac{\overline{\phi}}{\overline{\rho}} \Big) \, \mathrm{d}z = \overline{\phi} h \overline{u} - \overline{\phi} h D_{sx} \tag{2.83a}$$

$$\int_{z_b}^{z_s} u_y \phi \, \mathrm{d}z = \overline{\phi} h \overline{v} + \int_{z_b}^{z_s} \rho (u_y - \overline{v}) \Big(\frac{\phi}{\rho} - \frac{\overline{\phi}}{\overline{\rho}} \Big) \, \mathrm{d}z = \overline{\phi} h \overline{v} - \overline{\phi} h D_{sy} \tag{2.83b}$$

with (D_{sx}, D_{sy}) accounting for the depth-averaged dispersive flux due to the non-uniformity of both the velocity and solid concentration profiles throughout the flow column, and defined as

$$D_{sx} = -\frac{1}{\overline{\phi} h} \int_{z_b}^{z_s} \rho (u_x - \overline{u}) \Big(\frac{\phi}{\rho} - \frac{\overline{\phi}}{\overline{\rho}} \Big) \, \mathrm{d}z \tag{2.84a}$$

$$D_{sy} = -\frac{1}{\overline{\phi} h} \int_{z_b}^{z_s} \rho (u_y - \overline{v}) \Big(\frac{\phi}{\rho} - \frac{\overline{\phi}}{\overline{\rho}} \Big) \, \mathrm{d}z \tag{2.84b}$$

Therefore, replacing (2.82) and (2.83) into (2.81) and considering the kinematic boundary conditions at both the bed interface (2.3) and free surface (2.2), the depth-integrated equation for the solid phase in the flow column (2.80) reduces to

$$\begin{aligned} \frac{\partial (\overline{\phi} h)}{\partial t} + \frac{\partial}{\partial x} (\overline{\phi} h \overline{u}) + \frac{\partial}{\partial y} (\overline{\phi} h \overline{v}) &= -(\phi)_b N_b \\ &+ \frac{\partial}{\partial x} (\overline{\phi} h D_{sx}) + \frac{\partial}{\partial y} (\overline{\phi} h D_{sy}) \\ &+ \int_{z_b}^{z_s} \nabla \cdot \Big(\frac{\rho_f}{\rho} \mathbf{q_w} \, \phi \Big) \, \mathrm{d}z \end{aligned} \tag{2.85}$$

where $(\phi)_b$ denotes the solid concentration in the bed layer surface z_b and the last term on the right hand side accounts for the depth-integrated solid flux associated to the drag exerted by the liquid phase on the solid particles. This term is directly related to the solid particles dilation rate, i.e. the porosity creation in the flow column during the movement.

Furthermore, assuming that the volumetric solid concentration in the bed layer is $1 - \xi$ with ξ denoting the bulk porosity of the bed layer, the

solid mass conservation in the bed layer requires that

$$(1-\xi)\frac{\partial z_b}{\partial t} = (\phi)_b N_b \tag{2.86}$$

2.2.2 Dilation and pore-fluid pressure in densely-packed flows

The mass-balance equations for the solid and fluid phases in the mixture read

$$\frac{\partial n}{\partial t} + \nabla \cdot (\mathbf{u_f} n) = 0 \tag{2.87a}$$

$$\frac{\partial \phi}{\partial t} + \nabla \cdot (\mathbf{u_s} \phi) = 0 \tag{2.87b}$$

where $n = 1-\phi$ is the liquid volume fraction in the flow column or mixture porosity. We define the local dilation rate of the solid-liquid mixture as the divergence of the solid velocity $\nabla \cdot \mathbf{u_s}$, which is related by (2.87b) to the temporal evolution of the solid volumetric concentration ϕ as

$$\nabla \cdot \mathbf{u_s} = -\frac{1}{\phi}\frac{\mathrm{d}\phi}{\mathrm{d}t} \tag{2.88}$$

being $\mathrm{d}\phi/\mathrm{d}t = \partial\phi/\partial t + \mathbf{u_s}\cdot\nabla\phi$ the material time derivative of the solid volumetric concentration in a frame of reference which moves with the solid velocity [57]. Therefore, positive dilation rates are related to porosity creation states in which pores enlarge within the flow column, whereas negative dilation rates are accompanied by the contraction of the solid phase and, hence, increasing solid concentrations (Figure 2.11).

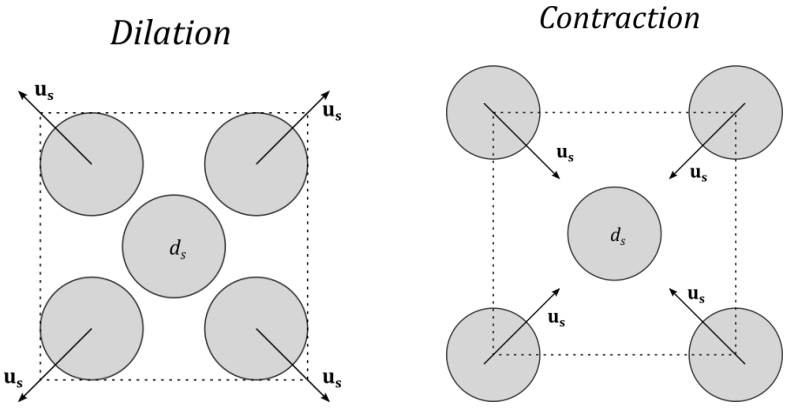

Figure 2.11: Dilation rate in (left) porosity creation states and (right) contraction states.

Estimation of the dilation rate involves several steps. First, we assume the dilatancy law

$$\nabla \cdot \mathbf{u_s} = \dot{\gamma}\tan\psi \tag{2.89}$$

as closure relation for the mechanical effects of the mixture movement on the solid phase evolution, being $\dot{\gamma}$ the macroscopic shear rate and ψ the shear-induced dilatancy, a state-dependent property of the solid granular materials which is usually expressed as an angle ($-\pi/2 \leq \psi \leq \pi/2$). For

the sake of simplicity, we assume here that $\dot{\gamma}\tan\psi$ is uniform along the flow column, implying that also the dilation rate is uniform.

Considering a steady shearing state, i.e. $\dot{\gamma} = \text{const} \neq 0$, (2.88) and (2.89) indicate that the solid grains divergence is also constant in time and hence leads to unbounded evolution of the solid volumetric concentration ϕ. This demonstrates that the shear-induced dilatancy ψ must evolve with the local mixture conditions. Forterre & Pouliquen [40] and Pailha & Pouliquen [113] suggested a linear dependency of $\tan\psi$ on the difference $(\overline{\phi}-\phi_{eq})$ as follows

$$\tan\psi = k_1(\overline{\phi} - \phi_{eq}) \tag{2.90}$$

being k_1 a positive calibration coefficient and ϕ_{eq} an equilibrium value of the solid concentration which is balanced with the local stress and shear rate. The effects of the stress and shear rate on the equilibrium solid concentration is assessed using the dimensionless ratio N_v between the characteristic time for local grain rearrangement μ/σ_e and the characteristic time for bulk shear deformation $1/\dot{\gamma}$ [43], being μ the pore-fluid viscosity and σ_e the effective normal stress. Considering the characteristic effective stress $\sigma_e \approx (\overline{\rho} - \rho_f)g_n h$, the timescale ratio N_v can be expressed as

$$N_v = \frac{\mu\dot{\gamma}}{(\overline{\rho} - \rho_f)g_n h} \tag{2.91}$$

Note that N_v is the reciprocal of the friction number identified by [55] to describe the stress state in debris flows. Since values of N_v vary from 0 in static state to ∞ for mature quasi-liquefied flows, a non-linear dependence of ϕ_{eq} on N_v is included as

$$\phi_{eq} = \phi_{crit}(1 - k_2\tanh N_v) \tag{2.92}$$

where k_2 is a positive coefficient which requires calibration and ϕ_{crit} is the equilibrium solid concentration for the static state in which the stresses are lithostatic [57]. It is worth noting that (2.92) implies that the equilibrium solid concentration ϕ_{eq} reduces monotonically in response to decreasing normal stresses and increasing shear rates but in a bounded range.

Second, adding (2.87a) and (2.87b) allows to relate the local dilation rate to the volumetric flux of pore-fluid per unit area of mixture $\mathbf{q_w}$ as

$$\nabla\cdot\mathbf{u_s} = -\nabla\cdot(\mathbf{u_f} - \mathbf{u_s})n = -\nabla\cdot\mathbf{q_w} \tag{2.93}$$

indicating that a positive dilation rate (porosity creation) is balanced by a local influx of fluid that fills the enlarging pores, whereas a negative dilation (porosity contraction) is accompanied by a local pore-fluid outflux leading to a denser packed mixture (Figure 2.12).

Considering the Darcy Law

$$\mathbf{q_w} = -\frac{\kappa}{\mu}\nabla p_e \tag{2.94}$$

being κ the hydraulic permeability of the granular aggregate and p_e the excess of pore-fluid pressure over the hydrostatic value

Replacing (2.89) and (2.94) into (2.93) leads to

$$\dot{\gamma}\tan\psi = \frac{\kappa}{\mu}\nabla^2 p_e \tag{2.95}$$

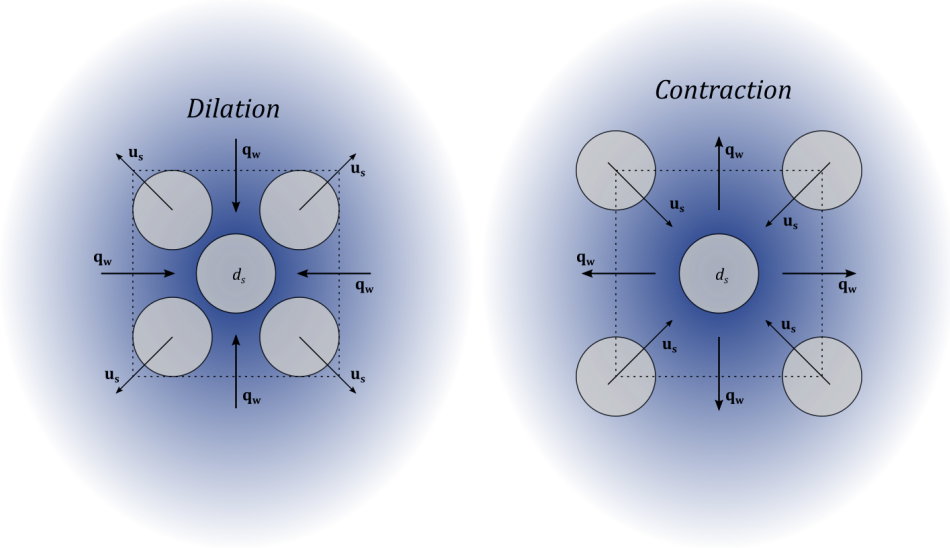

Figure 2.12: Dilation rate and pore-fluid flux balance for (left) a porosity creation state and (right) contraction state.

assuming that κ and μ are uniform. Invoking the shallow-flow scaling, $L >> H$ where L is the characteristic horizontal length of the flow and H is the characteristic flow depth, indicates that $\partial^2/\partial z^2 >> (\partial^2/\partial x^2, \partial^2/\partial y^2)$, since $\partial^2/\partial z^2$ scales with $1/H^2$ whereas $(\partial^2/\partial x^2, \partial^2/\partial y^2)$ scale with $1/L^2$ [57]. Therefore, the horizontal derivatives can be neglected and (2.95) reduces to

$$\frac{\partial^2 p_e}{\partial z^2} = \frac{\mu}{\kappa}\dot{\gamma}\tan\psi = \text{const} \tag{2.96}$$

which can been integrated twice throughout the flow column leading to

$$p_e(z) = \frac{\mu}{2\kappa}\dot{\gamma}\tan\psi(z - z_b)^2 + A(z - z_b) + B \tag{2.97}$$

being A and B two integration constants.

We assume that the excess pore pressure at the flow free surface is null, $p_e(z = z_s) = 0$, since the pore pressure is the atmospheric value. At the bed surface, we impose that the excess pore pressure can be written as $p_e(z = z_b) = \mathcal{E}_b\rho_f g_n h$, being $\mathcal{E}_b$ a dimensionless parameter which expresses the basal excess pore pressure as a fraction of the hydrostatic pressure value at the bed level. Furthermore, at the bed surface, the specific discharge $\mathbf{q_w}$ is null since the solid and liquid phase velocities are assumed equal (non-penetration condition) and hence, using (2.94), we impose $\partial p_e/\partial z(z = z_b) = 0$. Imposing these boundary conditions, we find that the excess pore pressure along the flow column satisfies the quadratic expression

$$p_e(z) = \frac{\mu}{2\kappa}\dot{\gamma}\tan\psi(z - z_b)^2 + \mathcal{E}_b\rho_f g_n h \tag{2.98}$$

being the basal excess pore pressure parameter $\mathcal{E}_b$

$$\mathcal{E}_b = \frac{-\mu h}{2\kappa\rho_f g_n}\dot{\gamma}\tan\psi \tag{2.99}$$

and the depth-averaged shear rate is estimated as $\dot{\gamma} = 2|\mathbf{u}|/h$. Note that (2.98) indicates that the value of the excess pore pressure depends on the shearing-state of the flow and it is null, i.e. hydrostatic pore-fluid pressure, for the lithostatic case.

In order to assess the behaviour predicted by (2.98) for the excess pore pressure in a realistic mature dense-packed flow, we set $\mu = 10^{-3}\,Pa \cdot s$, $\kappa = 10^{-8}\,m^2$ $h = 10\,m$, $\dot{\gamma} = 6\,s^{-1}$, $\phi_{eq} = 0.6$, $k_1 = 0.05$, $\rho_f = 1000\,kgm^{-3}$, $g = 9.81\,ms^{-2}$, $\varphi_b = 15°$ and vary $\overline{\phi}$ from 0.50 to 0.65. Figure 2.13 depicts the normalised pore-fluid pressure $\mathcal{P}^*(z)$ defined as

$$\mathcal{P}^*(z) = \frac{\mathcal{P}(z)}{\rho_f g_n h} = \frac{p_h(z) + p_e(z)}{\rho_f g_n h} \tag{2.100}$$

along the normalised flow depth $z^* = (z - z_b)/h$ for the different solid volumetric concentration considered.

Positive excess pore pressure p_e values, i.e. a pore-fluid pressure $\mathcal{P}$ higher than the hydrostatic value p_h, are associated to negative dilatancy values $\tan\psi < 0$ and hence to porosity contraction states. Contrarily, negative excess pore pressure p_e values, i.e. a pore-fluid pressure $\mathcal{P}$ lower than the hydrostatic value p_h, denote positive dilatancy values $\tan\psi > 0$ associated to porosity creation states.

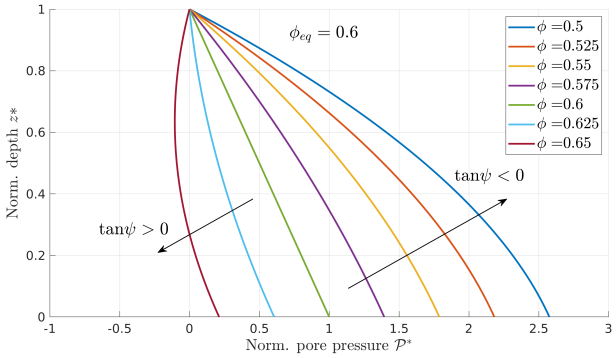

Figure 2.13: Pore-fluid pressure as a function of the solid volumetric concentration ϕ.

The expression (2.98) estimates a behaviour for the excess pore-fluid pressure which depends on the shear rate, with the hydrostatic pressure corresponding to the lithostatic stress case. Figure 2.14 shows the reduction of the normalised pore-fluid pressure $\mathcal{P}^*(z)$ with increasing depth-averaged shear rates $\dot{\gamma}$ for an idealised case with the above parameters and considering a positive dilatancy value $\overline{\phi} = 0.65 > \phi_{eq}$.

Contrarily, Figure 2.15 shows the increment of the normalised pore-fluid pressure $\mathcal{P}^*(z)$ with increasing depth-averaged shear rates $\dot{\gamma}$ for the same idealised case with a negative dilatancy value $\overline{\phi} = 0.55 < \phi_{eq}$.

The excess pore pressure distribution estimated with (2.98) shows a similar behaviour to that obtained by George & Iverson [43, 57]. However, here the value of the basal pore-fluid pressure $\mathcal{P}_b$ is directly determined from the local characteristics of the flow and mixture state as

$$\mathcal{P}_b = (1 + \mathcal{E}_b)\rho_f g_n h \tag{2.101}$$

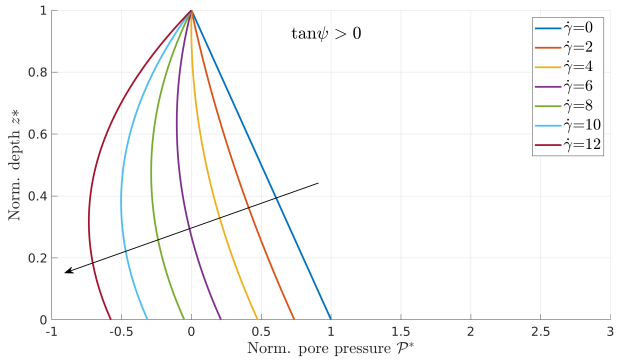

Figure 2.14: Pore-fluid pressure as a function of the shear rate $\dot{\gamma}$ for a positive dilatancy state $\tan\psi > 0$.

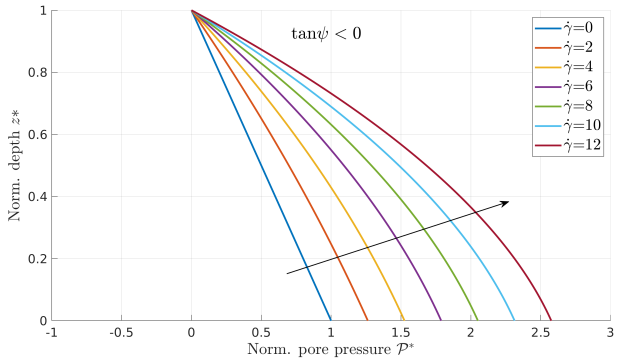

Figure 2.15: Pore-fluid pressure as a function of the shear rate $\dot{\gamma}$ for a negative dilatancy state $\tan\psi < 0$.

Iverson & George [57] also reported a quadratic expression for the pore-fluid pressure but they require to solve an additional advection-diffusion equation for the basal pore fluid pressure.

2.2.3 Deviatoric solid flux due to dilation effects

The last source term in the depth-averaged solid transport equation (2.85), caused by porosity creation/contraction processes due to the shear-induced dilation of the solid phase, mus be addressed now. It is repeated here as

$$\int_{z_b}^{z_s} \frac{\partial}{\partial x}\left(\rho_f \frac{\phi}{\rho} q_{wx}\right) + \frac{\partial}{\partial y}\left(\rho_f \frac{\phi}{\rho} q_{wy}\right) + \frac{\partial}{\partial z}\left(\rho_f \frac{\phi}{\rho} q_{wz}\right) \mathrm{d}z \tag{2.102}$$

being (q_{wx}, q_{wy}, q_{wz}) the components of the specific solid discharge $\mathbf{q_w}$. Applying the Leibnitz rule

$$\int_{z_b}^{z_s} \frac{\partial}{\partial x}\left(\rho_f \frac{\phi}{\rho} q_{wx}\right) \mathrm{d}z = \frac{\partial}{\partial x} \int_{z_b}^{z_s} \left(\rho_f \frac{\phi}{\rho} q_{wx}\right) \mathrm{d}z - \left(\rho_f \frac{\phi}{\rho} q_{wx}\right)_s \frac{\partial z_s}{\partial x} + \left(\rho_f \frac{\phi}{\rho} q_{wx}\right)_b \frac{\partial z_b}{\partial x} \tag{2.103a}$$

$$\int_{z_b}^{z_s} \frac{\partial}{\partial y}\left(\rho_f \frac{\phi}{\rho} q_{wy}\right) \mathrm{d}z = \frac{\partial}{\partial y} \int_{z_b}^{z_s} \left(\rho_f \frac{\phi}{\rho} q_{wy}\right) \mathrm{d}z - \left(\rho_f \frac{\phi}{\rho} q_{wy}\right)_s \frac{\partial z_s}{\partial y} + \left(\rho_f \frac{\phi}{\rho} q_{wy}\right)_b \frac{\partial z_b}{\partial y} \tag{2.103b}$$

$$\int_{z_b}^{z_s} \frac{\partial}{\partial z}\left(\rho_f \frac{\phi}{\rho} q_{wz}\right) \mathrm{d}z = \left(\rho_f \frac{\phi}{\rho} q_{wz}\right)_s - \left(\rho_f \frac{\phi}{\rho} q_{wz}\right)_b \tag{2.103c}$$

At the bed surface boundary z_b we assume that the solid and liquid phases move with the same velocity, leading to a nil specific discharge

$$(q_{wx}, q_{wy}, q_{wz})_b = 0 \tag{2.104}$$

whereas, at the flow free surface z_s, the kinematic condition

$$(q_{wx})_s \frac{\partial z_s}{\partial x} + (q_{wy})_s \frac{\partial z_s}{\partial y} - (q_{wz})_s = 0 \tag{2.105}$$

is imposed, which implies that the free surfaces for the solid and liquid phases are the same at any moment and move with the flow free surface $z_s = z_s(t, x, y)$.

Replacing (2.104) and (2.105) into (2.103), and considering the Darcy Law (2.94) relating the specific discharge $\mathbf{q_w}$ to the excess pore pressure gradient, the depth-averaged source term (2.102) can be rewritten as

$$-\frac{\partial}{\partial x} \int_{z_b}^{z_s} \left(\rho_f \frac{\phi}{\rho} \frac{\kappa}{\mu} \frac{\partial p_e}{\partial x}\right) \mathrm{d}z - \frac{\partial}{\partial y} \int_{z_b}^{z_s} \left(\rho_f \frac{\phi}{\rho} \frac{\kappa}{\mu} \frac{\partial p_e}{\partial y}\right) \mathrm{d}z \tag{2.106}$$

transforming the non-conservative dilation source term [57] into a conservative advective contribution to the solid phase flux $(\mathcal{L}_x, \mathcal{L}_y)$. Hence, the depth-averaged solid phase transport equation (2.85) now reads

$$\begin{aligned} \frac{\partial(\overline{\phi}h)}{\partial t} + \frac{\partial}{\partial x}(\overline{\phi}h\overline{u} + \mathcal{L}_x) + \frac{\partial}{\partial y}(\overline{\phi}h\overline{v} + \mathcal{L}_y) = -(\phi)_b N_b \\ + \frac{\partial}{\partial x}(\overline{\phi}hD_{sx}) + \frac{\partial}{\partial y}(\overline{\phi}hD_{sy}) \end{aligned} \tag{2.107}$$

with $(\mathcal{L}_x, \mathcal{L}_y)$ being the solid dilation flux depending on the pore-fluid pressure gradient and defined as

$$\mathcal{L}_x = \int_{z_b}^{z_s} \left(\rho_f \frac{\phi}{\rho} \frac{\kappa}{\mu} \frac{\partial p_e}{\partial x} \right) \mathrm{d}z \tag{2.108a}$$

$$\mathcal{L}_y = \int_{z_b}^{z_s} \left(\rho_f \frac{\phi}{\rho} \frac{\kappa}{\mu} \frac{\partial p_e}{\partial y} \right) \mathrm{d}z \tag{2.108b}$$

In order to obtain an expression for the depth-integrated $(\mathcal{L}_x, \mathcal{L}_y)$ fluxes and, for the sake of simplicity, we assume the approximation $\phi/\rho = \overline{\phi}/\overline{\rho}$ and uniform mixture permeability κ and pore-fluid viscosity μ. Applying the Leibnitz rule to (2.108) leads to

$$\int_{z_b}^{z_s} \left(\rho_f \frac{\phi}{\rho} \frac{\kappa}{\mu} \frac{\partial p_e}{\partial x} \right) \mathrm{d}z = \overline{\phi} \frac{\rho_f \kappa}{\overline{\rho} \mu} \left(\frac{\partial}{\partial x} \int_{z_b}^{z_s} p_e \, \mathrm{d}z - (p_e)_s \frac{\partial z_s}{\partial x} + (p_e)_b \frac{\partial z_b}{\partial x} \right) \tag{2.109a}$$

$$\int_{z_b}^{z_s} \left(\rho_f \frac{\phi}{\rho} \frac{\kappa}{\mu} \frac{\partial p_e}{\partial y} \right) \mathrm{d}z = \overline{\phi} \frac{\rho_f \kappa}{\overline{\rho} \mu} \left(\frac{\partial}{\partial y} \int_{z_b}^{z_s} p_e \, \mathrm{d}z - (p_e)_s \frac{\partial z_s}{\partial y} + (p_e)_b \frac{\partial z_b}{\partial y} \right) \tag{2.109b}$$

and, considering the excess pore pressure distribution (2.98) throughout the flow depth, the dilation contributions can be expressed as

$$\mathcal{L}_x = \overline{\phi} \frac{\rho_f \kappa}{\overline{\rho} \mu} \left(\frac{\partial \mathcal{P}_e}{\partial x} + \mathcal{E}_b \rho_f g h \cos\varphi_b \frac{\partial z_b}{\partial x} \right) \tag{2.110a}$$

$$\mathcal{L}_y = \overline{\phi} \frac{\rho_f \kappa}{\overline{\rho} \mu} \left(\frac{\partial \mathcal{P}_e}{\partial y} + \mathcal{E}_b \rho_f g h \cos\varphi_b \frac{\partial z_b}{\partial y} \right) \tag{2.110b}$$

where $\mathcal{E}_b$ is the basal excess pore pressure parameter defined in (2.99) and $\mathcal{P}_e$ is the excess pore pressure integrated throughout the flow column, which reduces to

$$\mathcal{P}_e = \int_{z_b}^{z_s} p_e \, \mathrm{d}z = \frac{-\mu h^3}{3\kappa} \dot{\gamma} \tan\psi \tag{2.111}$$

2.2.4 Net mass exchange between bed and flow layers

The net volumetric exchange N_b between the underlying bed layer and the mixture flow column at the bed surface $z_b(t, x, y)$, appearing in (2.8), (2.22), (2.23), (2.85) and (2.86), is modelled as the balance between the erosion and the deposition vertical solid fluxes, E_b and D_b respectively, leading to

$$N_b = \frac{1}{(\phi)_b} (D_b - E_b) \tag{2.112}$$

Note that N_b includes solid and pore volumes whereas E_b and D_b are expressed in terms of solid volume, hence the solid volumetric concentration at the bed surface $(\phi)_b$ must be included in (2.112). For the sake of simplicity, the solid concentration at the bed surface z_b is usually set to that of the underlying bed layer $(\phi)_b = 1 - \xi$.

The deposition rate D_b is commonly related to the solid particles settling velocity in the mixture ω_{sm} and to the near-bed solid concentration in the flow $\phi_{z\to z_b}$. The near-bed solid concentration is not a dependent variable to be solved, hence it is usually related to the depth-averaged solid concentration in the flow as $\phi_{z\to z_b} = \alpha\overline{\phi}$ being α an adaptation or recovery coefficient. Therefore, the vertical deposition flux can be expressed as

$$D_b = \alpha\,\omega_{sm}\,\overline{\phi} \tag{2.113}$$

The settling velocity of the solid particles ω_{sm} in highly concentrated mixtures is influenced by the presence of other solid particles. Furthermore, in dense-packed mixtures with moderate plastic fine fractions in the flow column such as muddy slurries, the particle settling velocity can be strongly reduced by the development of internal yield stresses in the pore-fluid. There exist several relationships in the specialised literature to estimate the hindering effects of high solid concentration in the settling velocity. Richardson & Zaki [124] proposed $\omega_{sm} = (1-\overline{\phi})^m\omega_s$, being ω_s the settling velocity of the sediment particles in clear water and m a hindering empirical exponent depending on the Reynolds particle number ($Re_p = \omega_s\,d_s/\nu$, with ν the clear water kinematic viscosity) which usually takes values close to $m = 4$. Therefore, for the sake of simplicity, we assume that the vertical deposition rate D_b in dense-packed mixtures is expressed as

$$D_b = \alpha_d\,\omega_s\,\overline{\phi}\,(1-\overline{\phi})^4 \tag{2.114}$$

where α_d is a dimensionless parameter which requires calibration.

The erosion solid flux E_b is directly related to the turbulent fluctuation of the volumetric solid concentration and flow velocity near the bed surface. We assume that this near-bed erosion rate is at the capacity of the flow to entrain solid material from the underlying bed layer, hence it is related to the settling velocity of the particles in clear water ω_s and the near equilibrium concentration $\phi^*_{z\to z_b}$. The near-bed equilibrium concentration is related to the depth-averaged equilibrium concentration $\overline{\phi^*}$ as $\phi^*_{z\to z_b} = \alpha^*\overline{\phi^*}$, being α^* an adaptation coefficient under equilibrium conditions. When equilibrium solid transport states are reached, the adaptation coefficients α and α^* coincide but in non-equilibrium states $\alpha^* \neq \alpha$ generally. Therefore, for the sake of simplicity, we assume that the vertical erosion rate E_b is expressed as

$$E_b = \alpha_e\omega_s\,\overline{\phi^*} \tag{2.115}$$

where α_e is a dimensionless empirical parameter which requires calibration. The capacity solid concentration $\overline{\phi^*}$ is usually computed as

$$\overline{\phi^*} = \frac{|\mathbf{q}^*_\mathbf{s}|}{h|\mathbf{u}|} \tag{2.116}$$

where $|\mathbf{q}_\mathbf{s}^*|$ accounts for the value of the solid transport throughout the flow column in capacity or equilibrium condition, which can be estimated using the multiple empirical relationships from the local hydrodynamic variables [144].

2.3 Bedload transport

2.3.1 Solid mass conservation in bedload transport

The bedload transport occurs in a thin top layer of the bed, between the exchange interface $z_e = z_e(t,x,y)$ separating the static and moving bed layers and the top surface of the bed layer $z_b = z_b(t,x,y)$. The solid mass conservation at the bedload transport layer reads

$$\frac{\partial(\rho_s\phi_b)}{\partial t} + \frac{\partial}{\partial x}(u_{bx}\rho_s\phi_b) + \frac{\partial}{\partial y}(u_{by}\rho_s\phi_b) + \frac{\partial}{\partial z}(u_{bz}\rho_s\phi_b) = 0 \tag{2.117}$$

where ϕ_b is the volumetric solid concentration and $[u_{bx}, u_{by}, u_{bz}]$ are the components of the velocity of the solid particles $\mathbf{u_b}$ in the bedload layer. Considering that the solid and liquid phases move with the same velocity $\mathbf{u_b}$ in the transport layer, the kinematic boundary conditions at the z_e and z_b surfaces can be expressed as

$$\frac{\partial z_b}{\partial t} + (u_{bx})_b\frac{\partial z_b}{\partial x} + (u_{by})_b\frac{\partial z_b}{\partial y} = (u_{bz})_b \tag{2.118}$$

$$\frac{\partial z_e}{\partial t} + (u_{bx})_e\frac{\partial z_e}{\partial x} + (u_{by})_e\frac{\partial z_e}{\partial y} = (u_{bz})_e + N_e \tag{2.119}$$

being N_e the volumetric exchange flux between the bedload transport layer and the underlying static stratum along the $z-$coordinate. It is worth noting that the net exchange flux between the bed layer and the flow is not considered in (2.118), assuming that the suspended solid transport is negligible.

The transport equation (2.117) is integrated along the bedload moving or transport layer as

$$\int_{z_e}^{z_b} \partial_t(\phi_b)\,\mathrm{d}z + \int_{z_e}^{z_b} \partial_x(u_{bx}\phi_b)\,\mathrm{d}z + \int_{z_e}^{z_b} \partial_y(u_{by}\phi_b)\,\mathrm{d}z + \int_{z_e}^{z_b} \partial_z(u_{bz}\phi_b)\,\mathrm{d}z = 0 \tag{2.120}$$

and the Leibnitz's rule is applied to each term as follows

$$\int_{z_e}^{z_b} \partial_t(\phi_b)\,\mathrm{d}z = \frac{\partial}{\partial t}\int_{z_e}^{z_b} \phi_b\,\mathrm{d}z - (\phi_b)_b\frac{\partial z_b}{\partial t} + (\phi_b)_e\frac{\partial z_e}{\partial t} \tag{2.121a}$$

$$\int_{z_e}^{z_b} \partial_x(u_{bx}\phi_b)\,\mathrm{d}z = \frac{\partial}{\partial x}\int_{z_e}^{z_b} u_{bx}\phi_b\,\mathrm{d}z - (u_{bx}\phi_b)_b\frac{\partial z_b}{\partial x} + (u_{bx}\phi_b)_e\frac{\partial z_e}{\partial x} \tag{2.121b}$$

$$\int_{z_e}^{z_b} \partial_y(u_{by}\phi_b)\,\mathrm{d}z = \frac{\partial}{\partial y}\int_{z_e}^{z_b} u_{by}\phi_b\,\mathrm{d}z - (u_{by}\phi_b)_b\frac{\partial z_b}{\partial y} + (u_{by}\phi_b)_e\frac{\partial z_e}{\partial y} \tag{2.121c}$$

$$\int_{z_e}^{z_b} \partial_z(u_{bz}\phi_b)\,\mathrm{d}z = (u_{bz}\phi_b)_b - (u_{bz}\phi_b)_e \tag{2.121d}$$

The volumetric solid concentration in the transport layer is assumed uniform and approximately the same as in the underlying static stratum, $\phi_b \approx 1-\xi$ with ξ denoting the bulk porosity of the bed layer. Therefore, the solid mass integral in (2.121a) is expressed as

$$\int_{z_e}^{z_b} \phi_b\,\mathrm{d}z = (1-\xi)\eta \tag{2.122}$$

where $\eta = z_b - z_e$ is the bedload transport layer thickness. Accordingly, the linear momentum integrals in (2.121b) and (2.121c) are reduced to

$$\int_{z_e}^{z_b} u_{bx}\phi_b\,\mathrm{d}z = (1-\xi)\eta\,\overline{u_b} = q_{bx} \tag{2.123a}$$

$$\int_{z_e}^{z_b} u_{by}\phi_b\,\mathrm{d}z = (1-\xi)\eta\,\overline{v_b} = q_{yx} \tag{2.123b}$$

being $(\overline{u_b}, \overline{v_b})$ the components of the depth-averaged bedload velocity $\overline{\mathbf{u_b}}$, defined as

$$\overline{u_b} = \frac{1}{\eta}\int_{z_e}^{z_b} u_{bx}\,\mathrm{d}z \qquad \overline{v_b} = \frac{1}{\eta}\int_{z_e}^{z_b} u_{by}\,\mathrm{d}z \tag{2.124}$$

and hence (q_{bx}, q_{by}) are the components of the bedload solid transport rate $\mathbf{q_b}$ along the $x-$ and $y-$coordinates respectively.

Replacing (2.122) and (2.123) into (2.121), and considering the boundary conditions at both the exchange interface (2.119) and the bed surface (2.118), the depth-integrated transport equation for the bedload layer (2.120) is reduced to

$$(1-\xi)\frac{\partial \eta}{\partial t} + \frac{\partial}{\partial x}(q_{bx}) + \frac{\partial}{\partial y}(q_{by}) = -(1-\xi)N_e \tag{2.125}$$

The first term on the left hand side of (2.125) accounts for the solid mass storage in the bedload transport layer whereas the term on the right hand

side represents the net solid flux across the exchange interface separating the static stratum and the moving bedload layer.

Furthermore, the solid mass continuity in the static underlying bed layer, $z \in (z_r, z_e)$ being z_r the elevation of lower non-erodible stratum taken as reference, requires that

$$(1-\xi)\frac{\partial z_e}{\partial t} = (1-\xi)N_e \tag{2.126}$$

The volumetric exchange between the bedload transport layer and the underlying static stratum N_e is expressed by the balance between the deposition flux $\dot{\eta}_D$ and the entrainment flux $\dot{\eta}_E$ as

$$N_e = \dot{\eta}_D - \dot{\eta}_E \tag{2.127}$$

Finally, adding (2.125) and (2.126) leads to the continuity equation for the solid mass in the bed layer

$$\frac{\partial z_b}{\partial t} + \frac{1}{1-\xi}\frac{\partial}{\partial x}(q_{bx}) + \frac{1}{1-\xi}\frac{\partial}{\partial y}(q_{by}) = 0 \tag{2.128}$$

which estimates the bed elevation changes in flows with bedload transport.

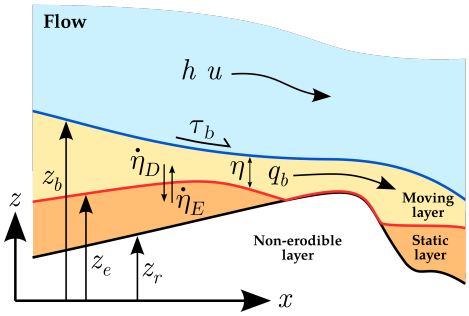

Figure 2.16: Sketch of the bedload sediment transport.

The bedload transport rate $\mathbf{q_b} = (q_{bx}, q_{by})$, required in (2.125) and (2.128), accounts for the volumetric solid discharge (excluding porosity) integrated in the bedload transport layer and needs a closure model which relates the $\mathbf{q_b}$ to the local flow features. The solid particles can be transported under equilibrium (capacity or saturated) conditions or non-capacity (non-equilibrium or unsaturated) conditions. The classical equilibrium approach assumes that the actual sediment transport rate is equal to the capacity of the flow to carry solid weight. This equilibrium bedload rate $\mathbf{q_b^*}$ is only determined by instantaneous local flow features and can be formulated by different empirical closure relations found in literature [149]. On the other hand, in non-capacity transport, the actual bedload rate is computed through advection and mass exchange with the static erodible bed. Natural morphodynamical systems such as alluvial rivers are always changing in time and space and hence absolute equilibrium states rarely exist in natural conditions. Therefore, intuitively, non-capacity approaches are more suitable than models based on the equilibrium assumption since they account for the temporal and spatial delay of the actual sediment transport rate with respect to its potential capacity. However, if the adaptation delay is sufficiently small, equilibrium models can be also applied at least in theory [144].

Therefore, under equilibrium conditions $\dot{\eta}_D = \dot{\eta}_E$, (2.126) can be neglected since $\partial z_e/\partial t = 0$ and (2.125) reduces to the widespread Exner equation

$$(1-\xi)\frac{\partial z_b}{\partial t} + \frac{\partial}{\partial x}(q^*_{bx}) + \frac{\partial}{\partial y}(q^*_{by}) = 0 \tag{2.129}$$

for capacity bedload models [35] since $\partial \eta^*/\partial t = \partial z_b/\partial t$, being η^* the transport layer thickness under capacity conditions and (q^*_{bx}, q^*_{by}) the components of the capacity bedload rate $\mathbf{q^*_b}$ along the $x-$ and $y-$coordinates.

2.3.2 Entrainment and deposition rates for bedload transport

The derivation of the expressions used in this thesis for the bedload entrainment and deposition fluxes, $\dot{\eta}_E$ and $\dot{\eta}_D$ respectively used in (2.127), is based on the grain-scale inertial analysis proposed by Charru [25] for the exchange of solid particles between the static and moving bed layers in the bedload transport process.

The particle deposition rate $\dot{\mathcal{N}}_D$ is related to the number of particles $\mathcal{N}$ moving in the bedload transport layer and the characteristic deposition time t_D following

$$\dot{\mathcal{N}}_D = \frac{\mathcal{N}}{t_D} \qquad \left[Part.\,T^{-1}\right] \tag{2.130}$$

The characteristic time of the deposition process is controlled by gravity and depends on the deposition velocity ω_s and the particle diameter d_s following

$$\frac{1}{t_D} \propto \frac{\omega_s}{d_s} \qquad \rightarrow \qquad \frac{1}{t_D} = k_D \frac{\sqrt{(\rho_s/\rho_f - 1) g d_s}}{d_s} \tag{2.131}$$

being k_D a dimensionless deposition constant. Therefore, replacing (2.131) into (2.130), the particle deposition rate can be expressed as

$$\dot{\mathcal{N}}_D = k_D \frac{\mathcal{N}}{d_s} \frac{\sqrt{(\rho_s/\rho_f - 1) g d_s^3}}{d_s} \tag{2.132}$$

The number of particles in movement on a bed surface of area $\Delta A = \Delta x\, \Delta y$ and which are affected by deposition in a time step t_D is related to the thickness of the bedload transport layer η as

$$\mathcal{N} = \frac{\eta\, \Delta A}{d_s^3/(1-\xi)} \tag{2.133}$$

Using (2.133), the relation between the particle deposition rate $\dot{\mathcal{N}}_D$ and the exchange flux due to deposition $\dot{\eta}_D$ in a bed area ΔA is expressed as

$$\dot{\eta}_D = \frac{\dot{\mathcal{N}}_D\, d_s^3}{(1-\xi)\Delta A} \tag{2.134}$$

Therefore, replacing (2.132) and (2.133) into (2.134), the volumetric exchange flux between the moving and the static bed layers due to deposition can be expressed as

$$\dot{\eta}_D = k_D \frac{\eta}{d_s} \frac{\sqrt{(\rho_s/\rho_f - 1) g d_s^3}}{d_s} \qquad \left[L\,T^{-1}\right] \tag{2.135}$$

Similarly, in order to derive an expression for the volumetric entrainment flux $\dot{\eta}_E$, we consider that the particle entrainment rate $\dot{\mathcal{N}}_E$ is related to the number of static particles exposed to the flow action $\mathcal{N}_E$ and the characteristic entrainment time t_E:

$$\dot{\mathcal{N}}_E = \frac{\mathcal{N}_E}{t_E} \qquad \left[Part.\,T^{-1}\right] \tag{2.136}$$

The number of particles which are exposed to the flow shear stress in a surface of area $\Delta A = \Delta x\,\Delta y$ and which can be incorporated to the moving layer in a time step t_E are placed on the top layer of the static sediment column and hence

$$\mathcal{N}_E = \frac{d_s\,\Delta A}{d_s^3/(1-\xi)} \tag{2.137}$$

and replacing (2.137) into (2.136) leads to

$$\dot{\mathcal{N}}_E = \frac{(1-\xi)\Delta A}{t_E\,d_s^2} \tag{2.138}$$

The characteristic entrainment time t_E for turbulent flow is proportional to the inertial balance between the settling momentum of the sediment particles and the stress forces exerted by the flow on them:

$$\frac{1}{t_E} \propto \frac{\Delta\tau\,d_s^2}{\rho_s d_s^3\,\omega_s} \tag{2.139}$$

where $\Delta\tau = |\boldsymbol{\tau_b}| - |\boldsymbol{\tau_c}|$ denotes a positive excess of boundary shear stress $|\boldsymbol{\tau_b}|$ over the critical value for the incipient motion of the solid particles $|\boldsymbol{\tau_c}|$. Considering that $|\boldsymbol{\tau_b}|$ and $|\boldsymbol{\tau_c}|$ can be expressed in terms of dimensionless Shields stress as

$$\theta = \frac{|\boldsymbol{\tau_b}|}{(\rho_s - \rho_w) g d_s} \tag{2.140a}$$

$$\theta_c = \frac{|\boldsymbol{\tau_c}|}{(\rho_s - \rho_w) g d_s} \tag{2.140b}$$

being θ and θ_c the boundary Shields stress and the corresponding Shields stress value for the incipient motion respectively, (2.139) is rewritten as

$$\frac{1}{t_E} = k_E \frac{\Delta\theta}{\rho_s/\rho_f\,d_s} \sqrt{(\rho_s/\rho_f - 1) g d_s} \tag{2.141}$$

being $\Delta\theta = \theta - \theta_c$ a positive excess of boundary Shields stress over the critical value for the incipient motion and k_E a dimensionless entrainment constant.

The relation between the particle entrainment rate $\dot{\mathcal{N}}_E$ and the volumetric exchange flux due to entrainment $\dot{\eta}_E$ in a bed area ΔA is expressed as

$$\dot{\eta}_E = \frac{\dot{\mathcal{N}}_E \, d_s^3}{(1-\xi)\Delta A} \tag{2.142}$$

and, replacing (2.138) and (2.141) into (2.142), the volumentric exchange flux caused by entrainment is expressed as

$$\dot{\eta}_E = k_E \frac{\Delta\theta}{\rho_s/\rho_f} \frac{\sqrt{(\rho_s/\rho_f - 1) g d_s^3}}{d_s} \qquad \left[L\,T^{-1}\right] \tag{2.143}$$

Note that, for the equilibrium case in which the entrainment and deposition fluxes are equal ($\dot{\eta}_E = \dot{\eta}_D$), the relation $\mathcal{N}\, d_s^2 \propto \Delta\theta$ is recovered. This linear relation for the number of particles in the moving layer agrees with the experimental observations reported by Luque & Beek [82] and Bagnold [3], and is used to derive most of the classical solid transport rate in capacity regime reported in literature.

2.3.3 Generalized non-capacity bedload rate

Closure relations found in literature were derived under capacity (equilibrium) conditions and can be generally written as

$$|\mathbf{q}_\mathbf{b}^*| = c\,\theta^{m_1}\,(\Delta\theta)^{m_2}\,\sqrt{(\rho_s/\rho_f - 1) g d_s^3} \tag{2.144}$$

where $|\mathbf{q}_\mathbf{b}^*|$ denotes the bedload rate module under equilibrium conditions, c is a constant dimensionless coefficient, m_1 and m_2 are two constant exponents, and $\Delta\theta = \theta - \theta_c$ is the positive excess of Shields stress θ over the critical Shields value for the incipient motion θ_c [100]. Values of c, m_1, m_2 and θ_c depends on the closure relation and are summarised in Table 2.2 for some widespread bedload transport rate formula.

Formulation	c	m_1	m_2	θ_c
MPM [97]	8	0	3/2	0.047
Nielsen [108]	12	1/2	1	0.047
Fernández-Luque [82]	5.7	0	3/2	0.037
Wong [143]	3.97	0	3/2	0.0495
Smart [132]	$4.2\,S_0^{0.6}\,\frac{h^{1/6}}{n\sqrt{g}}$	1/2	1	0.047
Wu [144]	$0.0053\,\frac{(\Delta\theta)^{0.7}}{\theta_c^{2.2}}$	0	3/2	0.030

Table 2.2: Coefficient c, m_1, m_2 and θ_c for different capacity solid transport rate formulations (2.144). In the Smart formulation, the parameter S_0 is the bed slope.

For the bedload transport process, the boundary shear stress at the bed surface z_b is assumed fully turbulent and is modelled using the Manning

roughness parameter $n_b\,[TL^{-1/3}]$ as $|\boldsymbol{\tau_b}| = \rho_f g n_b^2 |\mathbf{u}|^2/h^{1/3}$. Hence, from (2.140), the boundary Shields stress θ reads

$$\theta = \frac{n_b^2\,|\mathbf{u}|^2}{(\rho_s/\rho_f - 1)d_s h^{1/3}} \tag{2.145}$$

Replacing (2.145) into (2.144) for all the formulations in Table 2.2, it can be demonstrated that $|\mathbf{q_b^*}| \propto h^{-1/2}\,|\mathbf{u}|^3$ and hence a general formulation for the solid transport rate based on the Grass law

$$|\mathbf{q_b^*}| = G(h,\theta)\,|\mathbf{u}|^3 \tag{2.146}$$

has been adopted by other authors [65, 86, 100]. The Grass formulation (2.146) relates the equilibrium bedload sediment discharge with the depth-averaged flow velocity by means of the factor $G(h,\theta)\ [T^2L^{-1}]$ which represents the interaction between the flow and the bed layer and which depends only on the flow characteristics.

Considering the expressions (2.135) and (2.143) for the entrainment and deposition rates respectively of solid material from/to the underlying static bed layer, the capacity approach for the bedload transport layer establishes $\dot{\eta}_D = \dot{\eta}_E$) and hence the transport layer thickness under equilibrium conditions η^* can be expressed as

$$\eta^* = \frac{k_E}{\rho_s/\rho_f\,k_D}\,\Delta\theta\,d_s \tag{2.147}$$

Note that, in capacity state, the moving layer thickness depends only on the Shields dimensionless stress excess $\Delta\theta$, the grain size d_s and the relation between the entrainment and deposition constants k_E/k_D. Furthermore, combining the expressions for the entrainment and deposition rates, leads to

$$\frac{\dot{\eta}_E}{\dot{\eta}_D} = \frac{1}{\eta}\frac{k_E}{\rho_s/\rho_f\,k_D}\,\Delta\theta d_s \quad \rightarrow \quad \frac{\eta}{\eta^*} = \frac{\dot{\eta}_D}{\dot{\eta}_E} \tag{2.148}$$

indicating that values of the transport layer thickness η greater than the equilibrium thickness η^* are related to a net deposition flux from the moving layer to the static stratum ($\dot{\eta}_D > \dot{\eta}_E$), whereas values of the transport layer thickness η greater than the equilibrium thickness η^* lead to a net entrainment flux from the static layer to the transport layer ($\dot{\eta}_D < \dot{\eta}_E$).

From (2.123), the bedload discharge modulus is defined as

$$|\mathbf{q_b}| = (1-\xi)\,\eta\,|\mathbf{u_b}| \tag{2.149}$$

and hence a direct proportionality between the transport layer thickness η and the actual solid transport rate $|\mathbf{q_b}|$ can be assumed. Therefore, using (2.144), (2.147), (2.148) and (2.149), we derive a closure relation for the non-capacity solid transport rate as

$$|\mathbf{q_b}| = c\,\theta^{m_1}\,\Delta\theta^{(m_2-1)}\,\frac{\rho_s/\rho_f\,k_D}{k_E\,d_s}\eta\sqrt{(\rho_s/\rho_f - 1)g d_s^3} \tag{2.150}$$

and hence the averaged velocity of the bedload transport layer $|\mathbf{u_b}|$ is expressed as

$$|\mathbf{u_b}| = c\,\theta^{m_1}\,\Delta\theta^{(m_2-1)}\,\frac{\rho_s/\rho_f\,k_D}{(1-\xi)k_E}\,\frac{\sqrt{(\rho_s/\rho_f-1)gd_s^3}}{d_s} \tag{2.151}$$

Rewriting the non-capacity bedload rate (2.150) in the Grass law form, the solid discharge in the transport layer can be expressed as

$$\mathbf{q_b} = G(h,\theta,\eta)\,|\mathbf{u}|^2\mathbf{u} \tag{2.152}$$

where the bed-flow interaction parameter G becomes not only a function of the water depth h and the dimensionless Shields stress θ, but it also depends on the moving layer thickness η as

$$G = \Gamma_1(h)\,\Gamma_2(\theta)\,\Gamma_3(\eta) \tag{2.153}$$

Table 2.3 summarises the expression of the non-capacity Grass interaction factor $G(h,\theta,\eta)$ derived from some of the most common equilibrium closure relations. Note that Γ_3 is similar for all the relations, whereas Γ_1 and Γ_2 depend on the selected formulation.

Formulation	$\Gamma_1(h)$	$\Gamma_2(\theta)$	$\Gamma_3(\eta)$	θ_c
MPM	$\frac{n_b^3\sqrt{g}}{(\rho_s/\rho_f-1)\sqrt{h}}$	$\frac{8\sqrt{\Delta\theta}}{\theta^{3/2}}$	$\frac{\rho_s/\rho_f\,k_D}{k_E}\frac{\eta}{d_s}$	0.047
Nielsen	$\frac{n_b^3\sqrt{g}}{(\rho_s/\rho_f-1)\sqrt{h}}$	$\frac{12}{\theta}$	$\frac{\rho_s/\rho_f\,k_D}{k_E}\frac{\eta}{d_s}$	0.047
Fernandez-Luque	$\frac{n_b^3\sqrt{g}}{(\rho_s/\rho_f-1)\sqrt{h}}$	$\frac{5.7\sqrt{\Delta\theta}}{\theta^{3/2}}$	$\frac{\rho_s/\rho_f\,k_D}{k_E}\frac{\eta}{d_s}$	0.037
Wong	$\frac{n_b^3\sqrt{g}}{(\rho_s/\rho_f-1)\sqrt{h}}$	$\frac{3.97\sqrt{\Delta\theta}}{\theta^{3/2}}$	$\frac{\rho_s/\rho_f\,k_D}{k_E}\frac{\eta}{d_s}$	0.0495
Smart	$\frac{n_b^2}{(\rho_s/\rho_f-1)h^{1/3}}$	$S_0^{0.6}\frac{4.2}{\theta}$	$\frac{\rho_s/\rho_f\,k_D}{k_E}\frac{\eta}{d_s}$	0.047
Wu	$\frac{n_b^3\sqrt{g}}{(\rho_s/\rho_f-1)\sqrt{h}}$	$\frac{0.0053\sqrt{\Delta\theta}}{\theta_c^{2.2}\,\theta^{3/2}}$	$\frac{\rho_s/\rho_f\,k_D}{k_E}\frac{\eta}{d_s}$	0.030

Table 2.3: Non-capacity Grass interaction factor G for different solid transport rate formulations.

This new generalised model for the non-capacity bedload transport (2.152) requires to compute the thickness η of the moving layer using (2.125), but it is able to account for the temporal and spatial delay of the actual sediment transport rate with respect to its potential capacity in highly unsteady flows. Moreover, if time, flow local features and sediment availability are enough to develop steady states in the bedload transport process, the entrainment and deposition rates ($\dot{\eta}_E$ and $\dot{\eta}_D$ respectively) tend to be equal and the bedload rate recovers the common closure relation (2.144) for equilibrium transport conditions. Therefore, the equilibrium state is a particular case of the generalised non-capacity model where $\eta = \eta^*$.

In order to illustrate the temporal-spatial behaviour of the generalised non-capacity bedload model (2.152), a simple idealised test is included here considering the following flow conditions

$$h|\mathbf{u}|(t,x,y) = \quad 2\,m^2 s^{-1} \qquad \forall t, \quad \forall x$$
$$|\mathbf{u}|(t,x,y) = \begin{cases} 2\,m/s & \text{if} \quad t = 0\,s, & \forall x \\ 4\,m/s & \text{if} \quad t > 0\,s, & 20\,m \leq x \leq 70\,m \\ 2\,m/s & \text{if} \quad t > 0\,s, & otherwise \end{cases}$$

with $\rho_s/\rho_f = 2.65$, $g = 9.81\,ms^{-2}$, $\xi = 0.35$, $d_s = 1\,mm$, $n_b = 0.035\,sm^{-1/3}$, $k_E/k_D = 20$ and the MPM relation (see Table 2.3). Using (2.144), these local flow features lead to a uniform bedload discharge at the initial time $t = 0\,s$ and a stepped capacity transport rate $|\mathbf{q_b^*}|$ for any $t > 0\,s$, as depicted in Figure 2.17.

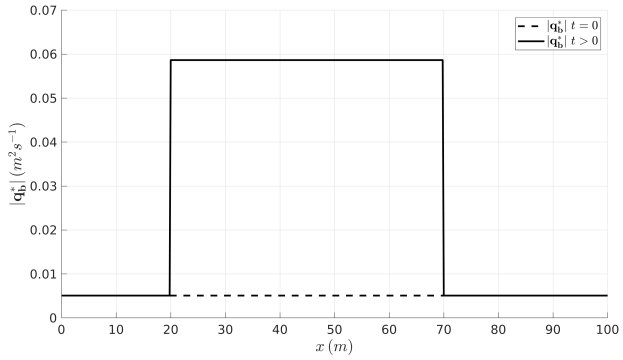

Figure 2.17: Bedload transport rate evolution for classical capacity models.

The generalised non-capacity model introduces a temporal and spatial delay of the actual transport rate with respect to the capacity value. Figure 2.18 shows the temporal evolution of the bedload rate $|\mathbf{q_b}|$ in the spatial domain computed using the non-capacity model (2.152), with (top) $k_E = 0.06$ and (bottom) $k_E = 0.015$. As time increases, the actual solid rate adapts progressively to the capacity rate. Nevertheless, sudden spatial changes of the local flow features, as occurs at $x = 20\,m$ and $x = 70\,m$, need a length for the actual transport rate to adapt to the equilibrium value even with $t \to \infty$. Furthermore, it is worth noting that the temporal a spatial delay of the non-capacity solid discharge respect to the corresponding equilibrium state increases as the entrainment constant k_E decreases.

To analyse the influence of the entrainment and deposition constants, k_E and k_D respectively, in the non-equilibrium state of the bedload discharge, the net exchange flux through the static-moving bed layers interface can be calculated as $N_e = \dot{\eta}_D - \dot{\eta}_E$ (2.127). Figure 2.19 shows the temporal evolution of the net exchange flux in the spatial domain with (top) $k_E = 0.06$ and (bottom) $k_E = 0.015$. A net entrainment flux $\dot{\eta}_E > \dot{\eta}_D$ occurs for $20\,m \leq x \leq 70\,m$ since initially $\eta < \eta^*$ and the actual solid rate must increase to reach the capacity value. As time increases and $|\mathbf{q_b}|$ grows to $|\mathbf{q_b^*}|$, the entrainment and deposition rates tend to balance and the net exchange reduces. Contrarily, for $x > 70\,m$ initially the bedload discharge is in equilibrium but, as time increases and the upstream solid rate reaches the higher capacity value, a net deposition exchange flux appears to recover the lower equilibrium value downstream the step.

Previous non-capacity bedload models [33, 134, 144, 146] assumed a spatial length L_b $[L]$ for the adaptation of the actual bedload discharge to

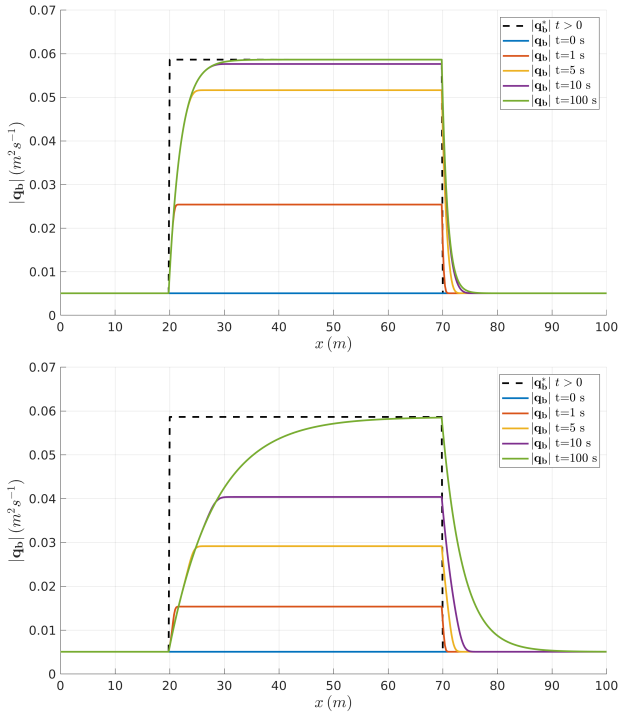

Figure 2.18: Bedload transport rate evolution for the generalised non-capacity models with (top) $k_E = 0.06$ and (bottom) $k_E = 0.015$.

its equilibrium state and calculated the net exchange flux as

$$N_e = \frac{1}{1-\xi}\frac{|\mathbf{q_b}| - |\mathbf{q_b^*}|}{L_b} \tag{2.154}$$

where L_b is a constant parameter which needs to be calibrated for each case. Comparison of both methods to determine the entrainment-deposition net flux N_e indicates that the proposed model assumes a dynamic value for the adaptation length L_b which is scaled following

$$L_b \propto \frac{\sqrt{\theta}}{k_E}\, d_s \tag{2.155}$$

According to (2.155), the reduction of the entrainment constant k_E leads to increasing dynamic adaptation length values and enhances non-equilibrium bedload transport states (see Figures 2.18 and 2.19) . On the other hand, the higher the Shields stress θ, the longer the distance that the bedload discharge needs to reach its equilibrium state. Hence highly erosive flows lead to higher values of the adaptation length L_b. This dependency of the bedload adaptation length with the shear stress has not been previously derived. Instead, most of the models assume a global constant value based on the dominant bed form [144].

To analyse the influence of the Shields stress on the dynamic adaptation of actual non-capacity bedload rate to the equilibrium state, we use the above case but setting a entrainment constant $k_E = 0.025$ and increasing flow discharges $h|\mathbf{u}|(t,x,y) = [1,2,3,4]\,m^2s^{-1}$. For $t = 0\,s$ the flow is uniform, with $h = 1\,m$ along the whole spatial domain regardless of the discharge, whereas for $t > 0\,s$ a steady step in the flow features is set between $20\,m \leq x \leq 70\,m$ which agrees $|\mathbf{q_b^*}| = 2|\mathbf{q_b^*}|_{t=0}$ regardless of the flow

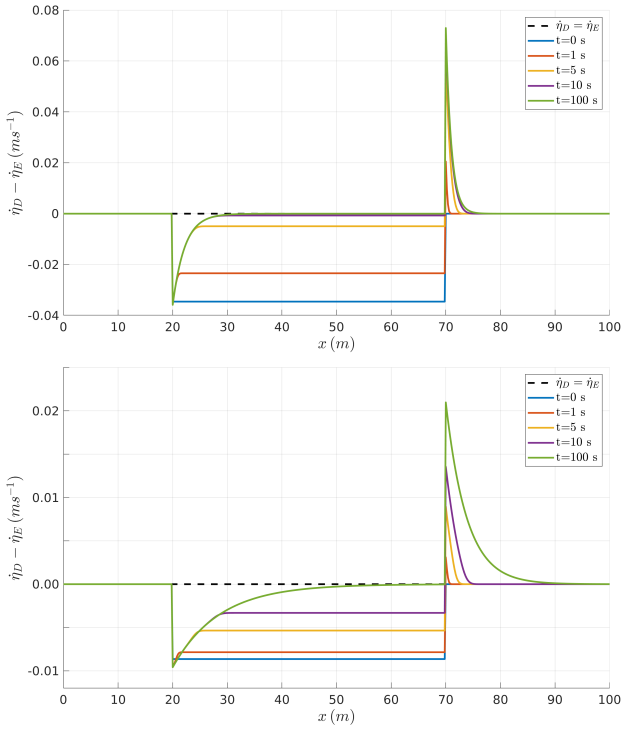

Figure 2.19: Ned exchange flux $N_e = \dot{\eta}_D - \dot{\eta}_E$ for the generalised non-capacity models with (top) $k_E = 0.06$ and (bottom) $k_E = 0.015$.

discharge. The shear stress at the bed surface, hence the Shields stress θ, increases progressively with the flow discharge as $\theta = [1.18, 4.71, 10.6, 18.9]$ respectively. Figure 2.20 shows the non-capacity bedload rate $|\mathbf{q_b}|$ for $t = 100\ s$, normalised by the initial uniform equilibrium value $|\mathbf{q_b^*}|_{t=0}$, along the whole spatial domain. As the Shields stress at the bed surface increases, the adaptation length increases and enhances the non-capacity state in the bedload transport.

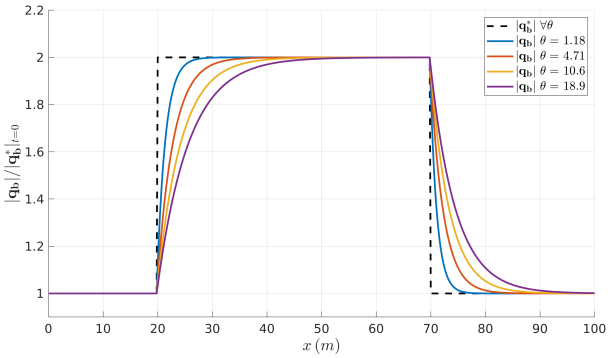

Figure 2.20: Normalised bedload transport rate for the generalised non-capacity models with increasing Shields stresses θ.

2.4 In Closing

In this chapter, we have derived the generalized two-dimensional system of depth-averaged conservation laws for environmental surface flows of water-sediment mixtures over movable bed conditions, as well as the essential relationships for the system closure. Furthermore, four are the main novelties presented in this chapter:

1. A new closure relation for the shear-induced pore-fluid pressure during the movement of dense-packed solid-liquid mixtures has been obtained and analyzed (Section 2.2.2).

2. Using this new pore pressure distribution, the effects of the sediment particles dilation have been included into the depth-averaged solid transport equation, leading to a novel formulation for the advective solid fluxes which accounts for the shear-induced separation of the solid a liquid phases (Section 2.2.3).

3. The mathematical model for the bedload transport has been reformulated. A new closure relation for the mass exchange between the flow and the underlying static stratum is proposed from a grain-scale inertial analysis (Section 2.3.2).

4. Additionally, a novel generalized non-capacity model for the bedload transport rate is proposed and compared with the classical capacity/equilibrium assumption (Section 2.3.3).

Chapter 3

Two-dimensional model for variable-density mud/debris flows

The main goals of this chapter are:

- To derive a robust and accurate numerical scheme to solve variable-density flows of water-sediment mixtures including the exchange of material between the bed and the flow.
- To assess the effects that the shear-induced solid phase dilation phenomenon has on the mobility and the spatial segregation of the solid phase in rapid mixture flows.
- To compare the computational efficiency of CPU-parallelized and GPU-based implementations of the numerical model when they are faced to large-scale and long-term realistic mud/debris flow simulations.

3.1 Governing equations

The depth-averaged 2D model for the variable-density multi-grain mixture flows over non-uniform erodible beds involves the continuity equations for the liquid-solid mixture mass (2.8), rewritten here as

$$\frac{\partial(\rho h)}{\partial t} + \frac{\partial}{\partial x}(\rho h u) + \frac{\partial}{\partial y}(\rho h v) = \mathcal{M}_b \tag{3.1}$$

and the conservation laws of the bulk linear momentum along the $x-$ and $y-$ coordinates, (2.22) and (2.23) respectively, which can be expressed as

$$\frac{\partial(\rho h u)}{\partial t} + \frac{\partial}{\partial x}(\rho h u^2 + \frac{1}{2} g_n \rho h^2) + \frac{\partial}{\partial y}(\rho h u v) = -g_n \rho h \frac{\partial z_b}{\partial x} - \tau_{bx} \tag{3.2a}$$

$$\frac{\partial(\rho h v)}{\partial t} + \frac{\partial}{\partial x}(\rho h u v) + \frac{\partial}{\partial y}(\rho h v^2 + \frac{1}{2} g_n \rho h^2) = -g_n \rho h \frac{\partial z_b}{\partial x} - \tau_{by} \tag{3.2b}$$

being ρ the depth-averaged bulk density, h the vertical flow depth and $(u,\, v)$ the components of the depth-averaged flow velocity vector $\mathbf{u}$, z_b the bed layer elevation, $(\tau_{bx},\, \tau_{by})$ the components of the depth-averaged basal resistance vector $\boldsymbol{\tau_b}$ and $\mathcal{M}_b$ the net mass exchange between the flow and the underlying bed layer. It is worth noting that the dispersive terms on the

righ hand side have been neglected and a simple shear flow has been assumed for the depth-integrated stress terms (see Section 2.1.3). The local bed-normal projection of the gravity has been used here to integrate the pressure and volumetric force terms (see Section 2.1.4) with $g_n = g\cos^2\varphi_b$, being g the gravitational acceleration and φ_b the bed-normal angle respect to the vertical axis [64].

The solid phase is exprese here in terms of a multi-grain mixture of water and $p = 1, \ldots, N$ different sediment classes. Using (2.74), the bulk mixture density ρ in the flow column is hence expressed as

$$\rho = \rho_w + \sum_{p=1}^{N} (\rho_{s,p} - \rho_w)\,\phi_p \tag{3.3}$$

where ρ_w is the pore-water density, and $\rho_{s,p}$ and ϕ_p are the density and depth-averaged volumetric concentration of the pth solid phase respectively.

The depth-averaged transport equations (2.107) for the pth sediment class reads

$$\frac{\partial(h\phi_p)}{\partial t} + \frac{\partial}{\partial x}(hu\phi_p + \mathcal{L}_{x,p}) + \frac{\partial}{\partial y}(hv\phi_p + \mathcal{L}_{y,p}) = -(D_b - E_b)_p \tag{3.4}$$

where $(\mathcal{L}_{x,p}, \mathcal{L}_{y,p})$ are the deviatoric fluxes associated to the shear-induced dilation of the pth sediment class (see Section 2.2.3), which can be expressed as a function of the pore-fluid pressure excess as

$$\mathcal{L}_{x,p} = \phi_p \frac{\rho_w \kappa}{\rho\mu}\left(\frac{\partial \mathcal{P}_e}{\partial x} + \mathcal{E}_b \rho_w g_n h \frac{\partial z_b}{\partial x}\right) \tag{3.5a}$$

$$\mathcal{L}_{y,p} = \phi_p \frac{\rho_w \kappa}{\rho\mu}\left(\frac{\partial \mathcal{P}_e}{\partial y} + \mathcal{E}_b \rho_w g_n h \frac{\partial z_b}{\partial y}\right) \tag{3.5b}$$

where $\mathcal{E}_b$ is the basal pore pressure excess parameter and $\mathcal{P}_e$ is the integral of the pore pressure excess throughout the flow column. They can be estimated as

$$\mathcal{E}_b = \frac{-\mu h}{2\kappa\rho_w g_n}\dot{\gamma}\tan\psi \tag{3.6a}$$

$$\mathcal{P}_e = \frac{-\mu h^3}{3\kappa}\dot{\gamma}\tan\psi \tag{3.6b}$$

being κ the hydraulic permeability of the granular aggregate, μ the pore-fluid dynamic viscosity, $\tan\psi$ the shear-induced dilatancy estimated as in (2.90), and $\dot{\gamma} = 2|\mathbf{u}|/h$ the depth-averaged macroscopic shear rate for simple-shear flow.

The shear induced dilatancy $\tan\psi$ is calculated in this model using the linear dependency (2.90) proposed by [40, 113] following

$$\tan\psi = k_1(\phi_0 - \phi_{eq}) \tag{3.7}$$

being k_1 a positive calibration coefficient. The term $\phi_0 = \sum_{p=1}^{N} \phi_p$ is the bulk solid concentration in the flow column and ϕ_{eq} an equilibrium value of the solid concentration which implies null dilatancy. For the sake of simplicity, a constant $0.4 \leq \phi_{eq} \leq 0.8$ is adopted in this work as a case dependent parameter.

The net bed-flow exchange flux $(D_b - E_b)_p$ in (3.4) accounts for the balance between the size-specific volumetric deposition and entrainment rates (see Section 2.2.4). Therefore, the bulk mass exchange between the flow and the bed layers, i.e. the term $\mathcal{M}_b$ on the right hand side of (3.1), can be expressed as

$$\mathcal{M}_b = -\frac{\rho_b}{1-\xi} \sum_{p=1}^{N} (D_b - E_b)_p \tag{3.8}$$

and the conservation equation (2.86) allows to solve the temporal-spatial evolution of the non-uniform bed layer elevation

$$\sum_{p=1}^{N} F_{b,p} \, (1-\xi) \frac{\partial z_b}{\partial t} = \sum_{p=1}^{N} (D_b - E_b)_p \tag{3.9}$$

being ξ the porosity of the non-uniform bed layer and ρ_b the corresponding bed layer bulk density, which is estimated here as

$$\rho_b = \rho_w C_{bw} + (1-\xi) \sum_{p=1}^{N} F_{b,p} \, \rho_{s,p} \tag{3.10}$$

where $F_{b,p}$ denotes the fraction of the pth sediment class in the bed layer, which is considered constant in time and space with $\sum_{p=1}^{N} F_{b,p} = 1$, and C_{bw} is the pore-fluid content in the bed layer.

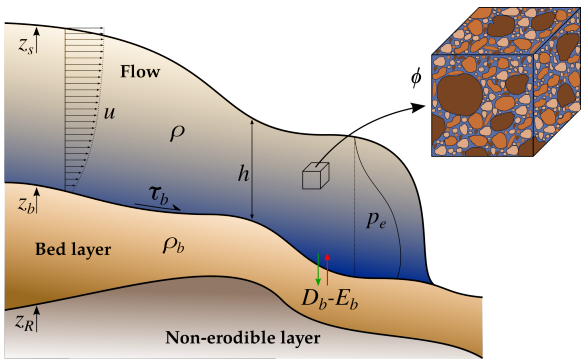

Figure 3.1: Main variables involved in the variable-density mixture flow over erodible bed.

Figure 3.1 shows a scheme with the main variables involved in the system of equations used for modeling variable-density water-sediment mixture flows over erodible beds. Additionally, some closure definitions are required to complete the system. The bed porosity (3.11) is estimated here using the Wu relation for non-uniform deposits [144]

$$\xi = 0.13 + 0.21 \left(0.002 + 10^3 \sum_{p=1}^{N} F_{b,p} \, d_{s,p} \right)^{-0.21} \tag{3.11}$$

being $d_{s,p}$ the characterisctic diameter of the pth sediment class in meters.

The deposition $D_{b,p}$ and erosion $E_{b,p}$ rates for the pth solid phase are estimated using

$$\begin{aligned} D_{b,p} &= \alpha_p \, \omega_{s,p} \, \phi_p (1-\phi_0)^4 \\ E_{b,p} &= \alpha_p \, \omega_{s,p} \, F_{b,p} \, \frac{|\mathbf{q}^*_{\mathbf{s,p}}|}{h|\mathbf{u}|} \end{aligned} \tag{3.12}$$

where α_p is an empirical parameter representing the difference between the near-bed concentration and the depth-averaged concentration for the pth solid phase, $|\mathbf{q}^*_{\mathbf{s,p}}|$ accounts for the modulus of the specific solid transport throughout the mixture column in capacity regime and $\omega_{s,p}$ denotes the specific settling velocity of the sediment particles in clear water, computed here using the Zhang & Xie [151] formula as

$$\omega_{s,p} = \left[\left(13.95 \, \frac{\nu}{d_{s,p}} \right)^2 + 1.09 \, \frac{\rho_{s,p} - \rho_w}{\rho_w} \, g \, d_{s,p} \right]^{1/2} - 13.95 \, \frac{\nu}{d_{s,p}} \tag{3.13}$$

being ν the kinematic viscosity of water. For mud/debris flows in this thesis, solid and liquid phases are assumed generally well mixed along the flow column hence $\alpha_p = 1$ is adopted, and the specific capacity solid flux $|\mathbf{q}^*_{\mathbf{s,p}}|$ is calculated using the Wu [144] formula

$$\begin{aligned} \frac{|\mathbf{q}^*_{\mathbf{s,p}}|}{\beta_T \sqrt{(\rho_{s,p}/\rho_w) g d^3_{s,p}}} &= 5.3 \cdot 10^{-3} \left[\left(\frac{n_p}{n_b} \right)^{1.5} \frac{\theta_{b,p}}{\theta_{c,p}} - 1 \right]^{2.2} \\ &+ 2.62 \cdot 10^{-5} \left[\left(\frac{\theta_{w,p}}{\theta_{c,p}} - 1 \right) \frac{|\mathbf{u}|}{\omega_{s,p}} \right]^{1.74} \end{aligned} \tag{3.14}$$

being $n_p = 1/21 \, d_{s,p}^{1/6}$ the Manning roughness parameter corresponding to grain resistance of the pth class, n_b the global Manning roughness parameter, $\theta_{c,p}$ the critical Shields stress for the incipient motion of the pth sediment class which must include the hiding/exposure mechanism in non-uniform beds [32]. The term $\theta_{b,p} = \tau_b/[(\rho_{s,p} - \rho_w) g d_{s,p}]$ is the specific Shields stress corresponding to the basal resistance, $\theta_{w,p} = \tau_w/[(\rho_{s,p} - \rho_w) g d_{s,p}]$ the specific Shields stress throughout the wetted perimeter, with τ_w accounting for the pore-fluid turbulent shear stress within the mixture column. The parameter β_T is a modification coefficient which is considered equal for all the solid phases composing the mixture.

The basal shear stress vector in the momentum equations (3.2) is expressed as

$$\boldsymbol{\tau_b} = (\tau_{bx}, \tau_{by}) = \tau_b \, \mathbf{n_u} \tag{3.15}$$

being τ_b the basal shear stress modulus and $\mathbf{n_u}$ the velocity unit vector (see Section 2.1.3). To close the depth-averaged basal resistance term, the relations show in Table 3.1 have been considered for this variable-density mud/debris flow model, with τ_y $[Pa]$ the cohesive yield strength, μ_B $[Pa \cdot s]$ the dynamic viscosity and μ_P $[Pa \cdot s^2]$ the plastic viscosity ($m = 2$) of the

material. The frictional yield stress τ_f $[Pa]$ is calculated using the Coulomb-type relation

$$\tau_f = \left(\rho g_n h - \mathcal{P}_b\right) \tan \delta_f \tag{3.16}$$

where $\mathcal{P}_b = (1 + \mathcal{E}_b)\rho_w g_n h$ $[Pa]$ is the basal pore pressure, being $\mathcal{E}_b$ the dimensionless shear-induced pore pressure excess parameter (3.6a).

	Formulation	**Basal resistance**
PT	Pure Turbulent	$\tau_b = \rho g \frac{n_b^2}{h^{1/3}} \lvert\mathbf{u}\rvert^2$
CB	Cohesive Bingham	$2\tau_b^3 - 3\left(\tau_y + 2\mu_B \frac{\lvert\mathbf{u}\rvert}{h}\right)\tau_b^2 + \tau_y^3 = 0$
CT	Cohesive Turbulent	$\tau_b = \tau_y + \frac{24}{8}\mu_B \frac{\lvert\mathbf{u}\rvert}{h} + \rho g \frac{n_b^2}{h^{1/3}} \lvert\mathbf{u}\rvert^2$
FD	Frictional Dilatant	$\tau_b = \tau_f + \frac{25}{4}\frac{\mu_P}{h^2} \lvert\mathbf{u}\rvert^2$
FP	Frictional Plastic	$2\tau_b^3 - 3\left(\tau_f + 2\mu_B \frac{\lvert\mathbf{u}\rvert}{h}\right)\tau_b^2 + \tau_f^3 = 0$
FT	Frictional Turbulent	$\tau_b = \tau_f + \rho g \frac{n_b^2}{h^{1/3}} \lvert\mathbf{u}\rvert^2$

Table 3.1: Depth-averaged basal resistance formulations for the mud/debris flow model.

The resulting system is composed by $3 + N + 1$ conservation equations accounting for the mixture flow (3.1)–(3.2a)–(3.2b), the transport in the flow of the N sediment classes (3.4) and the bed elevation evolution (3.9). Considering that the bulk density of the fluid-solid mixture is a function of the total solid concentration, the dimensionless bulk density r can be expressed by defining a new variable ϕ^χ, referred to as buoyant solid concentration

$$r = \frac{\rho}{\rho_w} = 1 + \phi^\chi \qquad \text{with:} \quad \phi^\chi = \sum_{p=1}^{N} \frac{\rho_{s,p} - \rho_w}{\rho_w} \phi_p \tag{3.17}$$

Using (3.17), the equations forming the system can be recast as five conservation laws and rewritten in vector form as

$$\frac{\partial \mathbf{U}}{\partial t} + \nabla \cdot \mathbf{E}(\mathbf{U}) = \mathbf{S_b}(\mathbf{U}) + \mathbf{S_\tau}(\mathbf{U}) - \nabla \cdot \mathbf{L}(\mathbf{U}) + \mathbf{E_b}(\mathbf{U}) \tag{3.18}$$

where $\mathbf{U}$ is the vector of conserved variables

$$\mathbf{U} = \left(\; rh, \quad rhu, \quad rhv, \quad h\phi^\chi, \quad z_b \; \right)^T \tag{3.19}$$

and $\mathbf{E}(\mathbf{U}) = \big(\mathbf{F}(\mathbf{U}), \mathbf{G}(\mathbf{U})\big)$ are the convective fluxes along the $\mathbf{X} = (x, y)$ horizontal coordinates respectively.

$$\mathbf{F}(\mathbf{U}) = \begin{pmatrix} rhu \\ rhu^2 + \frac{1}{2} g_n r h^2 \\ rhuv \\ hu\,\phi^{\chi} \\ 0 \end{pmatrix} \quad \mathbf{G}(\mathbf{U}) = \begin{pmatrix} rhv \\ rhuv \\ rhv^2 + \frac{1}{2} g_n r h^2 \\ hv\,\phi^{\chi} \\ 0 \end{pmatrix} \tag{3.20}$$

It is worth noting that the dimensionless mixture density r and flow features (h, u, v) are coupled in the conserved variables and convective fluxes on the left hand side of (3.18).

The vector $\mathbf{S_b}(\mathbf{U})$ accounts for the momentum source term associated to the variation of the pressure force on the bed interface, whereas $\mathbf{S}_{\tau}(\mathbf{U})$ is the momentum dissipation due to the basal resistance.

$$\mathbf{S_b}(\mathbf{U}) = \begin{pmatrix} 0 \\ -g_n r h \frac{\partial z_b}{\partial x} \\ -g_n r h \frac{\partial z_b}{\partial y} \\ 0 \\ 0 \end{pmatrix} \qquad \mathbf{S_\tau}(\mathbf{U}) = \begin{pmatrix} 0 \\ -\frac{\tau_b}{\rho_w}\, n_{ux} \\ -\frac{\tau_b}{\rho_w}\, n_{uy} \\ 0 \\ 0 \end{pmatrix} \tag{3.21}$$

The term $\nabla \cdot \mathbf{L}(\mathbf{U})$ involves the deviatoric sediment fluxes caused by the shear-induced dilation of the solid phase and only affects to the fourh equation. The bulk deviatoric flux $\mathbf{L}(\mathbf{U}) = \big(\mathbf{L_x}(\mathbf{U}), \mathbf{L_y}(\mathbf{U})\big)$ reads

$$\mathbf{L_x}(\mathbf{U}) = \begin{pmatrix} 0 \\ 0 \\ 0 \\ \sum_{p=1}^{N} \frac{\rho_{s,p} - \rho_w}{\rho_w}\, \mathcal{L}_{x,p} \\ 0 \end{pmatrix} \qquad \mathbf{L_y}(\mathbf{U}) = \begin{pmatrix} 0 \\ 0 \\ 0 \\ \sum_{p=1}^{N} \frac{\rho_{s,p} - \rho_w}{\rho_w}\, \mathcal{L}_{y,p} \\ 0 \end{pmatrix} \tag{3.22}$$

The source term $\mathbf{E_b}(\mathbf{U})$ accounts for the bulk mass exchange between the mixture flow and the bed layer.

$$\mathbf{E_b}(\mathbf{U}) = \begin{pmatrix} -\frac{\rho_b}{\rho_w (1-\xi)} \sum_{p=1}^{N} (D_b - E_b)_p \\ 0 \\ 0 \\ -\sum_{p=1}^{N} \frac{\rho_{s,p} - \rho_w}{\rho_w} (D_b - E_b)_p \\ \frac{1}{1-\xi} \sum_{p=1}^{N} (D_b - E_b)_p \end{pmatrix} \tag{3.23}$$

This model is suitable for highly transient sediment-laden flows with noticeable density gradients, as occurs is densely-packed mud/debris flows over erodible steep beds. It will be referred to as **vdMD** (variable-density mud/debris) model from now on.

3.2 Finite Volume method for variable-density flows with source terms

This section is devoted to the derivation of a new Finite Volume (FV) numerical scheme for 2D variable-density multi-grain mixture flow considering net exchange mass flux between the mixture and the bed layer and dilation of the solid phase. System (3.18) is time dependent, non linear and contains mass and momentum source terms. Under the hypothesis of dominant advection it can be classified as belonging to the family of hyperbolic systems. In order to obtain a numerical solution, the spatial domain is divided in computational cells using a fixed-in-time mesh and system (3.18) is integrated in each cell Ω_i. Applying the Gauss theorem leads to

$$\begin{aligned}\frac{\mathrm{d}}{\mathrm{d}t}\int_{\Omega_i}\mathbf{U}\,\mathrm{d}\Omega+\oint_{\partial\Omega_i}\mathbf{E}(\mathbf{U})\cdot\mathbf{n}\,\mathrm{d}l=\int_{\Omega_i}\mathbf{S_b}(\mathbf{U})\,\mathrm{d}\Omega+\int_{\Omega_i}\mathbf{S_\tau}(\mathbf{U})\,\mathrm{d}\Omega\\ -\oint_{\partial\Omega_i}\mathbf{L}(\mathbf{U})\cdot\mathbf{n}\,\mathrm{d}l+\int_{\Omega_i}\mathbf{E_b}(\mathbf{U})\,\mathrm{d}\Omega\end{aligned} \tag{3.24}$$

being $\mathbf{E}(\mathbf{U})\cdot\mathbf{n}$ the normal flux and $\mathbf{n}=(n_x,\,n_y)$ the outward unit normal vector along the i cell boundary $\partial\Omega_i$. Assuming a piecewise uniform representation of the conserved variables $\mathbf{U}$ at the cell Ω_i, the integrated system (3.24) can be expressed as

$$\begin{aligned}\frac{\mathrm{d}}{\mathrm{d}t}\int_{\Omega_i}\mathbf{U}\,\mathrm{d}\Omega+\sum_{k=1}^{\mathrm{NE}}(\mathbf{E}\cdot\mathbf{n})_k\,l_k=\int_{\Omega_i}\mathbf{S_b}(\mathbf{U})\,\mathrm{d}\Omega+\int_{\Omega_i}\mathbf{S_\tau}(\mathbf{U})\,\mathrm{d}\Omega+\\ -\sum_{k=1}^{\mathrm{NE}}(\mathbf{L}\cdot\mathbf{n})_k\,l_k+\int_{\Omega_i}\mathbf{E_b}(\mathbf{U})\,\mathrm{d}\Omega\end{aligned} \tag{3.25}$$

being NE the number of edges for the i cell, $(\mathbf{E}\cdot\mathbf{n})_k$ the value of the normal flux through the kth edge, l_k the length of the edge (Figure 3.2).

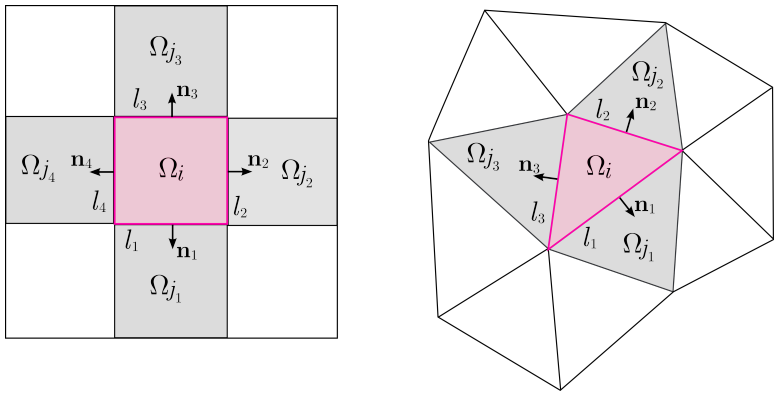

Figure 3.2: Computational cells in (left) orthogonal and (right) triangular meshes.

The left hand side of (3.18), also called homogeneous part, satisfies the rotation invariant property [44]

$$\nabla \cdot \mathbf{E}(\mathbf{U}) = \mathbf{R}^{-1}\, \hat{\nabla} \cdot \mathbf{E}(\mathbf{R}\mathbf{U}) \tag{3.26}$$

being $\hat{\nabla} = \mathbf{R}\nabla$ and $\mathbf{R}$ a rotation matrix which projects the global orthogonal coordinates $\mathbf{X} = (x, y)$ into the local framework $\hat{\mathbf{X}} = \mathbf{R}\mathbf{X} = (\hat{x}, \hat{y})$ of the kth cell edge (Figure 3.3). Assuming that $(\hat{x}, \hat{y})$ correspond to the normal and the tangential directions to the edge respectively, the rotation matrix $\mathbf{R}_k$ and its inverse $\mathbf{R}_k^{-1}$ are defined as

$$\mathbf{R}_k = \begin{pmatrix} 1 & 0 & 0 & 0 & 0 \\ 0 & n_x & n_y & 0 & 0 \\ 0 & -n_y & n_x & 0 & 0 \\ 0 & 0 & 0 & 1 & 0 \\ 0 & 0 & 0 & 0 & 1 \end{pmatrix}_k \qquad \mathbf{R}_k^{-1} = \begin{pmatrix} 1 & 0 & 0 & 0 & 0 \\ 0 & n_x & -n_y & 0 & 0 \\ 0 & n_y & n_x & 0 & 0 \\ 0 & 0 & 0 & 1 & 0 \\ 0 & 0 & 0 & 0 & 1 \end{pmatrix}_k \tag{3.27}$$

and the convective flux term in (3.25) satisfies the condition [138]

$$(\mathbf{E} \cdot \mathbf{n})_k = \left[\mathbf{F}(\mathbf{U})\, n_x + \mathbf{G}(\mathbf{U})\, n_y\right]_k = \mathbf{R}_k^{-1}\, \mathbf{F}(\mathbf{R}_k \mathbf{U}) \tag{3.28}$$

Using , the homogeneous left hand side of (3.25) can be expressed in the local framework $\hat{\mathbf{X}} = (\hat{x}, \hat{y})$ as

$$\frac{\mathrm{d}}{\mathrm{d}t} \int_{\Omega_i} \mathbf{R}_k \mathbf{U}\, \mathrm{d}\Omega + \sum_{k=1}^{\mathrm{NE}} \mathbf{F}(\mathbf{R}_k \mathbf{U})\, l_k \tag{3.29}$$

where $\mathbf{F}(\mathbf{R}_k \mathbf{U})$ denotes the homogeneous normal fluxes throughout the kth cell edges expressed in the local framework.

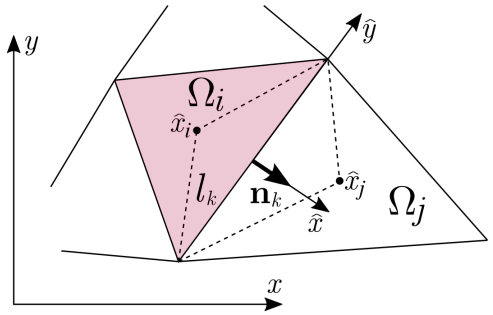

Figure 3.3: Local coordinates at the kth cell edge.

The set of local conserved variables $\hat{\mathbf{U}} \equiv \mathbf{R}_k \mathbf{U}$ at the cell edge is defined as

$$\hat{\mathbf{U}} \equiv \mathbf{R}_k \mathbf{U} = \left(\; rh, \quad rh\,\hat{u}, \quad rh\,\hat{v}, \quad h\phi^{\chi}, \quad z_b \; \right)^T \tag{3.30}$$

where $\hat{u} = un_x + vn_y$ and $\hat{v} = -un_y + vn_x$ are the components of the flow velocity $\hat{\mathbf{u}}$ in the local framework, hence $\hat{\mathbf{u}} = \mathbf{R}_k \mathbf{u}$, and the homogeneous

flux vector $\mathbf{F}(\hat{\mathbf{U}})_k \equiv \mathbf{F}(\mathbf{R}_k\mathbf{U})$ is expressed as

$$\mathbf{F}(\hat{\mathbf{U}})_k \equiv \mathbf{F}(\mathbf{R}_k\mathbf{U}) = \begin{pmatrix} rh\hat{u} \\ rh\hat{u}^2 + \frac{1}{2}g_n rh^2 \\ rh\hat{u}\hat{v} \\ h\hat{u}\,\phi^{\chi} \\ 0 \end{pmatrix} \tag{3.31}$$

The value of the fluxes through the kth cell edge can be augmented incorporating the non-conservative contribution of the momentum source terms $\mathbf{S_b}$ and $\mathbf{S_\tau}$ into the homogeneous normal fluxes $\mathbf{F}(\hat{\mathbf{U}})_k$ [103]. The bed-pressure term $\mathbf{S_b}$ is unconditionally invariant under rotation [21] and can be included within the local framework $(\hat{x}, \hat{y})$ using the spatial discretization

$$\int_{\Omega_i} \mathbf{S_b}(\mathbf{U})\,\mathrm{d}\Omega = \sum_{k=1}^{\mathrm{NE}} \mathbf{R}_k^{-1}\,\mathbf{H}(\hat{\mathbf{U}})_k\,l_k \tag{3.32}$$

where $\mathbf{H}(\hat{\mathbf{U}})_k = (0, H, 0, 0, 0)^T$, being

$$H = -g_n rh\,\Delta z_b \tag{3.33}$$

the integrated value of the bed pressure at the kth cell edge [101] expressed in the local framework (see Section 3.3.1).

The spatial discretization of the basal resistance integral is open to different possibilities since, contrarily to bed-pressure momentum source contribution, the maintenance of the rotation invariant property is not straightforward for the 2D shear stresses. In Section 3.2.1, two different strategies for the upwind discretization of the 2D basal resistance term at the cell edges are presented. Summarizing here, both procedures allow to rewrite the cell-centered integral of the the basal shear stress as a sum of edge-contributions

$$\int_{\Omega_i} \mathbf{S_\tau}(\mathbf{U})\,\mathrm{d}\Omega = \sum_{k=1}^{\mathrm{NE}} \mathbf{R}_k^{-1}\,\mathbf{T}(\hat{\mathbf{U}})_k\,l_k \tag{3.34}$$

where $\mathbf{T}(\hat{\mathbf{U}})_k$ is the integrated basal resistance throughout the kth cell edge, expressed in the local framework (see Section 3.2.1).

Using (3.32) and (3.34), the local homogenous equation (3.29) can be augmented with the momentum source contributions as

$$\frac{\mathrm{d}}{\mathrm{d}t}\int_{\Omega_i} \mathbf{R}_k\mathbf{U}\,\mathrm{d}\Omega + \sum_{k=1}^{\mathrm{NE}} \mathbf{F}(\hat{\mathbf{U}})_k\,l_k = \sum_{k=1}^{\mathrm{NE}} \Big(\mathbf{H}(\hat{\mathbf{U}}) + \mathbf{T}(\hat{\mathbf{U}})\Big)_k\,l_k \tag{3.35}$$

allowing to define an augmented numerical flux $\mathbf{F}(\hat{\mathbf{U}})_k^{\downarrow}$ for the kth cell edge defined as

$$\mathbf{F}(\hat{\mathbf{U}})_k^{\downarrow} = \Big(\mathbf{F}(\hat{\mathbf{U}}) - \mathbf{H}(\hat{\mathbf{U}}) - \mathbf{T}(\hat{\mathbf{U}})\Big)_k \tag{3.36}$$

As the homogeneous convective fluxes, the deviatoric flux associated to the dilation of the solid phase $\mathbf{L}(\mathbf{U})$ (3.22) also satisfies the rotation invariant property

$$\nabla \cdot \mathbf{L}(\mathbf{U}) = \mathbf{R}_k^{-1}\, \hat{\nabla} \cdot \hat{\mathbf{L}}(\mathbf{R}_k \mathbf{U}) \tag{3.37}$$

being $\hat{\nabla} = \mathbf{R}_k \nabla$ and

$$\hat{\mathbf{L}}(\mathbf{R}_k \mathbf{U}) = \left(\hat{\mathbf{L}}_{\mathbf{x}}(\hat{\mathbf{U}}), \hat{\mathbf{L}}_{\mathbf{y}}(\hat{\mathbf{U}})\right) \equiv \mathbf{L}(\mathbf{R}_k \mathbf{X}, \mathbf{R}_k \mathbf{U}) \tag{3.38}$$

Hence, the property (3.2) allows to express the solid phase dilation contribution in (3.25) as

$$\sum_{k=1}^{\mathrm{NE}} (\mathbf{L} \cdot \mathbf{n})_k\, l_k = \sum_{k=1}^{\mathrm{NE}} \mathbf{R}_k^{-1}\, \hat{\mathbf{L}}_{\mathbf{x}}(\hat{\mathbf{U}})_k\, l_k \tag{3.39}$$

with

$$\hat{\mathbf{L}}_{\mathbf{x}}(\hat{\mathbf{U}})_k = \begin{pmatrix} 0 \\ 0 \\ 0 \\ \sum_{p=1}^{N} \frac{\rho_{s,p} - \rho_w}{\rho_w}\, \hat{\mathcal{L}}_{x,p} \\ 0 \end{pmatrix} \tag{3.40a}$$

$$\hat{\mathcal{L}}_{x,p} = \phi_p \frac{\rho_w\, \kappa}{\rho\, \mu} \left(\frac{\partial \mathcal{P}_e}{\partial \hat{x}} + \mathcal{E}_b \rho_w g_n h \frac{\partial z_b}{\partial \hat{x}} \right) \tag{3.40b}$$

The deviatoric dilation flux can be included into the local framework problem (3.35) as

$$\frac{\mathrm{d}}{\mathrm{d}t} \int_{\Omega_i} \mathbf{R}_k \mathbf{U}\, \mathrm{d}\Omega = -\sum_{k=1}^{\mathrm{NE}} \left(\mathbf{F}(\hat{\mathbf{U}})^{\downarrow} + \hat{\mathbf{L}}_{\mathbf{x}}(\hat{\mathbf{U}}) \right)_k l_k \tag{3.41}$$

where $\mathbf{F}(\hat{\mathbf{U}})_k^{\downarrow}$ is the the augmented flux including the momentum source terms (3.36) at the kth cell edge.

Furthermore, the net exchange flux term $\mathbf{E_b}(\mathbf{U})$ accounts for a vertical mass exchange between the bed and the flow layers and hence its nature is different from the other source terms on the right hand side of (3.25). For the sake of simplicity, it is discretized in space as

$$\int_{\Omega_i} \mathbf{E_b}(\mathbf{U})\, d\Omega \approx A_i\, \mathbf{E_b}(\mathbf{U}_i) = \boldsymbol{\mathcal{B}}_i \tag{3.42}$$

where A_i id the discrete cell area.

Restoring (3.41) to the global coordinates $\mathbf{X} = (x, y)$ and replacing (3.42), the integrated system (3.25) can be expressed as

$$\frac{\mathrm{d}}{\mathrm{d}t} \int_{\Omega_i} \mathbf{U}\, \mathrm{d}\Omega = -\sum_{k=1}^{\mathrm{NE}} \mathbf{R}_k^{-1} \left(\mathbf{F}(\hat{\mathbf{U}})^{\downarrow} + \hat{\mathbf{L}}_{\mathbf{x}}(\hat{\mathbf{U}}) \right)_k l_k + \boldsymbol{\mathcal{B}}_i \tag{3.43}$$

$\mathbf{U}$ at the i cell for the time $t = t^n$

$$\mathbf{U}_i^n = \frac{1}{A_i} \int_{\Omega_i} \mathbf{U}(x, y, t^n)\, \mathrm{d}\Omega \tag{3.44}$$

where A_i is the cell area, Assuming a piecewise uniform representation of the conserved variables $\mathbf{U}$ at the i cell for the time $t = t^n$

$$\mathbf{U}_i^n = \frac{1}{A_i} \int_{\Omega_i} \mathbf{U}(x, y, t^n)\, \mathrm{d}\Omega \tag{3.45}$$

and using explicit temporal integration for the mass and momentum source terms, the updating formulation for the conserved variables $\mathbf{U}$ at the each cell is expressed as

$$\mathbf{U}_i^{n+1} = \mathbf{U}_i^n - \frac{\Delta t}{A_i} \sum_{k=1}^{\mathrm{NE}} \mathbf{R}_k^{-1}\, \boldsymbol{\mathcal{F}}_k^{\downarrow}\, l_k + \frac{\Delta t}{A_i}\, \boldsymbol{\mathcal{B}}_i^n \tag{3.46}$$

being $\Delta t = t^{n+1} - t^n$ the time step and

$$\boldsymbol{\mathcal{F}}_k^{\downarrow} = \mathbf{F}(\hat{\mathbf{U}}_i^n, \hat{\mathbf{U}}_j^n)_k^{\downarrow} + \hat{\mathbf{L}}_{\mathbf{x}}(\hat{\mathbf{U}}_i^n, \hat{\mathbf{U}}_j^n)_k \tag{3.47a}$$

$$\boldsymbol{\mathcal{B}}_i^n = A_i\, \mathbf{E}_{\mathbf{b}}(\mathbf{U}_i^n) \tag{3.47b}$$

with the subscripts i and j denoting the left and right cells at the kth cell edge, respectively.

Hence the resolution procedure needs to compute the numerical fluxes $\boldsymbol{\mathcal{F}}_k^{\downarrow}$ at the cell edges. In the next section, we propose a new approximated Riemann solver for variable-density flows based on the augmented Roe solver (A-Roe) approach [103, 127, 138] for the formulation of those fluxes.

3.2.1 Edge-discretization of the basal resistance term

The numerical treatment of the basal shear stress source term has received less attention in literature than the integration of the bed-pressure term but involves a higher complexity, specially when dealing with non-Newtonian flows. Most of the proposed schemes for non-Newtonian flows use centered integration techniques for the computation of the basal resistance at the spatial cells [2, 12, 42, 81, 111], hence requiring implicit [148] or semi-implicit [147] resolution to gain stability. In this Section, and following the foundations proposed by Murillo & García-Navarro [102], two different novel strategies for the discretization of the basal resistance source term (3.34) are proposed, both allowing the explicit computation at the cell edges of an basal resistance edge-contribution.

Integral approach for the edge-contribution

The contribution of the basal resistance to the momentum equation in the integrated problem (3.25) is divided in subcell contributions associated to

the cell edges as

$$\int_{\Omega_i} \mathbf{S}_{\boldsymbol{\tau}}(\mathbf{U})\,\mathrm{d}\Omega = \sum_{k=1}^{\mathrm{NE}} \mathbf{R}_k^{-1} \int_{\Omega_{k,i}} \mathbf{R}_k\,\mathbf{S}_{\boldsymbol{\tau}}(\mathbf{U})\,\mathrm{d}\Omega \tag{3.48}$$

where $\Omega_{k,i}$ is the area of the i cell associated to the kth cell edge, satisfying $\sum_{k=1}^{\mathrm{NE}} \Omega_{k,i} = \Omega_i$. Assuming a piecewise representation of the conserved variables at the cells, the integral of the basal resistance associated to each edge can be expressed as

$$\int_{\Omega_{k,i}} \mathbf{R}_k\,\mathbf{S}_{\boldsymbol{\tau}}(\mathbf{U})\,\mathrm{d}\Omega = \mathbf{R}_k\,\mathbf{S}_{\boldsymbol{\tau}}(\mathbf{U})\,\frac{1}{2} d_{n,i}\,l_k \tag{3.49}$$

being $d_{n,i}$ the normal distance from the center of the i cell to the edge. The piecewise basal resistance vector projected into the local framework can be rewritten as

$$\mathbf{R}_k\,\mathbf{S}_{\boldsymbol{\tau}}(\mathbf{U}) = \mathbf{S}_{\boldsymbol{\tau}}(\mathbf{R_k}\,\mathbf{U}) = \begin{pmatrix} 0 \\ -\frac{\tau_b}{\rho_w}\,\mathbf{n_u}\cdot\mathbf{n} \\ -\frac{\tau_b}{\rho_w}\,\mathbf{n_u}\cdot\mathbf{t} \\ 0 \\ 0 \end{pmatrix} \tag{3.50}$$

where $\mathbf{n} = (n_x, n_y)$ and $\mathbf{t} = (-n_y, n_x)$ are the normal and tangential unit vectors to the kth cell edge respectively. Replacing (3.49) and (3.50) into (3.48) leads to the expression

$$\int_{\Omega_i} \mathbf{S}_{\boldsymbol{\tau}}(\mathbf{U})\,\mathrm{d}\Omega = \sum_{k=1}^{\mathrm{NE}} \mathbf{R}_k^{-1}\,\mathbf{S}_{\boldsymbol{\tau}}(\hat{\mathbf{U}})\,\frac{1}{2} d_{n,i}\,l_k = \sum_{k=1}^{\mathrm{NE}} \mathbf{R}_k^{-1}\,\mathbf{T}(\hat{\mathbf{U}})_k\,l_k \tag{3.51}$$

used in (3.34) for the edge-discretization of the basal resistance term, with

$$\mathbf{T}(\hat{\mathbf{U}})_k = \mathbf{S}_{\boldsymbol{\tau}}(\hat{\mathbf{U}})\,\frac{1}{2} d_{n,i} \tag{3.52}$$

Differential approach for the edge-contribution

The differential strategy is based on treating the friction source term as a non-conservative momentum flux across the cell boundary. Assuming a basal resistance flux matrix $\mathbf{Q}(\mathbf{U}, \mathbf{D})$, depending on both the conserved variables $\mathbf{U}$ and the integration-distance vector $\mathbf{D} = (0, \Delta x, \Delta y, 0, 0)^T$, which satisfies the condition

$$\mathbf{S}_{\boldsymbol{\tau}}(\mathbf{U}) = \nabla \cdot \mathbf{Q}(\mathbf{U}, \mathbf{D}) \tag{3.53}$$

the Gauss theorem can be used to rewrite the basal resistance contribution at the cell as

$$\int_{\Omega_i} \mathbf{S}_{\boldsymbol{\tau}}(\mathbf{U})\,\mathrm{d}\Omega = \int_{\Omega_i} \nabla \cdot \mathbf{Q}(\mathbf{U}, \mathbf{D})\,\mathrm{d}\Omega = \oint_{\partial\Omega_i} \mathbf{Q}(\mathbf{U}, \mathbf{D}) \cdot \mathbf{n}\,\mathrm{d}l \tag{3.54}$$

Therefore, a valid expression for the resistance flux matrix $\mathbf{Q}(\mathbf{U},\mathbf{D})$ is

$$\begin{aligned}\mathbf{Q}(\mathbf{U},\mathbf{D}) &= \left(\begin{array}{c|c} \mathbf{Q_x}(\mathbf{U},\mathbf{D}) & \mathbf{Q_y}(\mathbf{U},\mathbf{D}) \end{array}\right) = \\ &= \left(\begin{array}{c|c} 0 & 0 \\ -\frac{\tau_b}{\rho_w}\,\mathbf{n_u}\cdot\mathbf{d_c} & 0 \\ 0 & -\frac{\tau_b}{\rho_w}\,\mathbf{n_u}\cdot\mathbf{d_c} \\ 0 & 0 \\ 0 & 0 \end{array}\right)\end{aligned} \tag{3.55}$$

with $\mathbf{n_u} = (n_{ux}, n_{uy})$ and $\mathbf{d_c} = (\Delta x, \Delta y)$. Furthermore, (3.55) is invariant under rotation

$$\nabla\cdot\mathbf{Q}(\mathbf{U},\mathbf{D}) = \mathbf{R}_k^{-1}\,\hat{\nabla}\cdot\mathbf{Q}(\mathbf{R}_k\mathbf{U},\mathbf{R}_k\mathbf{D}) \tag{3.56}$$

with $\hat{\nabla} = \mathbf{R}_k\nabla$, allowing to express

$$\mathbf{Q}(\mathbf{U},\mathbf{D})\cdot\mathbf{n} = \mathbf{R}_k^{-1}\,\mathbf{Q_x}(\mathbf{R}_k\mathbf{U},\mathbf{R}_k\mathbf{D}) \tag{3.57}$$

It is worth noting that, in this case, $\mathbf{Q_x}(\mathbf{R}_k\mathbf{U},\mathbf{R}_k\mathbf{D}) \equiv \mathbf{Q_x}(\hat{\mathbf{U}},\hat{\mathbf{D}}) = \mathbf{Q_x}(\mathbf{U},\mathbf{D})$ due to the rotation invariance of the scalar product $\mathbf{n_u}\cdot\mathbf{d_c}$ [44].

Replacing (3.57) into (3.54) leads to the expression

$$\int_{\Omega_i}\mathbf{S}_{\boldsymbol{\tau}}(\mathbf{U})\,\mathrm{d}\Omega = \sum_{k=1}^{\mathrm{NE}}\mathbf{R}_k^{-1}\,\mathbf{Q_x}(\hat{\mathbf{U}},\hat{\mathbf{D}})_k\,l_k = \sum_{k=1}^{\mathrm{NE}}\mathbf{R}_k^{-1}\,\mathbf{T}(\hat{\mathbf{U}})_k\,l_k \tag{3.58}$$

used in (3.34) for the edge-discretization of the basal resistance term, with

$$\mathbf{T}(\hat{\mathbf{U}})_k = \mathbf{Q_x}(\hat{\mathbf{U}},\hat{\mathbf{D}})_k = \begin{pmatrix} 0 \\ -\frac{\tau_b}{\rho_w}\,\mathbf{n_u}\cdot\mathbf{d_c} \\ 0 \\ 0 \\ 0 \end{pmatrix}_k \tag{3.59}$$

3.2.2 Riemann solver for variable-density flows

The augmented numerical flux $\boldsymbol{\mathcal{F}}_k^{\downarrow}$ in the local framework $\hat{\mathbf{X}} = (\hat{x},\hat{y})$ can be computed solving the local equation (3.41) for the kth edge, separating the left i cell and the right j cell. An approximate solution of (3.41) can be obtained using a constant coefficient linear Riemann problem (RP) [138] defined as

$$\begin{aligned}&\frac{\partial\hat{\mathbf{U}}}{\partial t} + \widetilde{\mathbf{J}}_k\frac{\partial\hat{\mathbf{U}}}{\partial\hat{x}} = \hat{\mathbf{S}}_{\mathbf{b}} + \hat{\mathbf{S}}_{\boldsymbol{\tau}} - \frac{\partial\hat{\mathbf{L}}_{\mathbf{x}}}{\partial\hat{x}} \\ &\hat{\mathbf{U}}(\hat{x},0) = \begin{cases} \hat{\mathbf{U}}_i = \mathbf{R}_k\mathbf{U}_i^n & \text{if} \quad \hat{x} < 0 \\ \hat{\mathbf{U}}_j = \mathbf{R}_k\mathbf{U}_j^n & \text{if} \quad \hat{x} > 0 \end{cases}\end{aligned} \tag{3.60}$$

where $\widetilde{\mathbf{J}}_k = \widetilde{\mathbf{J}}_k(\hat{\mathbf{U}}_i,\hat{\mathbf{U}}_j)$ is a constant coefficient matrix which locally approximates the Jacobian of the non-linear RP, whereas $\hat{\mathbf{S}}_{\mathbf{b}}$ and $\hat{\mathbf{S}}_{\boldsymbol{\tau}}$ are the bed-pressure and basal resistance source terms in the local framework.

Integrating the homogeneous left hand side of (3.60) over the discrete space $\hat{x}_i \leq \hat{x} \leq \hat{x}_j$ leads to the following constraint involving conservation across discontinuities

$$\boldsymbol{\delta}\mathbf{F}_k = \widetilde{\mathbf{J}}_k \, \boldsymbol{\delta}\hat{\mathbf{U}}_k \tag{3.61}$$

where $\boldsymbol{\delta}\hat{\mathbf{U}}_k = \hat{\mathbf{U}}_j - \hat{\mathbf{U}}_i$ and $\boldsymbol{\delta}\mathbf{F}_k = \mathbf{F}(\hat{\mathbf{U}}_j) - \mathbf{F}(\hat{\mathbf{U}}_i)$ are the conserved variables and the homogeneous fluxes increment at the kth edge, respectively.

It is worth noting that in (3.31), the convective flux for the bed evolution equation is null and that the mixture mass and momentum convective fluxes do not depend on the bed level variable z_b. Moreover, the influence of the bed-pressure, basal resistance and deviatoric dilation flux terms on the bed elevation does not exist. Hence, the bed evolution equation can be discarded in (3.60) and the numerical flux for the bed elevation updating is $\boldsymbol{\mathcal{F}}_k^{\downarrow\{5\}} = 0$.

Using the Roe strategy [138], the approximate Jacobian $\widetilde{\mathbf{J}}_k$ reduces to a 4×4 constant matrix defined as

$$\widetilde{\mathbf{J}}_k = \begin{pmatrix} 0 & 1 & 0 & 0 \\ \frac{1}{2} g_n \widetilde{h}(1+\widetilde{r}) - \widetilde{u}^2 & 2\widetilde{u} & 0 & -\frac{1}{2} g_n \widetilde{h} \widetilde{r} \\ -\widetilde{u}\,\widetilde{v} & \widetilde{v} & \widetilde{u} & 0 \\ -\widetilde{u}\,\widetilde{\phi}^{\chi}/\widetilde{r} & \widetilde{\phi}^{\chi}/\widetilde{r} & 0 & \widetilde{u} \end{pmatrix}_k \tag{3.62}$$

which satisfies (3.61) with the wall-averaged quantities

$$\widetilde{r} = \frac{r_i h_i + r_j h_j}{h_i + h_j} \tag{3.63a}$$

$$\widetilde{h} = \frac{h_i + h_j}{2} \tag{3.63b}$$

$$\widetilde{u} = \frac{\hat{u}_i \sqrt{r_i h_i} + \hat{u}_j \sqrt{r_j h_j}}{\sqrt{r_i h_i} + \sqrt{r_j h_j}} \tag{3.63c}$$

$$\widetilde{v} = \frac{\hat{v}_i \sqrt{r_i h_i} + \hat{v}_j \sqrt{r_j h_j}}{\sqrt{r_i h_i} + \sqrt{r_j h_j}} \tag{3.63d}$$

$$\widetilde{\phi}^{\chi} = \widetilde{r} \, \frac{\phi_i^{\chi} \, h_i \sqrt{r_j h_j} + \phi_j^{\chi} \, h_j \sqrt{r_i h_i}}{r_i h_i \sqrt{r_j h_j} + r_j h_j \sqrt{r_i h_i}} \tag{3.63e}$$

The approximate matrix $\widetilde{\mathbf{J}}_k$ (3.62) is diagonalizable with four real eigenvalues

$$\widetilde{\lambda}_{1,k} = (\widetilde{u} - \widetilde{c})_k \qquad \widetilde{\lambda}_{2,k} = \widetilde{u}_k \qquad \widetilde{\lambda}_{3,k} = (\widetilde{u} + \widetilde{c})_k \qquad \widetilde{\lambda}_{4,k} = \widetilde{u}_k \tag{3.64}$$

where the averaged celerity $\widetilde{c}_k$ is defined as

$$\widetilde{c}_k = \left(\sqrt{\frac{1}{2} g_n \widetilde{h} \, \left(1 + \widetilde{r} - \widetilde{\phi}^{\chi}\right)} \right)_k \tag{3.65}$$

Therefore, using the associated orthogonal basis of eigenvectors $(\widetilde{\mathbf{e}}_m)_k$ of $\widetilde{\mathbf{J}}_k$, it is possible to build a matrix $\widetilde{\mathbf{P}}_k = (\widetilde{\mathbf{e}}_1, \widetilde{\mathbf{e}}_2, \widetilde{\mathbf{e}}_3, \widetilde{\mathbf{e}}_4)_k$

$$\widetilde{\mathbf{P}}_k = \begin{pmatrix} 1 & 0 & 1 & \widetilde{r} \\ \widetilde{\lambda}_1 & 0 & \widetilde{\lambda}_3 & \widetilde{r}\,\widetilde{u} \\ \widetilde{v} & \widetilde{c} & \widetilde{v} & \widetilde{r}\,\widetilde{v} \\ \widetilde{\phi}^{\chi}/\widetilde{r} & 0 & \widetilde{\phi}^{\chi}/\widetilde{r} & 1+\widetilde{r} \end{pmatrix}_k \tag{3.66}$$

which satisfies

$$\widetilde{\mathbf{J}}_k = (\widetilde{\mathbf{P}}\widetilde{\mathbf{\Lambda}}\widetilde{\mathbf{P}}^{-1})_k \qquad \widetilde{\mathbf{\Lambda}}_k = \begin{pmatrix} \widetilde{\lambda}_1 & & 0 \\ & \ddots & \\ 0 & & \widetilde{\lambda}_4 \end{pmatrix}_k \tag{3.67}$$

being $\widetilde{\mathbf{P}}_k^{-1}$ the inverse matrix of $\widetilde{\mathbf{P}}_k$.

Following [138], the conserved variable gradient $\boldsymbol{\delta}\hat{\mathbf{U}}_k$ is projected on the eigenvector basis in order to obtain the wave strength vectors $\widetilde{\mathbf{A}}_k$ as

$$\widetilde{\mathbf{A}}_k = (\widetilde{\alpha}_1, \ldots, \widetilde{\alpha}_4)_k^T = \widetilde{\mathbf{P}}_k^{-1}\,\boldsymbol{\delta}\hat{\mathbf{U}}_k \quad \longrightarrow \quad \boldsymbol{\delta}\hat{\mathbf{U}}_k = \sum_{m=1}^{4} (\widetilde{\alpha}_m \widetilde{\mathbf{e}}_m)_k \tag{3.68}$$

$$\begin{aligned}
\widetilde{\alpha}_1 &= \frac{\left[(1+\widetilde{r})\widetilde{c} + (1+\widetilde{r}-\widetilde{\phi}^{\chi})\widetilde{u}\right]\delta(rh) - (1+\widetilde{r}-\widetilde{\phi}^{\chi})\,\delta(rh\hat{u}) - \widetilde{r}\widetilde{c}\,\delta(h\phi^{\chi})}{2(1+\widetilde{r}-\widetilde{\phi}^{\chi})\widetilde{c}} \\
\widetilde{\alpha}_2 &= \frac{\delta(rh\hat{v}) - \widetilde{v}\,\delta(rh)}{\widetilde{c}} \\
\widetilde{\alpha}_3 &= \frac{\left[(1+\widetilde{r})\widetilde{c} - (1+\widetilde{r}-\widetilde{\phi}^{\chi})\widetilde{u}\right]\delta(rh) + (1+\widetilde{r}-\widetilde{\phi}^{\chi})\,\delta(rh\hat{u}) - \widetilde{r}\widetilde{c}\,\delta(h\phi^{\chi})}{2(1+\widetilde{r}-\widetilde{\phi}^{\chi})\widetilde{c}} \\
\widetilde{\alpha}_4 &= \frac{\delta(h\phi^{\chi}) - \widetilde{\phi}^{\chi}/\widetilde{r}\,\delta(rh)}{1+\widetilde{r}-\widetilde{\phi}^{\chi}}
\end{aligned}$$

The bed-pressure and basal resistance momentun source terms on the right hand side of (3.60) are integrated over the discrete space $\hat{x}_i \leq \hat{x} \leq \hat{x}_j$ as

$$\int_{\hat{x}_i}^{\hat{x}_j} \hat{\mathbf{S}}_{\mathbf{b}}\, \mathrm{d}\hat{x} = \mathbf{H}(\hat{\mathbf{U}}_i, \hat{\mathbf{U}}_j) = \mathbf{H}_k = (0, H_2, H_3, 0)^T \tag{3.69a}$$

$$\int_{\hat{x}_i}^{\hat{x}_j} \hat{\mathbf{S}}_{\boldsymbol{\tau}}\, \mathrm{d}\hat{x} = \mathbf{T}(\hat{\mathbf{U}}_i, \hat{\mathbf{U}}_j) = \mathbf{T}_k = (0, T_2, T_3, 0)^T \tag{3.69b}$$

It is worth mentioning that the condition (3.69b), with $\mathbf{T}_k$ as in (3.52) for the integral approach or (3.59) for the differential approach, must be satisfied to guarantee the rotation invariance of the edge-discretized basal resistance contribution. This is essential for avoiding the mesh dependence introduced by other edge-discretization methods [102] for non-Newtonian flows.

Following [103], these momentum edge-contributions can be projected on the eigenvector basis in order to obtain the source strength vectors as

$$(\widetilde{\mathbf{B}}_{\mathbf{b}})_k = (\widetilde{\beta}_{b1}, \ldots, \widetilde{\beta}_{b4})_k^T = \widetilde{\mathbf{P}}_k^{-1}\,\mathbf{H}_k \quad \longrightarrow \quad \mathbf{H}_k = \sum_{m=1}^{4} (\widetilde{\beta}_{bm}\widetilde{\mathbf{e}}_m)_k \tag{3.70a}$$

$$(\widetilde{\mathbf{B}}_{\boldsymbol{\tau}})_k = (\widetilde{\beta}_{\tau 1}, \ldots, \widetilde{\beta}_{\tau 4})_k^T = \widetilde{\mathbf{P}}_k^{-1}\,\mathbf{T}_k \quad \longrightarrow \quad \mathbf{T}_k = \sum_{m=1}^{4} (\widetilde{\beta}_{\tau m}\widetilde{\mathbf{e}}_m)_k \tag{3.70b}$$

and the total source strength reads

$$\widetilde{\mathbf{B}}_k = (\widetilde{\beta}_1, \ldots, \widetilde{\beta}_4)_k^T = (\widetilde{\mathbf{B}}_{\mathbf{b}} + \widetilde{\mathbf{B}}_{\boldsymbol{\tau}})_k \tag{3.71}$$

$$\begin{aligned}
\widetilde{\beta}_1 &= \frac{-(H_2 + T_2)}{2\,\widetilde{c}} \\
\widetilde{\beta}_2 &= \frac{H_3 + T_3}{\widetilde{c}} \\
\widetilde{\beta}_3 &= \frac{H_2 + T_2}{2\,\widetilde{c}} \\
\widetilde{\beta}_4 &= 0
\end{aligned}$$

Note that this procedure allows to include the upwind contribution of the real 2D bed-pressure and basal resistance source terms into the plane RP at the cell edges.

One result of Roe's linearization is that the approximate Riemann solution consists of only discontinuities and hence $\hat{\mathbf{U}}(\hat{x}, t)$ is constructed as a sum of jumps or shocks. The approximated solution $\hat{\mathbf{U}}(\hat{x}, t)$ is governed by the celerities in $\widetilde{\mathbf{\Lambda}}_k$ and consists of four regions connected by 5 waves, one of them a contact wave with null celerity accounting for the integrated source term at $\hat{x} = 0$. Figures 3.4 and 3.5 show the wave strecture of the approximate solution for subcritical and supercritical flow regimes respectively. The intermediate states (blue regions) of the approximate solution at the left and right side of the kth edge, $\hat{\mathbf{U}}_i^-$ and $\hat{\mathbf{U}}_j^+$ respectively, are defined as

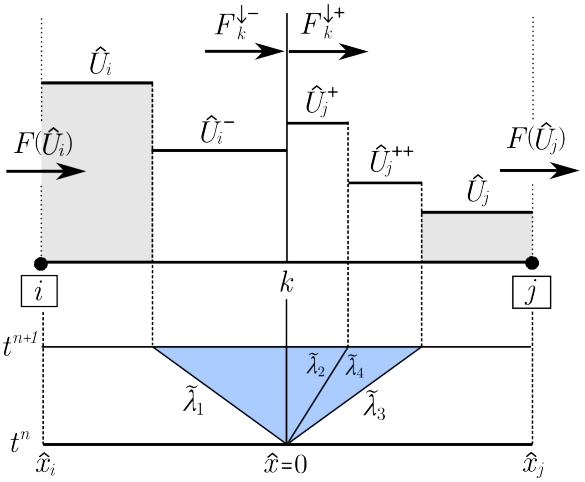

Figure 3.4: Approximate solution for the local plane RP at the kth cell edge for subcritical regime.

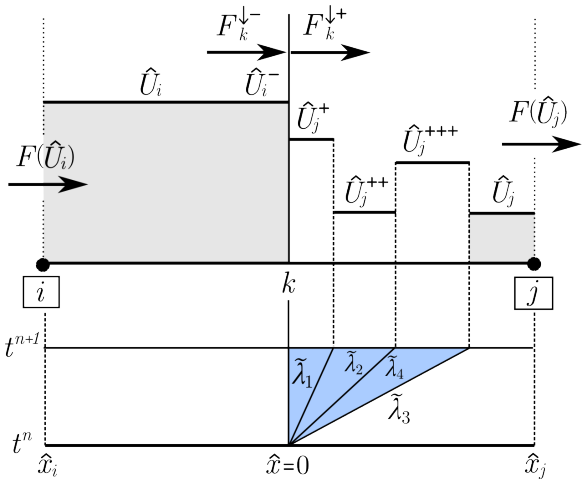

Figure 3.5: Approximate solution for the local plane RP at the kth cell edge for supercritical regime.

$$\hat{\mathbf{U}}_i^- = \lim_{\hat{x}\to 0^-} \hat{\mathbf{U}}(\hat{x},t) \qquad\qquad \hat{\mathbf{U}}_j^+ = \lim_{\hat{x}\to 0^+} \hat{\mathbf{U}}(\hat{x},t) \tag{3.72}$$

Using (3.68) and (3.71), the reconstruction of the approximated solution $\hat{\mathbf{U}}(\hat{x},t)$ at the left and right sides of the cell edge, $\hat{\mathbf{U}}_i^-$ and $\hat{\mathbf{U}}_j^+$ respectively, can be expressed as

$$\begin{aligned} \hat{\mathbf{U}}_i^- &= \hat{\mathbf{U}}_i + \sum_{m-} (\widetilde{\gamma}_m \widetilde{\mathbf{e}}_m)_k \\ \hat{\mathbf{U}}_j^+ &= \hat{\mathbf{U}}_j - \sum_{m+} (\widetilde{\gamma}_m \widetilde{\mathbf{e}}_m)_k \end{aligned} \tag{3.73}$$

where $\widetilde{\gamma}_m = \widetilde{\alpha}_m - \widetilde{\beta}_m/\widetilde{\lambda}_m$ and the subscript $m-$ and $m+$ under the sums indicate waves travelling inward and outward the i cell [103]. Note that at $\hat{x} = 0$ the solution includes a steady jump between the intermediate states $\hat{\mathbf{U}}_i^-$ and $\hat{\mathbf{U}}_j^+$ [78, 128] as a consequence of including the momentum source terms into the local plane RP. This steady jump can be expressed as

$$\hat{\mathbf{U}}_j^+ - \hat{\mathbf{U}}_i^- = \sum_{m=1}^{4} \left(\frac{\widetilde{\beta}_m}{\widetilde{\lambda}_m} \widetilde{\mathbf{e}}_m \right)_k \tag{3.74}$$

According to the Godunov-type method, it is sufficient to provide the approximate solution at the intercell position $\hat{x} = 0$ in order to obtain the augmented numerical fluxes $\mathbf{F}_k^{\downarrow}$ throughout the edge (3.36). The numerical flux at the left and right side of the kth cell edge can be estimated using an approximate flux function $\hat{\mathbf{F}}(\hat{x},t)$ as

$$\mathbf{F}_k^{\downarrow}(\hat{x}\to 0^-) = \lim_{\hat{x}\to 0^-} \hat{\mathbf{F}}(\hat{x},t) \equiv \mathbf{F}_k^{\downarrow -} \tag{3.75a}$$

$$\mathbf{F}_k^{\downarrow}(\hat{x}\to 0^+) = \lim_{\hat{x}\to 0^+} \hat{\mathbf{F}}(\hat{x},t) \equiv \mathbf{F}_k^{\downarrow +} \tag{3.75b}$$

Therefore, the approximated solution for the flux function $\mathbf{F}(\hat{x},t)$ can

also be constructed by defining appropriate Rankine-Hugoniot (RH) relations across each moving wave. The solution of the approximate flux function provides the definition of the numerical fluxes at the left and right sides, $\mathbf{F}_k^{\downarrow -}$ and $\mathbf{F}_k^{\downarrow +}$ respectively, of the kth cell edge

$$\begin{aligned} \mathbf{F}_k^{\downarrow -} &= \mathbf{F}(\hat{\mathbf{U}}_i) + \sum_{m-} (\widetilde{\lambda}_m \widetilde{\gamma}_m \widetilde{\mathbf{e}}_m)_k \\ \mathbf{F}_k^{\downarrow +} &= \mathbf{F}(\hat{\mathbf{U}}_j) - \sum_{m+} (\widetilde{\lambda}_m \widetilde{\gamma}_m \widetilde{\mathbf{e}}_m)_k \end{aligned} \tag{3.76}$$

where the subscript $m-$ and $m+$ under the sums indicate waves travelling inward and outward the i cell.

Note that, when momentum source terms are incorporated into the Riemann solver, it is no longer possible to define a unique value of the numerical flux at both sides of the cell edge. The relation between the approximate fluxes $\mathbf{F}_k^{\downarrow -}$ and $\mathbf{F}_k^{\downarrow +}$ can be analyzed using the Rankine-Hugoniot (RH) relation at $\hat{x} = 0$, which includes the steady contact wave accounting for the momentum sources. The corresponding flux jump is given by

$$\mathbf{F}_k^{\downarrow +} - \mathbf{F}_k^{\downarrow -} = \sum_{m=1}^{4} (\widetilde{\beta}_m \widetilde{\mathbf{e}}_m)_k = \mathbf{H}_k + \mathbf{T}_k \tag{3.77}$$

The numerical flux vector $\boldsymbol{\mathcal{F}}_k^{\downarrow}$ (3.47) also incorporates the contribution of the solid phase dilation at the cell edges $\hat{\mathbf{L}}_{\mathbf{x}}(\hat{\mathbf{U}}_i, \hat{\mathbf{U}}_j)_k \equiv \hat{\mathbf{L}}_k^{\downarrow}$ (3.40). This dilation contribution to the numerical solid flux at the cell edge is expressed as

$$\hat{\mathbf{L}}_k^{\downarrow} = \left(0,\, 0,\, 0,\, \widetilde{L}_k \right)^T \tag{3.78}$$

being $\widetilde{L}_k$ is the deviatoric solid flux related to dilation effects at the kth cell edge.

Hence the numerical flux used in the updating formula (3.46) for the kth edge is written as

$$\begin{aligned} \boldsymbol{\mathcal{F}}_k^{\downarrow\{1,\dots,4\}} &= \mathbf{F}_k^{\downarrow -} + \hat{\mathbf{L}}_k^{\downarrow} \\ \boldsymbol{\mathcal{F}}_k^{\downarrow\{5\}} &= 0 \end{aligned} \tag{3.79}$$

Finally, in order to ensure the stability of the explicitly computed numerical solution, the time step should be small enough to avoid the interaction of waves from neighbouring Riemann problems. The dynamical limitation of the time step at each k edge is addressed here assuming that the fastest wave celerity corresponds to the absolute maximum of the eigenvalues of $\widetilde{\mathbf{J}}_k$ (3.62) as

$$\Delta t_k = \frac{\min(A_i, A_j)}{l_k \left[\max(|\widetilde{\lambda}_1|, |\widetilde{\lambda}_3|) \right]_k} \tag{3.80}$$

and the global time step $\Delta t = t^{n+1} - t^n$ is limited using the Courant-Friedrichs-Lewy (CFL) condition

$$\Delta t = \text{CFL} \min_k (\Delta t_k) \tag{3.81}$$

with CFL < 0.5 for square orthogonal meshes and CFL < 1 for the triangular mesh topology and 1D-mesh cases.

3.2.3 Decoupling of liquid and solid phases

The bulk conserved variables are updated to $\mathbf{U}_i^{n+1}$ using (3.46) which incorporates explicitly the upwind contribution of the convective transport at the cell edges $\boldsymbol{\mathcal{F}}_k^{\downarrow}$ (3.79) and the centered contribution of the net exchange between the flow and the bed layer $\boldsymbol{\mathcal{B}}_i$ (3.47b). Now it is necessary to compute separately the flow depth h and mixture density ρ at the next time t^{n+1}.

From the values of the first and fourth bulk conserved variables, $\mathbf{U}_i^{\{1\}n+1}$ and $\mathbf{U}_i^{\{4\}n+1}$ respectively, the updated values of depth and density can be directly calculated as

$$\begin{aligned} h_i^{n+1} &= \mathbf{U}_i^{\{1\}n+1} - \mathbf{U}_i^{\{4\}n+1} \\ \rho_i^{n+1} &= \rho_w \, \frac{\mathbf{U}_i^{\{1\}n+1}}{h_i^{n+1}} \end{aligned} \tag{3.82}$$

Furthermore, in order to ensure solid mass conservation when dealing with multi-grain mixture flows, the volume fraction of each pth sediment class in the flow column $(h\phi_p)_i$ must be updated separately as follows

$$(h\phi_p)_i^{n+1} = (h\phi_p)_i^n - \frac{\Delta t}{A_i} \sum_{k=1}^{\mathrm{NE}} (F_p^s)_k^{\downarrow} \, l_k - \Delta t \, (D_b - E_b)_{p,i}^n \tag{3.83}$$

where $(F_p^s)_k^{\downarrow}$ is the numerical solid flux at the kth edge for each pth sediment class composing the solid phase in the mixture and $(D_b - E_b)_{p,i}^n$ is the class-specific net exchange at the i cell between the flow and the underlying bed.

Then the volumetric concentration of the pth sediment class at the next time step $t = t^{n+1}$ is computed as

$$(\phi_p)_i^{n+1} = \frac{(h\phi_p)_i^{n+1}}{h_i^{n+1}} \tag{3.84}$$

3.3 Explicit integration of momentum source terms

The correct integration of the momentum source terms $\mathbf{H}_k$ (3.69a) and $\mathbf{T}_k$ (3.69b) for the local plane RP associated to the kth cell edge ensures the well-balanced property of the augmented Riemann solver [104]. This well-balanced character ensures equilibrium in quiescent and steady states, as well as avoids numerical oscillations in the solution when large momentum sources appear, especially associated to the non-Newtonian basal resistance [13, 106].

3.3.1 Well-balanced bed-pressure contribution

Following (3.32), the bed-pressure contribution in the local plane RP for the kth cell edge $\mathbf{H}_k$ (3.69a) is discretized as

$$\mathbf{H}_k = \left(\, 0, \, \widetilde{H}_k, \, 0, \, 0 \, \right)^T \tag{3.85}$$

being $\widetilde{H}_k$ a suitable edge-averaged value accounting for the integrated bed-pressure. In quiescent conditions $\hat{u}_i = \hat{u}_j = 0$ and assuming frictionless flow, the momentum equation along the $\hat{x}-$coordinate in the discrete local RP (3.60) edge reduces to

$$\frac{1}{2} g_n (r_j h_j^2 - r_i h_i^2) = \widetilde{H}_k \tag{3.86}$$

Under these conditions, there exist two different equilibrium configurations which must be maintained [77, 88]. First, considering uniform density $r_i = r_j = \widetilde{r}_k$, the flat free surface condition must be guaranteed

$$(\Delta z_b + \Delta h)_k = 0 \tag{3.87}$$

and second, considering uniform flow depth $h_i = h_j = \widetilde{h}_k$, the discrete density jump must satisfy

$$(\Delta r)_k = -2 \frac{\widetilde{r}_k}{\widetilde{h}_k} (\Delta z_b)_k \tag{3.88}$$

Imposing (3.87) and (3.88) into (3.86) leads to express the well-balanced value of the integrated bed-pressure contribution as

$$\widetilde{H}_k = -g_n \widetilde{r}_k \, \widetilde{h}_k \, (\Delta z_b)_k \tag{3.89}$$

with $\widetilde{r}_k$ and $\widetilde{h}_k$ as defined in (3.63). Hence, the source strengths linked to the bed-pressure contribution read

$$\begin{aligned}
\widetilde{\beta}_{b1} &= \frac{-\widetilde{H}_k}{2\,\widetilde{c}_k} \\
\widetilde{\beta}_{b2} &= 0 \\
\widetilde{\beta}_{b3} &= \frac{\widetilde{H}_k}{2\,\widetilde{c}_k} \\
\widetilde{\beta}_{b4} &= 0
\end{aligned}$$

Test 3.3.1.A: Quiescent equilibrium states with variable density

This idealized benchmark case with exact solution was initially proposed by Leighton *et al.* [77] for ensuring the well-balanced character of compressible shallow-flows in the presence of bed level variations and adapted by Martínez-Aranda *et al.* [88] for variable-density water-solid mixture flows. For a pure one-dimensional flow under quiescent equilibrium (null velocity), frictionless conditions and null net exchange between the bed and the flow, the temporal derivatives of both the mixture and the solid phase mass reduce to zero and the 1D momentum equation becomes

$$\frac{1}{2} \frac{d(r h^2)}{dx} = -r h \frac{dz_b}{dx} \tag{3.90}$$

which can be reordered as

$$\frac{h}{r}\frac{dr}{dx} + 2\frac{dh}{dx} = -2\frac{dz_b}{dx} \tag{3.91}$$

In the generic solution of (3.91), density and flow depth are both variable in space. Nonetheless, there exist two particular solutions interesting for numerical models validation and easy to compute exactly: a) a variable-depth solution with constant density and b) a variable-density solution with constant depth. Following [77], here the bed level profile is defined as

$$z_b(x) = A\left[1 - \cos\frac{2\pi x}{L}\right] \tag{3.92}$$

being A the amplitude and L the length of the idealized 1D channel. The depth-variable equilibrium equation leads to following conditions for the suspended volumetric concentration and flow depth

$$\phi(x) = \frac{r_0 - 1}{\chi} \qquad h(x) = h_0 - A\left[1 - \cos\frac{2\pi x}{L}\right] \tag{3.93}$$

whereas the density-variable solution can be expressed as

$$\phi(x) = \frac{1}{\chi}\left(r_0 \exp\left[\frac{2A}{h_0}\cos\frac{2\pi x}{L}\right] - 1\right) \qquad h(x) = h_0 \tag{3.94}$$

being r_0 and h_0 the reference values for the normalized mixture density and the flow depth, respectively. The relation between the normalized density r of the mixture and the solid concentration ϕ is given by $r = 1 + \chi\phi$, being χ the normalized bouyant density of the solids.

In order to demonstrate the well-balanced charater of the proposed bed-pressure upwind integration, a channel of $L = 100\,m$ is discretized using a 1D mesh of square cells with $\Delta x = 0.1\,m$. Values $A = 0.1\,m$, $h_0 = 1\,m$ and $r_0 = 1.8$ are set, considering a unique sediment class with $\chi = 1.65$. The exact depth-variable and density-variable solutions are imposed as initial conditions for the flow depth and the suspended concentrations. The exhange flux between flow and the bed layer is neglected. The CFL is 1.0 and the final simulation time is $1000\,s$.

Figures 3.6 and 3.7 show the comparison of the exact depth-variable and density-variable solutions, respectively, with the corresponding numerical results at $t = 1000\,s$. The depth and concentrations flow do not vary along the simulation time for both exact solution cases. The exact quiescent equilibrium of the numerical solution is shown by the null velocity values computed along the whole domain at $t = 1000\,s$ for both cases (see Figures 3.6–right and 3.7–right). This demonstrates the well-balance character of the proposed scheme for the simulation of variable-density shallow-flows involving topography variations.

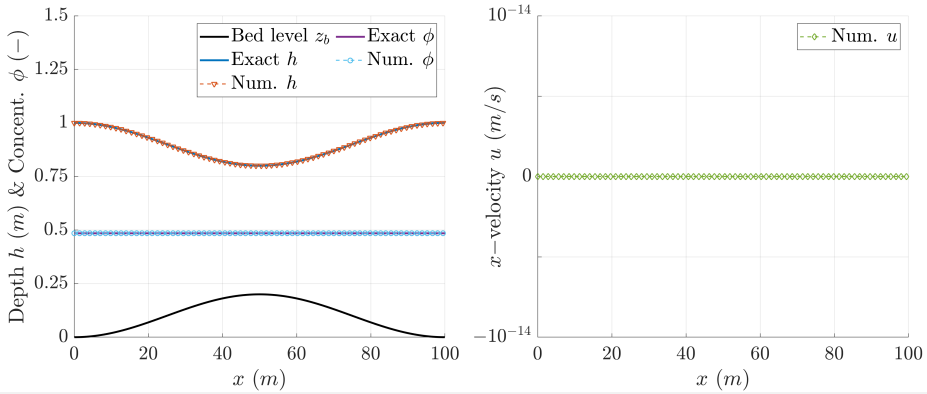

Figure 3.6: Test 3.3.1.A – Exact variable-depth quiescent equilibrium and simulation results at $t = 1000\,s$: (left) flow depth and solid concentration and (right) flow velocity.

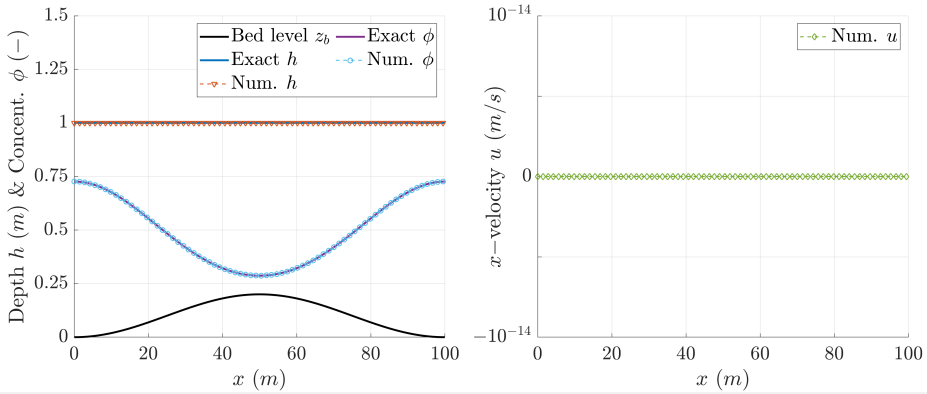

Figure 3.7: Test 3.3.1.A – Exact variable-density quiescent equilibrium and simulation results at $t = 1000\,s$: (left) flow depth and solid concentration and (right) flow velocity.

3.3.2 P-correction for the bed-pressure contribution

Despite the bed-pressure integration (3.89) ensures the balance of momentum sources and convective fluxes at wet-wet cell edges, unbalanced intermediate states of the approximate Riemann solution can appear at wet-dry edges. These unbalanced states may lead to unphysical values of the cell-averaged mixture mass and require a numerical fix. To illustrate this problematic, we considered the wet-dry quiescent equilibrium state at the kth cell edge with

$$\begin{aligned} h_i &\neq 0 \qquad h_j = 0 \\ \hat{u}_i &= 0 \qquad \hat{u}_j = 0 \end{aligned} \tag{3.95}$$

Considering these wet-dry condition, the wall-averaged quantities take the values

$$\widetilde{r}_k = r_i, \quad \widetilde{h}_k = h_i/2, \quad \widetilde{u}_k = 0, \quad \widetilde{v}_k = v_i, \quad \widetilde{\phi}^{\chi}_k = \phi^{\chi}_i \tag{3.96}$$

From now on, the subscript k is suppressed for the sake of clarity. The wave strengths for the linearised RP are

$$\widetilde{\alpha}_1 = -r_i h_i/2, \quad \widetilde{\alpha}_2 = 0, \quad \widetilde{\alpha}_3 = -r_i h_i/2, \quad \widetilde{\alpha}_4 = 0 \tag{3.97}$$

The homogeneous intermediate state for the mixture mass $(rh)^\star$ is constant throughout the edge and always positive. It can be calculated as

$$(rh)^\star = r_i h_i + \widetilde{\alpha}_1 = r_j h_j - \widetilde{\alpha}_3 = \frac{r_i h_i}{2} \tag{3.98}$$

and hence the augmented intermediate states for the mixture mass at the left and right side of the edge, $(rh)^-_i$ and $(rh)^+_j$ respectively, read

$$(rh)^-_i = (rh)^\star - \widetilde{\beta}_{b1}/\widetilde{\lambda}_1 = \frac{1}{2}(r_i h_i + r_i \Delta z_b) \tag{3.99a}$$

$$(rh)^+_j = (rh)^\star + \widetilde{\beta}_{b3}/\widetilde{\lambda}_3 = \frac{1}{2}(r_i h_i - r_i \Delta z_b) \tag{3.99b}$$

On the one hand, considering the quiescent condition (3.95) with $\Delta z_b > 0$, the intermediate state $(rh)^-_i$ is always positive but $(rh)^+_j$ is negative for $\Delta z_b > h_i$ (red region in Figure 3.8–left), leading to unphysical negative values of the cell-averaged mixture mass in the right dry j cell at the next time step.

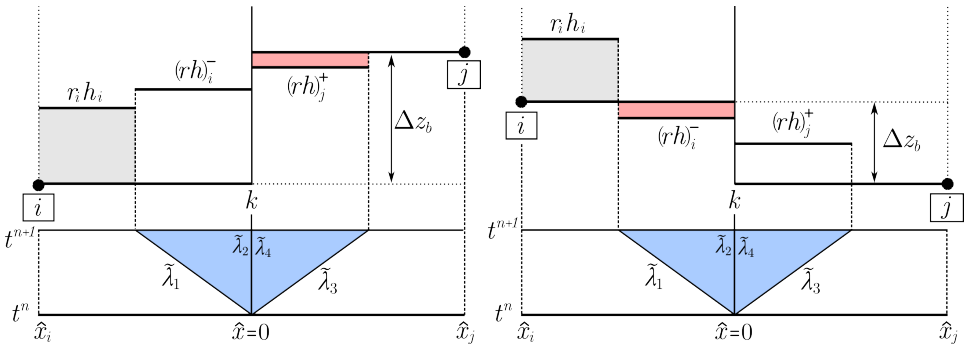

Figure 3.8: Quiescent intermediate states in wet-dry edges: (left) positive bed slope case and (right) negative bed slope case.

On the other hand, assuming the quiescent wet-dry condition (3.95) with $(\Delta z_b) < 0$ causes always positive values at the right dry cell. Nevertheless, the intermediate state $(rh)^-_i$ is negative for $|\Delta z_b| > h_i$ (see red region in Figure 3.8–right) and, hence, may cause unphysical negative values of the cell-averaged mixture mass at the next time step if the initial water in the i cell is small enough.

The non-quiescent conditions $\hat{u}_i \neq 0$ in wet-dry edges can even lead to more noticeable negative intermediate states. Furthermore, wet-wet edges can also suffer from these positivity problems in the inner states of the mixture mass approximate solution when the momentum sources are large

enough. In order to prevent the unphysical values of the cell-averaged mixture mass under any kind of dynamic conditions and bed-pressure momentum source terms, a numerical fix for ensuring the positivity of the intermediate states in the approximate RP solution, called P-correction from now on, is proposed in this thesis.

Considering the approximated solution reconstruction depicted in Figure 3.9 for the mixture mass at the kth cell edge under subcritical flow regime, the intermediate state at the left side $(rh)_i^-$ of the edge is expressed as

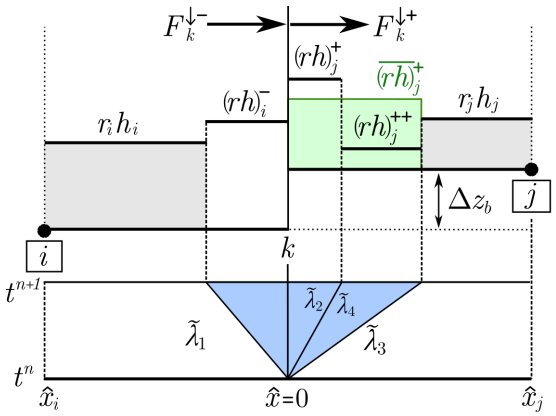

Figure 3.9: Inner states for the mixture mass solution in edges with right-direction subcritical flow.

$$(rh)_i^- = (rh)^\star - \frac{\widetilde{\beta}_{b1}}{\widetilde{\lambda}_1} \tag{3.100}$$

being

$$(rh)^\star = r_i h_i + \widetilde{\alpha}_1 = r_j h_j - \widetilde{\alpha}_3 - \widetilde{\alpha}_4 \widetilde{r} \tag{3.101}$$

the homogeneous intermediate state for the mixture mass at the edge region. Therefore, imposing positivity $(rh)_i^- \geq 0$ leads to an upper-bound for the integrated value of the bed-pressure contribution as

$$\widetilde{H}_k \leq 2\widetilde{c}\,|\widetilde{\lambda}_1|\,(rh)^\star \tag{3.102}$$

The cell-averaged value of the mixture mass at the right side of the kth edge involves two different intermediate states of the approximate solution, $(rh)_j^+$ and $(rh)_j^{++}$. In order to limit the bed-pressure contribution, it is possible to define an averaged intermediate state for the homogeneous RP at the right cell $(\overline{rh})_j^\star$ as

$$(\overline{rh})_j^\star = r_j h_j - \widetilde{\alpha}_3 - \frac{\widetilde{\lambda}_4}{\widetilde{\lambda}_3}\widetilde{\alpha}_4 \widetilde{r} \tag{3.103}$$

and hence the averaged augmented intermediate state at the right side (green region in Figure 3.9) reads

$$(\overline{rh})_j^+ = (\overline{rh})_j^\star + \frac{\widetilde{\beta}_{b3}}{\widetilde{\lambda}_3} \tag{3.104}$$

Then, impossing positivity $(\overline{rh})_j^+ \geq 0$ allows to determine the following lower-bound for the bed pressure contribution as

$$\widetilde{H}_k \geq -2\widetilde{c}\,\widetilde{\lambda}_3\,(\overline{rh})_j^\star \tag{3.105}$$

which avoids negative cell-averaged values of the mixture mass at the next time $t^{n+1} = t + \Delta t$.

In supercritical flow regime, the updated cell-averaged value of the mixture mass does not depend directly on the bed-pressure contribution but exclusively on the convective fluxes increment at the cell edge. However, ensuring positive intermediate states of the approximate solution is possible by separating the RP at the cell edge into two zones: one from the edge to the slower wave $\widetilde{\lambda}_1$ and other from that to the faster wave $\widetilde{\lambda}_3$ (see Figure 3.10). On one hand, the intermediate state $(rh)_j^+$ is achieved using the RH condition throughout the contact wave at $\hat{x} = 0$ (3.74) as

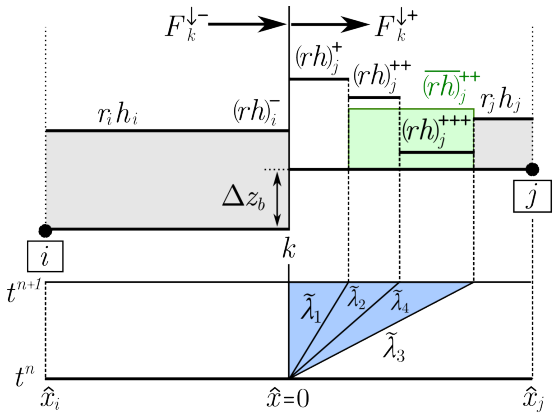

Figure 3.10: Inner states for the mixture mass solution in edges with right-direction supercritical flow.

$$(rh)_j^+ = (rh)_i + \left(\frac{\widetilde{\beta}_{b1}}{\widetilde{\lambda}_1} + \frac{\widetilde{\beta}_{b3}}{\widetilde{\lambda}_3}\right) \tag{3.106}$$

and imposing positivity $(rh)_j^+ \geq 0$ leads to an upper-bound for integrated value of the bed-pressure contribution as

$$\widetilde{H}_k \leq \widetilde{\lambda}_1\,\widetilde{\lambda}_3\,(rh)_i \tag{3.107}$$

On the other hand, the mean intermediate state $(\overline{rh})_j^{++}$ between the waves $\widetilde{\lambda}_1$ and $\widetilde{\lambda}_3$ (green region in Figure 3.10) is obtained averaging $(rh)_j^{++}$ and $(rh)_j^{+++}$, and can be expressed as

$$(\overline{rh})_j^{++} = (\overline{rh})_j^\star + \frac{\widetilde{\beta}_{b3}}{\widetilde{\lambda}_3} \tag{3.108}$$

with $(\overline{rh})_j^\star$ as in (3.103) and, imposing positivity $(\overline{rh})_j^{++} \geq 0$, allows to determine a lower-bound for the bed-pressure contribution in supercritical edges as

$$\widetilde{H}_k \geq -2\widetilde{c}\,\widetilde{\lambda}_3\,(\overline{rh})_j^\star \tag{3.109}$$

Table 3.2 summarizes the P-correction procedure for the bed-pressure momentum contribution $\widetilde{H}_k$ in subcritical and supercritical flow edges. It is worth noting that the above procedure is derived for edges with right-direction flow $\widetilde{u}_k \geq 0$ but it can be straightforwardly extended to left-direction flow $\widetilde{u}_k < 0$.

Bound type	Sucritical edge $\widetilde{u}_k < \widetilde{c}_k$	Supercritical edge $\widetilde{u}_k > \widetilde{c}_k$
Upper-bound	$\widetilde{H}_k \leq 2\widetilde{c}\,\lvert\widetilde{\lambda}_1\rvert\,(rh)^\star$	$\widetilde{H}_k \leq \widetilde{\lambda}_1\,\widetilde{\lambda}_3\,(rh)_i$
Lower-bound	$\widetilde{H}_k \geq -2\widetilde{c}\,\widetilde{\lambda}_3\,(\overline{rh})^\star_j$	$\widetilde{H}_k \geq -2\widetilde{c}\,\widetilde{\lambda}_3\,(\overline{rh})^\star_j$
	with:	
	$(rh)^\star = r_i h_i + \widetilde{\alpha}_1 = r_j h_j - \widetilde{\alpha}_3 - \widetilde{\alpha}_4 \widetilde{r}$	
	$(\overline{rh})^\star_j = r_j h_j - \widetilde{\alpha}_3 - \widetilde{\lambda}_4/\widetilde{\lambda}_3\,\widetilde{\alpha}_4 \widetilde{r}$	

Table 3.2: Summary of the bed-pressure P-correction procedure for edges with right-direction flow.

Test 3.3.1.B: Dambreak wet-dry advance over discontinuous bed

In order to demonstrate the capability of the proposed P-correction 3.2 to deal with flow advance over dry bed involving a step, ensuring conservation and stability, a channel $100\,m$ long is discretized using a 1D mesh of square cells with $\Delta x = 0.1\,m$. The initial flow and bed levels are depicted in Figure (3.11) and quiescent state is considered for the initial flow velocity. A uniform normalized bulk density $r_0 = 1.8$ is set at the initial time, considering a unique sediment class with concentration $\phi = 0.5$ and density $\rho_s = 2600\,kg/m^3$. The exchange flux bewteen the flow and the bed layer is neglected during the whole simulation, as well as the effects of the solid phase dilation. The basal resistance contribution is also suppresed. The CFL is 1.0 and the final simulation time is $100\,s$.

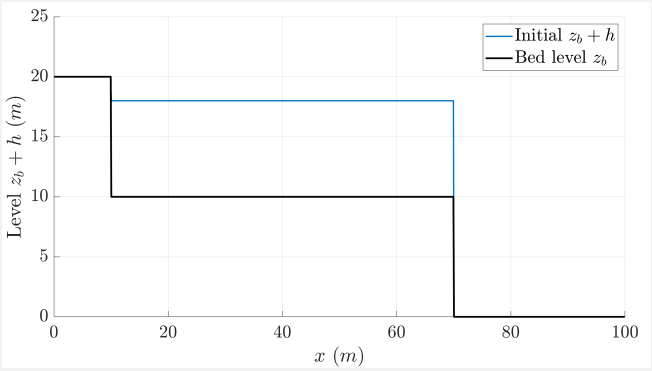

Figure 3.11: Test 3.3.1.B – Initial conditions for test 3.3.1.B.

Figure 3.12 shows the temporal evolution of the dambreak flow during the first 10 seconds. The solutions with and without the P-correction (solid blue and dashed orange lines, respectively) are compared. When the P-correction is not applied, the appearance of unphysical negative values in the mixture mass solution is addressed by limiting the time step.

First, the behaviour of the solution with both methods at the left wet-dry interface $x = 10\,m$ is assessed. On the one hand, for the first stages $t < 6\,s$, the unbalance between the quiescent convective flux and the bed-pressure contribution generates a small unphysical flux at the left wet-dry interface when the P-correction is not applied (dashed orange line), whereas a perfect quiescent balance is maintained with the P-correction (solid blue line). On the other hand, for times $t > 6\,s$, the rarefaction wave of the dambreak reaches the left wet-dry interface and the unbalance in the solution without the P-correction grows suddenly due to the velocity at the right cell but the P-correction, generating a high slope in the flow free surface. The solution using the P-correction is smooth and the velocity increases progressively along the rarefaction region.

Second, at the right wet-dry interface, the dambreak wave progresses over the negative bed step with different velocities for the solutions with and without P-correction, specially at the first stages $t < 1\,s$. This difference is mainly caused at the negative bed step $\hat{x} = 70\,m$, where the unbalance between the homogeneous flux and bed-pressure source terms if the P-correction is not applied generates a more marked discontinuity in the flow depth and velocity. Moreover, the dambreak front seems to show a lower numerical diffusion for the P-corrected solution.

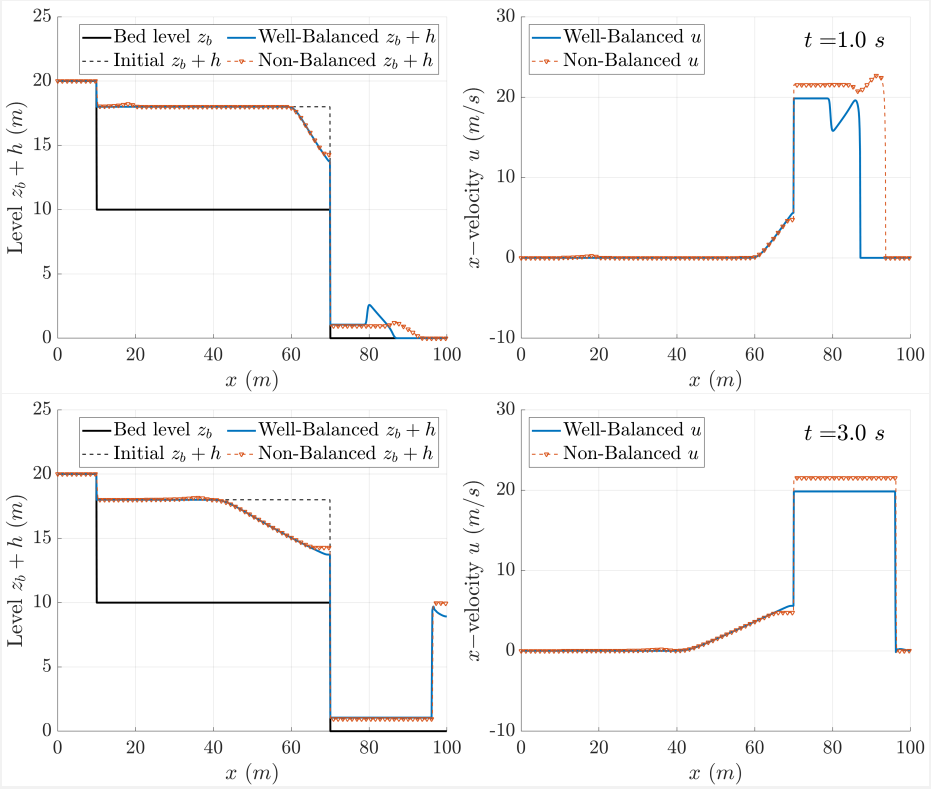

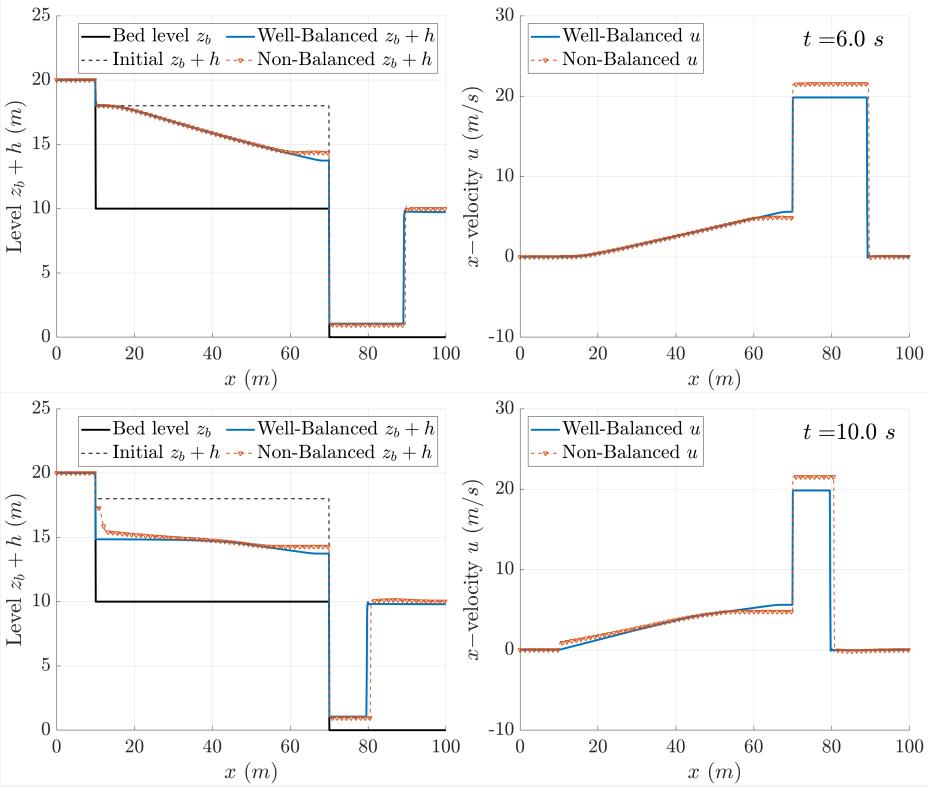

Figure 3.12: Test 3.3.1.B – Temporal evolution of the dambreak flow over step dry bed: (left) flow free surface and (right) flow velocty. From top to bottom: $t = 1\,s$, $t = 3\,s$, $t = 6\,s$ and $t = 10\,s$.

Finally, it is worth mentioning that, if the P-correction is not applied, the mixture mass positivity issues that appear at the wet-dry interfaces are addressed by reducing the time step in order to maintain the mass conservation error under a suitable upper-bound. Figure 3.13 shows the time step size evolution during the dambreak simulation with and without the P-correction. For each procedure, both the time step limitation obtained from the Jacobian wave celerities $\widetilde{\lambda}_m$ (solid red line) and the maximum time step allowed for ensuring mixture mass positivity (dashed blue line) are depicted. If the P-correction is applied, the time step applied is time step associated to the Jacobian waves and the solution positivity is guaranteed without requiring additional time step limitations. Contrarily, if the P-correction is not applied, the time step must be reduced one order of magnitude mainly to deal with positivity problems at the left wet-dry interface $\hat{x} = 10\,m$. This affects considerably to the numerical scheme performance, leading to a high efficiency loss.

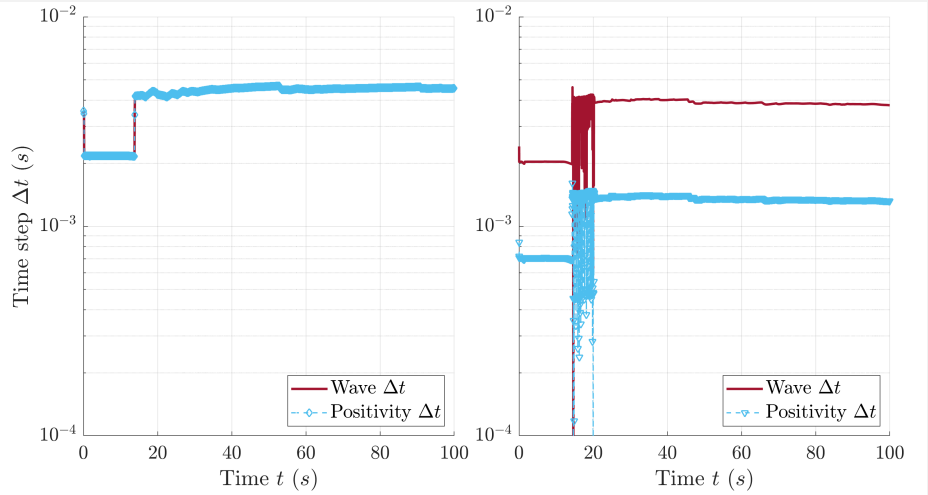

Figure 3.13: Test 3.3.1.B – Time step evolution for the dambreak flow over step dry bed: (left) with P-correction and (right) with time step reduction procedures.

3.3.3 Enhanced basal resistance contribution

The explicit integration of the basal resistance term $\mathbf{T}_k$ (3.69b) is not straight-forward and requires a careful treatment in order to avoid numerical instabilities and additional time step restrictions even using the common hydraulic resistance formulations [13, 106] based on the Turbulent-Newtonian model (see Table 2.1). These additional time step restrictions can lead to a marked increase of the computational time required by the model. The consequence is a reduction of the efficiency, regardless of how the scheme is implemented (programming language, parallel computing, available hardware, etc). When non-Newtonian flow behavior is considered the influence of the basal resistance contribution in the well-balanced solution increases as the boundary shear stress magnitude grows considerably. Moreover, under quiescent conditions, the basal resistance contribution may not be null due to the existence of a frictional/cohesive yield strength and the well-balanced behavior of the solution must be reexamined.

Two different approaches for the upwind discretization of the resistance terms (3.69b) in two-dimensional numerical models for variable-density shallow-flows are described in Section (3.2.1). This section is devoted to the correct explicit integration of the basal resistance contribution at the cell edges using both approaches, paying especial attention to ensuring the balance between homogeneous fluxes and momentum sources in order to avoid numerical oscillations or additional time step restrictions.

Integral upwind contribution

Using the integral approach (3.52) for the spatial discretization of the 2D resistance contribution at the kth cell edge, the associated momentum contribution $\mathbf{T}_k$ (3.69b) in the local plane RP is defined as

$$\mathbf{T}_k = \mathbf{T}(\hat{\mathbf{U}}_i, \hat{\mathbf{U}}_j) = \begin{pmatrix} 0 \\ \widetilde{T}_n \\ \widetilde{T}_t \\ 0 \\ 0 \end{pmatrix}_k \tag{3.110}$$

where $(\widetilde{T}_n)_k$ and $(\widetilde{T}_t)_k$ represent suitable values of the integrated basal resistance contribution along the normal and tangential directions to the kth cell edge.

Using (3.71), the source strengths linked to the basal resistance contribution are expressed as

$$\begin{aligned} \widetilde{\beta}_{\tau 1} &= \frac{-(\widetilde{T}_n)_k}{2\,\widetilde{c}_k} \\ \widetilde{\beta}_{\tau 2} &= \frac{(\widetilde{T}_t)_k}{\widetilde{c}} \\ \widetilde{\beta}_{\tau 3} &= \frac{(\widetilde{T}_n)_k}{2\,\widetilde{c}_k} \\ \widetilde{\beta}_{\tau 4} &= 0 \end{aligned} \tag{3.111}$$

Physically, while the bed-pressure momentum term can accelerate or decelerate the flow depending on the directions of both the flow velocity and the bed slope, the basal resistance term should always act slowing down the flow. In the extreme case, the non-Newtonian resistance contribution must stop the flow completely, maintaining the quiescent equilibrium when the component of the gravitational force tangential to the bed surface remains below the frictional/cohesive yield strength. Therefore, it is important to stress first that the basal resistance contribution at the kth cell edge should be opposite to the discharge and is hence defined as

$$(\widetilde{T}_n)_k = -\mathrm{sgn}(F_n)_k \left(\frac{\widetilde{\tau}_b}{\rho_w} \frac{|\widetilde{u}|}{\sqrt{\widetilde{u}^2 + \widetilde{v}^2}} \frac{1}{2} d_n \right)_k \tag{3.112a}$$

$$(\widetilde{T}_t)_k = -\mathrm{sgn}(F_t)_k \left(\frac{\widetilde{\tau}_b}{\rho_w} \frac{|\widetilde{v}|}{\sqrt{\widetilde{u}^2 + \widetilde{v}^2}} \frac{1}{2} d_n \right)_k \tag{3.112b}$$

where $(d_n)_k = d_{n,i} + d_{n,j}$ is the distance between the centers of the left i and right j cells along the normal direction to the edge and $(\widetilde{\tau}_b)_k = \frac{1}{2}(\tau_{b,i} + \tau_{b,j})$ is the averaged bed shear stress at the kth cell edge, being $\tau_{b,i}$ and $\tau_{b,j}$ the corresponding neighboring cell value computed using the formulations in Table 3.1. Note that $\mathrm{sgn}(F_n)_k$ and $\mathrm{sgn}(F_t)_k$ in (3.112) denote the frictionless discharge along the normal and tangential directions to the kth cell edge, respectively.

Focusing on the normal direction to the k cell edge and assuming subcritical right-direction flow (see Figure 3.14), the inner state at the edge of

the normal discharge including the homogeneous component and the bed-pressure contribution $(rh\hat{u})^\star$ remains constant at both sides of the edge and reads

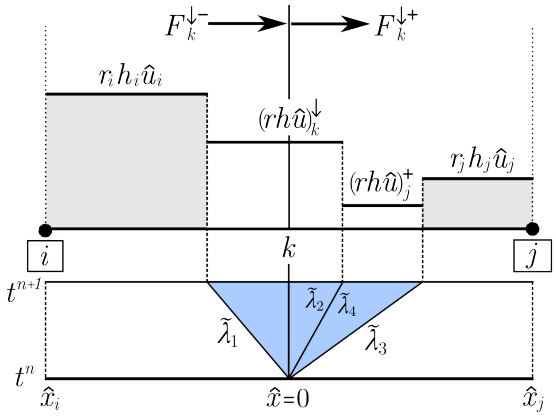

Figure 3.14: Inner states for the normal discharge solution in edges with right-direction subcritical flow.

$$(rh\hat{u})^\star = r_i h_i \hat{u}_i + \widetilde{\alpha}_1 \widetilde{\lambda}_1 - \widetilde{\beta}_{b1} = r_j h_j \hat{u}_j - \widetilde{\alpha}_3 \widetilde{\lambda}_3 - \widetilde{\alpha}_4 \widetilde{r}\widetilde{u} + \widetilde{\beta}_{b3} \tag{3.113}$$

and hence $\mathrm{sgn}(F_n)_k = (rh\hat{u})^\star$. Including the basal resistance contribution into (3.113) leads to the augmented normal discharge, which also remains constant at both sides of the cell edge and can be expressed as

$$(rh\hat{u})^{\downarrow} = (rh\hat{u})^\star - \widetilde{\beta}_{\tau 1} = (rh\hat{u})^\star + \widetilde{\beta}_{\tau 3} = (rh\hat{u})^\star + \frac{\widetilde{T}_n}{2\,\widetilde{c}} \tag{3.114}$$

Therefore, imposing that the basal resistance contribution should not change the direction of the frictionless normal discharge at the edge allows to define the following limitation for the resistance source strengths

$$\begin{aligned} \widetilde{\beta}_{\tau 1} &= \begin{cases} -\widetilde{T}_n/(2\,\widetilde{c}) & \text{if} \quad (rh\hat{u})^{\downarrow}\,(rh\hat{u})^\star > 0 \\ (rh\hat{u})_b^\star & \text{if} \quad (rh\hat{u})^{\downarrow}\,(rh\hat{u})^\star \leq 0 \end{cases} \\ \widetilde{\beta}_{\tau 3} &= -\widetilde{\beta}_{\tau 1} \end{aligned} \tag{3.115}$$

When the flow at the cell edge is supercritical, all the waves travel to the right and the resistance source strengths do not affect the value of the normal discharge at the cell edge (Figure 3.15). However, it is possible to define an averaged inner state between the waves $\widetilde{\lambda}_1$ and $\widetilde{\lambda}_3$ for the right j cell including both the homogeneous and the bed-pressure components $(\overline{rh\hat{u}})_j^\star$ as

$$(\overline{rh\hat{u}})_j^\star = r_j h_j \hat{u}_j - \widetilde{\alpha}_3 \widetilde{\lambda}_3 - \frac{\widetilde{\lambda}_4}{\widetilde{\lambda}_3} \widetilde{\alpha}_4 \widetilde{r}\widetilde{u} + \widetilde{\beta}_{b3} \tag{3.116}$$

and hence $\mathrm{sgn}(F_n)_k = (rh\hat{u})_j^\star$. Including the basal resistance contribution into (3.116) leads to the averaged inner state for the normal discharge

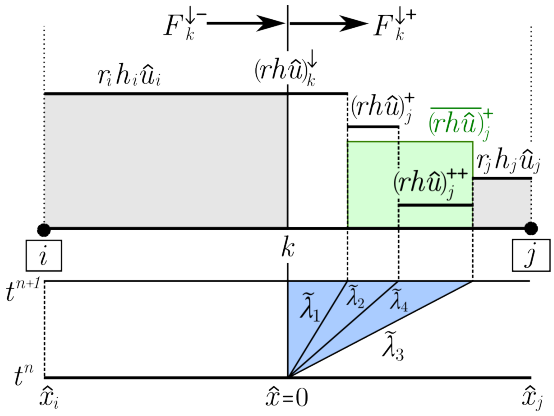

Figure 3.15: Inner states for the normal discharge solution in edges with right-direction supercritical flow.

$(\overline{rh\hat{u}})_j^+$ between the waves $\widetilde{\lambda}_1$ and $\widetilde{\lambda}_3$, which can be expressed as

$$(\overline{rh\hat{u}})_j^+ = (\overline{rh\hat{u}})_j^\star + \widetilde{\beta}_{\tau 3} = (\overline{rh\hat{u}})_j^\star + \frac{\widetilde{T}_n}{2\,\widetilde{c}} \tag{3.117}$$

Therefore, imposing that the basal resistance contribution does not change the direction of the frictionless inner value of the normal discharge allows to obtain a limitation for the resistance source strengths in supercritical edges as

$$\begin{aligned} \widetilde{\beta}_{\tau 3} &= \begin{cases} \widetilde{T}_n/(2\,\widetilde{c}) & \text{if} \quad (\overline{rh\hat{u}})_j^+ \, (\overline{rh\hat{u}})_j^\star > 0 \\ -(\overline{rh\hat{u}})_j^\star & \text{if} \quad (\overline{rh\hat{u}})_j^+ \, (\overline{rh\hat{u}})_j^\star \leq 0 \end{cases} \\ \widetilde{\beta}_{\tau 1} &= -\widetilde{\beta}_{\tau 3} \end{aligned} \tag{3.118}$$

From now on, these limits over the basal resistance contributions are called R-correction and can be straightforwardly extended to the case with negative velocity ($\widetilde{u}_k < 0$) at the kth cell edge.

Regarding the tangential component of the basal resistance contribution $(\widetilde{T}_t)_k$, it is associated exclusively to the momentum source strength $\widetilde{\beta}_{\tau 2}$ (3.111) and hence to the wave $\widetilde{\lambda}_2$. Note that, due to the definition of the eigenvector $\widetilde{\mathbf{e}}_\mathbf{2} = (0, 0, \widetilde{c}, 0)^T$ (3.66), the wave $\widetilde{\lambda}_2$ only participates in the approximate solution for the tangential discharge $(rh\hat{v})$. Furthermore, the tangential basal resistance contribution only affects to the averaged value of the tangential discharge on the right cell since $\widetilde{\lambda}_2 = \widetilde{u}$.

In order to correctly integrate explicitly the tangential basal resistance component, we propose here the following procedure. First, assuming right-direction subcritical flow at the edge (Figure 3.16), the averaged inner value of the tangential discharge at the right j cell including the homogeneous, the bed-pressure and the normal resistance components $(\overline{rh\hat{v}})_j^+$ is defined as

$$(\overline{rh\hat{v}})_j^\star = r_j h_j \hat{v}_j - \widetilde{\alpha}_3 \widetilde{v} - \frac{\widetilde{\lambda}_2}{\widetilde{\lambda}_3} \widetilde{\alpha}_2 \widetilde{c} - \frac{\widetilde{\lambda}_4}{\widetilde{\lambda}_3} \widetilde{\alpha}_4 \widetilde{rv} + \frac{\widetilde{\beta}_{b3} + \widetilde{\beta}_{\tau 3}}{\widetilde{\lambda}_3} \widetilde{v} \tag{3.119}$$

whereas, for supercritical right-direction edges 3.17, the averaged inner state at the right cells includes all the waves and hence do not depend on

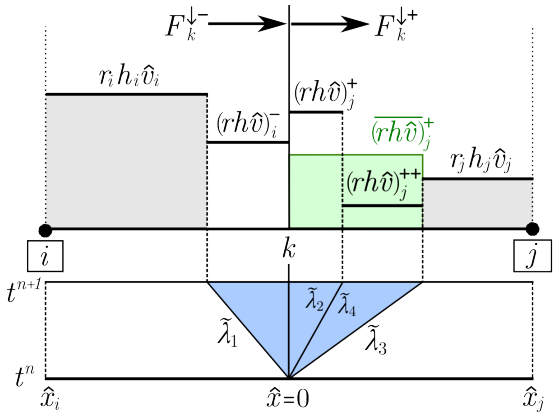

Figure 3.16: Inner states for the tangential discharge solution in edges with right-direction subcritical flow.

the bed-pressure and normal resistance source strengths, reading

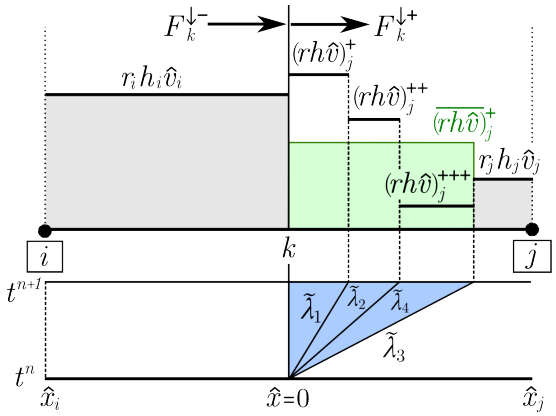

Figure 3.17: Inner states for the tangential discharge solution in edges with right-direction supercritical flow.

$$
\begin{aligned}
(\overline{rh\hat{v}})_j^\star &= r_j h_j \hat{v}_j - \widetilde{\alpha}_3\widetilde{v} - \frac{\widetilde{\lambda}_2}{\widetilde{\lambda}_3}\widetilde{\alpha}_2\widetilde{c} - \frac{\widetilde{\lambda}_4}{\widetilde{\lambda}_3}\widetilde{\alpha}_4\widetilde{rv} - \frac{\widetilde{\lambda}_1}{\widetilde{\lambda}_3}\widetilde{\alpha}_1\widetilde{v} \\
&\quad + \frac{\widetilde{\beta}_{b3} + \widetilde{\beta}_{\tau 3}}{\widetilde{\lambda}_3}\widetilde{v} + \frac{\widetilde{\lambda}_1}{\widetilde{\lambda}_3}\frac{\widetilde{\beta}_{b1} + \widetilde{\beta}_{\tau 1}}{\widetilde{\lambda}_1}\widetilde{v} \\
&= r_j h_j \hat{v}_j - \frac{1}{\widetilde{\lambda}_3}(\widetilde{\alpha}_1\widetilde{v} + \widetilde{\alpha}_2\widetilde{c} + \widetilde{\alpha}_3\widetilde{v} + \widetilde{\alpha}_4\widetilde{rv}) \\
&= r_j h_j \hat{v}_j - \frac{\delta(rh\hat{v}\hat{u})}{\widetilde{\lambda}_3}
\end{aligned}
\tag{3.120}
$$

Therefore, the direction of the tangential basal resistance contribution is defined as $\mathrm{sgn}(F_t)_k = (rh\hat{v})_j^\star$ and the augmented tangential discharge in

both edge types can be expressed as

$$\begin{aligned}(\overline{rh\hat{v}})_j^+ &= (\overline{rh\hat{v}})_j^\star + \frac{\widetilde{\lambda}_2}{\widetilde{\lambda}_3}\frac{\widetilde{\beta}_{\tau 2}}{\widetilde{\lambda}_2}\widetilde{c} \\ &= (\overline{rh\hat{v}})_j^\star + \frac{\widetilde{\beta}_{\tau 2}}{\widetilde{\lambda}_3}\widetilde{c} \\ &= (\overline{rh\hat{v}})_j^\star + \frac{\widetilde{T}_t}{\widetilde{\lambda}_3}\end{aligned} \tag{3.121}$$

Imposing that the tangential basal resistance contribution does not change the direction of the frictionless inner value of the tangential discharge allows to obtain a R-correction for the tangential resistance strength $\widetilde{\beta}_{\tau 2}$ in both subcritical and supercritical edges as

$$\widetilde{\beta}_{\tau 2} = \begin{cases} \widetilde{T}_t/\widetilde{c} & \text{if} \quad (\overline{rh\hat{v}})_j^+ \, (\overline{rh\hat{v}})_j^\star > 0 \\ -\widetilde{\lambda}_3 (\overline{rh\hat{v}})_j^\star/\widetilde{c} & \text{if} \quad (\overline{rh\hat{v}})_j^+ \, (\overline{rh\hat{v}})_j^\star \leq 0 \end{cases} \tag{3.122}$$

This procedure can be straightforwardly extended to the case with negative velocity ($\widetilde{u}_k < 0$) at the kth cell edge.

Differential upwind contribution

Using now the differential discretization strategy (3.59) for the spatial discretization of the 2D resistance contribution at the kth cell edge, the associated momentum contribution $\mathbf{T}_k$ is defined as

$$\mathbf{T}_k = \mathbf{T}(\hat{\mathbf{U}}_i, \hat{\mathbf{U}}_j) = \begin{pmatrix} 0 \\ \widetilde{T} \\ 0 \\ 0 \\ 0 \end{pmatrix}_k \tag{3.123}$$

where $(\widetilde{T})_k$ represents suitable values of the integrated basal resistance contribution (3.69b) in the local plane RP at the kth cell edge and the source strengths (3.71) linked to the basal resistance contribution are hence expressed as

$$\begin{aligned}\widetilde{\beta}_{\tau 1} &= \frac{-\widetilde{T}_k}{2\,\widetilde{c}_k} \\ \widetilde{\beta}_{\tau 2} &= 0 \\ \widetilde{\beta}_{\tau 3} &= \frac{\widetilde{T}_k}{2\,\widetilde{c}_k} \\ \widetilde{\beta}_{\tau 4} &= 0\end{aligned} \tag{3.124}$$

As in the integral approach, the basal resistance term should always act slowing down the flow and, in the extreme case, should conserve the quiescent equilibrium when the component of the gravitational force tangential to the bed surface remains below the yield strength. Therefore, the

basal resistance contribution at the kth cell edge should be opposite to the discharge and is hence defined as

$$\widetilde{T}_k = -\mathrm{sgn}(F_n)_k \left(\frac{\widetilde{\tau}_b}{\rho_w} \left| \widetilde{n}_{ux} \Delta x + \widetilde{n}_{uy} \Delta y \right| \right)_k \tag{3.125}$$

where $(\Delta x, \Delta y)_k$ are the distance between the cell centers along the global $x-$ and $y-$coordinates, respectively. The averaged basal shear stress at the kth cell edge is computed as $(\widetilde{\tau}_b)_k = \frac{1}{2}(\tau_{b,i} + \tau_{b,j})$, being $\tau_{b,i}$ and $\tau_{b,j}$ the corresponding values at the left i and right j cells computed using the formulations in Table 3.1, and $\mathrm{sgn}(F_n)_k$ denotes the direction of the frictionless discharge throughout the edge. The components $(\widetilde{n}_{ux}, \widetilde{n}_{uy})_k$ of the unity vector of the flow direction at the kth edge in the global framework (x, y) are calculated as

$$(\widetilde{n}_{ux})_k = \frac{1}{2} \left(\frac{u_i}{\sqrt{u_i^2 + v_i^2}} + \frac{u_j}{\sqrt{u_j^2 + v_j^2}} \right)_k \tag{3.126a}$$

$$(\widetilde{n}_{uy})_k = \frac{1}{2} \left(\frac{v_i}{\sqrt{u_i^2 + v_i^2}} + \frac{v_j}{\sqrt{u_j^2 + v_j^2}} \right)_k \tag{3.126b}$$

It is worth mentioning that, using the differential approach leads to an estimation of the resistance force disconnected from the edge orientation but only depending on the flow direction and the distance between cell centers. Therefore, this procedure liberates the basal resistance force exerted against the flow from the mesh topology.

In order to correctly integrate the basal resistance contribution using the explicit upwind differential approach, the following R-correction procedure is applied (see above section for details).

Subcritical flow

$$\begin{aligned} &\mathrm{sgn}(F_n)_k = (rh\hat{u})^\star \\ &\widetilde{\beta}_{\tau 1} = \begin{cases} -\widetilde{T}_k / (2\,\widetilde{c}_k) & \text{if} \quad (rh\hat{u})^\downarrow \, (rh\hat{u})^\star > 0 \\ (rh\hat{u})_b^\star & \text{if} \quad (rh\hat{u})^\downarrow \, (rh\hat{u})^\star \leq 0 \end{cases} \\ &\widetilde{\beta}_{\tau 3} = -\widetilde{\beta}_{\tau 1} \end{aligned} \tag{3.127}$$

with $(rh\hat{u})^\star$ as (3.113) and $(rh\hat{u})^\downarrow$ as (3.114).

Supercritical flow

$$\begin{aligned} &\mathrm{sgn}(F_n)_k = (rh\hat{u})_j^\star \\ &\widetilde{\beta}_{\tau 3} = \begin{cases} \widetilde{T}_k / (2\,\widetilde{c}_k) & \text{if} \quad (\overline{rh\hat{u}})_j^+ \, (\overline{rh\hat{u}})_j^\star > 0 \\ -(\overline{rh\hat{u}})_j^\star & \text{if} \quad (\overline{rh\hat{u}})_j^+ \, (\overline{rh\hat{u}})_j^\star \leq 0 \end{cases} \\ &\widetilde{\beta}_{\tau 1} = -\widetilde{\beta}_{\tau 3} \end{aligned} \tag{3.128}$$

with $(rh\hat{u})_j^\star$ as (3.116) and $(rh\hat{u})_j^\downarrow$ as (3.117).

Test 3.3.3.A: One-directional dambreak of a Bingham fluid

The aim of this synthetic test is to analyze the behavior of the integral and differential procedures for the explicit upwind discretization of the basal resistance term. Hungr [53] used the theory of roll waves in plastic medium to derive an analytical 1D solution for the runout distance of a plastic-type dambreak assuming null inertial forces, constant work of the shear stress and parabolic free surface after the detention of the flow. Considering an initial $30.5\,m$ high and $305\,m$ long dambreak over fixed flat bed of a plastic fluid with constant $\rho = 1835\,kg/m^3$ density and $c = 2390\,Pa$ shear strength, the runout distance reached by the wave front is $x = 1896\,m$. Naef *et al.* [107] took this solution as benchmark test for their one-dimensional model and approximated the plastic resistance using a Bingham model with a yield strength $\tau_y = 1500\,Pa$ and a plastic viscosity $\mu_B = 100\,Pa \cdot s$, obtaining a runout distance of $x \approx 1850\,m$ (although the exact value was not provided).
For a pure one-dimensional RP, the integral and differential approaches for the basal resistance discretization should exactly converge to the same solution since

$$|(\widetilde{T}_n)_k| = \frac{\widetilde{\tau}_b}{\rho_w}\Delta x \qquad \text{and} \qquad |\widetilde{T}_k| = \frac{\widetilde{\tau}_b}{\rho_w}\Delta x$$
$$|(\widetilde{T}_t)_k| = 0$$

Considering a 1D mesh of square cells with $\Delta x = 1\,m$, CFL=1 and the cohesive Bingham resistance model (CB in Table 3.1) with $\rho = 1835\,kg/m^3$, $\mu_B = 100\,Pa \cdot s$ and $\tau_y = 1500\,Pa$, the temporal evolution of the free surface and velocity with the integral and the differential resistance integration strategies are shown in Figure 3.18. First, the solution obtained with both strategies is exactly the same and, second, both approaches are able to completely stop the flow with a final runout distance $x = 1885\,m$. This demonstrates that both strategies offer good approximations of the integrated basal resistance force acting against the flow and are able to predict the stop-going mechanism in non-Newtonian flows.

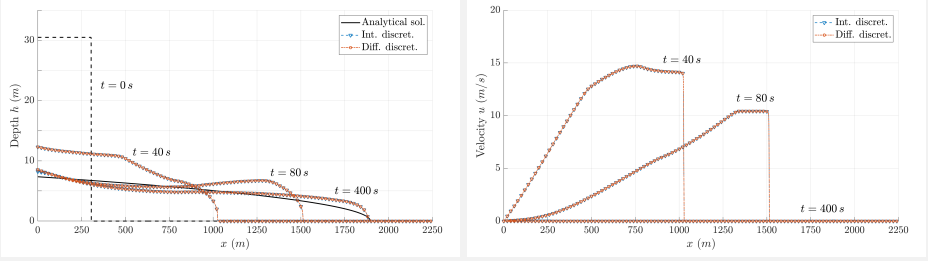

Figure 3.18: Test 3.3.3.A – Temporal evolution of the flow depth and velocity for the 1D plastic dambreak with the differential and integral approaches for the discretization of the basal resistance.

In order to analyze the dependence of the integral and differential resistance discretization on the mesh topology in 2D frameworks, this one-directional benchmark test is simulated assuming a $10\,m$ wide and $2500\,m$ long channel discretized using a 25000 cells orthogonal

mesh, a 50000 cells triangle-structured mesh and a 50361 cells triangle-unstructured mesh (Figure 3.19). The averaged edge length is $l_k \approx 1\,m$ for the three meshes, in order to use comparable mesh refinements. The CFL is 0.5 for the orthogonal mesh and 1.0 for the triangular meshes.

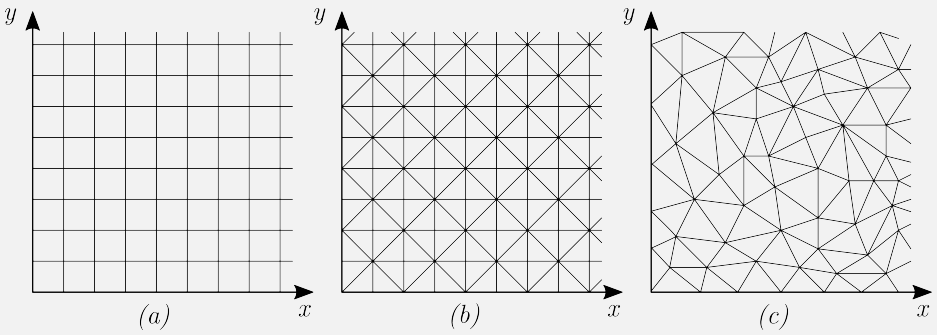

Figure 3.19: Test 3.3.3.A – Topology of the 2D meshes: (a) orthogonal mesh, (b) triangle structured and (c) triangle unstructured.

The results obtained with integral and differential approach are compared with the method proposed by Murillo & García-Navarro [102] and Juez *et al.* [64], which assumes

$$\mathbf{T}_k = \begin{pmatrix} 0 \\ -\dfrac{\widetilde{u}}{|\widetilde{u}|}\dfrac{\widetilde{\tau}_{bn}}{\rho_w}\,d_n \\ 0 \\ 0 \\ 0 \end{pmatrix}_k \tag{3.129}$$

where $(\widetilde{\tau}_{bn})_k$ is the averaged basal shear stress normal to the kth cell edge, which here is calculated solving the cubic Bingham equation

$$2\widetilde{\tau}_{bn}^3 - 3\left(\tau_y + 2\mu_B\frac{|\widetilde{u}_k|}{\widetilde{h}_k}\right)\widetilde{\tau}_{bn}^2 + \tau_y^3 = 0$$

using the Roe-averaged value of the normal velocity and flow depth at the cell edge, $\widetilde{u}_k$ and $\widetilde{h}_k$ respectively. From now on, this procedure is called normal-integrated discretization of the basal resistance contribution.

The final free surface after the detention of the one-directional dambreak wave is plotted in Figures 3.20, 3.21 and 3.22. The normal-integrated discretization dealing with non-Newtonian shear stresses [64, 102] involves a high mesh dependence, since the quantity of resistance force applied against the flow is directly influenced by edge orientation respect to the flow direction. The resistance force converges to the 1D-framework value when orthogonal meshes oriented with the flow direction are used, but shows important variations in triangular meshes depending on the mesh topology (Figure 3.20).

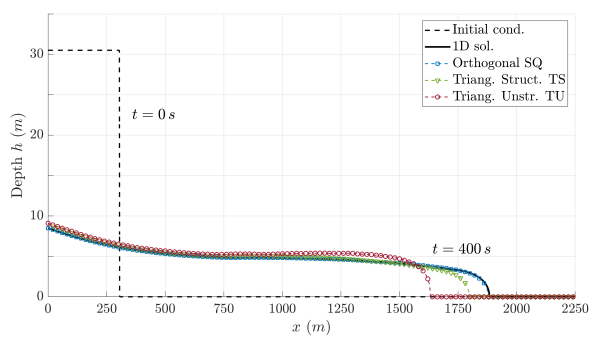

Figure 3.20: Test 3.3.3.A – Final profile for the one-directional plastic dambreak using and the **normal-integrated discretization** of the basal resistance in different 2D meshes.

Contrarily, the integral discretization of the basal resistance leads to mesh-independent results in the 2D framework (Figure 3.21). However, differences appear respect to the pure 1D-framework results. These differences are directly related to the closed boundary edges at the channel lateral sides, since it is required that these edges also insert a proportional quantity of resistance force against the flow in order to converge to the pure 1D-framework solution. However, in these edges the local RP is not defined and hence the resolution requires the implementation of special boundary conditions, which is not the scope of this thesis.

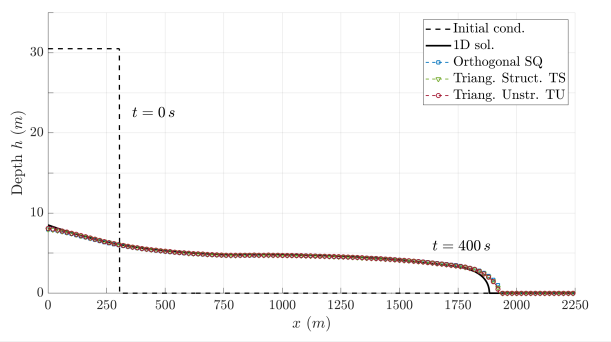

Figure 3.21: Test 3.3.3.A – Final profile for the one-directional plastic dambreak using the **integral discretization** of the basal resistance in different 2D meshes.

Finally, the results with the differential approach for the discretization of the basal resistance contribution show fully mesh-independence in the 2D framework (Figure 3.22) and also converging exactly to the solution obtained in the pure 1D-framework.

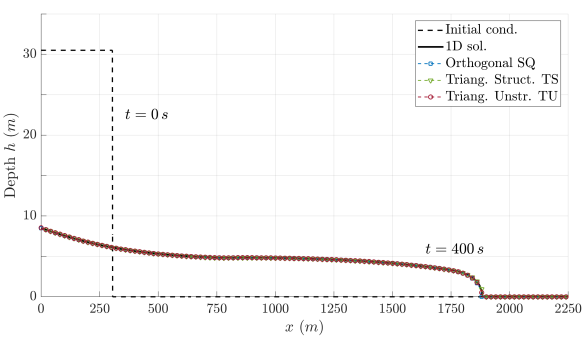

Figure 3.22: Test 3.3.3.A – Final profile for the one-directional plastic dambreak using the **differential discretization** of the basal resistance in different 2D meshes.

3.4 Shear-induced solid phase dilation contribution

The numerical flux vector at the cell edges $\boldsymbol{\mathcal{F}}_k^{\downarrow}$ (3.79) incorporates the bulk contribution of the solid phase dilation $\hat{\mathbf{L}}_k^{\downarrow} = \left(0,\, 0,\, 0,\, \widetilde{L}_k\right)^T$ (3.78), being $\widetilde{L}_k$ the bulk deviatoric solid flux related to the dilation process at the kth cell edge.

Using (3.40), the dilation solid flux $\widetilde{L}_k$ at the edge is computed as

$$\widetilde{L}_k = \begin{cases} F_k^{\{pe\}} \sum_{p=1}^{N} \frac{\rho_{s,p}-\rho_w}{\rho_w} (\phi_p)_i & \text{if} \quad \boldsymbol{\mathcal{F}}_k^{\downarrow\{1\}} \geq 0 \\ F_k^{\{pe\}} \sum_{p=1}^{N} \frac{\rho_{s,p}-\rho_w}{\rho_w} (\phi_p)_j & \text{if} \quad \boldsymbol{\mathcal{F}}_k^{\downarrow\{1\}} < 0 \end{cases} \tag{3.130}$$

where $\boldsymbol{\mathcal{F}}_k^{\downarrow\{1\}}$ is the first component of numerical flux vector (3.79) and $F_k^{\{pe\}}$ the volume flux associated to the gradients of pore pressure excess in the mixture, which is approximated at the kth cell edge as

$$F_k^{\{pe\}} = \frac{\kappa}{\widetilde{r}_k\, \mu} \left(\frac{\Delta \mathcal{P}_e}{d_n} + \widetilde{\mathcal{E}}_b \rho_w g_n \widetilde{h} \frac{\Delta z_b}{d_n} \right)_k \tag{3.131}$$

being d_n the normal-distance between cell centers.

The discrete edge-gradient $(\Delta \mathcal{P}_e)_k = \mathcal{P}_{e,j} - \mathcal{P}_{e,i}$ denotes the increment of integrated pore pressure excess at the edge (3.6b), computed as

$$\mathcal{P}_{e,i} = \frac{-\mu h_i^3}{3\kappa}\, \dot{\gamma}_i\, (\tan\psi)_i \tag{3.132}$$

The term $(\widetilde{\mathcal{E}}_b)_k = \frac{1}{2}(\mathcal{E}_{b,i} + \mathcal{E}_{b,j})$ is the edge-averaged value of the basal pore pressure excess parameter (3.6a), with

$$\mathcal{E}_{b,i} = \frac{-\mu h_i}{2\kappa \rho_w g_n}\, \dot{\gamma}_i\, (\tan\psi)_i \tag{3.133}$$

being $\dot{\gamma}_i = 2\sqrt{u_i^2 + v_i^2}/h_i$ the approximated macroscopic shear rate and $(\tan\psi)_i = k_1(\phi_{0,i} - \phi_{eq})$ the dilatancy at the i cell, with $\phi_{0,i} = \sum_{p=1}^{N}(\phi_p)_i$ the bulk solid concentration, ϕ_{eq} the equilibrium bulk solid concentration and k_1 a positive calibration constant.

Therefore, the first component of the numerical flux vector $\boldsymbol{\mathcal{F}}_k^{\downarrow\{1\}}$ accounts for the mixture mass transference normal to the cell edge (3.79)

$$\boldsymbol{\mathcal{F}}_k^{\downarrow\{1\}} = (rh\hat{u})_k^{\downarrow} \tag{3.134}$$

and, including the deviatoric dilation contribution (3.130), the numerical solid flux at the kth edge for each pth sediment class composing the solid phase in the mixture $(F_p^s)_k^{\downarrow}$, used to update the class-specific volume fractions in the flow column in (3.83), is hence computed as

$$(F_p^s)_k^{\downarrow} = \begin{cases} \left[\dfrac{(rh\hat{u})_k^{\downarrow}}{\widetilde{r}_k} + F_k^{\{pe\}}\right](\phi_p)_i^n & \text{if} \quad \boldsymbol{\mathcal{F}}_k^{\downarrow\{1\}} \geq 0 \\ \left[\dfrac{(rh\hat{u})_k^{\downarrow}}{\widetilde{r}_k} + F_k^{\{pe\}}\right](\phi_p)_j^n & \text{if} \quad \boldsymbol{\mathcal{F}}_k^{\downarrow\{1\}} < 0 \end{cases} \tag{3.135}$$

including both the bulk mixture flow contribution and the deviatoric solid dilation contribution to the class-specific numerical solid flux at the cell edge.

Therefore, the shear-induced dilation of the solid phase creates a pore pressure excess at the cells which modifies the solid flux at the cell edges due to the deviatoric component $F_k^{\{pe\}}$ (3.131), hence generating a segregation of the solid particles within the flow. Additionally, when a frictional-based basal resistance formulation (FD, FB and FT models in Table 3.1) is considered, the pore pressure excess changes the Coulomb-type yield strength at the cells following

$$\tau_{f,i} = (\rho_i - \rho_w) g_n h_i \tan\delta_f - \mathcal{E}_{b,i}\rho_w g_n h_i \tan\delta_f \tag{3.136}$$

where $\tan\delta_f$ is the frictional stability slope of the mud/debris material. The first term on the right hand side represents the hydrostatic component of the friction shear stress between solid grains whereas the second term accounts for the basal frictional shear stress related to the shear-induced pore pressure excess.

Test 3.4.A: 1D dambreak of a frictional fluid over a steep bed

In order to analyse the effects of the shear-induced solid phase dilation on the flow dynamics, the one-dimensional dambreak of a granular fluid over a rigid and dry step slope is simulated using a 1D mesh of 10000 square cells with $\Delta x = 0.5\,m$. The bed slope is $5\,\%$ and the initial material surface level is $30.5\,m$ for $x \leq 305\,m$. The granular fluid is composed of a mix of water ($\rho_w = 1000\,kg/m^3$) and one sediment class with density $\rho_s = 2518\,kg/m^3$, characteristic diameter $d_s = 1\,mm$ and uniform initial concentration $\phi = 0.55$, leading to a uniform bulk density of the granular fluid $\rho = 1835\,kg/m^3$. The net exchange with the bed is neglected, avoiding the entrainment from the bed and deposition of the solid phase.

The permeability of the porous media and viscosity of the pore-fluid are $\kappa = 10^{-8}\, m^2$ [57] and $\mu = 10^{-3}\, Pa \cdot s$ respectively. A positive constant $k_1 = 0.1$ is also set for the dilatancy formula. In order to asses the effects of the shear-induced solid phase dilatancy over the flow dynamics, the equilibrium solid concentration is varied to enable the three different initial material states

$$\begin{array}{lll} \text{Positive dilatancy:} & \phi_{eq} = 0.50 & \tan\psi > 0 \\ \text{Equilibrium state:} & \phi_{eq} = 0.55 & \tan\psi = 0 \\ \text{Negative dilatancy:} & \phi_{eq} = 0.60 & \tan\psi < 0 \end{array}$$

The basal resistance is considered pure frictional, hence $\tau_{b,i} = \tau_{f,i}$ (3.136), with a basal stability angle $\delta_f = 6°$ and discretized using the differential approach (see Section 3.3.3). Figure 3.23 shows the temporal evolution of the flow free surface for the equilibrium state $\tan\psi = 0$. The CFL is set to 1 and the final time simulated is $t = 100\, s$.

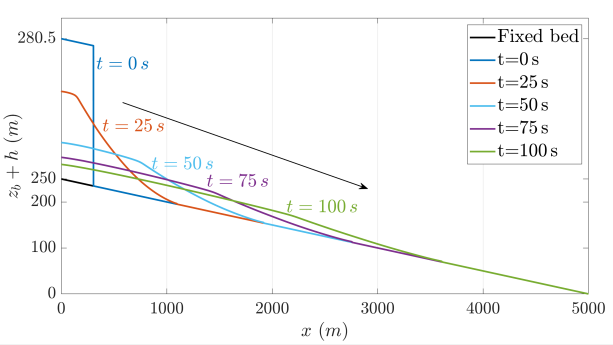

Figure 3.23: Test 3.4.A – Temporal evolution of the flow free surface for the equilibrium state $\tan\psi = 0$.

First, the effects of the shear-induced solid dilation over the flow mobility are analysed by neglecting the deviatoric term $F_k^{\{pe\}}$ (3.131) in the intercell solid flux (3.135), hence leading to $\widetilde{L}_k = 0$ (3.130). Figure 3.24 shows the runout distance of the flow at $t = 100\, s$ for the three material states considered. For the equilibrium state, $\tan\psi = 0$, the pore pressure is hydrostatic and the frictional basal resistance reduces to

$$\tau_{f,i} = (\rho_i - \rho_w) g_n h_i \tan\delta_f \tag{3.137}$$

Positive dilatancy states, $\tan\psi > 0$, are related to a solid concentration larger than the equilibrium value ϕ_{eq}. Under this condition, the pore pressure is smaller than the hydrostatic, leading to a negative basal pore pressure excess factor $\mathcal{E}_{b,i} < 0$ and increasing the frictional basal resistance $\tau_{f,i}$. Contrarily, negative dilatancy states ($\tan\psi > 0$) are associated to a solid concentration smaller than the equilibrium value and pore pressures larger than the hydrostatic. Hence, for these states, the basal pore pressure excess factor is positive $\mathcal{E}_{b,i} > 0$ and reduces the frictional basal resistance $\tau_{f,i}$. When $\mathcal{E}_{b,i} = r_i - 1$, being $r_i = \rho_i / \rho_w$ the normalized bulk density, the pore pressure balances the normal stresses within the flow column and the material is fully liquefied with null frictional shear

stress ($\tau_{f,i} = 0$). Therefore, solid concentrations larger than the equilibrium value (dense packed mixtures) are associated to a lower flow mobility whereas loose packed mixtures (liquefied slurries), with concentrations lower than the equilibrium value, are related to larger runout distances.

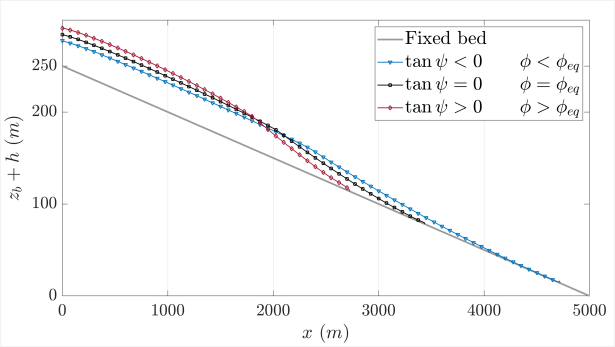

Figure 3.24: Test 3.4.A – Runout distance at $t = 100\,s$ for positive dilatancy $\tan\psi > 0$, equilibrium $\tan\psi = 0$ and negative dilatancy $\tan\psi < 0$ states.

Second, the effects of the shear-induced dilation on the solid phase distribution within the flow is analysed. In this case, the frictional basal resistance is considered always hydrostatic 3.137 in order to have similar runout distances regardless of the dilation state. Figure 3.25 depicts the temporal evolution of the integrated pore pressure excess and the basal pore pressure excess factor for the positive dilatancy $\tan\psi > 0$ simulation. Note that the lowest integrated pore pressure excess $\mathcal{P}_e$ corresponds to the center/tail region of the flow wave whereas the lowest basal pore pressure excess factor $\mathcal{E}_b$ are associated to the flow head region.

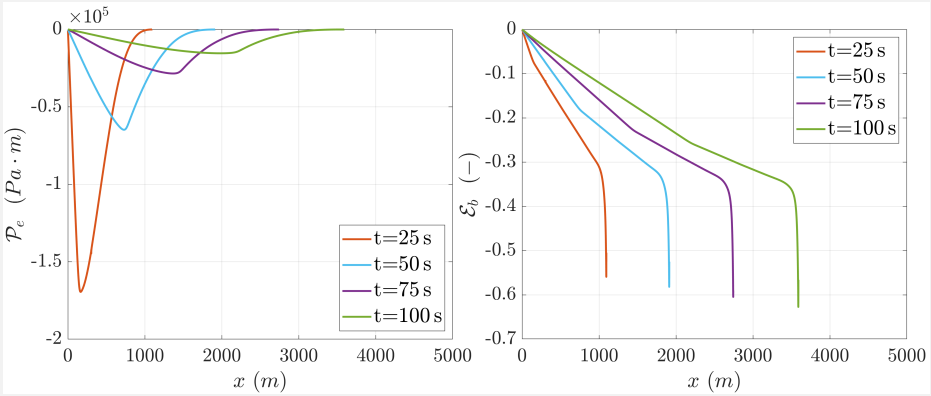

Figure 3.25: Test 3.4.A – Temporal evolution of (left) the integrated pore pressure excess $\mathcal{P}_e$ and (right) the basal pore pressure excess factor $\mathcal{E}_b$ for positive dilatancy $\tan\psi > 0$ states.

Contrarily, when the fluidized material undergoes negative dilation states with $\tan\psi < 0$ (see Figure 3.26), the highest integrated pore pressure excess $\mathcal{P}_e$ appears at the center region of the flow, but it is lower at the tail and head regions of the flow. The basal pore pressure excess

factor $\mathcal{E}_b$ reaches its maximum at the wave front and decreases progressively along the center and tail of the dambreak wave.

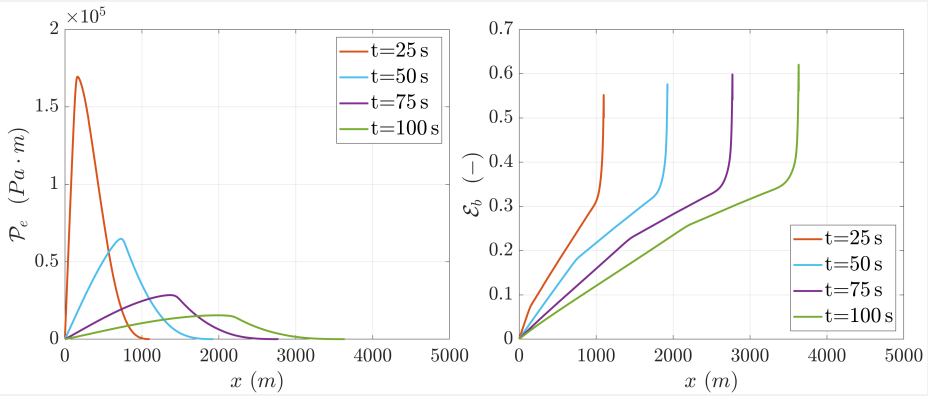

Figure 3.26: Test 3.4.A – Temporal evolution of (left) the integrated pore pressure excess $\mathcal{P}_e$ and (right) the basal pore pressure excess factor $\mathcal{E}_b$ for negative dilatancy $\tan\psi < 0$ states.

It is worth noting that, regardless of the dilation state, the integrated pore pressure excess reaches its maximum values for the first stages of the dambreak flow and relaxes progressively with time as the flow moves downstream. Nevertheless, the basal pore pressure excess factor $\mathcal{E}_b$ shows a more persistent behaviour but increasing slightly as the flow moves downstream. The spatial distribution of the solid phase within the dambreak wave is a consequence of the balance between the gradient of the integrated pore pressure excess $\frac{\Delta \mathcal{P}_e}{d_n}$ and the contribution of the basal pressure excess $\widetilde{\mathcal{E}}_b \rho_w g_n \widetilde{h} \frac{\Delta z_b}{d_n}$, resulting in the deviatoric solid flux (3.131). Figure 3.27 shows the solid phase distribution at $t = 100\,s$ along the dambreak wave for the positive dilation, negative dilation and equilibrium states.

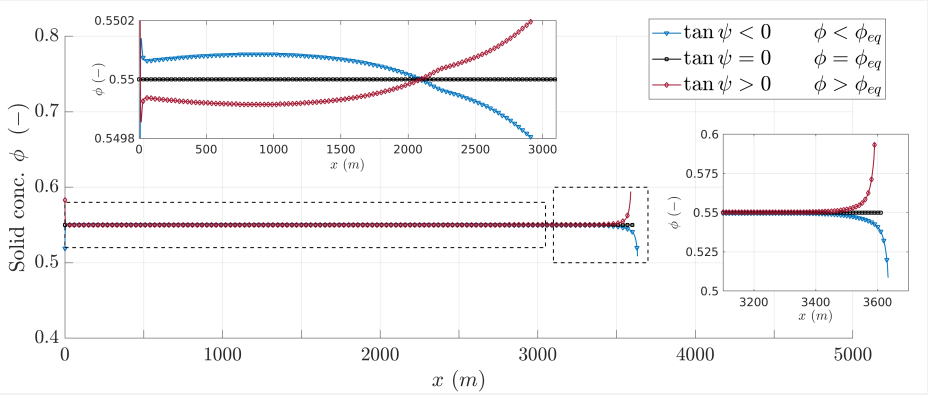

Figure 3.27: Test 3.4.A – Spatial distribution of the solid concentration at $t = 100\,s$ for positive dilatancy $\tan\psi > 0$, equilibrium $\tan\psi = 0$ and negative dilatancy $\tan\psi < 0$ states.

For the equilibrium state, $\tan\psi = 0$, the pore pressure is hydrostatic and the solid particles move with the mixture velocity. There not exist differences between the solid and liquid phases and hence the solid

concentration remains constant, maintaining the initial uniform value. When positive of negative dilation occur, pore pressure gradients appear within the flow and hence the solid particles move with a velocity different from the liquid phase velocity. Generally, the pore-fluid moves from high pressure to low pressure zones. Therefore, the sediment fraction in low pore pressure regions ($\phi_0 >> \phi_{eq}$) undergoes a porosity creation process, decreasing the solid concentration in those regions. Contrarily, high pressure regions ($\phi_0 << \phi_{eq}$) suffer an outlet liquid flow and the solid phase undergoes a contraction process, hence increasing its concentration. Both dilation states lead to the bulk solid concentration ϕ_0 converging to the equilibrium value ϕ_{eq} with time.
This simple reasoning explains the solid distribution shown in Figure 3.27. On the one hand, for positive dilation states ($\phi_0 > \phi_{eq}$ and $\tan\psi > 0$), the lower pore pressure values at the center/tail region of the dambreak wave (see Figure 3.25) lead to an incoming pore-fluid flux from the wave head. Therefore, the solid concentration at the tail and center zones slightly decreases $\phi_0 \rightarrow \phi_{eq}$, whereas the solid concentration at the head undergoes a marked increase due to the lower flow depths. On the other hand, for negative dilation states ($\phi_0 < \phi_{eq}$ and $\tan\psi < 0$), the center/tail region of the dambreak wave shows higher pore pressure values (see Figure 3.26) which create an outlet pore-fluid flux to the wave head. Consequently, the solid concentration at the tail and center zones slightly increases $\phi_0 \rightarrow \phi_{eq}$, decreasing the solid concentration at the head considerably because of the lower flow depths.

3.5 Benchmark and application cases

3.5.1 Synthetic case MF1: 2D large-scale spreading of a cylindrical non-Newtonian volume

The spreading of a cylindrical volume is one of the most extended benchmarking test to analyze the behavior of 2D numerical models for frictional flows [64, 119]. Using different mesh types helps to point out numerical issues in the discretization of the homogeneous fluxes and source terms, since the spreading wave must maintain the circular shape regardless of the mesh topology and refinement. These discretization problems are further aggravated in large-scale and long-term simulations. In order to analyze the performance of both the integral and the differential approaches for the discretization of the 2D basal resistance term, a quiescent semicircular volume with initial height $h_0 = 25\,m$ and radius $R_0 = 100\,m$ of a non-Newtonian material is considered. The two-dimensional flat-bed spatial domain, with $x = [-1200, 1200]\,m$ and $y = [0, 1200]\,m$, is discretized using the three different meshes (see Figure 3.19) which have been summarized in Table 3.3.

A uniform normalized bulk density $r_0 = 1.9$ is set at the initial time, considering a unique sediment class with concentration $\phi = 0.6$ and density $\rho_s = 2500\,kg/m^3$. The exchange flux bewteen the flow and the bed

Topology	Number of cells	Number of edges	Cell area	Edge length
Orthogonal (SQ)	115 200	231 120	$25\,m^2$	$5\,m$
Triangle structured (TS)	230 400	346 320	$12.5\,m^2$	$\approx 5\,m$
Triangle unstructured (TU)	230 555	346 498	$\approx 12.5\,m^2$	$\approx 5\,m$

Table 3.3: Synthetic case MF1 – 2D meshes considered for the spatial discretization.

layer is neglected during the whole simulation, as well as the effects of the solid phase dilation. The basal shear stress is modeled using the frictional dilatant rheology (FD) in Table 3.1, with plastic viscosity $\mu_P = 5\,Pa \cdot s^2$ and basal stability angle $\delta_f = 1°$. The pore pressure is considered hydrostatic during the simulation. The CFL is set to 0.5 for the orthogonal (SQ) mesh and 1.0 for both triangular (TS and TU) meshes. The final simulation time is $150\,s$, enough to ensure that the spreading wave stops.

For the sake of clarity, the integral and differential approaches, as well as the previous normal-integrated procedure [64, 88, 102], for the discretization of the 2D basal resistance term are summarized here as

- (a) Normal-integrated resistance contribution:

$$\mathbf{T}_k = \begin{pmatrix} 0 \\ -\mathrm{sgn}(\widetilde{u})\dfrac{\widetilde{\tau}_{bn}}{\rho_w}\,d_n \\ 0 \\ 0 \\ 0 \end{pmatrix}_k \tag{3.138}$$

  where $(\widetilde{\tau}_{bn})_k$ is the averaged basal shear stress normal to the kth cell edge, which here is estimated as

$$(\widetilde{\tau}_{bn})_k = \left(\rho_w(\widetilde{r}-1)g_n\widetilde{h}\tan\delta_f + \frac{25\mu_P}{4\,\widetilde{h}^2}\sqrt{\widetilde{u}^2+\widetilde{v}^2}\,|\widetilde{u}|\right)_k \tag{3.139}$$

  using the Roe-averaged values of the normal and tangential velocity, $\widetilde{u}_k$ and $\widetilde{v}_k$ respectively, the flow depth $\widetilde{h}_k$ and the normalized density $\widetilde{r}_k$ at the edge.

- (b) Integral resistance contribution:

$$\mathbf{T}_k = \begin{pmatrix} 0 \\ -\mathrm{sgn}(F_n)\,\dfrac{\widetilde{\tau}_b}{\rho_w}\,|\widetilde{u}|/\sqrt{\widetilde{u}^2+\widetilde{v}^2}\,\dfrac{1}{2}d_n \\ -\mathrm{sgn}(F_t)\,\dfrac{\widetilde{\tau}_b}{\rho_w}\,|\widetilde{v}|/\sqrt{\widetilde{u}^2+\widetilde{v}^2}\,\dfrac{1}{2}d_n \\ 0 \\ 0 \end{pmatrix}_k \tag{3.140}$$

where $(\widetilde{\tau}_b)_k = \frac{1}{2}(\tau_{b,i}+\tau_{b,j})$ is the averaged bed shear stress at the edge, with the cell value estimated as

$$\tau_{b,i} = (\rho_i - \rho_w) g_n h_i \tan\delta_f + \frac{25\mu_P}{4\,h_i^2}(u_i^2 + v_i^2) \tag{3.141}$$

and $\mathrm{sgn}(F_n)_k$ and $\mathrm{sgn}(F_t)_k$ denote the frictionless discharge along the normal and tangential directions to the kth cell edge, respectively.

- (c) Differential resistance contribution:

$$\mathbf{T}_k = \begin{pmatrix} 0 \\ -\mathrm{sgn}(F_n)\,\dfrac{\widetilde{\tau}_b}{\rho_w}\,|\widetilde{n}_{ux}\Delta x + \widetilde{n}_{uy}\Delta y| \\ 0 \\ 0 \\ 0 \end{pmatrix}_k \tag{3.142}$$

where $(\widetilde{\tau}_b)_k$ and $\mathrm{sgn}(F_n)_k$ as those in the integral approach, $(\Delta x, \Delta y)_k$ are the distance between the cell centers along the global $x-$ and $y-$coordinates, respectively, whereas the terms $(\widetilde{n}_{ux}, \widetilde{n}_{uy})_k$ represents the components of the unity vector of the flow direction at the kth edge in the global framework (x, y), calculated using (3.126).

Figure 3.28 shows the depth h with the orthogonal SQ mesh once the flow totally stops. The dashed red line represents a perfect circle $R = 1050\,m$. The normal-integrated procedure (a) is highly mesh dependent and tends to align markedly with the mesh main-directions $x = 0$ and $y = 0$. This behavior was previously reported by [119] and [64] but it was erroneously attributed to an insufficient mesh refinement, although further reducing the spatial discretization helps to slightly correct this undesirable effect in short-term and small-scale simulations [119]. Nevertheless, this large-scale numerical experiment shows that the alignment of the flow with the mesh main-directions is directly related to the loss of the rotation invariant property of the integrated basal resistance contribution. This loss of the invariance under rotation of the flow is caused by the erroneous procedure for including the 2D resistance term into the local plane RP at the cell edges.

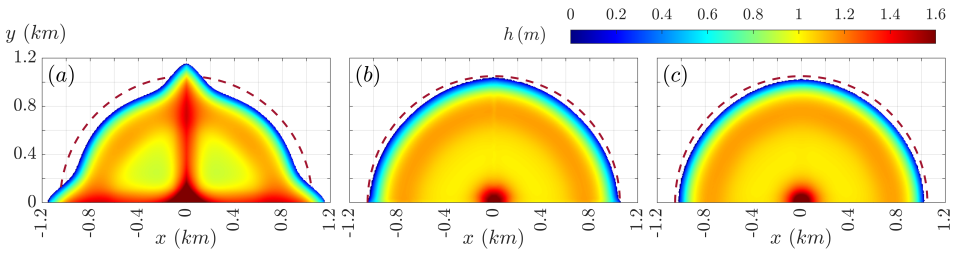

Figure 3.28: Synthetic case MF1 – Final depth $h\,(m)$ with the orthogonal SQ mesh: (a) Normal-integrated, (b) Integral and (c) differential basal resistance contributions.

Both the integral (b) and differential (c) approaches derived in this thesis maintain approximately the circular shape for the spreading wave until the flow detention, with as quite similar runout distance. However, the integral procedure shows slight alterations on the final flow depth aligned

with the mesh main-directions. This small variation on the wave spreading shape can be directly related to the estimation of the tangential basal resistance along the main-directions $x = 0$ and $y = 0$. Note that the tangential resistance contribution in the local RP is associated to the characteristic shear wave $\widetilde{\lambda}_2 = \widetilde{u}$ and at the main-direction edges $\widetilde{u} = 0$ is satisfied, hence the inner state of the tangential resistance remains undefined. It is worth mentioning that, during the first stages of the spreading ($t < 25\,s$), the normal-integrated procedure (a) is able to maintain approximately the circular wave shape but, as time progresses, the differences on the discretized resistance force depending on the mesh-flow alignment leads to an unphysical spreading shape at the final time.

Figure 3.29 depicts the depth h with the triangle structured TS mesh after the flow totally stops. The dashed red line represents a perfect circle $R = 1050\,m$. Again the normal-integrated procedure (a) tends to align with the mesh main-directions ($x = 0$, $y = 0$ and $|x| = |y|$) whereas both the integral (b) and differential (c) approaches maintain the circular shape for the spreading wave. Nevertheless, as with the orthogonal mesh, the integral procedure shows slight variations on the final flow depth aligned with the mesh main-directions.

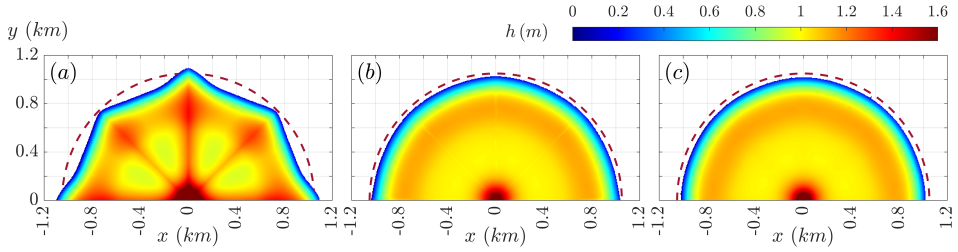

Figure 3.29: Synthetic case MF1 – Final depth $h\,(m)$ with the triangle structured TS mesh: (a) Normal-integrated, (b) Integral and (c) differential basal resistance contributions.

Regarding the triangular unstructured TU mesh (Figure 3.30), the three strategies for the integration of the basal resistance contribution are able to maintain the circular shape for the spreading wave since main-directions do not exist for this mesh topology. However, a marked roughness appears at the final free surface when the normal-integrated resistance strategy (a) is used. This free surface roughness with triangle unstructured meshes was also reported in [88, 102] and erroneously attributed to the depth data interpolation between cell center and nodes in [64]. Contrarily, the integral approach is able to avoid the free surface roughness and the differential strategy reduces these small-scale irregularities considerably, demonstrating that it is again an undesirable effect of the normal-integrated procedure for the integration of the 2D basal resistance vector.

The incorrect inclusion of the 2D basal resistance term into the local plane RP at the cell edges leads to highly mesh dependent results, since the quantity of integrated resistance force opposed to the flow movement is greatly affected by the edges orientation. Figure 3.31–left depicts the temporal evolution of the wave-front location along the diagonal line $x = y$ for the three integration strategies considered, whereas Figure 3.31–right shows the final depth along the same line. For the first stages of the spreading flow ($t < 25\,s$), the runout distance is quite similar with the three mesh

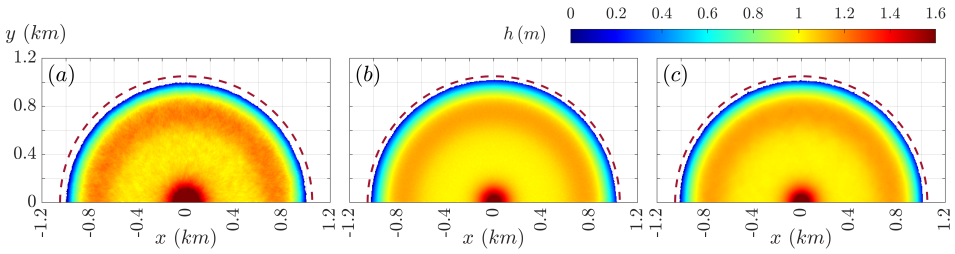

Figure 3.30: Synthetic case MF1 – Final depth $h\,(m)$ with the triangle unstructured TU mesh: (a) Normal-integrated, (b) Integral and (c) differential basal resistance contributions.

topologies analyzed, regardless of the basal resistance integration strategy. Only when the time-of-flow is large enough, thanks to the large-scale spatial domain of this numerical case, important deviations on the runout distance start to appear with the normal-integrated strategy (a) which depend on the mesh topology. These deviations are directly related to the orientation of the flow with the mesh main-directions and lead to different final depth profiles for each of the mesh topologies considered.

Contrarily, both the integral (b) and differential (c) strategies for the 2D basal resistance integration are able to maintain a runout distance evolution similar for the three mesh topologies considered. Only at the final spreading flow stages, slight deviations appear between the orthogonal SQ mesh and the triangular TS and TU meshes and these deviations are probably more associated to the different cell area (see Table 3.3) than to the orientation of the flow with the respective mesh main-directions. Therefore, both new approaches offer quite similar results for final depth along the diagonal $x = y$ line regardless of the mesh topology.

The comparison of the computational effort required for each integration procedure is summarized in Table 3.4. All the simulations are performed using a OMP-parallelized C++ code, running in four Intel Core i7-7700K CPU cores. Although differences in the required computational time appear depending on the mesh topology, the three integration procedures offer quite similar efficiency.

Topology	Normal-int. procedure (a)	Integral approach (b)	Differential approach (c)
Orthogonal (SQ)	43.601 s	45.597 s	39.425 s
Triangle struct. (TS)	104.283 s	102.905 s	110.696 s
Triangle unstruct. (TU)	174.091 s	174.935 s	186.183 s

Table 3.4: Synthetic case MF1 – Computational time for the the three 2D basal resistance integration strategies considered.

When a cohesive-type yield strength τ_y is involved in the rheology (CB and CT formula in Table 3.1) the effects of the loss of the invariant property of the 2D integrated resistance force lead to even more marked flaws in the numerical solution. This occurs because the yield strength opposed to the

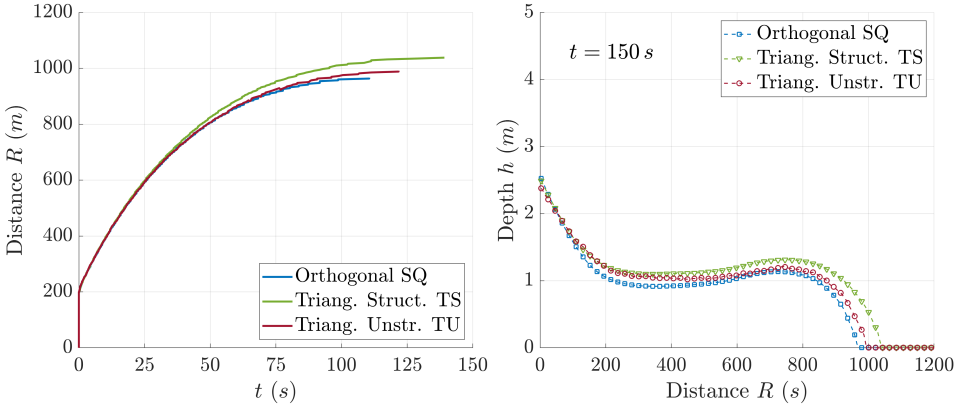

(a) Normal-integrated resistance contribution.

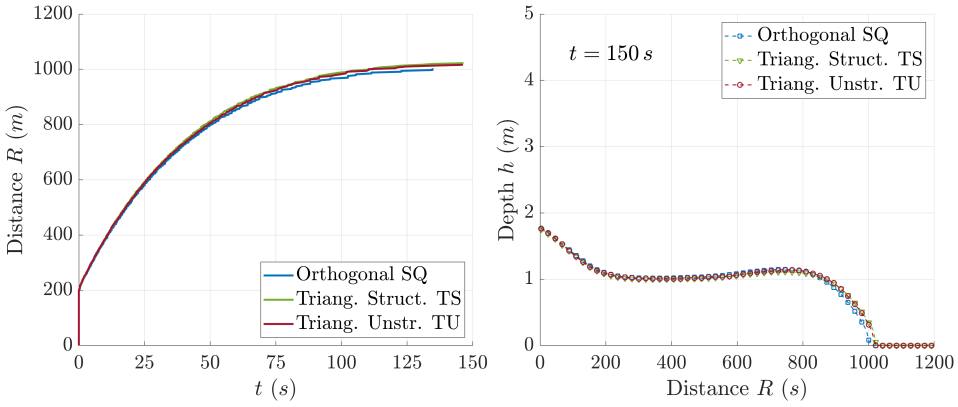

(b) Integral resistance contribution.

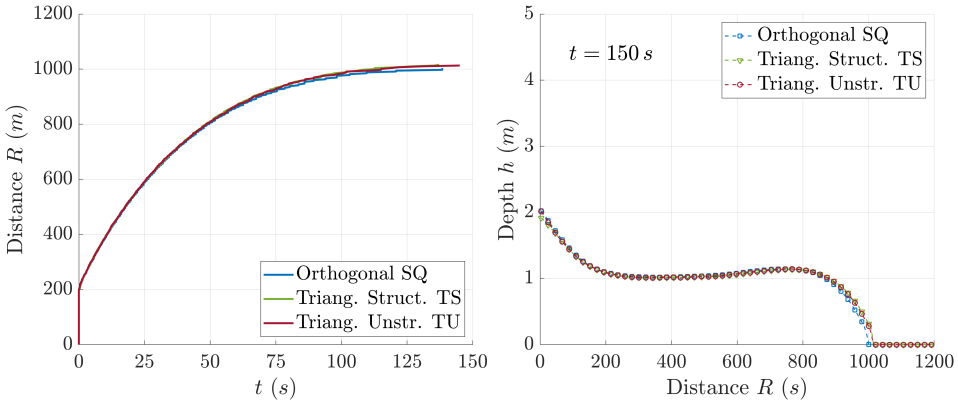

(c) Differential resistance contribution.

Figure 3.31: Synthetic case MF1 – (left) Temporal evolution of the runout distance and (right) final depth along the diagonal line $x = y$.

material movement does not depend on the flow depth h, as happens with frictional-type stresses, but takes a constant shear stress value.

Figure 3.32 shows the final depth h for the spreading of a large-scale quiescent semicircular volume with initial height $h_0 = 25\,m$ and radius $R_0 = 100\,m$ of a cohesive Bingham fluid. The domain extension, mesh topology and simulation setup are the same as in the above case with a frictional-type material. The cohesive yield strength is $500\,Pa$ and the dynamic viscosity of the material $\mu_B = 8\,Pa \cdot s$, with a bulk density

$\rho = 1900\,kg/m^3$. Results for the orthogonal, triangle structured and triangle unstructured mesh topologies are show with the three explicit upwind methods considered for the discretization of the 2D basal resistance contribution. The dashed red line represents a perfect circle $R = 1050\,m$.

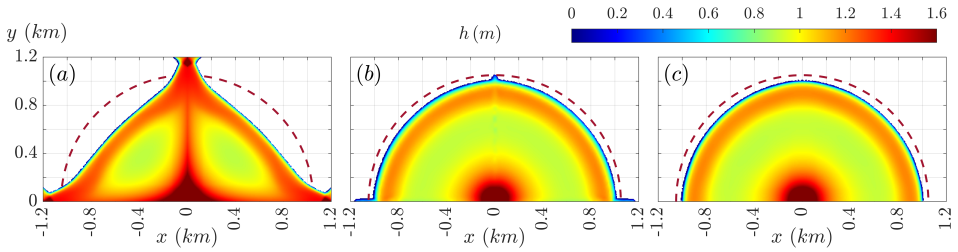

(i) Orthogonal mesh.

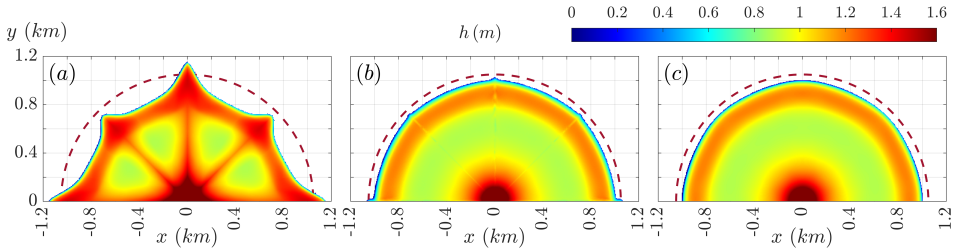

(ii) Triangle structured mesh.

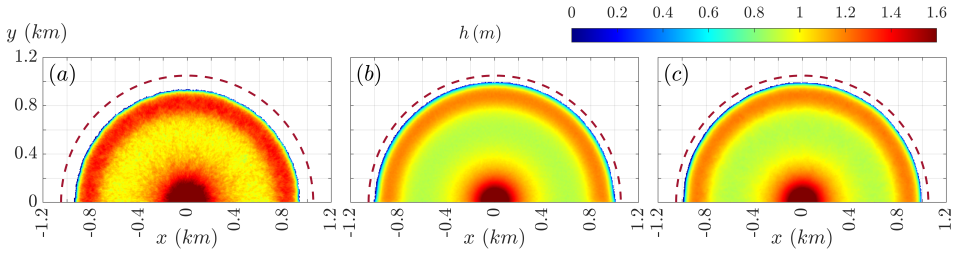

(iii) Triangle unstructured mesh.

Figure 3.32: Synthetic case MF1 – Final depth $h\,(m)$ with the Cohesive Bingham rheology: (a) Normal-integrated, (b) Integral and (c) differential basal resistance contributions.

On the one hand, in structured orthogonal and triangle meshes (see (i) and (ii) in Figure 3.32), the loss of the invariance under rotation of the 2D integrated basal resistance force with the normal-integrated procedure (a) for the Bingham rheology 3.129 is clear and even more marked than with the frictional dilatant relation. The integral approach (b) maintains reasonably well the circular shape but its flaws in cell edges perfectly aligned with the flow direction are evident here, leading to slightly larger runout distance along the mesh main-direction. Nevertheless, the differential approach (c) maintains the well the semicircular shape of the wave spreading and only an indiscernible asymmetry is observed.

On the other hand, in the triangular unstructured mesh (see (iii) in Figure 3.32), the three strategies for the explicit upwind discretization of the 2D basal resistance contribution maintain the circular shape of the spreading wave. However, the normal-integrated procedure (a) shows an smaller final runout distance and a marked roughness in the final free surface as

a consequence of the dependence of the mesh direction of the integrated resistance force. Both the integral (b) and differential (c) approaches show perfect circular spreading shapes, smooth free surface and final runout distances in agreement with those obtained in the orthogonal and the triangular structured meshes.

Based on these results, it is possible to conclude that both the integral (b) and differential (c) approaches represent a further improvement for the explicit upwind integration of the non-Newtonian basal resistance contribution in two-dimensional numerical schemes.

3.5.2 Experimental case MF2: USGS debris dambreak over rigid steep bed

In this benchmark case, the proposed variable-density model including the effects of the shear-induced solid phase dilation is validated using data from large-scale experiment consisting on dambreak debris flows over a step fixed bed. The experiment was carried out in the USGS large-scale debris-flow flume and data from two repetitions, called run I (date 12/9/2006) and J (date 19/6/2007), were reported by Iverson *et al.* [60]. The USGS debris-flow flume is a straight rectangular concrete channel $95\,m$ long, $2\,m$ wide and $1.2\,m$ deep with a vertical headgate placed $12.5\,m$ downstream the channel beginning, which retains the static debris fluid until the experiment initial time. Figure 3.33 shows a schematic representation of the USGS debris-flow flume for this fixed-bed experiments. All the longitudinal distances s are referred to the headgate position taken along the experimental flume floor. The channel has an 31° uniform slope until $s = 74\,m$, where the flume begins to flatten following a catenary curve and evolving to a 4° slope at $s = 82.5\,m$. Then, the flume debouches onto a $15\,m$ long, $8\,m$ wide and 2.4° slope concrete runout surface.

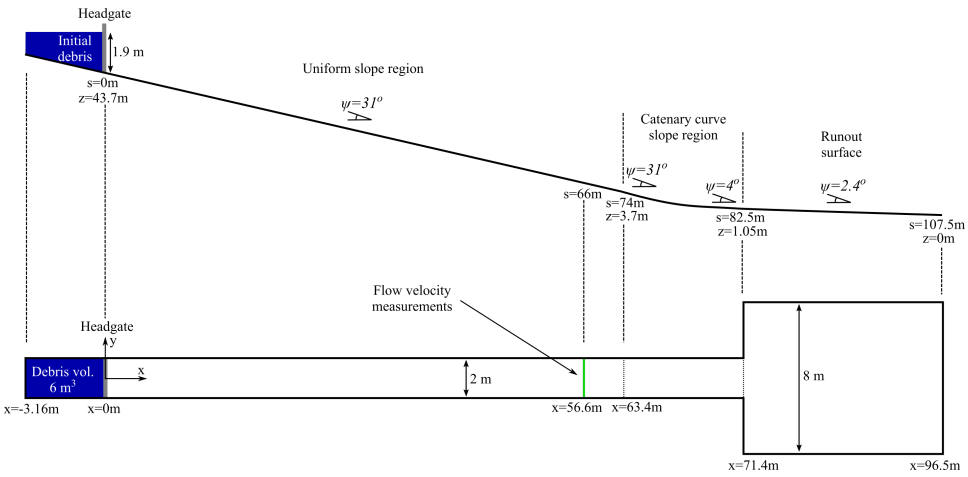

Figure 3.33: Experimental case MF2 – Sketch of the USGS debris dambreak experiments.

The initial features debris aggregate were previously reported in [61]. The initial debris volume is $6\,m^3$ and is composed by a fully saturated mixture of water and gravel, sand and mud grains with 60% bulk solid concentration. For the sake of simplicity, an unique bulk sediment class is considered here, with an equivalent characteristic diameter $d_s = 6.9\,mm$

and solid density $\rho_s = 2700\,kg/m^3$, leading to an initially uniform bulk density $\rho = 2020\,kg/m^3$. Table 3.5 shows the main parameter used in the simulations for characterizing the debris mixture. The pore-fluid is considered clear water ($\rho_w = 1000\,kg/m^3$ and $\mu = 0.001\,Pa \cdot s$) and the uniform porous-media permeability is set to $\kappa = 10^{-8}\,m^2$ [57]. In order to reduce the number of setup parameters involved in the simulations, a constant shearing-equilibrium concentration $\phi_{eq} = 0.65$ is considered. This value is slightly higher than the actual initial solid concentration, since an extra water amount was added to the debris mixture before the experiment beginning, but lower than the lithostatic deposition concentration $\phi_{max} = 0.73$ estimated with the Wu [144] empirical relation (3.11).

In the experiments, once the headgate was opened, the debris dambreak wave accelerated over the uniform-slope rigid bed region of the flume until it reached the catenary-slope zone and the runout surface where it stopped. For each run of the experiment, Iverson *et al.* [60] tracked the wave-front location during the flow advance using image techniques and video frames. The wave-front velocity was also measured between $s = 60\,m$ and $s = 70\,m$ from the video frames, as well as the final runout distance after flow detention. Moreover, video files of both experiments are available in https://pubs.usgs.gov/of/2007/1315/.

Debris volume	$6\,m^3$
Initial solid concentration ϕ_0	$60\,\%$
Debris water content	$40\,\%$
Bulk debris density ρ	$2020\,kg/m^3$
Solid particles diameter d_s	$6.9\,mm$
Solid density ρ_s	$2700\,kg/m^3$
Shearing-equilibrium concentration ϕ_{eq}	0.65
Pore-fluid density ρ_w	$1000\,kg/m^3$
Pore-fluid viscosity μ	$0.001\,Pa \cdot s$
Porous media permeability κ	$10^{-8}\,m^2$

Table 3.5: Experimental case MF2 – Characteristic values used for the simulation setup

The simulations are performed using an unstructured triangular mesh of 28 388 cells, with an averaged area of $200\,cm^2$. The CFL is set to 0.95 and the total time simulated is $25\,s$. Simulations are performed using C++ code, running in one Intel Core i7-7700K CPU core. Furthermore, for the sake of simplicity, the net exchange term of solid material between the bed and the flow is neglected. Following [79], the basal resistance is modeled using the frictional–turbulent FT closure in Table 3.1, setting a friction angle for the solid phase $\delta_f = 40°$ and a Manning's roughness parameter $n_b = 0.018\,sm^{-1/3}$ for the rigid flume bed. Note that these values for the resistance estimation have not been calibrated but directly taken from the original experimental data [61]. In order to analyze the influence of the shear-induced pore pressure excess on the flow mobility, the dilatancy $\tan\psi$ of the fluidized material is controlled by varying the tuning parameter k_1 in the range $0 \leq k_1 \leq 0.15$ (3.7).

Figure 3.34 shows the depth of the debris deposit after the flow detention ($t = 25\,s$). Note that the distances are expressed in the horizontal $x-$coordinate. The red rectangle at $x \approx 82\,m$ ($s \approx 93\,m$) indicates the wave front detention in the experimental runs. After the flow initialization, the dambreak wave progresses downslope rapidly until reaches the runout surface, where stops. Analysing the model behaviour, the debris material is undergone to increasing shearing states as accelerates over the step channel. These shearing states are associated to positive pore pressures in the throughout the flow column, since the fluidized material is initially under a negative dilatancy state $\tan\psi < 0$. This pore pressure excess modifies the basal resistance against the movement, as well as induces the segregation of the solid phase along the dambreak wave. As the tuning parameter k_1 is increased from the equilibrium state $k_1 = 0$ to the maximum dilation considered ($k_1 = 0.15$), the mobility of the debris flow grows and leads to larger runout distances. This enhanced mobility is explained by the reduction of the frictional yield strength as the basal value of the positive pore pressure excess increases.

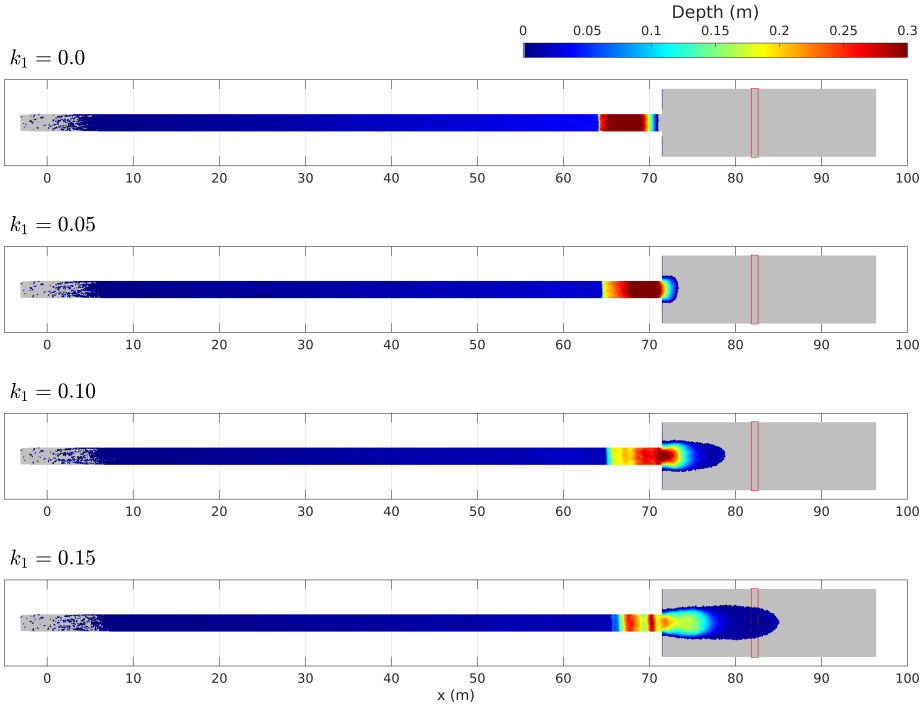

Figure 3.34: Experimental case MF2 – 2D deposit depth h after the flow detention ($t = 25\,s$) with values of the dilatancy tuning parameter $k_1 = 0$ (equilibrium), $k_1 = 0.05$, $k_1 = 0.10$ and $k_1 = 0.15$ (maximum dilation).

Figure 3.35 shows the basal pore pressure excess factor $\mathcal{E}_b$ records as the dambreak wave pass the probe section $x = 56.6\,m$ ($s = 66\,m$). First, the registered values of $\mathcal{E}_b$ increase with the the dilatancy $\tan\psi$. However, the relation between the shear-induced basal pore pressure excess and the hydrostatic basal pore pressure (only related to the flow depth h) is clearly non-linear and non-monotone, showing a relative hysteresis phenomenon regardless of the dilatancy parameter $k_1 > 0$ considered.

Therefore, as the dilatancy tuning parameter k_1 is increased, the positive basal pore pressure excess factor $\mathcal{E}_b$ also increases for equal values of

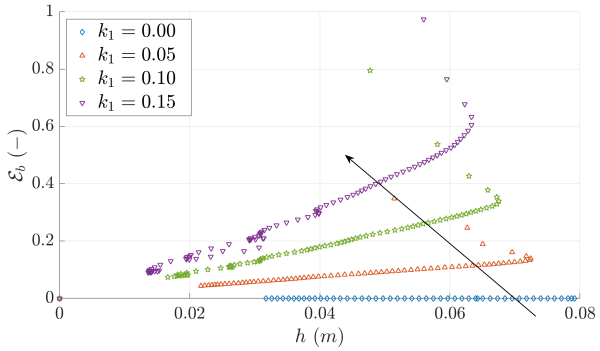

Figure 3.35: Experimental case MF2 – Basal pore pressure excess factor $\mathcal{E}_b$ at the probe section $x = 56.6\,m$ ($s = 66\,m$) with values of the dilatancy tuning parameter $k_1 = 0$ (equilibrium), $k_1 = 0.05$, $k_1 = 0.10$ and $k_1 = 0.15$ (maximum dilation).

flow density, depth and velocity, reducing the effective normal stress σ_e at the bed-flow interface. This reduction of the effective normal stress leads directly to the reduction of the basal frictional yield strength τ_f (3.136) and hence to lower basal resistance stresses against the dambreak wave advance over the step flume. Figure 3.36–(a) depicts the numerical wave-front location along the experimental channel as time progresses, compared with provided experimental data. As the dilatancy tuning parameter k_1 is increased, the acceleration of the front advance along the uniform-slope region of the flume also increases. Hence, the numerical wave-front location tends to adapt to the observed data when the shear-induced pore pressure is enhanced. Nevertheless, marked differences with the laboratory data appear along the runout region.

The acceleration of the dambreak advance is clearly observed in Figure 3.36–(b), where the numerical wave-front velocity has been depicted against the experimental data. Iverson *et al.* [60] reported a unique front velocity value at $60\,m < s < 70\,m$ of $12.5\,m/s$ for the experimental run I and $7.1\,m/s$ for the experimental run J (grey rectangle) but the velocity evolution can be derived from the experimental front location data. Increasing the dilation state of the fluidized material, i.e. increasing k_1, leads to a better prediction of the wave-front velocity compared with those of the equilibrium state ($\tan\psi = 0$) simulation. Note that for $k_1 \in [0.10, 0.15]$ the computed front velocity agrees with the experimental data all over the dambreak progression along the constrained channel but differences arise for the flow detention at the catenary and runout zones.

Figure 3.34 shows the 2D density distribution after the flow detention at $t = 25\,s$. As the dilatancy tuning parameter k_1 is increased, the positive pore pressure excess also increases and leads to the segregation of the solid phase throughout the dambreak wave. In the numerical simulations, as the dambreak progresses along the constrained channel ($s < 82.5\,m$), a fluidized wave head is predicted with a lower solid concentration and high pore pressure excess which enhances the debris mobility. Once the main dambreak wave reaches the runout surface, the velocity decreases and the induced pore pressure excess dissipates at the flow head, increasing the frictional stresses in the solid phase and stemming the wave-front finally. This fluidized head becomes more marked as the dilatancy tuning parameter k_1 is increased and can be observed in the video recording of the experiments.

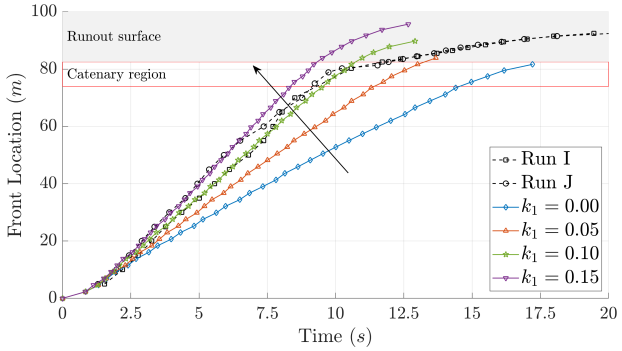

(a) Wave-front location.

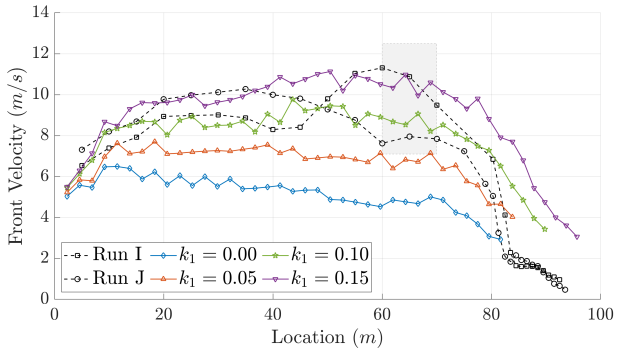

(b) Wave-front velocity.

Figure 3.36: Experimental case MF2 – Temporal evolution of the dambreak wave-front: (a) Time vs. Location and (b) Location vs. Velocity.

Nevertheless, although the main wave is stopped at the runout surface, the movement of the material at the uniform-slope region continues generating rolling waves which reaches progressively the detention zone. Figure 3.38 shows the cross-section averaged value of the basal pore pressure excess factor $\mathcal{E}_b$ at times $t = 6,\ 12,\ 15$ and $18\,s$ for the simulation with dilatancy tuning parameter $k_1 = 0.15$. The fully-fluidized flow head is observed for $t = 6\,s$ whereas the main wave detention occurs at $t = 12\,s$ approximately. Secondary rolling waves associated to increments of the shear-induced basal pore pressure are developed for $12 \leq t \leq 22$ along the constrained step channel and stop at the catenary region and at the beginning of the runout surface, increasing the final deposit head in these regions. These secondary rolling waves behind the main flow front are also been observed in the video recording of the experiments. This behavior is known as surge dynamics and is one of the mean features of the debris flows, mainly associated to the appearance of non-uniform shear stresses along the debris flow.

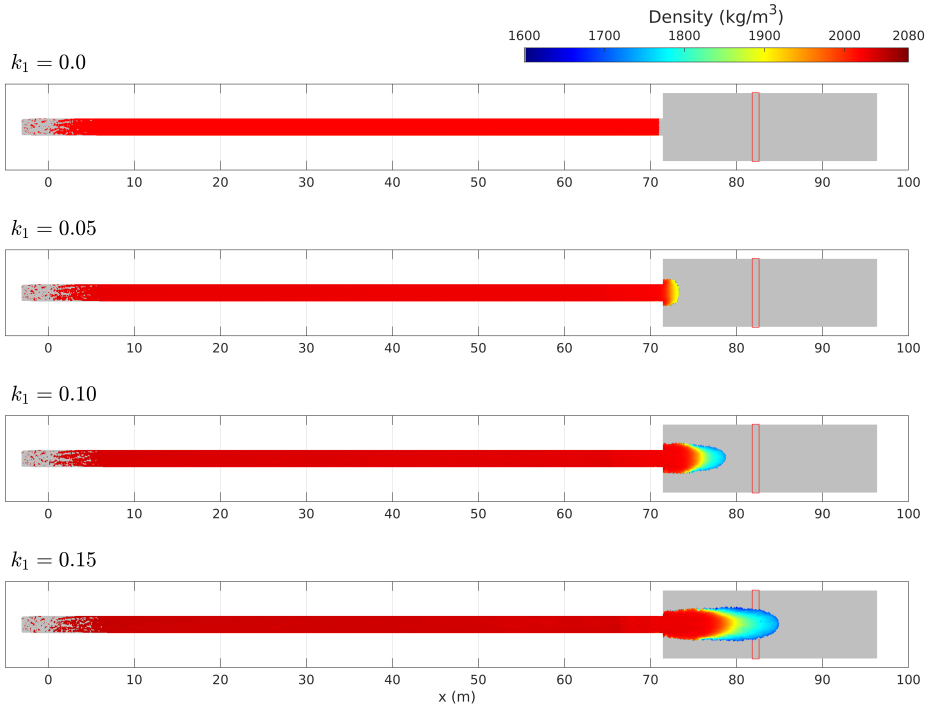

Figure 3.37: Experimental case MF2 – 2D deposit density h after the flow detention ($t = 25\,s$) with values of the dilatancy tuning parameter $k_1 = 0$ (equilibrium), $k_1 = 0.05$, $k_1 = 0.10$ and $k_1 = 0.15$ (maximum dilation).

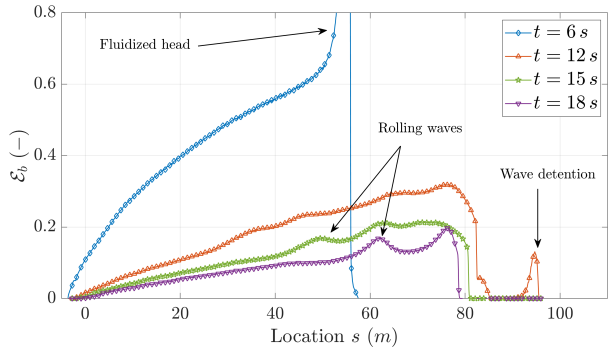

Figure 3.38: Experimental case MF2 – Longitudinal profile of the basal pore pressure excess factor $\mathcal{E}_b$ at times $t = 6,\ 12,\ 15$ and $18\,s$ for the simulation with dilatancy tuning parameter $k_1 = 0.15$

Finally, Figure 3.39 shows a 3D view of the final debris deposit features for the simulation with dilatancy tuning parameter $k_1 = 0.15$. It can be observed the accumulation of the denser material at the catenary zone and at the beginning of the runout surface, as well as the fluidized (lower density) dambreak wave-front.

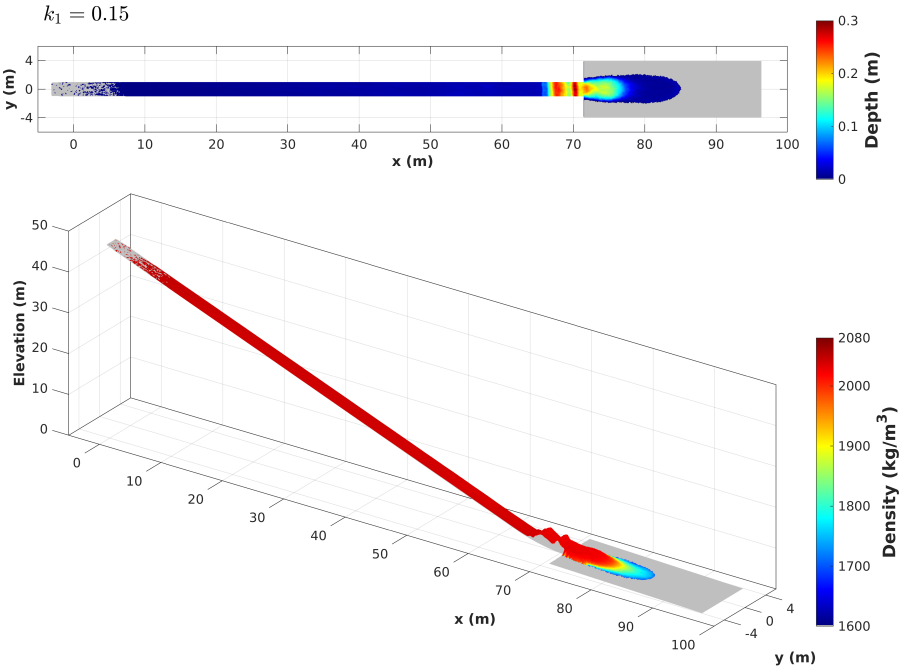

Figure 3.39: Experimental case MF2 – 3D view of the final debris deposit features for the simulation with dilatancy tuning parameter $k_1 = 0.15$.

3.5.3 Experimental case MF3: USGS debris dambreak over erodible steep bed

In this section the model predictions are validated using experimental data from large-scale dambreak debris flows over erodible bed. Eight different experiments were carried out in the USGS large-scale debris-flow flume (see Case 3.5.2 above for description of the facility). The available data, reported by Iverson *et al.* [60], include the wave-front location along time, the wave-front velocity at the end of the uniform-slope channel and the final volume eroded from the bed. Moreover, the flow thickness and bed deformation at different points were reported for two of the experiments. Figure 3.40 shows a schematic representation of the USGS flume setup for the erodible bed experiments. All the longitudinal distances s are referred to the headgate position taken along the experimental flume floor.

The initial debris volume is composed by a fully saturated mix of water and 56% gravel–37% sand–7% mud grains, called SGM mixture, where mud refers to particles smaller than $0.0625\,mm$ [61]. Table 3.6 shows the main parameter used in the simulation setup for characterizing the debris mixture. For all the experiments, the equivalent volumetric bulk concentration for the initial debris material is $\phi_0 = 0.6$ and the initial volume stored upstream the headgate is $6\,m^3$. The flume rigid floor is covered from $s = 6\,m$ ($x = 5.1\,m$) to $s = 53\,m$ ($x = 45.4\,m$) with a layer of partially saturated SGM mixture with $12\,cm$ uniform thickness.

In Table 3.7, the features of three sediment classes composing the SGM mixture have been summarized. Note that the critical Shields stress for the

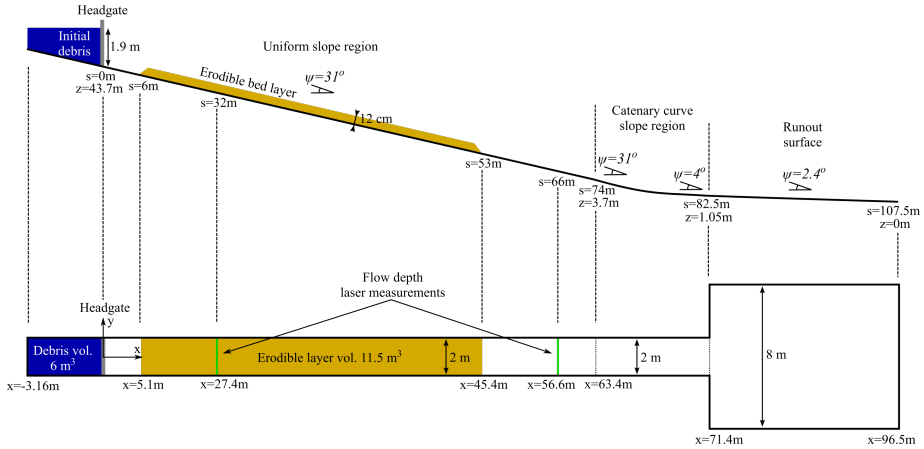

Figure 3.40: Experimental case MF3 – Sketch of the USGS flume for erodible bed experiments. Details of the equivalent horizontal distance, vertical elevation and channel slope are also indicated.

Debris volume	$6\,m^3$
Bulk solid conc. ϕ_0	$60\,\%$
Debris water content	$40\,\%$
Bulk debris density ρ	$2020\,kg/m^3$
Plastic viscosity μ_B	$1.66\,Pa \cdot s$
Cohesive yield strength τ_y	$393\,Pa$
Frictional stability angle δ_f	$40°$
Manning's rough. coeff. n_b	Concrete: $0.018\,sm^{-1/3}$ Erodible layer: $0.021\,sm^{-1/3}$
Pore-fluid density ρ_w	$1000\,kg/m^3$
Pore-fluid viscosity μ	$0.001\,Pa \cdot s$

Table 3.6: Experimental case MF3 – Characteristic of the initial debris material.

incipient motion $\theta_{c,p}$ has been graded using the Egiazaroff [32] hiding/exposure function depending on the diameter $d_{s,p}$ and the relative bed fraction $F_{b,p}$ of each sediment class.

Sediment classes N	3		
Sed. class type	Fines	Sand	Gravel
Grain diameter $d_{s,p}$	$0.016\,mm$	$0.4\,mm$	$12\,mm$
Solid density $\rho_{s,p}$	$2700\,kg/m^3$	$2700\,kg/m^3$	$2700\,kg/m^3$
Debris initial conc. ϕ_p	0.042	0.222	0.336
Bed layer fraction $F_{b,p}$	0.07	0.37	0.56
Critical Shields stress $\theta_{c,p}$	10.8575	0.4343	0.0212
Transport capacity modification param. β_T	0.3		
Bed porosity ξ	Depends on the test		
Bed water content C_{bw}	Depends on the test		

Table 3.7: Experimental case MF3 – Sediment classes composing the SGM mixture.

The porosity and water content of the erodible bed layer vary for each experiment, leading to different entrainment rates and wave-front velocities. Table 3.8 shows the water content C_{bw} and the bed bulk porosity ξ of the bed layer for each experiment taken from [60]. Furthermore, in order to account for the reduction of the frictional basal resistance due to pore-pressure in a simple way and following [79], the basal pore pressure excess factor $\mathcal{E}_b$ used in these simulations is set to a value (constant in time and space) between 0.5 and 0.8 depending on the bed water content of each experiment.

The simulations are performed using an unstructured triangular mesh of around 57000 cells, with an averaged area of $100\,cm^2$. The CFL is set to 0.95 and the total simulated time is $25\,s$ for each experiment. Simulations are performed in a NVIDIA Tesla K40c device with a CUDA-C++ code, whereas a Intel(R) Core(TM) i7-7700K @4.50GHz is used for the CPU-based algorithm.

Test	Bed water content $C_{bw}\,(-)$	Bed bulk porosity $\xi\,(-)$	Pore pressure excess factor $\mathcal{E}_b\,(-)$
A	0.282	0.51	1.70
B	0.257	0.46	1.67
C	0.253	0.48	1.65
D	0.244	0.43	1.62
E	0.227	0.39	1.60
F	0.220	0.43	1.58
G	0.183	0.42	1.56
D	0.148	0.49	1.55

Table 3.8: Experimental case MF3 – Features of the erodible bed layer for each experimental test.

As in the previous dambreak over rigid bed experiments, the wave-front position was tracked using image techniques and video frames, as well as the front velocity between $s = 60\,m$ and $s = 70\,m$. For each experiment, the entrainment from the erodible bed to the debris flow was estimated by measuring the bed layer volume before and after the passage of the dambreak wave. The flow thickness was measured at the control sections X1 $s = 32\,m$ and X2 $s = 66\,m$ for the test G and C using laser sensors mounted above the flume. Furthermore, the bed degradation was also measured using scour sensor placed in the erodible bed at $s = 13\,m$, $s = 23\,m$, $s = 33\,m$ and $s = 43\,m$ for tests G and C. Video files of all the experiments are available in https://pubs.usgs.gov/of/2007/1315/.

First, a complete analysis of the numerical results obtained using four different basal resistance closures from Table 3.1 is included herein for the tests G and C. The behavior of the dambreak flow is analyzed using the cohesive Bingham and turbulent rheology (CB and CT respectively) as well as with the frictional turbulent and plastic formulations (FT and FP respectively). Then, the results obtained by the rest of the experiments are also reported.

Experiment G

For test G, the lower part of Figure 3.41 shows the bulk debris density in color scale and the upper part depicts the longitudinal profile of the specific volumetric concentration for each sediment class in the mixture at $t = 6\,s$ and $t = 12\,s$ using the frictional turbulent FT rheology. Note that the flow depth in the 3D figure is multiplied by 5 to improve the visualization of the debris wave shape.

As the dambreak wave progresses downstream, bed material is incorporated into the flow, increasing the solid phase volume in the debris and hence its density. It is worth to mention that the coarse sediment fraction dominates along the front and central regions of the debris wave, whereas the finer sediment fraction shows higher concentrations along the tail zone. This sorting of the different solid phases composing the flow mixture is typical of debris flow dynamics and mainly caused by the differences on the solid phases velocity. However, in these simulation a unique velocity for all the solid phases since the dilation effects are neglected. Therefore, this sorting of the sediment classes obtained by the numerical model, although correct, may be related to different bed entrainment rates for each sediment fraction from the bed.

The temporal evolution of the flow free surface at the control sections $X1$ ($s = 32\,m$) and $X2$ ($s = 66\,m$) with the four different depth-averaged rheology relations for the basal resistance is depicted in Figure 3.42 in comparison with the measured data. Using the frictional turbulent FT formulation, the wave-front arrival time to the first control section $X1$ is slightly smaller than the observed data but predicts well the arrival of the wave front to the second control section $X2$. Moreover, the peaks of the free surface level corresponding to the wave head at both control section are also reasonably well predicted. The simulation performed with the frictional plastic FP relation predicts correctly the arrival time and wave head level at the first control section $X1$ but, for the second control section $X2$, the arrival time is larger and the peak of the free surface level higher than those observed in the experiment. The cohesive Bingham CB formulation shows a smaller arrival time at both control sections $X1$ and $X2$, indicating higher flow velocities, whereas the wave head level is also well predicted in both cases. Finally, The cohesive turbulent CT rheology shows a higher free surface level peak and a smaller arrival time at the first control section $X1$, whereas develops a double-wave flow structure at the second control section $X2$.

The dambreak wave-front position is plotted against time in Figure 3.43–(a) for the four rheology formulations simulated. The cohesive Bingham CB formulation shows higher wave-front velocities than those observed for the flow advance along constrained channel, whereas the frictional plastic FP closure relation predicts slower front velocities along this region. The cohesive turbulent CT formula overestimates the wave-front velocity at the first stages but the runout distance is smaller than that measured in the experiment. Only the frictional turbulent FT formulation is able to correctly estimate the wave-front advance process. Furthermore, bed degradation was not detected at any of the measurement section in the experiment, indicating that the maximum scour depth was lower than 2-3 cm. Figure 3.43–(b) shows the temporal evolution of the bed thickness at

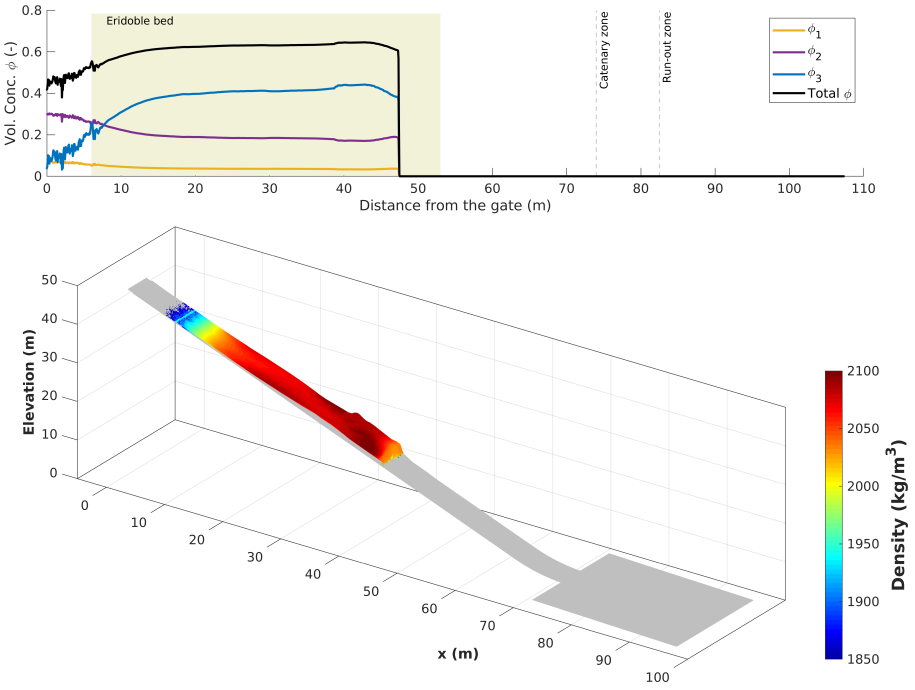

(a) $t = 6\,s$

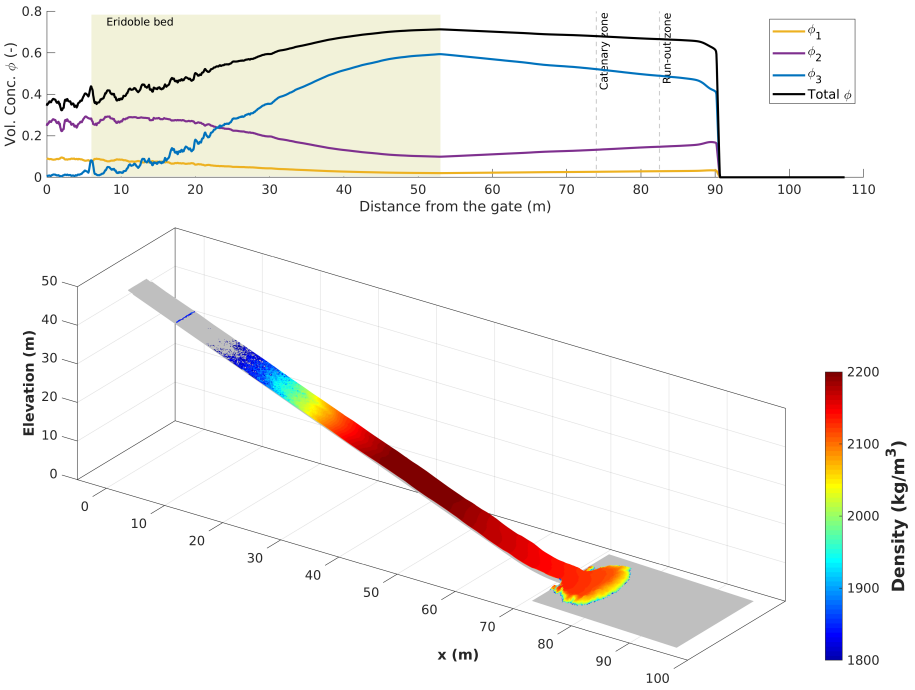

(b) $t = 12\,s$

Figure 3.41: Experimental case MF3 – Test G: 2D flow density and solid phase gradation at $t = 6\,s$ and $t = 12\,s$ using FT resistance.

section $X1$ ($s = 32\,m$) for all the resistance formulations used. The deepest scour is computed using the frictional turbulent FT relationship ($3.2\,cm$) whereas the rest of basal resistance formula predict bed scours lower than $2.4\,cm$. This is in agreement with the data measured during the experiment.

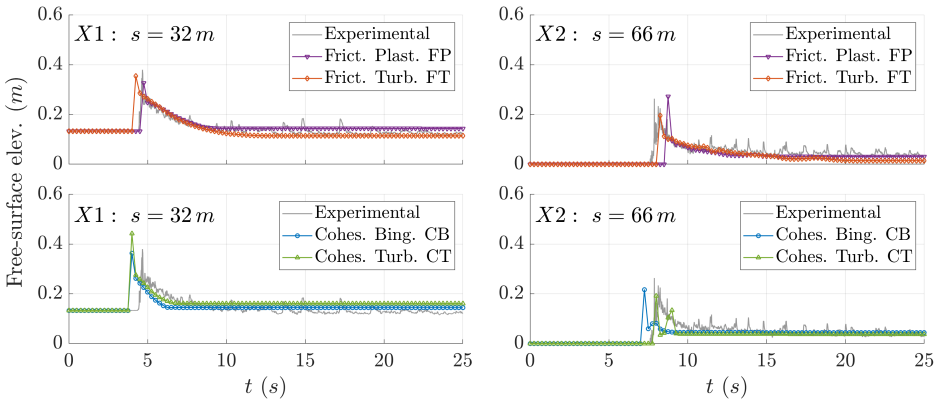

Figure 3.42: Experimental case MF3 – Test G: temporal evolution of the flow free surface at (left) $X1 : s = 32\,m$ and (right) $X2 : s = 66\,m$ with four different rheology closures for the debris basal resistance.

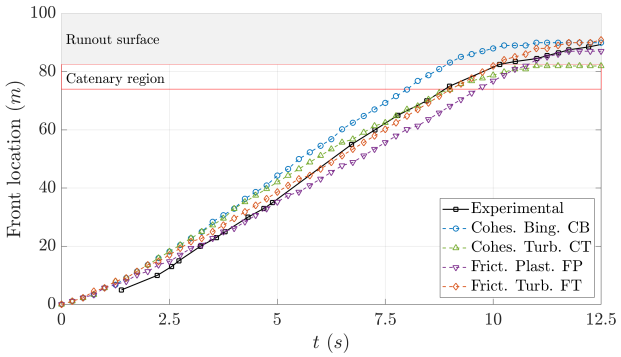

(a) Front location evolution.

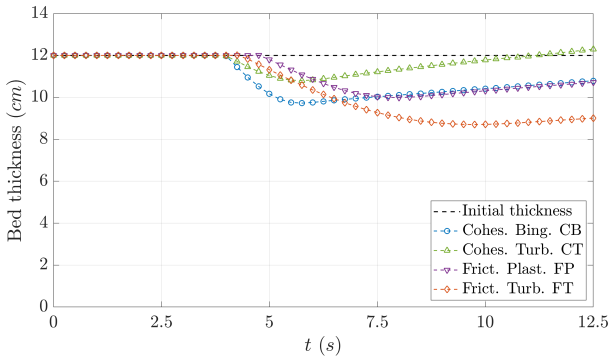

(b) Bed thickness evolution at $X1$.

Figure 3.43: Experimental case MF3 – Test G: temporal evolution of (top) the dambreak wave-front location and (bottom) the bed thickness at $X1$ ($s = 32\,m$) with four different rheology closures for the debris basal resistance.

Table 3.9 shows the Root Mean Square Error (RMSE) for the flow free surface level (fsl) at the control sections $X1$ ($s = 32\,m$) and $X2$ ($s = 66\,m$), as well as for the wave-front location, with the four different rheological relationships simulated. The lowest RMSE is obtained with the frictional plastic FP formulation for the free surface level at the control section $X1$, whereas the frictional turbulent FT relation shows the best results for both the free surface level at $X2$ and the temporal evolution of the wave-front location. The computational time required by the GPU-based algorithm to

complete the simulation is also reported in Table 3.9 for all the rheology formulations, including the file input-output time. The computational effort is quite similar with all the debris stress relationships, with the exception of the frictional turbulent FT formula which requires a larger time to complete the simulation.

Rheol.	RMSE fsl:$X1$ (m)	RMSE fsl: $X2$ (m)	RMSE Front loc. (m)	Comp. time Tesla k40c (s)
CB	$4.46 \cdot 10^{-2}$	$3.92 \cdot 10^{-2}$	5.97	21.43
CT	$5.16 \cdot 10^{-2}$	$2.94 \cdot 10^{-2}$	4.38	20.61
FP	$1.81 \cdot 10^{-2}$	$4.05 \cdot 10^{-2}$	3.55	21.73
FT	$3.83 \cdot 10^{-2}$	$2.56 \cdot 10^{-2}$	2.72	26.28

Table 3.9: Experimental case MF3 – Test G: RMSE for the flow free surface level at the control sections ($X1$ and $X2$) and for the wave-front location, and computational time required by the GPU-based algorithm.

Furthermore, the normalized wave-front speed S and the normalized post-entrainment flow volume V defined as

$$S = \frac{S_{measured}\,(ms^{-1})}{9.81\,(ms^{-1})} \qquad V = \frac{6\,(m^3) + V_{eroded}\,(m^3)}{6\,(m^3)} \tag{3.143}$$

with $S_{measured}$ the wave-front velocity measured at $s \in [60\,m, 70\,m]$ and V_{eroded} the volume incorporated from the bed layer into the flow, are also computed for all the rheology relationships and compared with the measured data. Table 3.10 shows the computed results and the relative error with respect to those observed in the experiment. Although the best approximations to the measured wave-front speed S are obtained with the frictional plastic FP resistance formulation, also the frictional turbulent FT and cohesive turbulent CT relations show acceptable relative errors lower than 10%. Moreover, only the frictional turbulent FT rheology reports a suitable approximation for the normalized post-entrainment volume V lower than 10% of the volume measured after the experiment.

Rheology	Norm. speed S Value $(-)$	Norm. speed S Rel. error $(\%)$	Norm. vol. V Value $(-)$	Norm. vol. V Rel. error $(\%)$
Measured	0.85	-	1.36	-
Coh. Bingham CB	1.0036	+18.06	1.1082	-17.91
Coh. Turb. CT	0.7702	-9.17	0.9604	-33.30
Frict. Plast. FP	0.8492	-0.10	1.1083	-17.90
Frict. Turb. FT	0.9263	+8.90	1.3904	+2.99

Table 3.10: Experimental case MF3 – Test G: normalized wave-front speed S and post-entrainment flow volume V with the four rheology closures simulated.

In order to assess the performance of the GPU-based algorithm for the computation of large-scale realistic debris/mud flow events, the computational time required with the above used mesh (taken as reference and called MR) is compared with the computational time running in a CPU-core, both including the file input-output time. All the computational times are obtained using the frictional turbulent FT rheology. Moreover, the scalable acceleration of the GPU-based algorithm is assessed by comparing the computational times using a mesh 5 times coarser than MR and referred to as M1 (11500 cells), as well as with a mesh 4 times finer than MR (referred to as M2), with 228000 cells approximately. The computational efforts required for the GPU-based and CPU-based versions of the algorithm with the three considered meshes are reported in Table 3.11. Results show that, for the reference mesh MR, the speed-up achieved by the GPU-based algorithm with respect to the CPU-based version is 12. Furthermore, the performance of the GPU-based algorithm increases as the mesh is refined and the number of cells involved in the simulation is higher, with a speed-up near 27 for mesh M2.

Mesh	Cells number $(-)$	Cell area cm^2	Cells increment $(-)$	Comp. time Tesla k40c GPU (s)	Comp. time i7-7700K CPU (s)	Speed-up cpu/gpu $(-)$
M1	11515	500	$\sim \frac{1}{5}\times$MR	4.497	12.073	$\times$2.7
MR	57212	100	–	26.284	327.619	$\times$12.5
M2	227803	25	$\sim 4\times$MR	155.904	4206.670	$\times$26.9

Table 3.11: Experimental case MF3 – Test G: computational effort required by the GPU-based algorithm with different mesh refinement level and speed-up with respect to the CPU-based version.

Experiment C

Test C is simulated using the two more suitable basal resistance formulations for the USGS debris flow experiments, the frictional plastic FP and the frictional turbulent FT rheology closures. The lower part of Figure 3.44 depicts the bulk debris density and the upper part shows longitudinal profile of the specific volumetric concentration of each sediment class at $t = 6\,s$ and $t = 12\,s$ using the frictional turbulent FT rheology relation. In experiment C the initial water content of the erodible bed was much higher than that of experiment G, leading to an enhancement of the bed material entrainment into the debris. The numerical results show that, when the flow progresses downstream and reaches the erodible bed, high concentration of the coarser solid phase appears rapidly at the wave-front whereas the volumetric concentrations of the finer solid phases reduce.

As in test G, the finer fraction gains importance along the tail of the debris wave, although the volumetric concentration of the gravel fraction continues being higher than those of the sand and silt fractions in the center region of the flow (see Figure 3.44). Furthermore, after the main wave-front reaches the runout zone and stops, secondary or roll waves are developed along the tail of the debris flow. These roll waves are associated to the solid phases sorting, with higher concentration of the coarse sediment class at

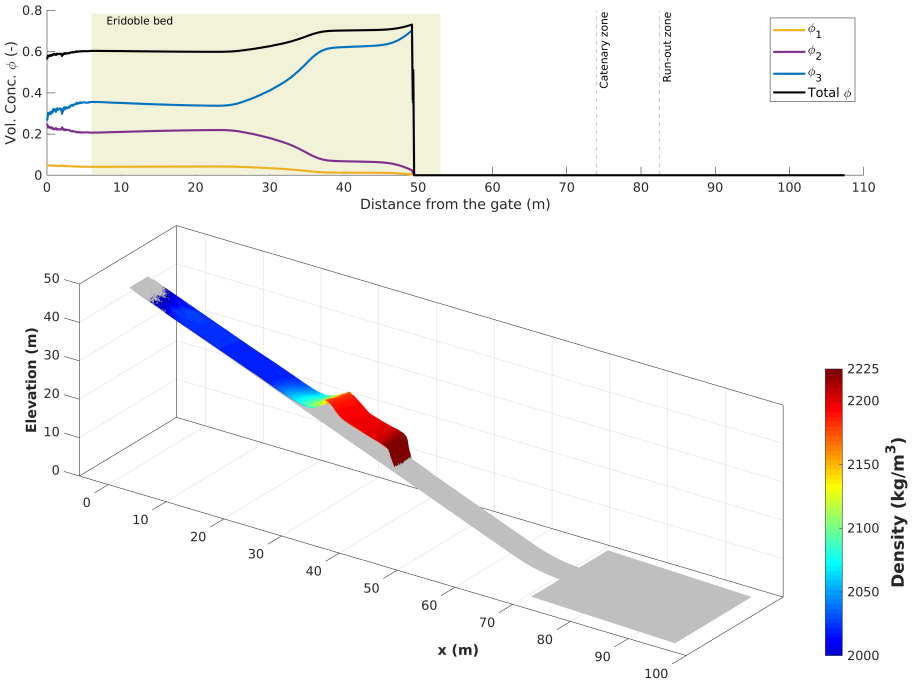

(a) $t = 6\,s$

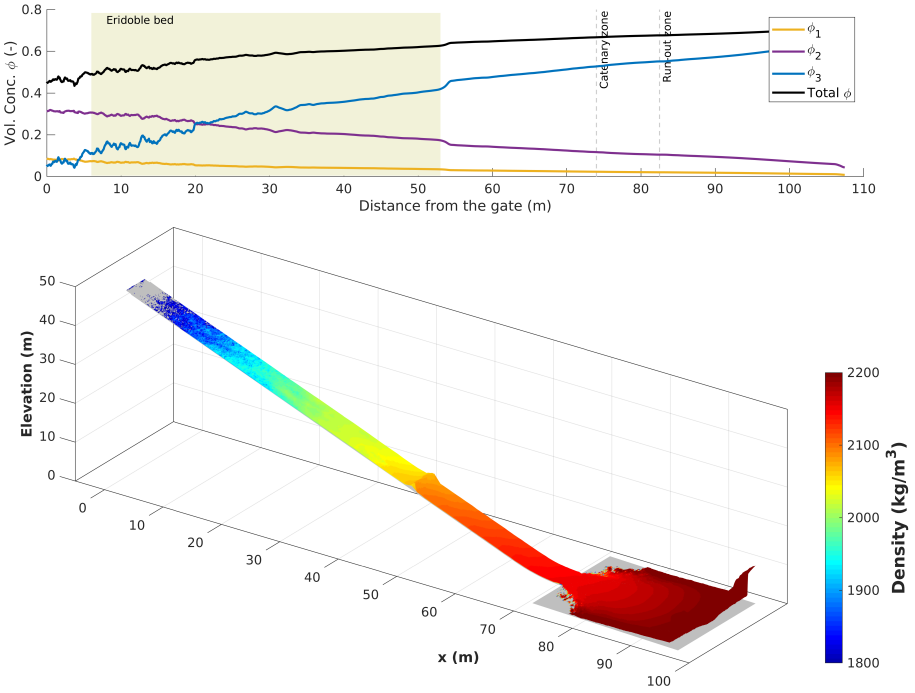

(b) $t = 12\,s$

Figure 3.44: Experimental case MF3 – Test C: spatial flow distribution at (a) $t = 3\,s$ and (b) $t = 12\,s$ after the gate opening and using the TC friction.

the wave head and finer grained more-liquefied tails [63]. Roll waves move downstream and also stop when they reach the runout zone.

The temporal evolution of the flow free surface at control sections $X1$

($s = 32\,m$) and $X2$ ($s = 66\,m$) has been depicted in Figure 3.45 in comparison with the measured data. The wave-front arrival time to both control sections is again well predicted using the frictional turbulent FT rheology, as well as the wave head level at the control section $X1$. However, the head level is slightly overestimated for the control section $X2$. Nevertheless, the frictional plastic FP formulation shows smaller arrival times and overestimates the free surface elevation of the wave head at both control sections, indicating higher flow velocities than those observed during the experiment.

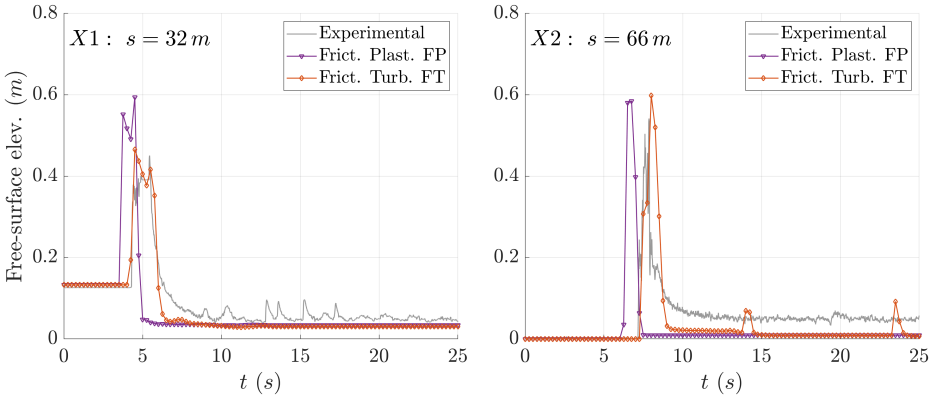

Figure 3.45: Experimental case MF3 – Test C: temporal evolution of the flow free surface at (left) $X1 : s = 32\,m$ and (right) $X2 : s = 66\,m$ with different rheology closures for the debris basal resistance.

The temporal evolution of the wave-front position is plotted in Figure 3.46–(a). The frictional plastic FP formulation shows much higher wave-front velocities than those observed during the experiment, whereas the frictional turbulent FT rheology relation predicts correctly the wave-front advance. Furthermore, Figure 3.46–(b) shows the computed temporal evolution of the bed thickness at $s = 13\,m$, $s = 23\,m$, $s = 33\,m$ and $s = 43\,m$ with both rheology closures compared with the measured data. Both basal resistance relations predict the rapid degradation of the bed layer, but the frictional turbulent FT formula shows a bed thickness evolution which agrees better with the measured data at all the control points.

In order to analyze the sensitivity of the model to some calibration parameters, additional simulations are performed taking the above results for test C with the FT resistance formulation as reference. Considering that the solid phase features and the experiment description shown in Tables 3.6, 3.7 and 3.8 are well-know from the original works [60, 61], the highest uncertainty arises from both the basal pore pressure coefficient $\mathcal{E}_b$ and the transport capacity modification parameter β_T. The 20% reduction of the basal pore pressure coefficient leads to a marked decrease of the wave propagation velocity whereas a 20% increment on $\mathcal{E}_b$ causes an increase of the wave propagation velocity, as it is depicted in Figure 3.47–(a). On the other hand, Figure 3.47–(b) shows that the variation of the transport capacity parameter β_T does not show a marked influence on the velocity propagation of the debris dambreak wave . Therefore, when the frictional-type closures are used for the basal resistance (see Table 3.1), a correct calibration of the the basal pore pressure excess coefficient $\mathcal{E}_b$ is essential.

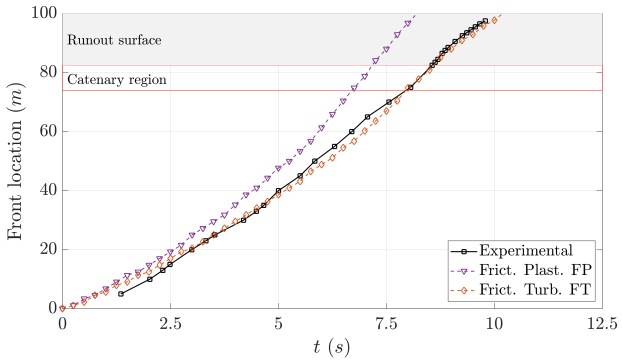

(a) Front location evolution.

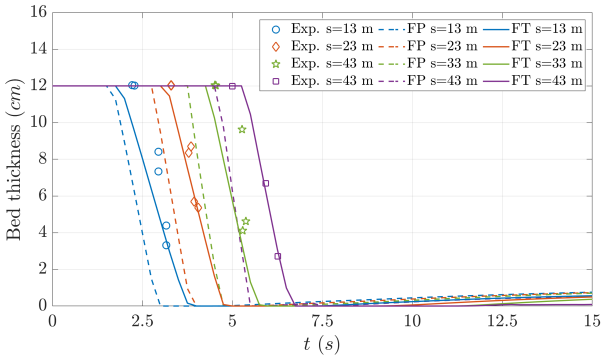

(b) Bed thickness evolution.

Figure 3.46: Experimental case MF3 – Test C: temporal evolution of (a) the dambreak wave-front location and (b) the bed thickness at $s = 13\,m$, $s = 23\,m$, $s = 33\,m$ and $s = 43\,m$ with FP and FT rheology closures for the debris basal resistance.

Complete set of experiments

As a main conclusion of the results shown above, the frictional-type rheology formulations for the debris resistance (specially the frictional turbulent FT) are considered more suitable to reproduce the USGS debris flume experiments than the resistance closure relations based on a cohesive yield strength. Furthermore, the FT relationship has also been used in other previous works to reproduce this set of experimental data [42, 79, 112, 147]. Therefore, the remaining six experiments are simulated using the FT rheology to estimate the basal resistance along the debris flow.

Figure 3.48 shows the computed wave-front position against time for all the tests carried out at the USGS flume, compared with the measured front evolutions. The proposed model is able to predict reasonably well the advance of the dambreak debris wave for most of the experiments. Nevertheless, important differences appear in some cases, especially in tests H and D where the model overestimates the velocity of the wave front at the catenary and runout regions with respect to those observed in the corresponding experiments.

Finally, Table 3.12 shows the normalized wave-front speed S between $s = 60\,m$ and $s = 70\,m$ and the normalized post-entrainment flow volume V, estimated as in (3.143), computed with frictional turbulent FT formulation for the all the experiments carried out at the USGS debris flume, compared with the measured data. The proposed model is able to correctly estimate both dynamic data with relative errors lower than 20% for all the

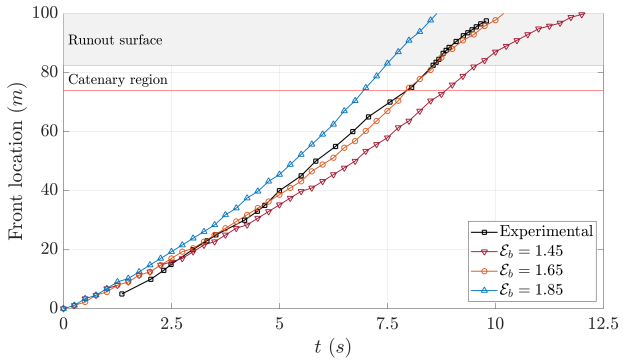

(a) Sensitivity to $\mathcal{E}_b$.

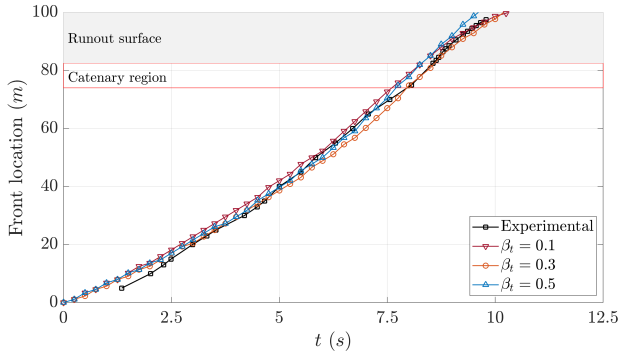

(b) Sensitivity to the capacity modification parameter β_T.

Figure 3.47: Experimental case MF3 – Test C: temporal evolution of the dambreak wave-front location with (a) increasing basal pore pressure coeffcients $\mathcal{E}_b$ and (b) increasing transport capacity modification parameter β_T.

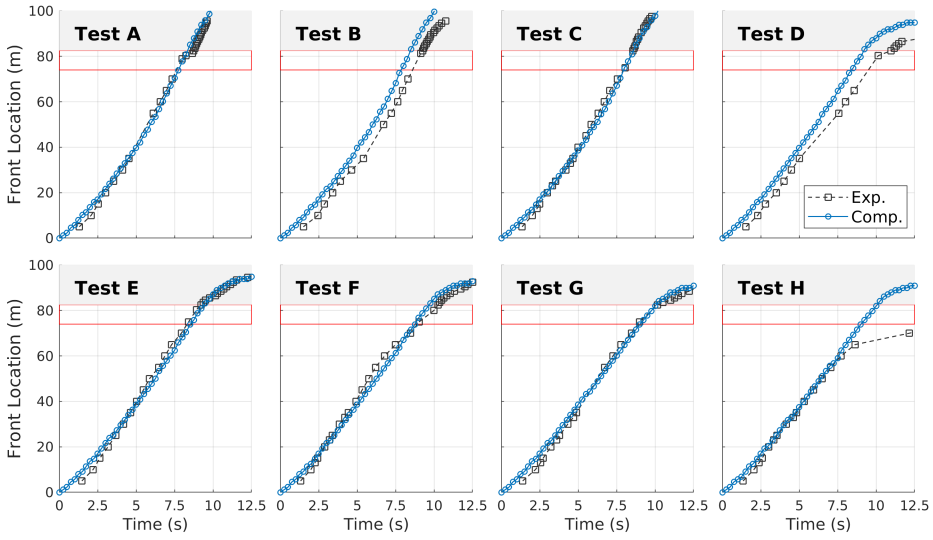

Figure 3.48: Experimental case MF3 – Temporal evolution of the dambreak wave-front location with FT rheology for the all the USGS debris bambreak over erodible bed experiments.

experiments, with the exception of the normalized wave-front velocity S for the tests H and F which shows important differences between experimental and computed values. Further developments of the physical model could be required to improved these numerical results.

Test	Front vel. S			Debris Vol. V		
	Meas. $(-)$	Sim. $(-)$	Error $(\%)$	Meas. $(-)$	Sim. $(-)$	Error $(\%)$
A	1.33	1.38	+4.5	3.05	2.73	-10.5
B	1.53	1.51	-1.6	2.59	2.64	+1.8
C	1.19	1.38	+17.5	2.27	2.61	+15.2
D	1.01	1.11	+10.0	2.20	2.21	+0.6
E	0.95	1.02	+7.2	2.24	2.18	-2.4
F	0.61	1.01	+67.0	1.52	1.63	+8.1
G	0.85	0.92	+8.9	1.36	1.39	+2.9
H	0.24	1.01	+324.5	1.56	1.48	-4.4

Table 3.12: Experimental case MF3 – Measured and computed normalized wave-front speeds S and post-entrainment flow volumes V with FT rheology for the all the USGS debris bambreak over erodible bed experiments.

3.5.4 Real-scale case MF4: Mine tailings dam failure in Brumadinho (Brasil)

The aim of this test is to assess the performance of the model for simulating a real large-scale highly unsteady mud flow, comparing the obtained results with the available field observations and gaining a better insight into the behavior of this kind of violent flows. On 25th January 2019 (12:28 p.m.), the Dam I at the C'orrego do Feijão Iron Ore Mine, located 9 km north-east of Brumadinho in the state of Minas Gerais (Brazil), suffered a sudden catastrophic failure, resulting in an extremely violent mud flow which traveled downstream more than 10 km and reached the Paraopeba River, a major tributary of the São Francisco River. This disaster caused more than 260 deaths and important economic and environmental losses. The dam consisted of $12 \cdot 10^6\, m^3$ mining waste tailings with a height of $70 - 80\, m$, constructed over a period of 37 years in 10 raises and covering an area of $4.13 \cdot 10^5\, m^2$. The initial failure extended across the face of the dam and the slope collapse was complete in less than 10 seconds. Most of the dam material flowed out of the dam in less than 5 minutes. The tailings in the dam showed a sudden and significant loss of strength and rapidly became a heavy liquid that flowed downstream at a high speed (about $120\, km/h$ in some zones). Based on the available videos, it is clear that the failure was the result of static liquefaction within the materials of the dam [126].

Table 3.13 shows some of the features of the materials in the dam. Tailings were composed by a mixture of water, sediments and heavy metals, mainly iron (Fe) 264.9 mg/g, aluminum 10.8 mg/g, manganese 4.8 mg/g and titanium 0.5 mg/g [141]. The size distribution consisted basically of a mineral sand fraction (38%) and a fines fraction (62%), accounting for mineral silt-clay and metals particles. The water content before the failure was estimated around 50% by volume with a specific weight of $22 - 26\, kN/m^3$ [126].

Figure 3.49 shows an aerial image of the mine site after the dam collapse, including the dam location and the original tailings elevation in meters above sea level ($m.o.s.l$). The area affected by the mud was $3.3 \cdot 10^6\, m^2$,

Dam capacity	$12 \cdot 10^6\ m^3$			
Dam area	$4.13 \cdot 10^5\ m^2$			
Solid concent. ϕ_0	50%			
Water content C_w	50%			
Specific weight	$22 - 26\ kN/m^3$			
Size distr.	Sand		Fines	
Rel. content	38%		62%	
Heavy metals	Fe	Al	Mn	Ti
Weight conc.	264.9 mg/g	10.8 mg/g	4.8 mg/g	0.5 mg/g
Rel. content	87%	10%	1.7%	0.3%

Table 3.13: Real-scale case MF4 – Brumadinho's dam and tailings features.

without including the original dam area, and reached the Paraopeba River $8.5\ km$ downstream the dam.

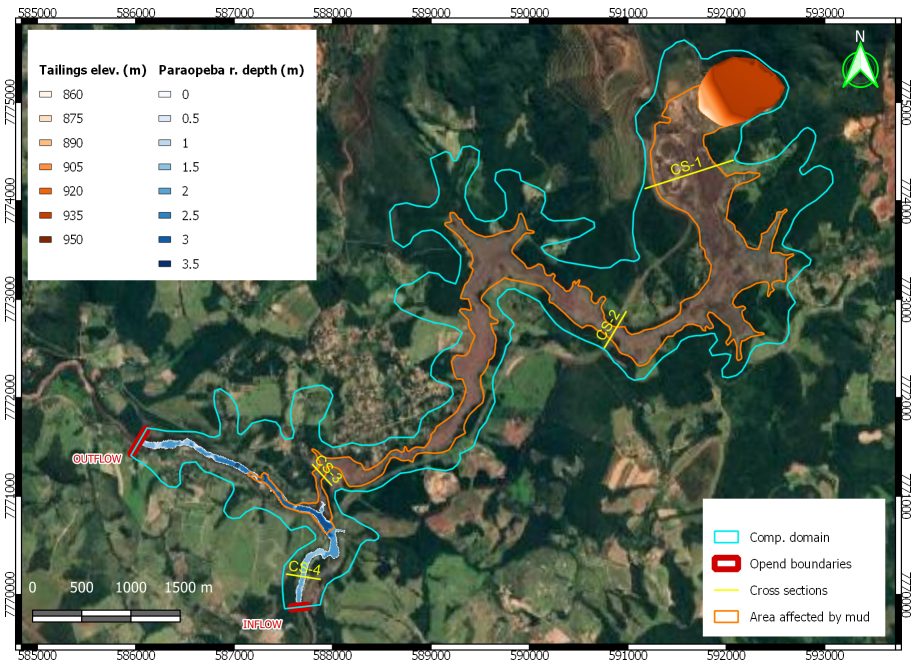

Figure 3.49: Real-scale case MF4 – Aerial image of the area affected by the mud and the computational domain used in the simulation.

In order to perform the simulations, a spatial domain of $10.396 \cdot 10^6\ m^2$ is discretized using a unstructured triangular mesh with $5.3 \cdot 10^5$ cells approximately and slightly refined in the dam area. Four control cross-sections are placed downstream of the dam at (CS-1) the mine stockpile area, (CS-2) the railway bridge, (CS-3) the Alberto Flores road and (CS-4) the Alberto Flores Gauge Station in the Paraopeba River. Furthermore, the base regime water depth and velocities in the Paraopeba River before to the mud arrival is assessed by a previous simulation (without considering the tailings dam collapse) setting a constant clear water inlet of $45.6\,m^3/s$ and uniform flow conditions at the outlet boundary. The mean thalweg slope in the Paraopeba River is $S_0 = 0.0025\,m/m$. This previous simulation runs until the solution converges to the base steady state. Numerical results show

that the maximum water depth in the Paraopeba River before the dam collapse is around $3.5\,m$ with a negligible sediment concentration at the outlet boundary (lower than 2% by volume) and maximum flow velocities about $2.5\,m/s$ (see Figure 3.49).

Figure 3.50 shows the terrain elevation ($1{\times}1\,m$ DTM) previous to the dam collapse. The thalweg elevation along the area covered by the mud varies between $860\,m.o.s.l$ at the dam-toe and $720\,m.o.s.l$ at the Paraopeba River, with an averaged longitudinal bed slope $S_0 = 0.0165\,m/m$. The initial tailings depth at the dam is estimated by comparing the terrain elevation before and after the dam failure using $1{\times}1\,m$ DTM's.

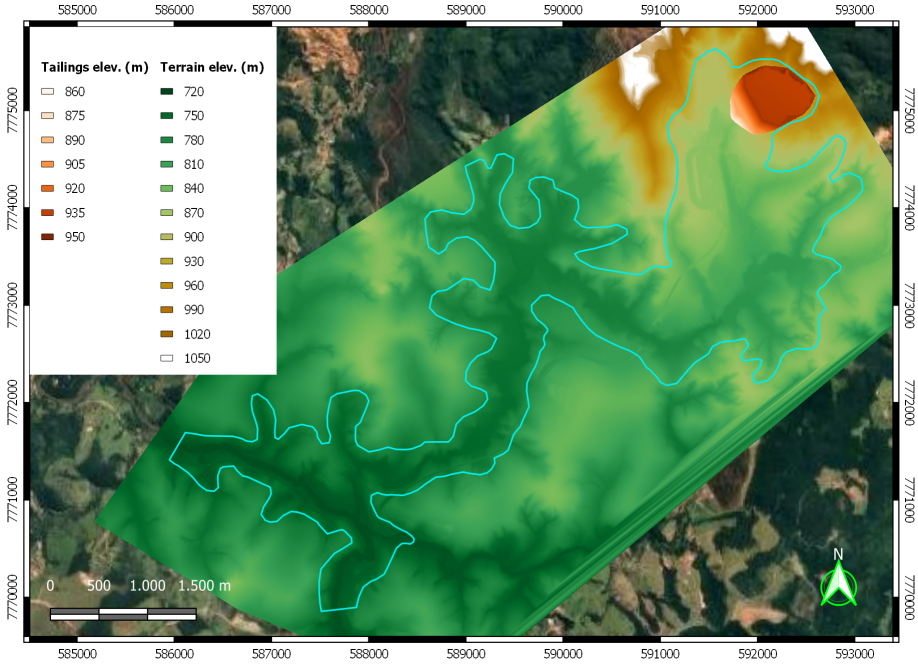

Figure 3.50: Real-scale case MF4 – Terrain elevation before the dam collapse ($1{\times}1\,m$ DTM).

Six different solid phases are set, including mineral sand, mineral silt, iron (Fe), aluminum (Al), manganese (Mn) and titanium (Ti). A summary of the main parameters used in the simulation is shown in Table 3.14. The tailings mixture is considered fully saturated with an initial bulk volumetric concentration of solids $\phi_0 = 0.5$, leading to a mixture density $\rho = 2247.5\,kg/m^3$. The specific initial volumetric concentration for each solid phase ϕ_p is estimated from the available literature [126, 129, 141]. The deposition porosity ξ_p for each sediment class is estimated using the Wu [144] relation and the bulk value for the bed layer ξ is estimated as a weighted mean. The hiding-exposure effects on the critical Shields stress for the incipient motion each solid phase $\theta_{c,p}$ are estimated using the Egiazaroff [32] formula.

As the mining tailings in the dam showed a low plasticity and high values of pore-fluid pressure [126] before the collapse, the frictional turbulent FT rheology is set for the estimation of the basal resistance contribution during the simulation. The land use along the area covered by mud was mainly forest and agriculture, hence a uniform Manning's roughness parameter $n_b = 0.065\,sm^{-1/3}$ is used and the transport capacity modification parameter is set to $\beta_T = 0.5$ for all the solid phases. A stability angle $\delta_f = 5°$

is estimated for the basal frictional resistance. The effect of the solid phase dilation of the material segregation are neglected and the pore-fluid pressure excess factor is set to the constant value $\mathcal{E}_b = 1.05$. The simulated time is 3 $hours$ from the dam collapse and the CFL is 0.95.

Initial mixt. density ρ	2247.5 kg/m^3					
Basal stab. angle δ_f	5°					
Manning's roug. n_b	0.065 $sm^{-1/3}$					
Pore-fluid dens. ρ_w	1000 kg/m^3					
Pore press. coeff. $\mathcal{E}_b$	1.05					
Sed. classes	6					
Crit. Shields stress θ_c	0.030					
Transp. cap. param. β_T	0.5					
Solid phase	Sand	Silt	Fe	Al	Mn	Ti
Diameter $d_{s,p}$ (mm)	0.4	0.075	0.075	0.075	0.075	0.075
Initial concent. ϕ_p	0.19	0.224	0.075	0.009	0.0015	0.0003
Solid dens. $\rho_{s,p}$ (kg/m^3)	2700	2700	7874	2700	7210	4506
Bed fraction $F_{b,p}$	0.38	0.62	0.0	0.0	0.0	0.0
Depos. porosity ξ_p	0.35	0.45	0.45	0.45	0.45	0.45
Crit. Shields stress $\theta_{c,p}$	0.020	0.067	0.067	0.067	0.067	0.067

Table 3.14: CReal-scale case MF4 – Parameters used for the simulation of the dam failure.

Figure 3.51 shows the mud flow depth (left) and velocity (right) at $t = 5\,min$, $t = 10\,min$ and $t = 35\,min$ after the dam collapse. The numerical results show that practically the whole initial tailing volume flows out of the dam in the first 5 minutes after the dam collapse, as it was observed in the available videos. The mud wave moves downstream with a computed height larger than $25\,m$ and with velocities higher than $15\,m/s$ $(54\,km/h)$ in some zones during the first minutes. Furthermore, the simulation results indicate that the mud reaches the mining treatment plant and the stockpile areas (CS-1), as happened during the real event. After this initial stage, the numerical results show that the dambreak wave decreases its velocity at $t = 10\,min$ but the computed mud depth is still higher than $20\,m$ when the wave-front reaches the railway bridge (CS-2). During the real event, the mud wave impact caused the collapse of the railway bridge structure. As the wave moves downstream, the velocity and depth of the mud reduce progressively along the whole flow, not only in the wave-front. Numerical results show that $35\,min$ after the event beginning, the mud wave-front is close to the Alberto Flores road (CS-3) and the flow is practically stopped in all zones. As it was observed during the real event, the simulation predicts that the wave-front reaches the Paraopeba River, flowing into the riverbed and creating a "dam" which increases progressively the upstream water level at the Alberto Flores Gauge Station (CS-4) along the following hours. The computed mud accumulation reaches $14.5\,m$ in some zones after the flow deposition.

Figure 3.52 depicts the predicted temporal evolution of the mud wave-front location and velocity along the thalweg each $2.5\,min$ during the first

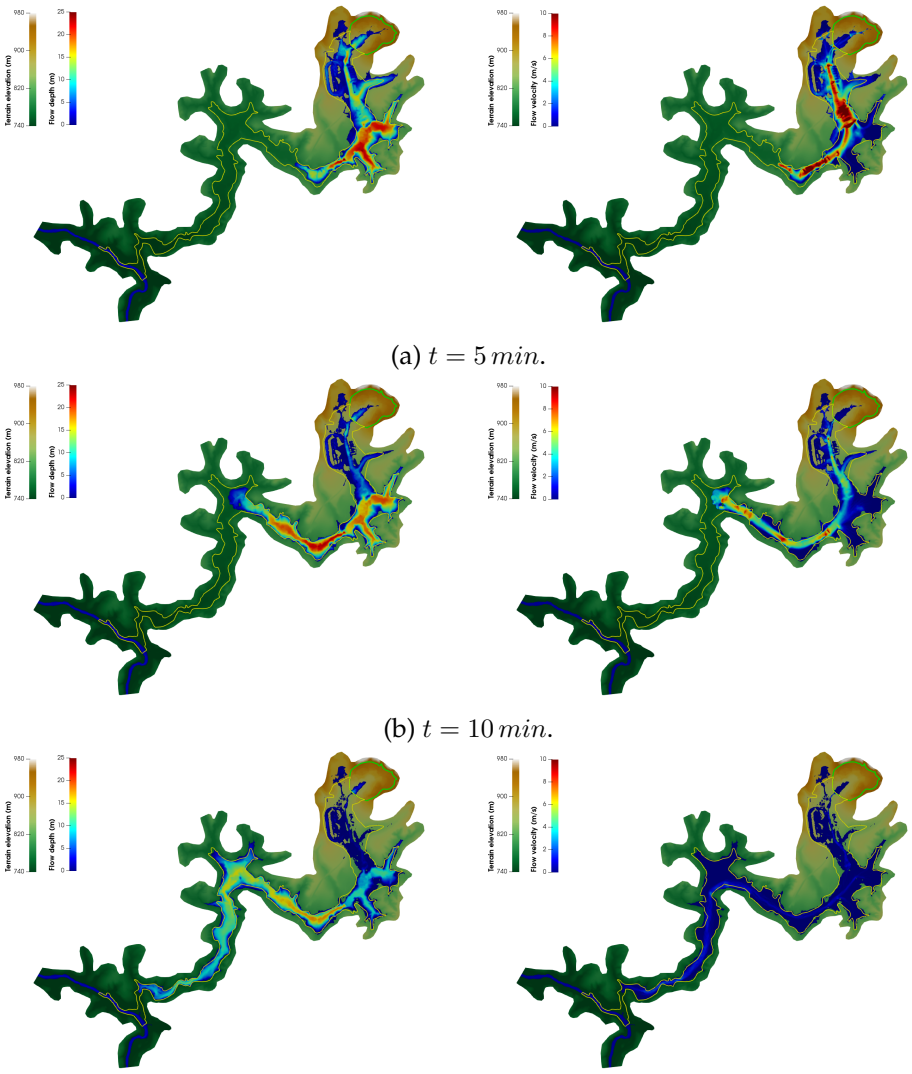

(a) $t = 5\,min.$

(b) $t = 10\,min.$

(c) $t = 35\,min.$

Figure 3.51: Real-scale case MF4 – (left) Mud flow depth and (right) flow velocity: (a) $t = 5\,min$, (b) $t = 10\,min$ and (c) $t = 35\,min$ after the dam collapse.

hour of the flow. At the first stages, the averaged velocity of the wave-front is around $50\,km/h$ and it is progressively decreasing as the flow progresses downstream until the wave-front reaches the Paraopeba River $43.5\,min$ after the dam collapse.

The predicted temporal evolution of the cross-section averaged flow depth and the total volume discharge (m^3/s) at the stockpile area (CS-1), the railway bridge (CS-2) and the Alberto Flores road (CS-3) are plotted in Figure 3.53. For cross-section CS-1, the discharge shows a peak of $38000\,m^3/s$ with an average mud depth of $7.5\,m$ at $t = 2.5\,min$. However, the flow has reduced its velocity considerably $10\,min$ after the dam failure and the deposited mud depth along this cross-section is lower than $0.2\,m$. In this zone just downstream the dam-toe, the simulation predicts that the mud wave erodes the original bed and gains mass and momentum during the first stages of the flow. The predicted increment of the volume involved in the flow is near 56% of the original mass due to entrainment from the erodible bed. Hence, when the flow reaches cross-section CS-2, the average flow

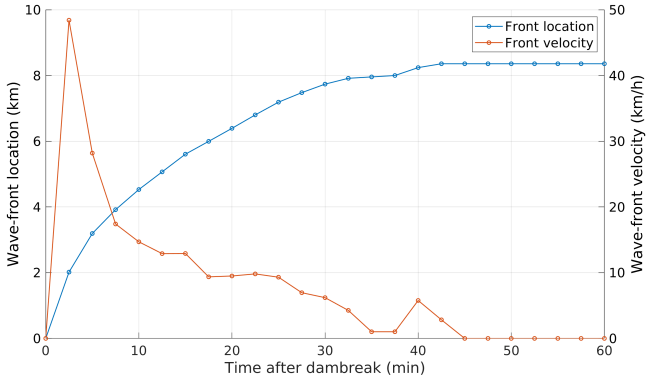

Figure 3.52: Real-scale case MF4 – Temporal evolution of the wave-front until the mud flow reached the Paraopeba River.

depth is near $12\,m$ although the discharge shows a lower peak ($14000\,m^3/s$) at $t = 5\,min$, caused by the reduction of the flow velocity. In this cross-section CS-2, the movement of the mud is practically stopped $50\,min$ after the dam failure. Nevertheless, the predicted temporal evolution of the flow at cross-section CS-3 shows a more progressive depth increment with time and a much lower discharge, needing more than $2\,hours$ after the dam failure before the mud is totally stopped.

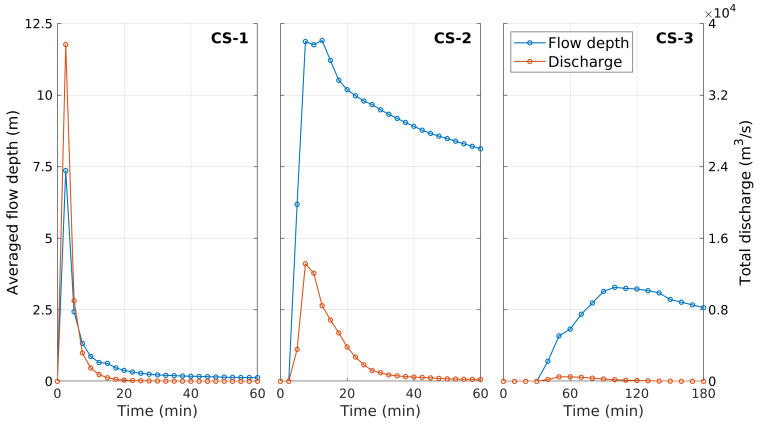

Figure 3.53: Real-scale case MF4 – Temporal evolution of the cross-section averaged flow depth and the total volume discharge at the stockpile area (CS-1), the railway bridge (CS-2) and the Alberto Flores road (CS-3).

Figure 3.54 shows the predicted mud density distribution (top) and iron solid phase volumetric concentration (bottom) for $t = 60\,min$ after the dam collapse. Generally, the flow density remains approximately constant and higher than $2100\,kg/m^3$ for the first stages of the flow. Then, the density progressively reduces as the flow moves downstream, especially at the upstream region and at the boundaries of the area affected by mud, where deposition of the solid phases dominates due to the lower velocities. In the center of the channel at the downstream region, where a slight movement of the flow continues even at $t = 60\,min$, the density shows important variations with respect to the original mud density. Once the flow reaches the Paraopeba River, the mud starts to mix with the "clear water" of the Paraopeba River and the flow density decreases abruptly along the mixing

interfaces. Spatial differences in the solid concentration are more marked for the iron phase, since it is more affected by deposition due to its higher density. Therefore, the iron volumetric concentration in the flow decreases more rapidly than the mineral solid phases or the mixture bulk density in the low velocity regions.

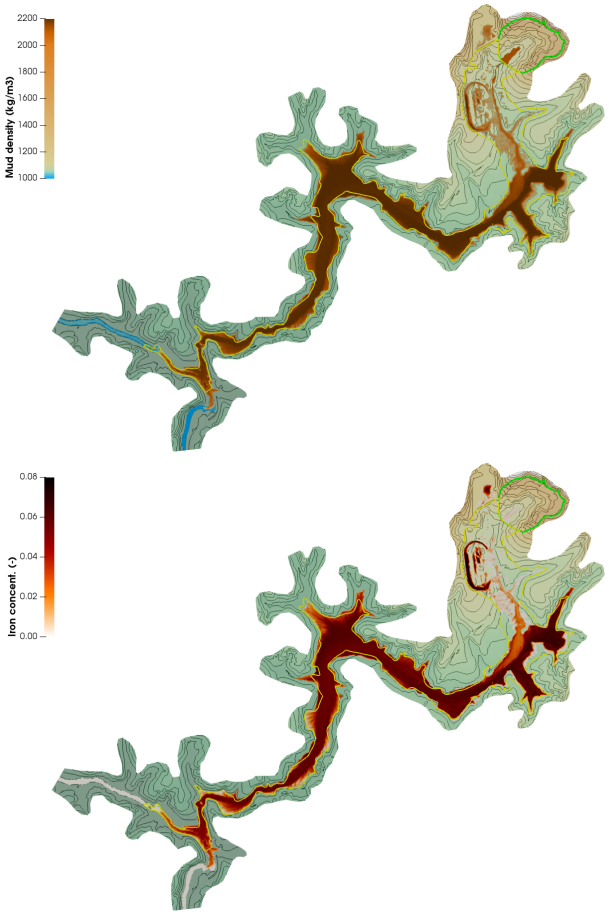

Figure 3.54: Real-scale case MF4 – Mud density (top) and iron volumetric concentration (left) for $t = 60\,min$ after the dam collapse.

The most important available observation during the real disaster is the arrival of the mud wave to the Paraopeba River. Herein we compare some observed data with the numerical results obtained by the model. At the Alberto Flores road (CS-3), the height of the mud once the flow stopped was estimated between 4-5 meters from published photographies. Figure 3.55–top shows the computed bed and flow free surface profiles at CS-3 for $t = 3\,hours$. The maximum mud depth is $4.9\,m$ and agrees with the observed data. Furthermore, the Alberto Flores Gauge Station in the Paraopeba River, upstream the mud-river confluence, also offers interesting data for comparison. This gauge station continuously recorded the free surface level each $15\,min$. During the real event, the mud flowing into the river created a "dam" in the confluence region, which temporally increased the free surface level in the Paraopeba River upstream the confluence region until the water reached the maximum elevation of the "dam" and started to flow over the mud. The observed temporal variation curve of the free surface level at the Alberto Flores Gauge Station can not be compared directly

with the numerical results obtained for the control cross-section CS-4, because of the different storage capacity upstream the confluence between the simulation domain and the real river. However, two important conclusions can be extracted from the recorded data. First, the river free surface level at the gauge station started to increase $32 - 47\,min$ after the dam collapse, capturing the arrival interval of the mud flow to the river. Second, the maximum level registered by the free surface was $5.11\,m$ above the base regime level previous to the mud arrival, indicating the height of the mud "dam" at the confluence region. Figure 3.55–bottom depicts the predicted temporal evolution of the river water depth and discharge at the control cross-section CS-4. The model is able to capture the arrival time of the mud flow to the river ($43.5\,min$). Moreover, the maximum increment of the free surface level at CS-4 is $4.06\,m$, showing a reasonably agreement with the observed data.

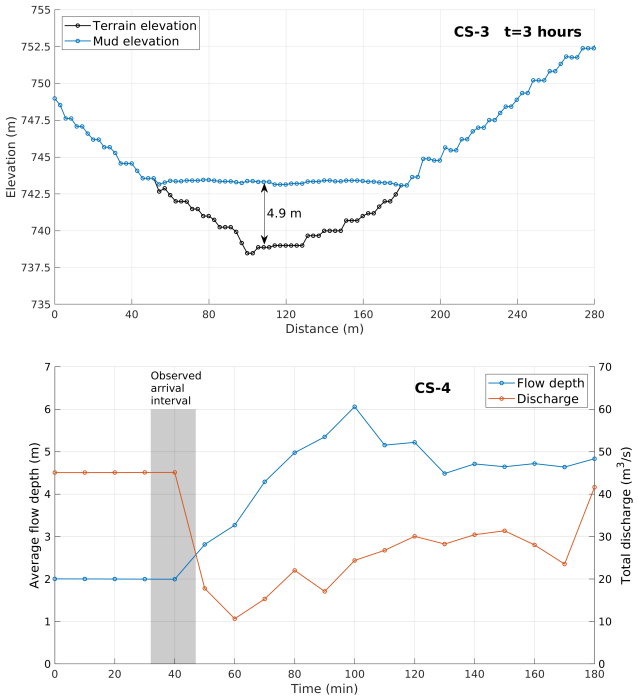

Figure 3.55: Real-scale case MF4 – Top: Bed and mud level profiles at CS-3 for $t = 3\,hours$. Bottom: Temporal evolution of the river water depth and discharge at CS-4.

Table 3.15 shows a comparison of the observed and computed data which can be extracted for this event. The model is able to correctly estimate the mud volume released and the area affected by mud. Furthermore, also the mud accumulation at the Alberto Flores road (CS-3) and the height of the mud "dam" at the confluence region showed a reasonable agreement, as well as the arrival time to the Paraopeba River (CS-4).

In order to assess the spatially distributed hazard level caused by the dam collapse, the maximum mud flow depth and velocity are continuously recorded at each computational cell during the whole simulation. Firstly, Figure 3.56–left shows that the maximum mud depth occurs downstream of the dam-toe and along the thalweg zone next to the stockpile area, with mud depth values higher than $35\,m$, but the flow depth is higher than $10\,m$ at some time during the simulation practically until the flow reaches the

	Observed	Computed
Released tailings volume (m^3)	$9.6 \cdot 10^6$	$9.747 \cdot 10^6$
Affected area (m^2)	$3.3 \cdot 10^6$	$3.604 \cdot 10^6$
Final mud elevation at CS-3 (m)	$\approx 4 - 5$	4.9
Arrival time to CS-4 (min)	$32 - 47$	43.5
Free surface increment at CS-4 (m)	5.11	4.06

Table 3.15: Real-scale case MF4 – Comparison of observed and computed data.

river. Secondly, the highest velocity is also computed downstream the dam-toe with values higher than $100\,km/h$ (see Figure 3.56–bottom). These results are also in agreement with the available observed data, since an approximated velocity of $120\,km/h$ for the wave-front was estimated at the first stage from the available videos of the dam collapse.

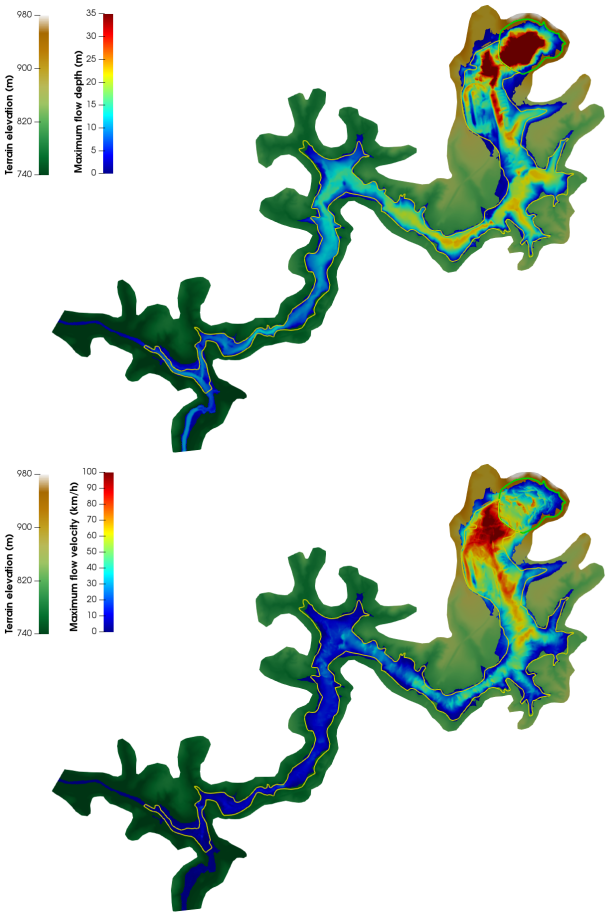

Figure 3.56: Real-scale case MF4 – Maximum mud depth (top) and velocity (bottom) during the $3\,hours$ simulated after the dam collapse.

Finally, Table 3.16 shows the computational time required for simulating the $3\,hours$ event using GPU-parallelization compared with the CPU-based version of the code, both including the file input-output time. Simulations are performed in a NVIDIA GeForce GTX 1080 Ti device with the GPU-based code, whereas the Intel(R) Core(TM) i7-3820 @3.60GHz is used for

the CPU-based algorithm. While the computational time for the CPU algorithm was almost 2.5 days, the GPU algorithm required less than $1\,hour$ to complete the simulation, representing a 61 speed-up. That means that for achieving the GPU-parallelized code performance with a CPU-based algorithm, a cluster with at least 76 CPU cores is required.

Comp. domain (m^2)	Number of cells	Comp. time GTX 1080 Ti $(hours)$	Comp. time i7-3820 $(hours)$	Speed-up cpu/gpu $(-)$
$10.396 \cdot 10^6$	529339	0.967	59.43	$\times 61.4$

Table 3.16: Real-scale case MF4 – Computational times with GPU-based and CPU-based algorithms.

3.6 In Closing

In this chapter, the system of 2D depth-averaged conservation laws (3.1)–(3.2a)–(3.2b)–(3.4)–(3.9) for geophysical surface flows of multi-grain water-sediment mixtures have been solved using a Finite Volume (FV) method supplemented with an upwind resolution of the intercell numerical fluxes based on the augmented Roe's approach. This approach involves the bed-pressure and non-Newtonian basal resistance momentum source terms into the numerical fluxes at the cell edges. The system of equations is formulated taking into account the net exchange flux between the underlying erodible bed layer and the mixture flow, which leads to the temporal evolution of the bed elevation. Furthermore, the effects of the shear-induced solid phase dilation on the pore-fluid pressure have also been included into the numerical fluxes solution. The resulting method demonstrated to be robust, accurate and efficient even when it is faced to complex large-scale and long-term debris flows.

The main novelties in this chapter are summarized as:

1. Two new strategies for the discretization of the 2D basal resistance force into local plane Riemann problem at the intercell edges are proposed here. These new methods, called respectively integral and differential approaches, allow to separate the cell-centered non-Newtonian shear stress force into upwind contributions to the local numerical fluxes at the cell edges ensuring the rotation invariant property of the integrated basal resistance term.

2. A new augmented Roe's Riemann solver for variable-density multi-grain flows is derived here. This solver allows the coupled upwind computation of the mass and momentum numerical fluxes including the density of the water-sediment mixture (Section 3.2.2). The addition of the bed-pressure momentum contribution into the local RP ensures the well-balanced character of the numerical solution in quiescent and steady states (Section 3.3.1).

3. Based on the previous results, explicit integration procedures for the upwind basal resistance contribution at the cell edges are derived.

These procedures allow not only to compute the explicit edge-value of the shear resistance contribution but also to limit its value in order to avoid numerical oscillations. Also, the correct edge-discretization of the basal resistance contribution ensures the non-dependence of the solution on the mesh topology (Section 3.3.3).

4. The effects of the shear-induced solid phase dilation on the pore-fluid pressure have been also included into the numerical model. Two important differences arrive here in comparison with previous models: first, the shear-induced segregation of the solid material within the flow is caused by a deviatoric contribution to the solid flux at the edges which ensures that the continuity equations of the system maintain their conservative character; second, it is possible to estimate a local value for the basal pore-pressure excess depending on the mixture packed state. Therefore, under the same flow conditions, dense packed mixtures are associated to a lower flow mobility whereas liquefied slurries are related to larger runout distances (Section 3.4).

Chapter 4

Two-dimensional models for suspended sediment transport

The main goals of this chapter are:

- To derive robust and efficient numerical schemes to solve the two-dimensional passive suspended sediment transport, including the mass exchange with the underlying movable bed.
- To assess the effects of the decoupling of the flow depth and density and the effects of the sediment concentration on the flow hydrodynamics.

4.1 Governing equations

The 2D model for suspended sediment transport over non-uniform erodible beds is derived from the system of depth-averaged conservation laws for variable-density mud/debris flows. Assuming equal velocity for the solid and liquid phases, i.e. neglecting the solid phase dilation, leads to the transport equation for the pth suspended sediment class (3.4) can be simplified as

$$\frac{\partial(h\phi_p)}{\partial t} + \frac{\partial}{\partial x}(hu\phi_p) + \frac{\partial}{\partial y}(hv\phi_p) = -(D_b - E_b)_p \tag{4.1}$$

being ϕ_p the depth-averaged volumetric concentration of the pth sediment class, h the vertical flow depth and (u, v) the components of the depth-averaged flow velocity vector $\mathbf{u}$. Furthermore, $(D_b - E_b)_p$ is the balance between the size-specific volumetric deposition and entrainment rates between the flow and the bed layer for the pth suspended sediment class, $D_{b,p}$ and $E_{b,p}$ respectively. Imposing a common solid density ρ_s for all the sediment classes being transported in the flow column, the bulk sediment-water density can be expressed as

$$\rho = \rho_w(1 - \phi_0) + \rho_s\phi_0 \tag{4.2}$$

where ρ_w denotes the water density and $\phi_0 = \sum_{p=1}^{N} \phi_p$ is the bulk solid concentration in the flow column.

Using (4.1) and (4.2) allows to extract the bulk solid-liquid density ρ from conserved variables and convective fluxes on the left hand side of

the conservation laws (3.1)–(3.2a)–(3.2b). Therefore, the resulting continuity equation for the flow volume reads

$$\frac{\partial h}{\partial t} + \frac{\partial}{\partial x}(hu) + \frac{\partial}{\partial y}(hv) = -\frac{\sum_{p=1}^{N}(D_b - E_b)_p}{1-\xi} \tag{4.3}$$

being ξ the bulk porosity of the non-uniform bed layer. The linear momentum conservation equations along the $x-$ and $y-$ coordinates can be expressed as

$$\begin{aligned}\frac{\partial(hu)}{\partial t} + \frac{\partial}{\partial x}(hu^2 + \frac{1}{2}gh^2) + \frac{\partial}{\partial y}(huv) = -gh\frac{\partial z_b}{\partial x} - \frac{\tau_{bx}}{\rho} \\ - \frac{1}{2}g\frac{h^2}{\rho}\frac{\partial \rho}{\partial x} - u\frac{\rho-\rho_b}{\rho}\frac{\sum_{p=1}^{N}(D_b - E_b)_p}{1-\xi}\end{aligned} \tag{4.4a}$$

$$\begin{aligned}\frac{\partial(hv)}{\partial t} + \frac{\partial}{\partial x}(huv) + \frac{\partial}{\partial y}(hv^2 + \frac{1}{2}gh^2) = -gh\frac{\partial z_b}{\partial y} - \frac{\tau_{by}}{\rho} \\ - \frac{1}{2}g\frac{h^2}{\rho}\frac{\partial \rho}{\partial y} - v\frac{\rho-\rho_b}{\rho}\frac{\sum_{p=1}^{N}(D_b - E_b)_p}{1-\xi}\end{aligned} \tag{4.4b}$$

being g the gravitational acceleration, z_b the bed layer elevation, $(\tau_{bx},\ \tau_{by})$ the components of the depth-averaged basal resistance vector $\boldsymbol{\tau_b}$ and $\rho_b = \rho_w\xi + \rho_s(1-\xi)$ the bulk density of the fully-saturated non-uniform bed layer. Note that here, the projection of the gravity force along the vertical direction is adopted under the hypothesis of small normal-bed angles.

Note that the decoupling of the flow depth h and density ρ causes the appearance of two additional terms on the right hand side of the momentum equations (4.4):

- The first one of these new momentum source terms accounts for effects of the bulk density gradients $\nabla\rho$ on the water-solid mixture momentum.
- The second term assumes that the entrainment/deposition of material from/to the bed layer also involves a momentum exchange between the flow and the underlying bed stratum. As $(\rho-\rho_b)/\rho < 0$ since the solid concentration in the flow is always lower than the deposition package in the bed layer, positive bulk exchange rates (net deposition when $\sum_{p=1}^{N}(D_b - E_b)_p > 0$) lead to an increment of the flow momentum. On the other hand, negative bulk exchange rates (net entrainment if $\sum_{p=1}^{N}(D_b - E_b)_p < 0$) involves a momentum reduction in the movement.

The evolution equation for the non-uniform bed layer elevation reads

$$\frac{\partial z_b}{\partial t} = \frac{\sum_{p=1}^{N}(D_b - E_b)_p}{1-\xi} \tag{4.5}$$

Additionally, some closures are required here to complete the system. The bed porosity ξ is estimated here using the Wu relation for non-uniform deposits [144]

$$\xi = 0.13 + 0.21 \left(0.002 + 10^3 \sum_{p=1}^{N} F_{b,p}\, d_{s,p}\right)^{-0.21} \tag{4.6}$$

where $d_{s,p}$ is the characterisctic diameter of the pth sediment class in meters and $F_{b,p}$ denotes the fraction of the pth sediment class in the bed layer, which is considered constant in time and space with $\sum_{p=1}^{N} F_{b,p} = 1$.

In order to enable quantitative comparison with the vdMD model (reported in the previous Chapter 3), the specific deposition $D_{b,p}$ and erosion $E_{b,p}$ rates for the pth sediment class are formulated here as

$$\begin{aligned} D_{b,p} &= \alpha_p\, \omega_{s,p}\, \phi_p (1-\phi_0)^4 \\ E_{b,p} &= \alpha_p\, \omega_{s,p}\, F_{b,p}\, \frac{|\mathbf{q}^*_{\mathbf{s,p}}|}{h|\mathbf{u}|} \end{aligned} \tag{4.7}$$

where α_p is an empirical parameter representing the difference between the near-bed concentration and the depth-averaged concentration for the pth solid phase and $|\mathbf{q}^*_{\mathbf{s,p}}|$ accounts for the modulus of the specific solid transport throughout the mixture column in capacity regime. For the sake of simplicity, $\alpha_p = 1$ is adopted in this thesis. However, it is worth mentioning that, contrarily to mud/debris flows, other environmental water flows usually show a marked variation of the sediment concentration along the flow column. Hence, α_p might be calibrated for realistic applications depending on the features of the case. The term $\omega_{s,p}$ denotes the specific settling velocity of the sediment particles in clear water, computed here using the Zhang & Xie [151] formula (3.13).

The specific capacity solid discharge $|\mathbf{q}^*_{\mathbf{s,p}}|$ is calculated using the Wu [144] formula for suspended sediment transport and reads

$$\frac{|\mathbf{q}^*_{\mathbf{s,p}}|}{\beta_T \sqrt{(\rho_s/\rho_w) g d^3_{s,p}}} = 2.62 \cdot 10^{-5} \left[\left(\frac{\theta_p}{\theta_{c,p}} - 1\right) \frac{|\mathbf{u}|}{\omega_{s,p}}\right]^{1.74} \tag{4.8}$$

being $n_p = 1/21\, d_{s,p}^{1/6}$ the Manning roughness parameter corresponding to grain resistance of the pth class, $\theta_{c,p}$ the critical Shields stress for the incipient motion of the pth sediment class which must include the hiding/exposure mechanism in non-uniform beds [32], $\theta_p = |\boldsymbol{\tau_b}|/[(\rho_s - \rho_w) g d_{s,p}]$ the specific Shields stress corresponding to the turbulent basal resistance and β_T a modification coefficient which is considered equal for all the sediment classes.

For suspended sediment transport in natural water bodies, the components of the shear resistance at the bed surface $\boldsymbol{\tau_b} = (\tau_{bx}, \tau_{by})$ are commonly estimated using the quadratic pure turbulent relation in Table 2.1, repeated here as

$$\begin{aligned} \tau_{bx} &= \rho g h C_f |\mathbf{u}| u \\ \tau_{by} &= \rho g h C_f |\mathbf{u}| v \end{aligned} \tag{4.9}$$

being $C_f = n_b^2\, h^{-4/3}$ a friction coefficient and n_b the bulk Manning's roughness parameter.

The resulting system is composed by the volume (4.3) and momentum (4.4) conservation equations for the flow layer, supplemented with the transport equation of the N sediment classes suspended in the flow (4.1) and the bed level evolution equation (4.5). The equations forming the system can be rewritten in vector form as

$$\frac{\partial \mathbf{U}}{\partial t} + \nabla \cdot \mathbf{E}(\mathbf{U}) = \mathbf{S_b}(\mathbf{U}) + \mathbf{S_\tau}(\mathbf{U}) + \mathbf{S_\rho}(\mathbf{U}) + \mathbf{E_b}(\mathbf{U}) \tag{4.10}$$

where $\mathbf{U}$ is the vector of conserved variables and $\mathbf{E}(\mathbf{U}) = \big(\mathbf{F}(\mathbf{U}), \mathbf{G}(\mathbf{U})\big)$ are the convective fluxes along the $\mathbf{X} = (x, y)$ horizontal coordinates respectively, expressed as

$$\mathbf{U} = \left(\; h,\; hu,\; hv,\; h\phi_1, \ldots, h\phi_N,\; z_b \; \right)^T \tag{4.11}$$

$$\mathbf{F}(\mathbf{U}) = \begin{pmatrix} hu \\ hu^2 + \frac{1}{2}gh^2 \\ huv \\ hu\,\phi_1 \\ \vdots \\ hu\,\phi_N \\ 0 \end{pmatrix} \qquad \mathbf{G}(\mathbf{U}) = \begin{pmatrix} hv \\ huv \\ hv^2 + \frac{1}{2}gh^2 \\ hv\,\phi_1 \\ \vdots \\ hv\,\phi_N \\ 0 \end{pmatrix} \tag{4.12}$$

The vector $\mathbf{S_b}(\mathbf{U})$ accounts for the momentum source term associated to the variation of the pressure force on the bed interface, whereas $\mathbf{S}_\tau(\mathbf{U})$ is the momentum dissipation due to the basal resistance.

$$\mathbf{S_b}(\mathbf{U}) = \begin{pmatrix} 0 \\ -gh\frac{\partial z_b}{\partial x} \\ -gh\frac{\partial z_b}{\partial y} \\ 0 \\ \vdots \\ 0 \\ 0 \end{pmatrix} \qquad \mathbf{S_\tau}(\mathbf{U}) = \begin{pmatrix} 0 \\ -ghC_f|\mathbf{u}|u \\ -ghC_f|\mathbf{u}|v \\ 0 \\ \vdots \\ 0 \\ 0 \end{pmatrix} \tag{4.13}$$

The momentum contribution generated by the artificial density decoupling is contained in the source vector $\mathbf{S_\rho}(\mathbf{U})$

$$\mathbf{S_\rho}(\mathbf{U}) = \begin{pmatrix} 0 \\ -\frac{1}{2}g\frac{h^2}{\rho}\frac{\partial \rho}{\partial x} \\ -\frac{1}{2}g\frac{h^2}{\rho}\frac{\partial \rho}{\partial x} \\ 0 \\ \vdots \\ 0 \\ 0 \end{pmatrix} \tag{4.14}$$

Finally, the source term $\mathbf{E_b}(\mathbf{U})$ accounts for the bulk mass and momentum exchange between the water-sediment flow and the bed layer, and can be expressed as

$$\mathbf{E_b}(\mathbf{U}) = \begin{pmatrix} -\frac{\sum_{p=1}^{N}(D_b - E_b)_p}{1-\xi} \\ u\frac{\rho-\rho_b}{\rho}\frac{\sum_{p=1}^{N}(D_b - E_b)_p}{1-\xi} \\ v\frac{\rho-\rho_b}{\rho}\frac{\sum_{p=1}^{N}(D_b - E_b)_p}{1-\xi} \\ (D_b - E_b)_1 \\ \vdots \\ (D_b - E_b)_N \\ \frac{\sum_{p=1}^{N}(D_b - E_b)_p}{1-\xi} \end{pmatrix} \tag{4.15}$$

Normally, 2D models dealing with suspended sediment transport only account for the density gradients when high solid concentration are expected, as in case of debris avalanches or muddy slurries. Some of these variable-density models include the bulk density into the conservative variables and fluxes, as we did in the vdMD model (see previous Chapter 3), but the common practice is to artificially decouple the flow depth h from the bulk density ρ and to treat the density gradients as specific momentum source terms, even for high sediment concentrations [12, 20, 42, 79, 112].

Two different models are proposed here for passive suspended sediment transport:

- **vdPST** (variable-density passive suspended transport) model: It solves the complete system 4.10, including the density-gradient momentum source term $\mathbf{S_\rho}(\mathbf{U})$ (4.14).
- **udPST** (uniform-density passive suspended transport) model: It solves the system 4.10 but neglecting the density-gradient momentum source term $\mathbf{S_\rho}(\mathbf{U})$ (4.14).

4.2 Finite Volume method for passive suspended transport

System (4.10) is time dependent, non linear and contains source terms. Under the hypothesis of dominant advection it can be classified as belonging to the family of hyperbolic systems. In order to obtain a numerical solution using a Finite Volume (FV) technique for the complete set of conserved variables, the spatial domain is divided in computational cells using a mesh fixed in time and system (4.10) is integrated in each cell using the Gauss theorem. Assuming a piecewise uniform representation of the conserved variables $\mathbf{U}$ at each computational cell Ω_i for the time $t = t^n$, the integrated system of equations in the global framework $\mathbf{X} = (x, y)$ can be expressed

for the i cell as

$$\frac{\mathrm{d}}{\mathrm{d}t}\int_{\Omega_i}\mathbf{U}\,\mathrm{d}\Omega+\sum_{k=1}^{\mathrm{NE}}(\mathbf{E}\cdot\mathbf{n})_k\,l_k=\int_{\Omega_i}\mathbf{S_b}(\mathbf{U})\,\mathrm{d}\Omega+\int_{\Omega_i}\mathbf{S}_{\boldsymbol{\tau}}(\mathbf{U})\,\mathrm{d}\Omega+\int_{\Omega_i}\mathbf{S}_{\boldsymbol{\rho}}(\mathbf{U})\,\mathrm{d}\Omega+\int_{\Omega_i}\mathbf{E_b}(\mathbf{U})\,\mathrm{d}\Omega \tag{4.16}$$

where the surface integral in the second term has been already replaced by a sum over the cell edges, being NE the number of edges for the i cell. The term $(\mathbf{E}\cdot\mathbf{n})_k$ denotes the value of the normal flux through the kth cell edge, $\mathbf{n}=(n_x,\,n_y)$ the outward unit normal vector to the edge and l_k the length of the edge.

The local framework for each kth cell edge is defined as $\hat{\mathbf{X}}=\mathbf{R}_k\mathbf{X}=(\hat{x},\hat{y})$, where the rotation matrix $\mathbf{R}_k$ is

$$\mathbf{R}_k=\begin{pmatrix}1&0&0&0&\dots&0&0\\0&n_x&n_y&0&\dots&0&0\\0&-n_y&n_x&0&\dots&0&0\\0&0&0&1&\dots&0&0\\\vdots&\vdots&\vdots&\vdots&\ddots&\vdots&\vdots\\0&0&0&0&\dots&1&0\\0&0&0&0&\dots&0&1\end{pmatrix}_k \tag{4.17}$$

As used before in Section 3.2, the rotation invariance property (3.26) of the convective flux matrix $\mathbf{E}(\mathbf{U})$ can be used to rewrite the normal fluxes throughout the edge [44, 138] as

$$(\mathbf{E}\cdot\mathbf{n})_k=\left[\mathbf{F}(\mathbf{U})\,n_x+\mathbf{G}(\mathbf{U})\,n_y\right]_k=\mathbf{R}_k^{-1}\,\mathbf{F}(\mathbf{R}_k\mathbf{U}) \tag{4.18}$$

being $\mathbf{R}_k^{-1}$ the inverse of the rotation matrix. Hence the left hand side of (4.16) is expressed in the local framework $\hat{\mathbf{X}}$ of the kth cell edge as

$$\frac{\mathrm{d}}{\mathrm{d}t}\int_{\Omega_i}\mathbf{R}_k\mathbf{U}\,\mathrm{d}\Omega+\sum_{k=1}^{\mathrm{NE}}\mathbf{F}(\mathbf{R}_k\mathbf{U})\,l_k \tag{4.19}$$

with the set of local conserved variables $\hat{\mathbf{U}}\equiv\mathbf{R}_k\mathbf{U}$

$$\hat{\mathbf{U}}\equiv\mathbf{R}_k\mathbf{U}=\left(\;h,\;h\hat{u},\;h\hat{v},\;h\phi_1,\dots,h\phi_N,\;z_b\;\right)^T \tag{4.20}$$

and the local homogeneous convective fluxes $\mathbf{F}(\hat{\mathbf{U}})_k\equiv\mathbf{F}(\mathbf{R}_k\mathbf{U})$

$$\mathbf{F}(\hat{\mathbf{U}})_k\equiv\mathbf{F}(\mathbf{R}_k\mathbf{U})=\begin{pmatrix}h\hat{u}\\h\hat{u}^2+\frac{1}{2}gh^2\\h\hat{u}\hat{v}\\h\hat{u}\,\phi_1\\\vdots\\h\hat{u}\,\phi_N\\0\end{pmatrix} \tag{4.21}$$

being $\hat{u} = un_x + vn_y$ and $\hat{v} = -un_y + vn_x$ the normal and tangential flow velocities respectively.

The bed-pressure vector $\mathbf{S_b}(\mathbf{U})$ on the right hand side of (4.16) is unconditionally invariant under rotation [21] and can also be expressed within the local framework $\hat{\mathbf{X}} = (\hat{x}, \hat{y})$ using the spatial discretization

$$\int_{\Omega_i} \mathbf{S_b}(\mathbf{U})\, \mathrm{d}\Omega = \sum_{k=1}^{\mathrm{NE}} \mathbf{R}_k^{-1}\, \mathbf{H}(\hat{\mathbf{U}})_k\, l_k \tag{4.22}$$

where

$$\mathbf{H}(\hat{\mathbf{U}})_k = \begin{pmatrix} 0 \\ -gh\,\Delta z_b \\ 0 \\ 0 \\ \vdots \\ 0 \\ 0 \end{pmatrix}_k \tag{4.23}$$

denotes the bed-pressure flux vector throughout the kth cell edge [103]. This allows to express the bed-pressure momentum source vector in the local framework $\hat{\mathbf{S}}_\mathbf{b}$ as

$$\hat{\mathbf{S}}_\mathbf{b} = \frac{\partial \mathbf{H}(\hat{\mathbf{U}})_k}{\partial \hat{x}} = \begin{pmatrix} 0 \\ -gh\,\dfrac{\partial z_b}{\partial \hat{x}} \\ 0 \\ 0 \\ \vdots \\ 0 \\ 0 \end{pmatrix}_k \tag{4.24}$$

The basal resistance contribution on the right hand side of (4.16) is discretized using the differential approach (see Section 3.2.1) as

$$\int_{\Omega_i} \mathbf{S}_{\boldsymbol{\tau}}(\mathbf{U})\, \mathrm{d}\Omega = \sum_{k=1}^{\mathrm{NE}} \mathbf{R}_k^{-1}\, \mathbf{T}(\hat{\mathbf{U}})_k\, l_k \tag{4.25}$$

where $\mathbf{T}(\hat{\mathbf{U}})_k$ is the integrated basal resistance throughout the kth cell edge, expressed in the local framework

$$\mathbf{T}(\hat{\mathbf{U}})_k = \begin{pmatrix} 0 \\ -ghC_f|\mathbf{u}|\,(\hat{u}\Delta\hat{x} + \hat{v}\Delta\hat{y}) \\ 0 \\ 0 \\ \vdots \\ 0 \\ 0 \end{pmatrix}_k \tag{4.26}$$

being $(\Delta\hat{x}, \Delta\hat{y})$ the integration distances along the local $\hat{x}-$ and $\hat{y}-$coordinates respectively. Hence, the basal resistance vector in the local

framework $\hat{\mathbf{S}}_{\boldsymbol{\tau}}$ reads

$$\hat{\mathbf{S}}_{\boldsymbol{\tau}} = \frac{\partial \mathbf{T}(\hat{\mathbf{U}})_k}{\partial \hat{x}} = \begin{pmatrix} 0 \\ -ghC_f|\mathbf{u}|\,\hat{u} \\ 0 \\ 0 \\ \vdots \\ 0 \\ 0 \end{pmatrix}_k \tag{4.27}$$

Similarly to the bed-pressure source term, the density gradient vector $\mathbf{S}_{\boldsymbol{\rho}}(\mathbf{U})$, also on the right hand side of (4.16), is unconditionally invariant under rotation and hence it can be edge-discretized as

$$\int_{\Omega_i} \mathbf{S}_{\boldsymbol{\rho}}(\mathbf{U})\,\mathrm{d}\Omega = \sum_{k=1}^{\mathrm{NE}} \mathbf{R}_k^{-\mathbf{1}}\,\mathbf{W}(\hat{\mathbf{U}})_k\,l_k \tag{4.28}$$

where $\mathbf{W}(\hat{\mathbf{U}})_k$ is defined as

$$\mathbf{W}(\hat{\mathbf{U}})_k = \begin{pmatrix} 0 \\ -\frac{1}{2}g\frac{h^2}{\rho}\,\Delta\rho \\ 0 \\ 0 \\ \vdots \\ 0 \\ 0 \end{pmatrix}_k \tag{4.29}$$

and denotes the density-gradient fluxes at the kth cell edge expressed in the local framework $\hat{\mathbf{X}} = (\hat{x}, \hat{y})$. This allows to express the density-gradient momentum source vector in the local framework $\hat{\mathbf{S}}_\rho$ as

$$\hat{\mathbf{S}}_\rho = \frac{\partial \mathbf{W}(\hat{\mathbf{U}})_k}{\partial \hat{x}} = \begin{pmatrix} 0 \\ -\frac{1}{2}g\frac{h^2}{\rho}\,\frac{\partial \rho}{\partial \hat{x}} \\ 0 \\ 0 \\ \vdots \\ 0 \\ 0 \end{pmatrix}_k \tag{4.30}$$

Using (4.19), (4.22), (4.25) and (4.28), both sides of (4.16) can be combined for each kth cell edge. Excluding the exchange source term $\mathbf{E}_{\mathbf{b}}(\mathbf{U})$, the locally-integrated system is expressed as

$$\begin{aligned} \frac{\mathrm{d}}{\mathrm{d}t}\int_{\Omega_i} \mathbf{R}_k\mathbf{U}\,\mathrm{d}\Omega + \sum_{k=1}^{\mathrm{NE}} \mathbf{F}(\hat{\mathbf{U}})_k\,l_k = \\ \sum_{k=1}^{\mathrm{NE}} \mathbf{H}(\hat{\mathbf{U}})_k\,l_k + \sum_{k=1}^{\mathrm{NE}} \mathbf{T}(\hat{\mathbf{U}})_k\,l_k + \sum_{k=1}^{\mathrm{NE}} \mathbf{W}(\hat{\mathbf{U}})_k\,l_k \end{aligned} \tag{4.31}$$

This type of formulation (4.31) is oriented to define an augmented numerical flux $\mathbf{F}_k^{\downarrow -}$ for the i cell at the kth edge which incorporates the integrated bed-pressure $\mathbf{H}(\hat{\mathbf{U}})_k$, basal resistance $\mathbf{T}(\hat{\mathbf{U}})_k$ and density-gradient $\mathbf{W}(\hat{\mathbf{U}})_k$ contributions into the homogeneous fluxes $\mathbf{F}(\hat{\mathbf{U}})_k$ at the cell edge.

$$\mathbf{F}_k^{\downarrow} = \Big[\mathbf{F}(\hat{\mathbf{U}}) - \mathbf{H}(\hat{\mathbf{U}}) - \mathbf{T}(\hat{\mathbf{U}}) - \mathbf{W}(\hat{\mathbf{U}})\Big]_k \tag{4.32}$$

It is worth mentioning that the addition of the source term edge-contributions to the homogeneous fluxes leads to the loss of the conservative character of the momentum flux but ensures the well-balance property for steady states [103, 104].

Furthermore, the net exchange flux term $\mathbf{E_b}(\mathbf{U})$ on the right hand side of (4.16) is discretized in space as a cell-centered term

$$\int_{\Omega_i} \mathbf{E_b}(\mathbf{U})\, d\Omega \approx A_i\, \mathbf{E_b}(\mathbf{U}_i) = \boldsymbol{\mathcal{B}}_i \tag{4.33}$$

where A_i is the discrete cell area.

Restoring the augmented flux (4.32) to the global framework $\mathbf{X} = (x, y)$ and including the vertical exchange term (4.33), the integrated system (4.16) is rewritten as

$$\frac{\mathrm{d}}{\mathrm{d}t}\int_{\Omega_i} \mathbf{U}\, \mathrm{d}\Omega = -\sum_{k=1}^{\mathrm{NE}} \mathbf{R}_k^{-\mathbf{1}}\, \mathbf{F}_k^{\downarrow}\, l_k + \boldsymbol{\mathcal{B}}_i \tag{4.34}$$

Assuming a piecewise uniform representation of the conserved variables $\mathbf{U}$ at the i cell for the time $t = t^n$

$$\mathbf{U}_i^n = \frac{1}{A_i}\int_{\Omega_i} \mathbf{U}(x, y, t^n)\, \mathrm{d}\Omega \tag{4.35}$$

and, using an explicit temporal integration for the mass and momentum source terms, the updating formulation for the conserved variables $\mathbf{U}$ at the each cell is expresed as

$$\mathbf{U}_i^{n+1} = \mathbf{U}_i^n - \frac{\Delta t}{A_i}\sum_{k=1}^{\mathrm{NE}} \mathbf{R}_k^{-\mathbf{1}}\, \mathbf{F}_k^{\downarrow}\, l_k + \frac{\Delta t}{A_i}\,\boldsymbol{\mathcal{B}}_i^n \tag{4.36}$$

where $\Delta t = t^{n+1} - t^n$ is the time step.

Hence the resolution procedure needs to compute the numerical fluxes $\mathbf{F}_k^{\downarrow}$ at the cell edges ensuring (4.32).

It is worth mentioning that in this decoupled formulation, the bulk density ρ (4.2) does not participated in the conservative part of the hydrodynamic equations. Hence a reduced set of conserved variables $\hat{\mathbf{U}}'$ including only the hydrodynamic component of the system can be defined as

$$\hat{\mathbf{U}}' = \big(\ h,\ h\hat{u},\ h\hat{v}\ \big)^T \tag{4.37}$$

and the corresponding hydrodynamical convective fluxes $\mathbf{F}'(\hat{\mathbf{U}}')_k$ are

$$\mathbf{F}'(\hat{\mathbf{U}}')_k = \begin{pmatrix} h\hat{u} \\ h\hat{u}^2 + \frac{1}{2}gh^2 \\ h\hat{u}\hat{v} \end{pmatrix} \tag{4.38}$$

where the superscript $(\cdot)'$ indicates the first three equations of the locally-integrated system (4.31), i.e. $(\cdot)' \equiv (\cdot)^{\{1,2,3\}}$.

Hence, the evolution of the flow features (h, u, v) and the solid content in the water column are totally decoupled. The sediment concentration works as a passive solute transport which does not affect the flow movement. Therefore, in order to compute the numerical fluxes at the cell edges, the Reduced Godunov method proposed by Murillo *et al.* [105] is implemented here forthe suspended sediment transport problem. Using this method, the hydrodynamical intercell fluxes $\mathbf{F}_k^{\downarrow\{1,2,3\}}$ for the kth cell edge are upwind computed by solving the local plane Riemann problem (RP) associated to the hydrodynamical variables $\mathbf{U}'$ (4.37), expressed as

$$\begin{gathered}\frac{\partial \hat{\mathbf{U}}'}{\partial t} + \frac{\partial \mathbf{F}'(\hat{\mathbf{U}}')}{\partial \hat{x}} = \hat{\mathbf{S}}'_{\mathbf{b}} + \hat{\mathbf{S}}'_{\boldsymbol{\tau}} + \hat{\mathbf{S}}'_{\boldsymbol{\rho}} \\ \hat{\mathbf{U}}(\hat{x}, 0) = \begin{cases} \hat{\mathbf{U}}'_i = \mathbf{R}_k(\mathbf{U}')_i^n & \text{if} \quad \hat{x} < 0 \\ \hat{\mathbf{U}}'_j = \mathbf{R}_k(\mathbf{U}')_j^n & \text{if} \quad \hat{x} > 0 \end{cases}\end{gathered} \tag{4.39}$$

where i and j denote the left and right neighbouring cells to the kth edge respectively. Then, the numerical fluxes for the passive solid transport of the N different sediment classes, $\mathbf{F}_k^{\downarrow\{3+1,\ldots,3+\mathrm{N}\}}$, are derived from the hydrodynamical intercell discharge. The last component of the numerical flux vector corresponding to the bed level intercell flux is set to $\mathbf{F}_k^{\downarrow\{3+\mathrm{N}+1\}} = 0$.

4.2.1 Reduced Riemann solver for passive suspended transport

The mass and momentum numerical fluxes in (4.36) for the hydrodynamical equations, referred to as $\mathbf{F}_k^{\downarrow\{1,2,3\}}$, are computed at each kth cell edge by approximating the solution of the local plane RP (4.39). From now on, as it is mentioned above, the superscript $(\cdot)'$ indicates the hydrodynamical components of the system , i.e. $(\cdot)' \equiv (\cdot)^{\{1,2,3\}}$. Following the Riemann weak-solution theory [103, 104], at each intercell edge the following constant-coefficients linear RP is defined

$$\begin{gathered}\frac{\partial \hat{\mathbf{U}}'}{\partial t} + \widetilde{\mathbf{J}}'_k \frac{\partial \hat{\mathbf{U}}'}{\partial \hat{x}} = (\widetilde{\mathbf{S}}'_{\mathbf{b}} + \widetilde{\mathbf{S}}'_{\boldsymbol{\tau}} + \widetilde{\mathbf{S}}'_{\boldsymbol{\rho}})_k \\ \hat{\mathbf{U}}'(\hat{x}, 0) = \begin{cases} \hat{\mathbf{U}}'_i = \mathbf{R}_k(\mathbf{U}')_i^n & \text{if} \quad \hat{x} < 0 \\ \hat{\mathbf{U}}'_j = \mathbf{R}_k(\mathbf{U}')_j^n & \text{if} \quad \hat{x} > 0 \end{cases}\end{gathered} \tag{4.40}$$

where $(\widetilde{\mathbf{S}}'_{\mathbf{b}})_k$ and $(\widetilde{\mathbf{S}}'_{\boldsymbol{\tau}})_k$ denote the edge-averaged bed-pressure and flow resistance momentum contributions, (4.24) and (4.27) respectively, and $(\widetilde{\mathbf{S}}'_{\boldsymbol{\rho}})_k$ accounts for the density-gradient momentum source. The matrix $\widetilde{\mathbf{J}}'_k = \mathbf{J}'_k(\hat{\mathbf{U}}'_i, \hat{\mathbf{U}}'_j)$ is the 3×3 constant coefficient Jacobian of the local hydrodynamical RP, defined as

$$\widetilde{\mathbf{J}}'_k = \begin{pmatrix} 0 & 1 & 0 \\ g\widetilde{h} - \widetilde{u}^2 & 2\widetilde{u} & 0 \\ -\widetilde{u}\widetilde{v} & \widetilde{v} & \widetilde{u} \end{pmatrix}_k \tag{4.41}$$

being the edge-averaged quantities defined as

$$\begin{aligned}\widetilde{h} &= \frac{h_i + h_j}{2} \\ \widetilde{u} &= \frac{\hat{u}_i\sqrt{h_i} + \hat{u}_j\sqrt{h_j}}{\sqrt{h_i} + \sqrt{h_j}} \\ \widetilde{v} &= \frac{\hat{v}_i\sqrt{h_i} + \hat{v}_j\sqrt{h_j}}{\sqrt{h_i} + \sqrt{h_j}}\end{aligned} \tag{4.42}$$

The three eigenvalues of $\widetilde{\mathbf{J}}'_k$ are

$$\widetilde{\lambda}'_{1,k} = (\widetilde{u} - \widetilde{c})_k < \widetilde{\lambda}'_{2,k} = \widetilde{u}_k < \widetilde{\lambda}'_{3,k} = (\widetilde{u} + \widetilde{c})_k \tag{4.43}$$

with $\widetilde{c}_k = \sqrt{g\widetilde{h}_k}$ the edge-averaged celerity of the surface waves. The basis matrix $\widetilde{\mathbf{P}}'_k$ is constructed with associated eigenvectors $\widetilde{\mathbf{e}}'_{m,k}$

$$\widetilde{\mathbf{P}}'_k = (\widetilde{\mathbf{e}}'_1, \widetilde{\mathbf{e}}'_2, \widetilde{\mathbf{e}}'_3)_k = \begin{pmatrix} 1 & 0 & 1 \\ \widetilde{\lambda}'_1 & 0 & \widetilde{\lambda}'_3 \\ \widetilde{v} & \widetilde{c} & \widetilde{v} \end{pmatrix}_k \tag{4.44}$$

The discrete gradients of the hydrodynamical conserved variables $\boldsymbol{\delta}\hat{\mathbf{U}}'_k$ are projected on the orthogonal basis of eigenvectors to obtain the wave strength vector, $\widetilde{\mathbf{A}}'_k$, as

$$\widetilde{\mathbf{A}}'_k = (\widetilde{\alpha}'_1, \ldots, \widetilde{\alpha}'_3)^T_k = \widetilde{\mathbf{P}}'^{-\mathbf{1}}_k \boldsymbol{\delta}\hat{\mathbf{U}}'_k \tag{4.45}$$

where the wave strengths $\widetilde{\alpha}'_m$ are

$$\widetilde{\mathbf{A}}'_k \equiv \begin{cases} \widetilde{\alpha}'_1 = \dfrac{\widetilde{c} - \widetilde{u}}{2\widetilde{c}}\,\delta(h) - \dfrac{1}{2\widetilde{c}}\,\delta(h\hat{u}) \\ \widetilde{\alpha}'_2 = \dfrac{-\widetilde{v}}{\widetilde{c}}\,\delta(h) + \dfrac{1}{\widetilde{c}}\,\delta(h\hat{v}) \\ \widetilde{\alpha}'_3 = \dfrac{\widetilde{c} + \widetilde{u}}{2\widetilde{c}}\,\delta(h) + \dfrac{1}{2\widetilde{c}}\,\delta(h\hat{u}) \end{cases} \tag{4.46}$$

The bed-pressure $\widetilde{\mathbf{H}}_k$ (4.23) and basal resistance $\widetilde{\mathbf{T}}_k$ (4.26) edge-contributions are also projected on the orthogonal basis of eigenvectors to obtain the source strength vector $\widetilde{\mathbf{B}}'_k$ as

$$\widetilde{\mathbf{B}}'_k = (\widetilde{\beta}'_1, \ldots, \widetilde{\beta}'_3)^T_k = \widetilde{\mathbf{P}}'^{-\mathbf{1}}_k \left(\widetilde{\mathbf{H}}_k + \widetilde{\mathbf{T}}_k\right) \tag{4.47}$$

with

$$\widetilde{\mathbf{B}}'_k \equiv \begin{cases} \widetilde{\beta}'_1 = -\dfrac{1}{2\widetilde{c}}\left(\widetilde{H}_k + \widetilde{T}_k\right) \\ \widetilde{\beta}'_2 = 0 \\ \widetilde{\beta}'_3 = \dfrac{1}{2\widetilde{c}}\left(\widetilde{H}_k + \widetilde{T}_k\right) \end{cases} \tag{4.48}$$

where $\widetilde{H}_k$ and $\widetilde{T}_k$ are suitable values of the integrated bed-pressure and resistance momentum contributions at the cell edge. They are computed

here following (3.89) and (3.125), respectively, as

$$\begin{aligned}\widetilde{H}_k &= -g\widetilde{h}_k(\Delta z_b)_k \\ \widetilde{T}_k &= -\mathrm{sgn}(F_n)_k \left(g\frac{n_b^2\sqrt{\widetilde{u}^2+\widetilde{v}^2}}{\widetilde{h}^{1/3}}\left(\widetilde{u}\Delta\hat{x}+\widetilde{v}\Delta\hat{y}\right)\right)_k\end{aligned} \tag{4.49}$$

being $\mathrm{sgn}(F_n)_k$ the sign of the frictionless normal discharge throughout the cell edge (see Section 3.3.3).

Furthermore, the density-gradient edge-contribution $\widetilde{\mathbf{W}}_k$ (4.29) is projected on the orthogonal basis of eigenvectors to obtain an additional source strength vector $\widetilde{\boldsymbol{\chi}}'_k$ as

$$\widetilde{\boldsymbol{\chi}}'_k = (\widetilde{\chi}'_1, \ldots, \widetilde{\chi}'_3)^T_k = \widetilde{\mathbf{P}}'^{-1}_k \widetilde{\mathbf{W}}_k \tag{4.50}$$

with

$$\widetilde{\boldsymbol{\chi}}'_k \equiv \begin{cases} \widetilde{\chi}'_1 = -\dfrac{1}{2\widetilde{c}}\widetilde{W}_k \\ \widetilde{\chi}'_2 = 0 \\ \widetilde{\chi}'_3 = \dfrac{1}{2\widetilde{c}}\widetilde{W}_k \end{cases} \tag{4.51}$$

where $\widetilde{W}_k$ is a suitable value of the integrated density-gradient momentum contributions at the cell edge, estimated as

$$\widetilde{W}_k = -\frac{1}{2}g\frac{\widetilde{h}_k^2}{\widetilde{\rho}_k}(\Delta\rho)_k \tag{4.52}$$

being $\widetilde{\rho}_k = (\rho_i + \rho_j)/2$ the averaged flow density at the cell edge, with $\rho_i = \rho_w + (\rho_s - \rho_w)\sum_{p=1}^{\mathrm{N}} \phi_{p,i}$ the value of the flow density at the i cell.

Therefore, the hydrodynamical fluxes on the left and right sides of the kth cell edge, $\mathbf{F}'^{\downarrow -}_k$ and $\mathbf{F}'^{\downarrow +}_k$ respectively, are computed as

$$\mathbf{F}'^{\downarrow -}_k = \mathbf{F}'(\hat{\mathbf{U}}'_i) + \sum_{m-}(\widetilde{\lambda}'_m\widetilde{\alpha}'_m\widetilde{\mathbf{e}}'_m)_k - \sum_{m-}(\widetilde{\beta}'_m\widetilde{\mathbf{e}}'_m)_k - \sum_{m-}(\widetilde{\chi}'_m\widetilde{\mathbf{e}}'_m)_k \tag{4.53a}$$

$$\mathbf{F}'^{\downarrow +}_k = \mathbf{F}'(\hat{\mathbf{U}}'_j) - \sum_{m+}(\widetilde{\lambda}'_m\widetilde{\alpha}'_m\widetilde{\mathbf{e}}'_m)_k + \sum_{m+}(\widetilde{\beta}'_m\widetilde{\mathbf{e}}'_m)_k + \sum_{m+}(\widetilde{\chi}'_m\widetilde{\mathbf{e}}'_m)_k \tag{4.53b}$$

where the subscript $m-$ and $m+$ under the sums indicate waves traveling inward and outward the i cell [90, 104].

The mass and momentum numerical fluxes in (4.36) for the hydrodynamical equations, referred to as $\mathbf{F}^{\downarrow\{1,2,3\}}_k$, are hence obtained using (4.53a) as

$$\mathbf{F}^{\downarrow\{1,2,3\}}_k = \mathbf{F}'^{\downarrow -}_k \tag{4.54}$$

Therefore, the first component of the hydrodynamical flux vector accounts for the flow volume transference normal to the cell edge, $\mathbf{F}^{\downarrow\{1\}}_k = (h\hat{u})^{\downarrow}_k$. The numerical solid flux at the kth edge for the pth suspended sediment class $\mathbf{F}^{\downarrow\{3+p\}}_k$ is computed as

$$\mathbf{F}^{\downarrow\{3+p\}}_k \equiv (h\hat{u}\phi_p)^{\downarrow}_k = \begin{cases} (h\hat{u})^{\downarrow}_k(\phi_p)^n_i & \text{if} \quad (h\hat{u})^{\downarrow}_k \geq 0 \\ (h\hat{u})^{\downarrow}_k(\phi_p)^n_j & \text{if} \quad (h\hat{u})^{\downarrow}_k < 0 \end{cases} \tag{4.55}$$

and the numerical flux for the bed level evolution equation is set to

$$\mathbf{F}_k^{\downarrow\{3+\mathrm{N}+1\}} = 0 \tag{4.56}$$

Finally, in order to ensure the stability of the explicitly computed numerical solution, the time step should be small enough to avoid the interaction of waves from neighbouring Riemann problems. The dynamical limitation of the time step at each k edge is addressed here assuming that the fastest wave celerity corresponds to the absolute maximum of the eigenvalues of $\widetilde{\mathbf{J}}_k$ (4.41) as

$$\Delta t_k = \frac{\min(A_i, A_j)}{l_k \left[\max(|\widetilde{\lambda}_1|, |\widetilde{\lambda}_3|)\right]_k} \tag{4.57}$$

and the global time step $\Delta t = t^{n+1} - t^n$ is limited using the Courant-Friedrichs-Lewy (CFL) condition

$$\Delta t = \mathrm{CFL} \min_k(\Delta t_k) \tag{4.58}$$

with $\mathrm{CFL} < 0.5$ for square orthogonal meshes and $\mathrm{CFL} < 1$ for the triangular mesh topology and 1D-mesh cases.

4.2.2 Numerical approaches for suspended transport

In this chapter we propose two strategies for dealing with these decoupled density gradients:

- **udPST model:** This approach does not take into account the momentum contribution of the density gradient $\mathbf{S}_{\boldsymbol{\rho}}(\mathbf{U})$ (4.14). This is the common practice in river and coast dynamics since it allows to use widespread numerical solvers for the shallow clear water system of equations without including important modifications in the numerical scheme. Therefore, the density-gradient source term $\mathbf{S}_{\boldsymbol{\rho}}(\mathbf{U})$ is neglected in the system of equation (4.10) and, using (4.53) and 4.54, the hydrodynamical intercell flux for this model are computed as

$$\mathbf{F}_k^{\downarrow\{1,2,3\}} = \mathbf{F}'(\hat{\mathbf{U}}'_i) + \sum_{m-}(\widetilde{\lambda}'_m \widetilde{\gamma}'_m \widetilde{\mathbf{e}}'_m)_k \tag{4.59}$$

  with $\widetilde{\gamma}'_m = \widetilde{\alpha}'_m - \widetilde{\beta}'_m/\widetilde{\lambda}'_m$ and the subscript $m-$ under the sums indicates waves traveling inward the i cell.

- **vdPST model:** It accounts for the decoupled momentum contribution of the density gradients $\mathbf{S}_{\boldsymbol{\rho}}(\mathbf{U})$ (4.14) into the system of equations (4.10). The source term $\mathbf{S}_{\boldsymbol{\rho}}(\mathbf{U})$ is projected onto the eigenstructure of the homogeneous Riemann problem at the intercell edges. Therefore, using (4.53) and (4.54), the hydrodynamical intercell fluxes for this model are computed as

$$\mathbf{F}_k^{\downarrow\{1,2,3\}} = \mathbf{F}'(\hat{\mathbf{U}}'_i) + \sum_{m-}(\widetilde{\lambda}'_m \widetilde{\gamma}'_m \widetilde{\mathbf{e}}'_m)_k - \sum_{m-}(\widetilde{\chi}'_m \widetilde{\mathbf{e}}'_m)_k \tag{4.60}$$

with $\widetilde{\gamma}'_m = \widetilde{\alpha}'_m - \widetilde{\beta}'_m/\widetilde{\lambda}'_m$, the strength $\widetilde{\chi}'_m$ accounting for the density-gradient momentum contribution (4.50) and the subscript $m-$ under the sums indicates waves traveling inward the i cell..

Regardless of the model selected for the hydrodynamical fluxes the intercell edges, $\mathbf{F}_k^{\downarrow\{1,2,3\}}$, the numerical sediment fluxes at the edges $\mathbf{F}_k^{\downarrow\{3+p\}}$ are computed using (4.55) and, hence, the full set of conserved variables $\mathbf{U}$ is updated using the formula (4.36).

Mathematically, the vdPST model (4.60) is suitable for highly sediment-laden flows as none of the terms is neglected. Having simply reordered the terms in the equations (4.10), this formulation might be considered equivalent to the variable-density mud/debris (vdMD) model proposed in the above Chapter 3. However, the fully-coupled numerical model keeps the density ρ included into the homogeneous component of the RP. This allows the sediment concentration to participate both in the complete eigenstructure of the approximate RP and in the upwind discretization of the bed-pressure and basal resistance source terms. However, a quantitative comparison between the artificially decoupled models and the equivalent fully-coupled models is not provided in the available literature.

Test 4.2.2.A: 1D mud dambreak over quiescent water reservoir

In order to assess the differences between passive-transport Models 1 (4.59) and vdPST model (4.60) respect to the fully-coupled model for variable-density mud/debris flows (see Section 3.2), we propose here an idealized test consisting of a 1D mud dambreak over a steep bed and reaching downstream a quiescent clear-water reservoir. The initial mud fluid ($0\,m \leq x \leq 500\,m$) is composed by water with 50% volumetric concentration of non-cohesive solid particles of $\rho_s = 2650\,kg/m^3$ and characteristic diameter $d_s = 1\,mm$, leading to a bulk density $\rho = 1825\,kg/m^3$. The clear-water reservoir is placed downstream ($2500\,m \leq x \leq 5000\,m$), with density $\rho_w = 1000\,kg/m^3$ and the water free surface has a constant elevation. The initial conditions have been sketched in Figure 4.1.

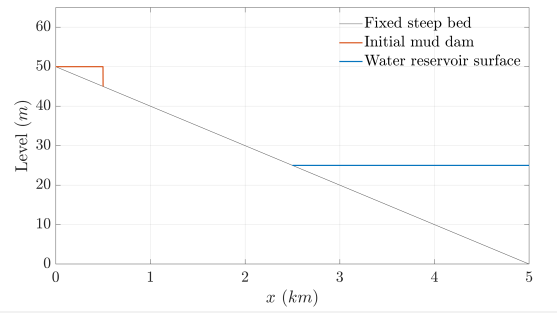

Figure 4.1: Test 4.2.2.A: Initial conditions for the mud dam and the clear-water reservoir.

The two proposed models for passive sediment transport, udPST and vdPST models, are compared here with the vdMD model reported in the

previous chapter. The basal resistance is estimated using the pure turbulent Manning's model, with a roughness parameter $n_b = 0.025\, sm^{-1/3}$. The exchange of material between the flow and the bed layer is neglected (rigid-bed assumption), as well as the effects of the solid phase dilation in the vdMD model. The spatial domain is discretized using a 1D-mesh of 5000 square cells with $\Delta x = 1\, m$. The simulated time is 10 min and CFL=1.0 is set.

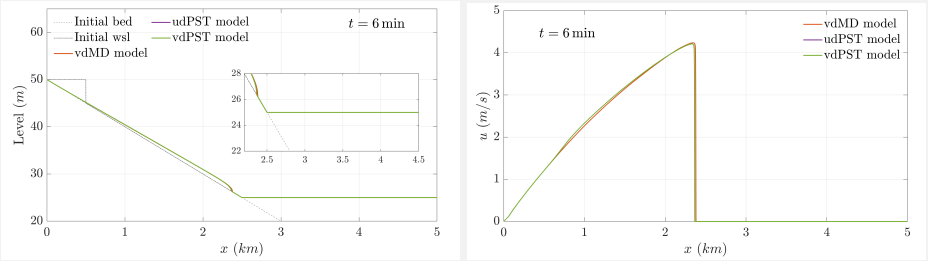

(a) $t = 6\, min$

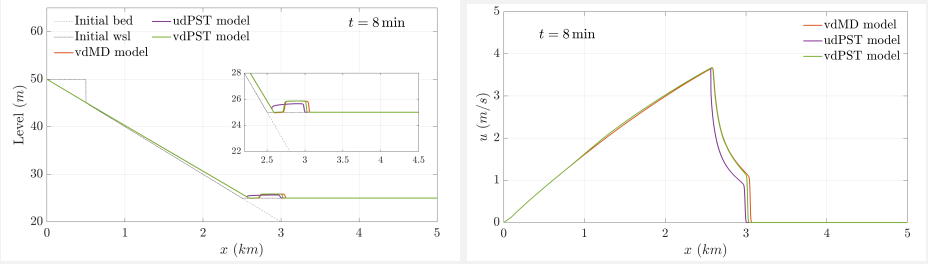

(b) $t = 8\, min$

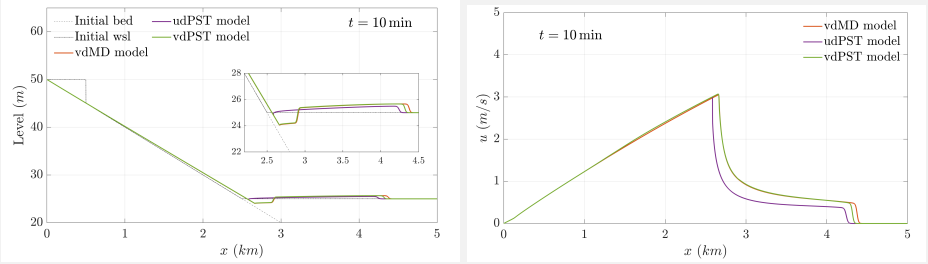

(c) $t = 10\, min$

Figure 4.2: Test 4.2.2.A: (lefft) free surface level and (right) flow velocity at (a) $t = 6\, min$, (b) $t = 8\, min$ and (c) $t = 10\, min$.

Figure 4.2 shows the flow surface level (left column) and depth-averaged velocity (right column) for the 1D mud dambreak flow at the times $t = 6\, min$, $t = 8\, min$ and $t = 10\, min$ with the three models analysed. Before the dambreak wave front reaches the downstream clear-water reservoir ($t \leq 6.5\, min$), the usPST and vdPST models show exactly the same results as the density remains constant along the flow and density gradients do not exist. The vdMD model shows slight velocity variations due to the inclusion of the flow density in the characteristic wave-speeds, but the differences with the passive-transport models are negligible.
Once the wave front reaches the clear-water reservoir at $x = 2500\, m$ ($t > 6.5\, min$), a sharp density gradient appears at the interface and the usPST and vdPST models show important differences (see Figure 4.2–b). The height and speed of the wave generated in the reservoir

are markedly lower when density gradients are not taken into account (udPST model). Furthermore, differences on the generated wave (specially on the wave-front speed) also appears between the vdPST model and the fully-coupled vdMD model, although they are less marked than those between the usPST and vdPST models.
As the generated wave progresses downstream over the quiescent reservoir, the results of the usPST and vdPST models show higher differences for both the wave height and speed 4.2–c). Furthermore, the difference on the generated wave speed between the vdPST model and the fully-coupled vdMd model also increases, despite they are considered as equivalent formulations in previous published works [12, 20, 42, 79, 112].

4.3 Benchmark cases

4.3.1 Synthetic case ST1: Large-scale long-term 1D dambreak over erodible flat bed

The aim of this test is to study the influence of the suspended sediment in the dynamics of dambreak waves for a relatively long channel and over a comparatively long period rather than under the typical laboratory scales. Here, the udPST (4.59) and the vdPST models (4.60) for passive suspended transport are compared against the fixed-bed clear-water model reported by Murillo & García-Navarro [103]. This idealized test for sediment transport model was firstly proposed by Cao *et al.* [18] and revisited in several works [20, 50].

The test consists of a one-dimensional large-scale long-term dambreak over an erodible uniform flat bed. Initially the fluid is clear water. The channel length is set to $50\,km$, the dam is initially located at $x = 25\,km$, and the initial water surface elevation is $h_L = 40\,m$ and $h_R = 2\,m$ on the left and right sides, respectively. The movable flat bed is made of a uniform non-cohesive sediment of diameter $d_s = 4\,mm$ and density $\rho_s = 2650\,kg/m^3$. The friction term is modeled using the turbulent Manning's relation and assuming a constant value of the roughness coefficient $n_b = 0.03\,sm^{-1/3}$. The modification parameter for the capacity solid transport (4.8) is set to $\beta_T = 10$ to increase the morphodynamical changes. A single-row square-cell mesh is used for the simulation with $\Delta x = 10\,m$. The simulated time is 30 min and CFL=1.0 is set.

Figure 4.3–left shows the flow free surface evolution and bed evolution at $t = 1\,min$, $t = 5\,min$, $t = 10\,min$ and $t = 30\,min$ after the dambreak starting. The results obtained with the udPST and the vdPST models for passive suspended transport are plotted against those of the fixed-bed clear-water model. For the passive transport models, sediments can be exchanged with the bed and transported as passive solutes, i.e. without directly influencing the hydrodynamics of the flow. The udPST model incorporates the effects of the sediment exchange as a cell-centered mass and momentum contribution. Moreover, the vdPST model also accounts for the density gradients,

caused by the sediment concentration differences in the flow, as a momentum source term. For the clear-water model, the bed layer is not eroded and hence the suspended sediment concentration is always null. In order to allow suitable comparisons, the three models are solved with the same numerical scheme but incorporating the required restrictions to each model.

The bed mobility considerably affects the free surface evolution compared to the fixed-bed clear-water case. The main differences are located at the wave front, where the passive transport models predict generally higher flow depths than the fixed-bed model, especially for the udPST model. This can be significant for flooding prediction as the wavefront progresses faster and with higher depths at long-term stages of the dambreak when bed mobility is considered.

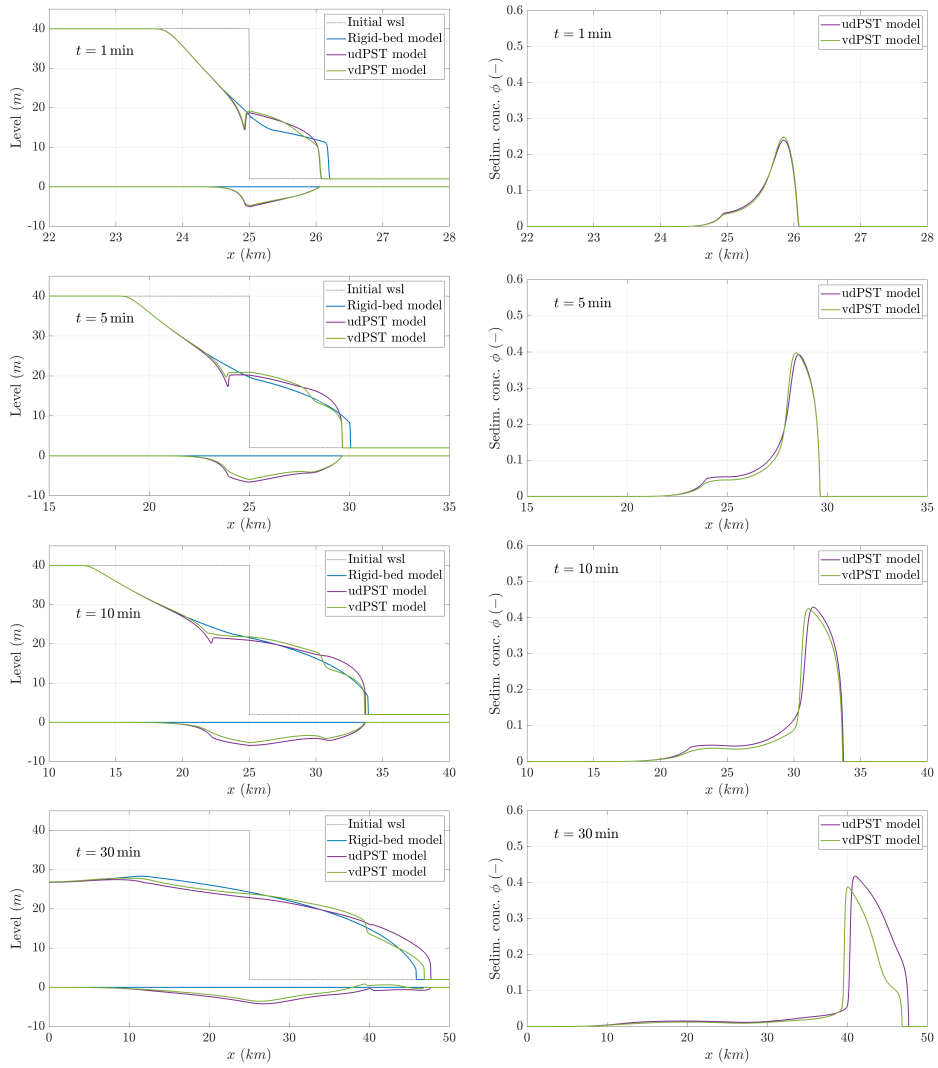

Figure 4.3: Synthetic case ST1 – Dambreak long-term hydraulics over mobile flat bed: (left) flow free surface and bed surface and (right) depth-averaged sediment concentration in the flow. Front top to bottom: $t = 1\,min$, $t = 5\,min$, $t = 10\,min$ and $t = 30\,min$.

Figure 4.3–right shows the volumetric sediment concentration at $t = 1\,min$, $t = 5\,min$, $t = 10\,min$ and $t = 30\,min$ after the dambreak starting with both the udPST and vdPST models. As the dambreak wave progresses downstream, the mass exchange term incorporates into the flow a

high quantity of sediment, leading to noticeable depth-averaged concentrations in the flow column as well as important changes in the bed elevation. The sediment concentration shows a sharp increment separating the wavefront from the middle reach of the dambreak wave, with values higher than 40% for the wavefront compared with volumetric concentrations lower than 0.05% at the middle reach. This sharp increment of the suspended concentration between the central reach and the wavefront causes a high density gradient in that region. When the passive transport vdPST model is considered, this sharp density gradient leads to the appearance of an intermediate shock wave in the flow surface upstream. However, the passive transport udPST model, which does not take into account density changes, is not able to predict this intermediate shock wave.

Regarding the dambreak wave propagation, the clear-water model predicts a larger wave front velocity for the short-term stages of the dambreak flow than the movable bed models (see Figure 4.4–left). This is caused by the flow momentum reduction associated to the sediment entrainment from the bed layer (4.15), which is in agreement with the "self-adaptation" principle in river dynamics [20]. However, as the dambreak progresses downstream and the sediment is incorporated into the flow column, the clear-water model tends to underestimate the front velocity respect to the results obtained with both the udPST and vdPST models. Furthermore, ignoring the influence of density gradients in the flow momentum (passive transport udPST model approach) leads to an overestimation of the front velocity propagation for long-term stages of the dambreak flow in comparison with the passive transport vdPST model.

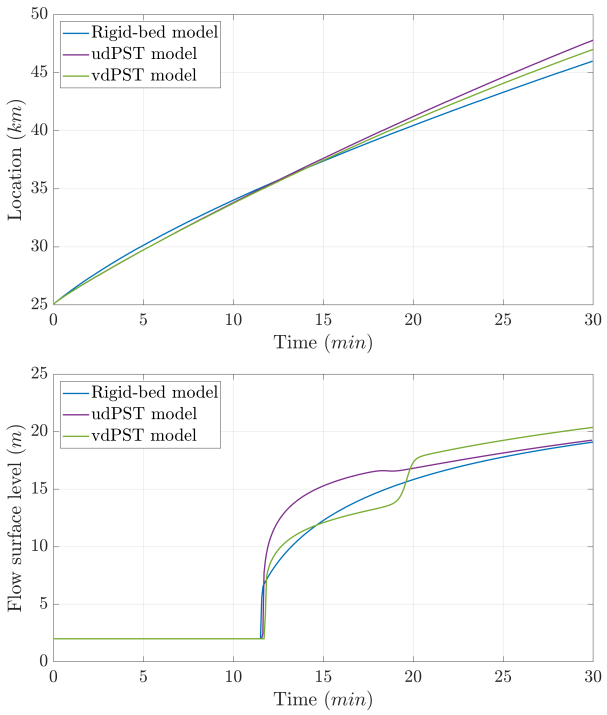

Figure 4.4: Synthetic case ST1 – Temporal evolution of the (left) wavefront position and (right) flow free surface elevation at $x = 35\,km$.

Figure 4.4-right shows the temporal evolution of flow free surface level at $x = 35\,km$, i.e. $10\,km$ downstream the initial dam location, with the

clear-water model and both the udPST and vdPST models. The flow level increment caused by the intermediate density shock wave in the vdPST model is unpredicted by the udPST and the clear-water models, with an important drawback for the hazards determination against severe flooding.

Finally, Figure 4.5 depicts the dynamic computational time step evolution along the simulation for the fixed-bed model, the passive-transport udPST model and the passive-transport vdPST model. The time step is closely related to the computational time required by the model to perform simulations and hence to its efficiency. For times lower than $2\,min$ after the dambreak starting, the fixed-bed model shows higher wavefront propagation velocities than the models considering bed mobility, leading to smaller time steps. However, for the larger times (long-term stages) the models incorporating the bed evolution into the equations requires smaller time steps to ensure the computational stability due to the higher wavefront velocity. Furthermore, as the passive transport udPST model overestimates the progression of the wavefront, it also shows much smaller dynamical time steps than the passive transport vdPST model. This leads to a loss of computational efficiency for real-scale and long-term morphodynamical computations.

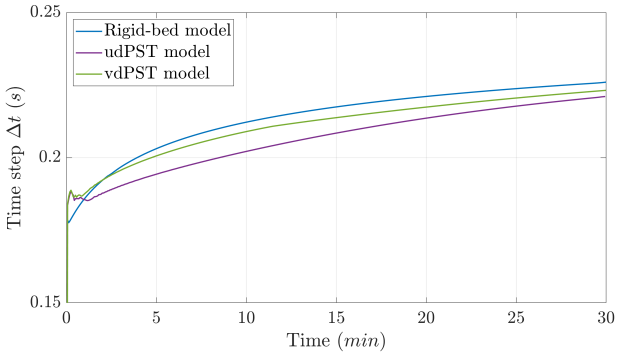

Figure 4.5: Synthetic case ST1 – Time step evolution.

4.3.2 Synthetic case ST2: Large-scale long-term 1D dambreak over non-uniform erodible beds

The aim of this idealized test is to assess the capability of the proposed models to deal with non-uniform beds and to study the influence of the mixture composition on the hydrodynamic behavior. The same large-scale and long-term one-dimensional dambreak test described in the above section is again used here but setting two different non-uniform sediment-size distributions in the bed layer. Both non-uniform beds consist of a mix of gravel ($d_s > 2\,mm$), medium sand ($d_s = 1\,mm$) and fine material ($d_s = 100\,\mu m$) weighted to maintain a constant median diameter $d_m = \sum_{p=1}^{N=3} F_{b,p} d_{s,p} = 4\,mm$. This equivalent median diameter allows to compare the results with those obtained in the above section for uniform bed. Table 4.1 shows the sediment-size distribution for both non-uniform beds considered. Non-uniform bed A is composed mainly of medium gravel with small fractions of coarse sand and fines and is assumed as a coarse graded bed. In the non-uniform bed B, fine material and medium

sand prevails over a small fraction of coarse gravel, hence it is considered as a fine graded bed.

	Bed A		Bed B	
Fines	$d_{s,1} = 100\,\mu m$	$F_{b,1} = 0.10$	$d_{s,1} = 100\,\mu m$	$F_{b,1} = 0.50$
Sand	$d_{s,2} = 1\,mm$	$F_{b,2} = 0.10$	$d_{s,2} = 1\,mm$	$F_{b,2} = 0.25$
Gravel	$d_{s,3} = 4.8625\,mm$	$F_{b,3} = 0.80$	$d_{s,3} = 14.8\,mm$	$F_{b,3} = 0.25$
Medium diameter	$d_m = 4\,mm$		$d_m = 4\,mm$	

Table 4.1: Synthetic case ST2 – Sediment-size distribution for non-uniform beds.

All the other parameters in simulations are set with the same values as in the above section. Only the passive-transport vdPST model is tested in this case, since the results are also applicable to the passive-transport udPST model.

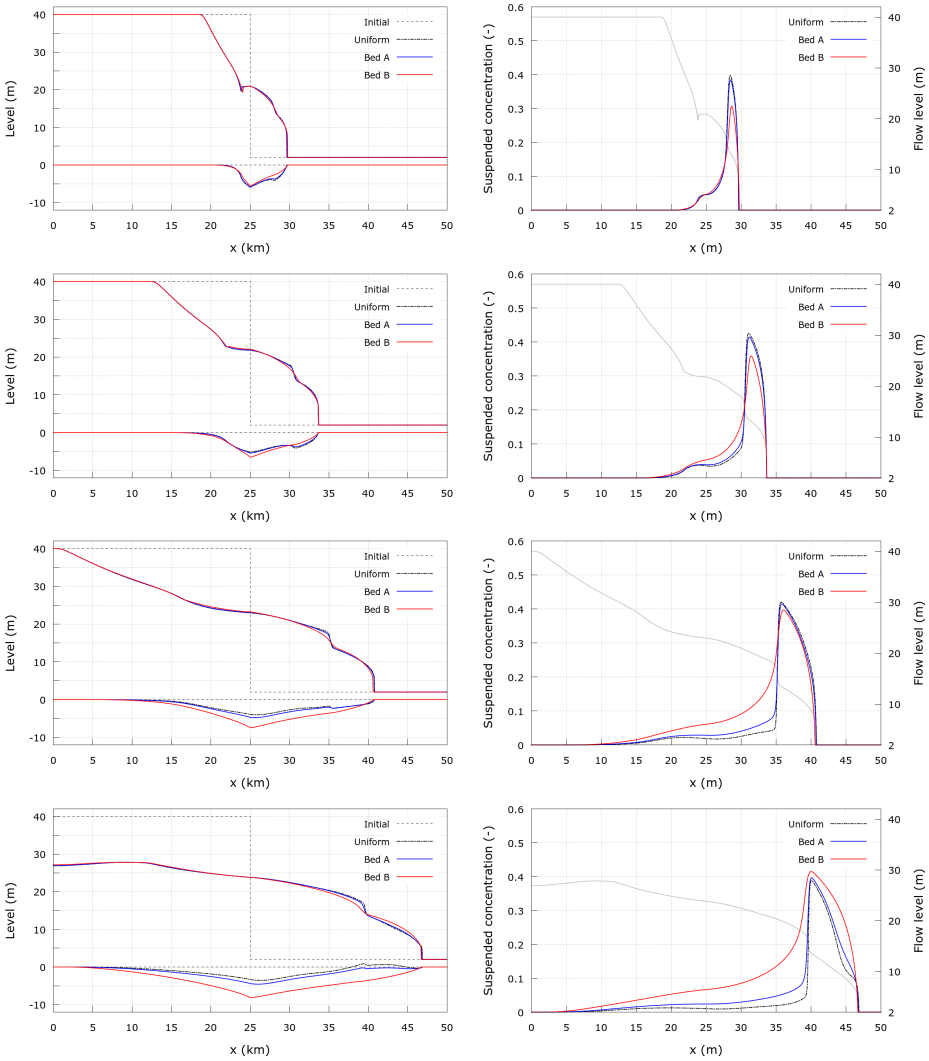

Figure 4.6: Synthetic case ST2 – Dambreak hydraulics over non-uniform bed: (left) flow free surface and bed surface and (right) total solid concentration. Front top to bottom, $t = 5\,min$, $t = 10\,min$, $t = 20\,min$ and $t = 30\,min$.

Figure 4.6–left shows the flow free surface evolution and bed evolution at $t = 5\,min$, $t = 10\,min$, $t = 20\,min$ and $t = 30\,min$ after the dambreak

starting, with the non-uniform beds A and B. The results obtained in the above section with uniform bed configuration are also depicted as reference. The non-uniform composition of the bed slightly affects the free surface evolution compared with the uniform bed. The more marked differences are detected in the density-wave region at long-term stages for the non-uniform bed B. The entrainment of fine materials from the bed to the flow makes smoother the jump in density accompanying the wavefront, which finally causes the appearance of the density-wave.

Figure 4.6–right shows the total volumetric concentration of solid phase in the flow. The fine material is incorporated into the mixture in the upstream region of the dambreak wave, where the erosive flow energy is lower, and hence it reduces the density difference between the wavefront and the upstream region. Furthermore, the density peak associated to the dambreak wavefront is reduced as the presence of fine materials in the bed increases. The main consequence is that the density-wave is smeared.

Nevertheless, the bed level evolution shows more marked differences than the free surface evolution, especially as the dambreak wave progresses downstream (see Figure 4.6–left). For the coarser non-uniform bed A, the bed level does not show significant deviations with respect to the uniform bed case, but a slightly higher erosion can be identified at long-term stages. The finer non-uniform bed B presents lower entrainment than the uniform bed configuration at short-term stages. Nevertheless, a much more marked erosion is detected at long-term stages as a consequence of the higher entrainment of fine material from the bed (Figure 4.7).

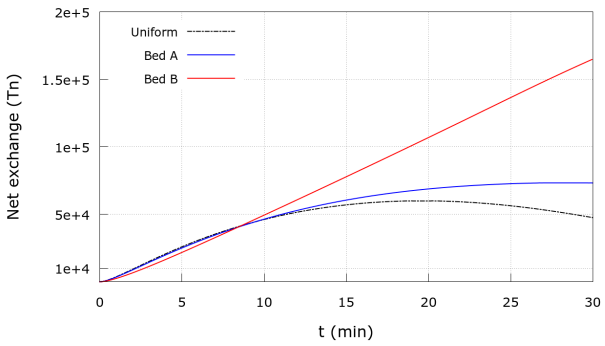

Figure 4.7: Synthetic case ST2 – Temporal evolution of the accumulated mass exchange between bed layer and flow.

Figure 4.8 depicts the volumetric concentration of each sediment size-class in the mixture flow for both non-uniform bed configurations at $t = 5\,min$, $t = 10\,min$, $t = 20\,min$ and $t = 30\,min$ after the dambreak starting. The free surface level has also been plotted for each case. The coarser non-uniform bed A shows higher concentrations of the gravel fraction at the wavefront during all the stages of the dambreak flow, which causes the density jump between the wavefront and the upstream region. Contrarily, the finer non-uniform bed configuration B presents a higher volumetric concentration of sand material at the wavefront during the early stages of the dambreak flow, whereas the fine material fraction prevails along the whole dambreak flow at the long-term stages. Moreover, the volumetric concentration of the finer fraction shows a progressive transition between

the upstream region and the wavefront region, avoiding the appearance of the marked density jump detected in the uniform bed case.

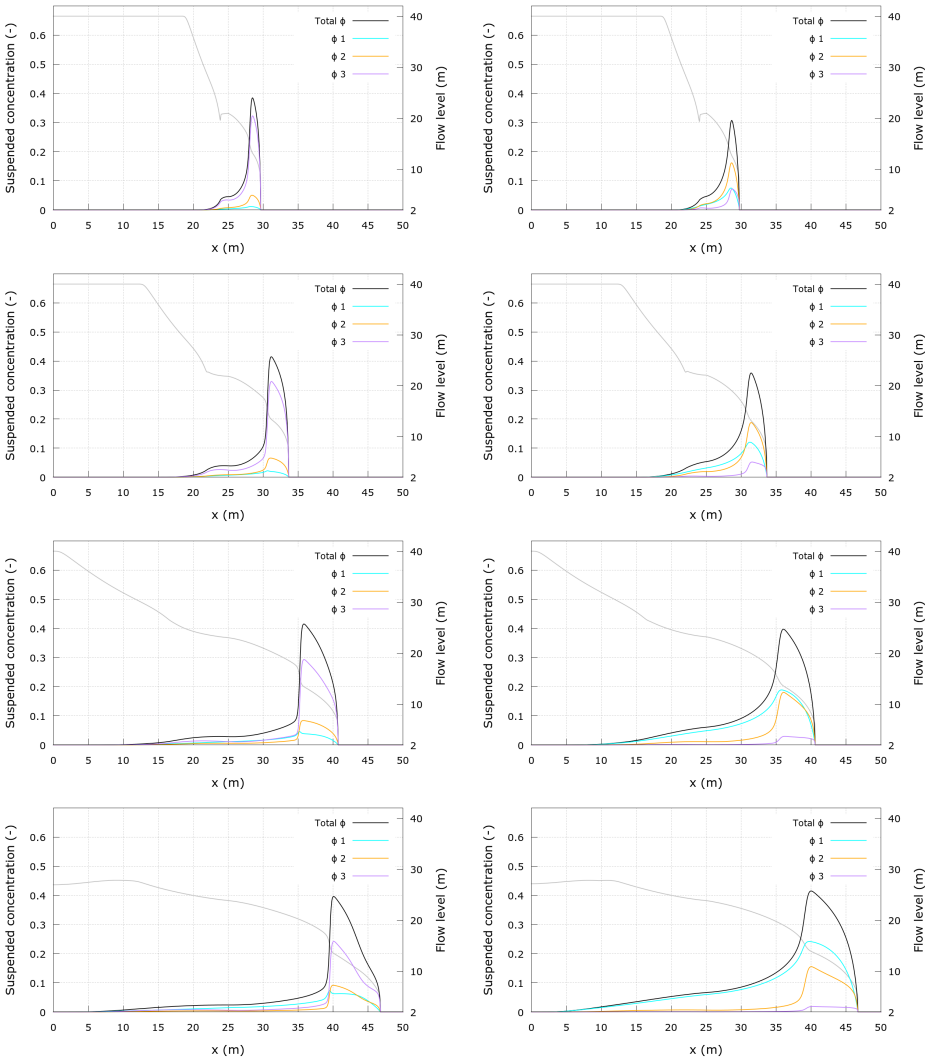

Figure 4.8: Synthetic case ST2 – Volumetric concentration of each sediment size-class in the flow: (left) non-uniform bed A (right) non-uniform bed B. Front top to bottom, $t = 5\,min$, $t = 10\,min$, $t = 20\,min$ and $t = 30\,min$.

4.3.3 Synthetic case ST3: 2D mixing of different density currents

The main goal of this idealized two-dimensional test is to assess the capability of the passive-transport udPST model and vdPST model to correctly deal with mixing of flows with a different sediment concentration and hence density gradients. In cases where two steady currents of equal discharge and different density converge, the influence of the spatial density gradients should domain the hydrodynamics of the mixing region [47, 75], without the appearance of spurious oscillations or numerical instabilities.

A symmetric confluence of two $565\,m$ long and $50\,m$ wide tributary channels into a main channels of length $1600\,m$ and width $100\,m$ is considered. The center axis of the tributary channels forms a $45°$ angle with the x

axis. A uniform longitudinal bed slope $S_0 = 0.0025$ is set for the tributary and main channels. Figure 4.9 shows a plane view of the test geometry.

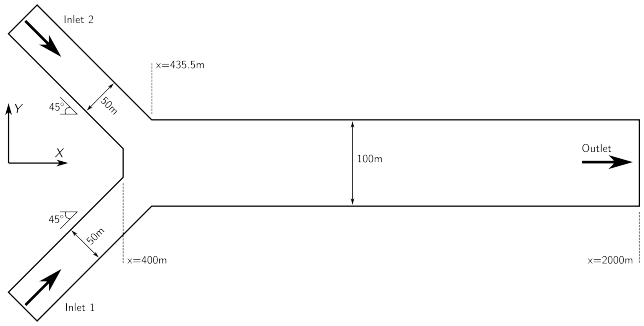

Figure 4.9: Synthetic case ST3 – Sketch of the geometrical configuration.

The setup parameters for this synthetic two-dimensional test are summarized in Table 4.2. The exchange term between the bed layer and the flow is neglected, avoiding erosion and deposition of the solid material. The basal shear stress in the flow is estimated using the pure turbulent Manning's formulation. The value of Manning's roughness parameter is calibrated for allowing the flow to reach a slight supercritical uniform regime ($Fr = 1.15$) along both the tributary and main channels.

Liquid density ρ_w	1000 kg/m^3
Sediment classes N	1
Solid density ρ_s	2700 kg/m^3
Grain diameter d_s	0.4 mm
Manning's roughness parameter n_b	0.016 $sm^{-1/3}$

Table 4.2: Synthetic case ST3 – Simulation setup parameters.

Constant discharge inflows $q_{inlet} = 10\,m^2/s$ per unit width are set at both inlets 1 and 2 during the whole simulation time ($t_{end} = 240\,min$). The temporal evolution of the solid phase volumetric concentration at inlet 1 ϕ^1_{inlet} remains null, whereas at inlet 2 the solid phase volumetric concentration ϕ^2_{inlet} varies with time following:

$$\text{Inlet 1}: \begin{cases} q^1_{inlet} & 10\,m^2/s \quad \text{for } 0 \leq t \leq 240\,min \\ \phi^1_{inlet} & 0.0 \quad \text{for } 0 \leq t \leq 240\,min \end{cases}$$

$$\text{Inlet 2}: \begin{cases} q^2_{inlet} & 10\,m^2/s \quad \text{for } 0 \leq t \leq 240\,min \\ \phi^2_{inlet} & \begin{cases} 0.0 & \text{if } t \leq 60\,min \\ 0.3 & \text{if } t > 60\,min \end{cases} \end{cases}$$

leading to a constant value of the inflow mixture density $\rho = 1510\,kg/m^3$ for inlet 2 for any time $t > 60\,min$. At the inlet boundaries only the specific mass flow rate is imposed. The value of the flow depth, and corresponding flow velocity, is computed by the numerical scheme applied at the boundary cell, but not directly imposed. At the outlet boundary, any condition is

imposed since the flow is supercritical. The spatial domain is discretized using an unstructured triangular mesh with 23500 cells approximately. The simulation starts form dry bed conditions and CFL=0.95 is set.

This case is simulated using the suspended transport udPST model and vdPST model. It is expected that, at $t \leq 60\,min$, a symmetric confluence state is developed for both models since the sediment concentration is null along both tributary channels. However, for larger times ($t > 60\,min$), the density gradients created by the different inlet concentrations should change the flow configuration at the confluence region with the vdPST model, reaching a new non-symmetric steady state at $t = 240\,min$, whereas the symmetry is maintained with the udPST model.

Figure 4.10 shows the flow depth and the Froude number contour levels for the steady state reached at $t = 240\,min$ with the passive transport udPST model. Red colors indicate supercritical flow whereas blue colors denotes subcritical regime. The flow at the tributary channels and in the main channel is slightly supercritical, however the mixing of both flows at the confluence region creates a subcritical flow zone which propagates upstream creating hydraulic jumps in the tributary channels. Although inflows 1 and 2 have a different sediment concentration, and hence a different density, the wave-structure in the tributary channels and in the main channel is totally symmetric since udPST model neglects the density-gradient contribution the flow momentum.

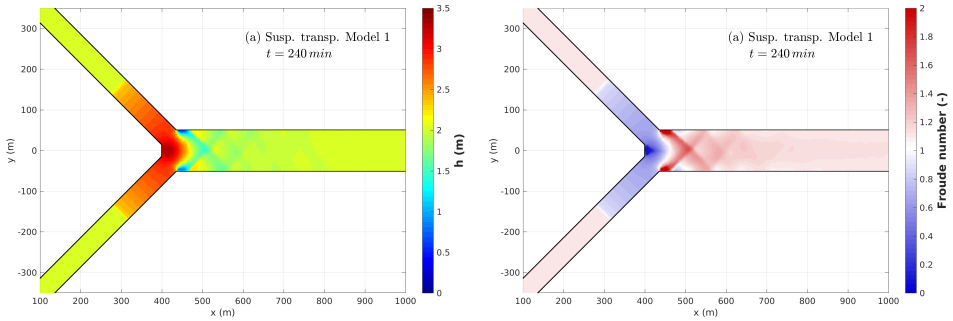

Figure 4.10: Synthetic case ST3 – Steady state at $t = 240\,min$ for the passive-transport udPST model: (left) flow depth and (right) Froude number.

For the passive suspended transport vdPST model, the symmetric structure in the confluence region is broken due to the density gradients generated by the higher sediment concentration of the inflow 2. Figure 4.11 shows the flow depth and the Froude number contour levels for the steady state reached at $t = 240\,min$. The hydraulic jump created by the presence of the confluence in the tributary channel 2 moves downstream whereas the hydraulic jump in the tributary channel 1 moves upstream. This is caused by the denser inflow at the tributary 1. Furthermore, the wave-structure downstream the confluence in the main channel shows also a non-symmetric configuration, following a sequence of alternative diagonal shock waves.

This behavior is directly caused by the inclusion of the density gradient into the numerical fluxes at the intercell edges as a momentum source term. This spatial density gradients modify the balance between homogeneous fluxes and momentum source terms in the approximated solution, leading

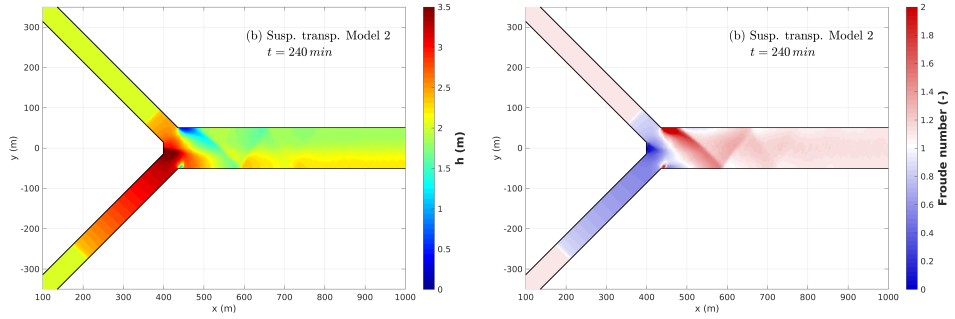

Figure 4.11: Synthetic case ST3 – Steady state at $t = 240\,min$ for the passive-transport vdPST model: (left) flow depth and (right) Froude number.

to a more realistic behavior of the scheme. This modification of the well-balanced states can not be achieved by models which do not consider density into the system of conservation laws for highly sediment-laden flows [20, 102, 112].

Figure 4.12 is a zoom view of the steady state velocity fields within the confluence region at $t = 240\,min$ with (left) udPST model and (right) vdPST model. The symmetric velocity pattern is broken when the density gradients created by the denser inflow 2 are included into the momentum equations. This leads to higher velocities at tributary channel 2 than those at channel 1, and modifies the symmetric velocity patterns in the main channel downstream the confluence.

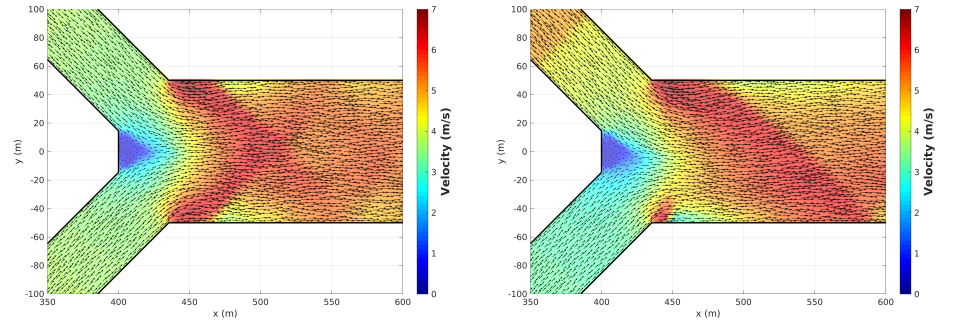

Figure 4.12: Synthetic case ST3 – 2D velocity fields at $t = 240\,min$ with (left) udPST model and (right) vdPST model.

The transient mixing of the inflows 1 and 2 is shown in Figure 4.13 for the passive transport udPST model and vdPST model. The main transient states occur during $60\,min \leq t \leq 70\,min$. Differences can be appreciated between the two numerical models. While the dense and the loose regions are almost symmetric for the udPST model, the dense region is wider than the loose region when the vdPST model is used. Therefore, the density gradient also influences the transient mixing process, not only the balanced steady state.

Finally, Figure 4.14 shows the mixing process along the main channel at $t = 240\,min$ with vdPST model. The sediment concentration profiles with both udPST and vdPST models are shown at different cross-sections downstream the confluence region. The mass and momentum exchange between

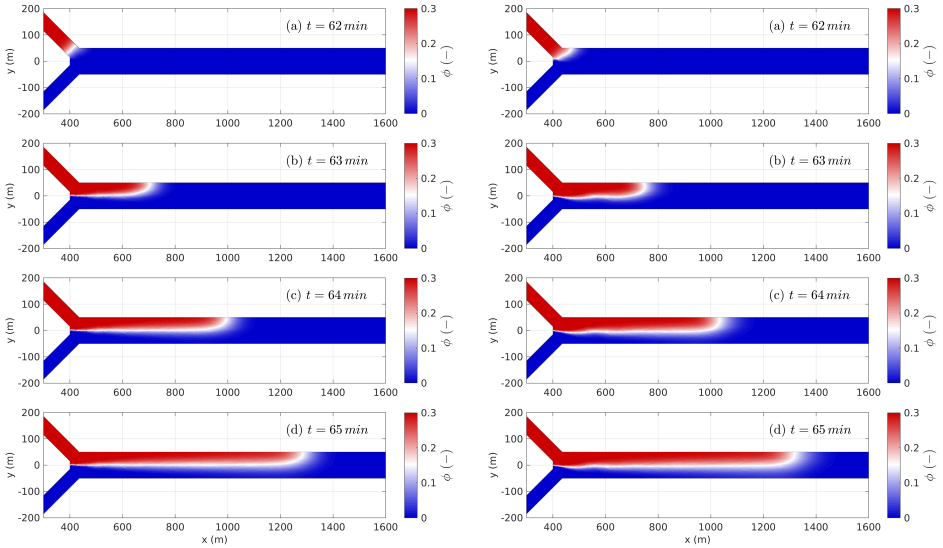

Figure 4.13: Synthetic case ST3 – 2D sediment concentration fields at $t = 62\,min$, $t = 63\,min$, $t = 64\,min$ and $t = 65\,min$. (left) udPST model and (right) vdPST model.

different density flows tends to create a uniform cross-section density profile downstream the confluence region. At $x = 500\,m$, a clear interface separating the denser flow from the clear water current appears. This mixing interface is displaced towards the loose region when vdPST model is used, whereas it remains at the main channel center with udPST model. The mixing interface is less marked at $x = 1000\,m$ as a consequence of the momentum exchange process whereas it practically disappears at $x = 1800\,m$. However, a uniform cross-section volumetric concentration profile has not been reached yet at the outlet boundary of the main channel..

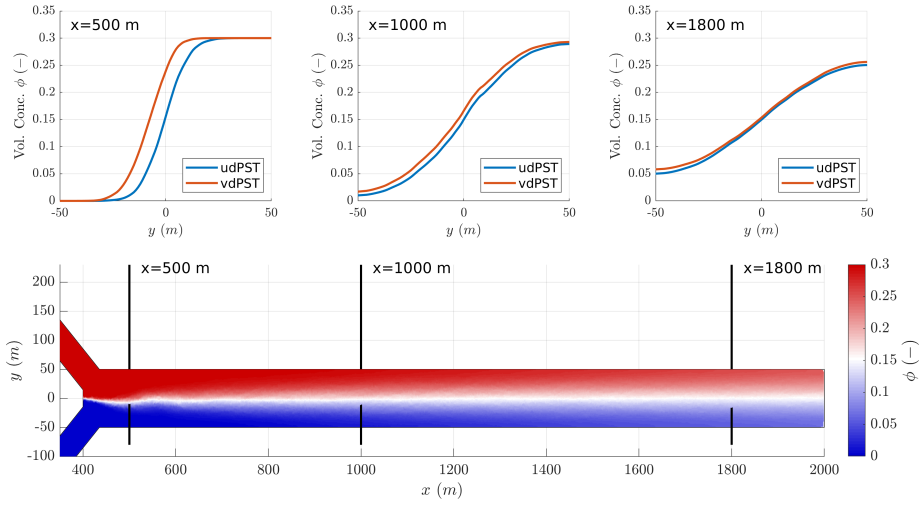

Figure 4.14: Synthetic case ST3 – Sediment concentration along the main channel at $t = 240\,min$ with the vdPST model. Cross-section profiles for the sediment volumetric concentration at $x = 500\,m$, $x = 1000\,m$ and $x = 1800\,m$ with the udPST model and vdPST model.

4.4 In Closing

In this chapter, the system of 2D depth-averaged conservation laws for the passive transport of multiple sediment classes has been solved using the Finite Volume (FV) approach. This system is based on the artificial decoupling of the flow depth h and density ρ in order to allows the use of widespread solvers designed for shallow clear-water problems. The system of equations is formulated taking into account the net exchange flux between the underlying erodible bed layer and the flow, as well as the effects of the density gradients in the flow hydrodynamics. The upwind intercell numerical fluxes for the hydrodynamical component of the system are solved using the augmented Roe's approach, whereas the passive transport of the different suspended sediment classes is achieved using a reduced formulation for the intercell flux.

The main novelties in this chapter are summarized as:

1. Two different robust and efficient numerical models are proposed for the resolution of the suspended sediment transport system. The first one, referred to as udPST model, accounts for the mass and momentum exchange between the bed layer and the flow, but does not include the effects of the sediment concentration in the flow dynamics. The the second one, referred to as vdPST model, also includes the contribution of the flow density gradients to the momentum equations as a new source term which is upwind discretized.

2. Important differences have been found between the results provided for udPST and vdPST models in different idealized benchmark tests. These results indicates that, when high solid concentrations are expected in the flow, it is necessary to include the density-gradients momentum contribution in order to obtain reliable results.

3. Finally, vdPST model is usually considered equivalent to maintain the flow density and the depth coupled in the conservative variables and fluxes and, hence, used for variable-density mud/debris flows [12, 20, 42, 79, 112]. However, for highly transient problems with important density gradients, the results obtained with vdPST model show differences respect to the obtained with the fully-coupled vdMD model described in the above Chapter 3.

Chapter 5

Two-dimensional models for generalized bedload transport

The main goals of this chapter are:

- To derive robust and accurate numerical schemes to solve the two-dimensional bedload transport problem, including the presence of finite-depth erodible layers.
- To assess the effects of the non-capacity bedload transport states in the bed level evolution for highly transient erosive problems.

5.1 Governing equations

The depth-averaged model for the multi-grain bedload transport is derived from the integration of the Navier-Stokes equations along the vertical direction throughout the flow column assuming hydrostatic pressure distribution and neglecting the changes on the bulk density caused by the solid particles (Section 2.3). This simplifies the 2D mass (2.8) and momentum conservation equations (2.22)–(2.23) for a clear-water shallow flow as

$$\frac{\partial h}{\partial t} + \frac{\partial}{\partial x}(hu) + \frac{\partial}{\partial y}(hv) = 0 \tag{5.1a}$$

$$\frac{\partial (hu)}{\partial t} + \frac{\partial}{\partial x}(hu^2 + \frac{1}{2}gh^2) + \frac{\partial}{\partial y}(huv) = -gh\frac{\partial z_b}{\partial x} - \frac{\tau_{bx}}{\rho_w} \tag{5.1b}$$

$$\frac{\partial (hv)}{\partial t} + \frac{\partial}{\partial x}(huv) + \frac{\partial}{\partial y}(hv^2 + \frac{1}{2}gh^2) = -gh\frac{\partial z_b}{\partial x} - \frac{\tau_{by}}{\rho_w} \tag{5.1c}$$

being h the vertical flow depth, $(u,\, v)$ the components of the depth-averaged flow velocity vector $\mathbf{u}$ along the global $x-$ and $y-$coordinates respectively, z_b the bed layer elevation, g the gravitational acceleration, $(\tau_{bx},\, \tau_{by})$ the components of the depth-averaged shear resistance at the bed interface $\boldsymbol{\tau_b}$, and ρ_w the density of the fluid. Note that here, the projection of the gravity force along the vertical direction is adopted under the hypothesis of small normal-bed angles.

Furthermore, the mass conservation equation for the non-uniform bedload transport layer (2.128) is expressed as

$$\frac{\partial z_b}{\partial t} + \frac{\partial}{\partial x}(q_{bx}) + \frac{\partial}{\partial y}(q_{by}) = 0 \tag{5.2}$$

where $(q_{bx},\ q_{by})$ are the components of the bulk bedload rate $\mathbf{q_b}$ along the global $(x,\ y)$ horizontal coordinates respectively. For a multi-grain bed layer composed by N different sediment classes, $\mathbf{q_b}$ can be estimated as [66, 88, 144]

$$\mathbf{q_b} = \frac{1}{1-\xi}\sum_{p=1}^{\mathrm{N}} F_{b,p} G_p |\mathbf{u}|^2 \mathbf{u} \tag{5.3}$$

being ξ the bulk porosity of the bed layer, G_p a Grass-type factor accounting for the interaction between the flow and the pth sediment class in the non-uniform bed layer (see Section 5.3) and $F_{b,p}$ the corresponding bed fraction, which is considered constant in time and uniform in space with $\sum_{p=1}^{\mathrm{N}} F_{b,p} = 1$. It is worth mentioning that here the volumetric effect of the porosity in the bed level evolution is included into the bulk bedload discharge $\mathbf{q_b}$. Note also that the vertical exchange between bedload layer and water is not present in the equations.

Therefore, it is possible to express the horizontal components of the bulk bedload rate $\mathbf{q_b} = (q_{bx},\ q_{by})$ in (5.3) as

$$\begin{aligned} q_{bx} &= \frac{1}{1-\xi} G\,|\mathbf{u}|^2 u \\ q_{by} &= \frac{1}{1-\xi} G\,|\mathbf{u}|^2 v \end{aligned} \tag{5.4}$$

with $G = \sum_{p=1}^{\mathrm{N}} F_{b,p} G_p$ the bulk Grass-type interaction factor. Closure for the Grass interaction factor G_p of each sediment class composing the non-uniform bed layer is required here to complete the system. The estimation of G_p based on the different empirical relations found in literature [144] is detailed in Section (5.3), regardless of the capacity or the non-capacity assumption is adopted for the bedload transport.

The shear resistance at the bed surface $\boldsymbol{\tau_b} = (\tau_{bx}, \tau_{by})$ is commonly estimated using the quadratic pure turbulent relation in Table 2.1, repeated here as

$$\begin{aligned} \tau_{bx} &= \rho_w g h C_f |\mathbf{u}| u \\ \tau_{by} &= \rho_w g h C_f |\mathbf{u}| v \end{aligned} \tag{5.5}$$

being $C_f = n_b^2\, h^{-4/3}$ a friction coefficient and n_b the bulk Manning's roughness parameter. The bulk porosity is estimated using the Wu [144] relation for non-uniform deposits

$$\xi = 0.13 + 0.21\left(0.002 + 10^3 \sum_{p=1}^{\mathrm{N}} F_{b,p}\, d_{s,p}\right)^{-0.21} \tag{5.6}$$

being $d_{s,p}$ the characteristic diameter of the pth sediment class in meters.

The equations forming the two-dimensional system (5.1)–(5.2) can be rewritten in vector form as

$$\frac{\partial \mathbf{U}}{\partial t} + \nabla \cdot \mathbf{E}(\mathbf{U}) = \mathbf{S_b}(\mathbf{U}) + \mathbf{S_\tau}(\mathbf{U}) \tag{5.7}$$

where $\mathbf{U}$ is the vector of conserved variables

$$\mathbf{U} = \begin{pmatrix} h, & hu, & hv, & z_b \end{pmatrix}^T \tag{5.8}$$

and $\mathbf{E}(\mathbf{U}) = \big(\mathbf{F}(\mathbf{U}), \mathbf{G}(\mathbf{U})\big)$ are the convective flux vectors along the $(x,\, y)$ horizontal coordinates respectively, expressed as

$$\mathbf{F}(\mathbf{U}) = \begin{pmatrix} hu \\ hu^2 + \frac{1}{2}gh^2 \\ huv \\ \frac{1}{1-\xi}G|\mathbf{u}|^2 u \end{pmatrix} \qquad \mathbf{G}(\mathbf{U}) = \begin{pmatrix} hv \\ huv \\ hv^2 + \frac{1}{2}gh^2 \\ \frac{1}{1-\xi}G|\mathbf{u}|^2 v \end{pmatrix} \tag{5.9}$$

The vector $\mathbf{S_b}(\mathbf{U})$ accounts for the momentum source term associated to the variation of the pressure force on the bed surface

$$\mathbf{S_b}(\mathbf{U}) = \begin{pmatrix} 0 \\ -gh\frac{\partial z_b}{\partial x} \\ -gh\frac{\partial z_b}{\partial y} \\ 0 \end{pmatrix} \tag{5.10}$$

and can also be expressed using the non-conservative product

$$\mathbf{S_b}(\mathbf{U}) = \mathbf{S_x}(\mathbf{U})\frac{\partial \mathbf{U}}{\partial x} + \mathbf{S_y}(\mathbf{U})\frac{\partial \mathbf{U}}{\partial y} \tag{5.11}$$

where $\mathbf{S_x}(\mathbf{U})$ and $\mathbf{S_y}(\mathbf{U})$ are the non-conservative matrices

$$\mathbf{S_x}(\mathbf{U}) = \begin{pmatrix} 0 & 0 & 0 & 0 \\ 0 & 0 & 0 & -gh \\ 0 & 0 & 0 & 0 \\ 0 & 0 & 0 & 0 \end{pmatrix} \qquad \mathbf{S_y}(\mathbf{U}) = \begin{pmatrix} 0 & 0 & 0 & 0 \\ 0 & 0 & 0 & 0 \\ 0 & 0 & 0 & -gh \\ 0 & 0 & 0 & 0 \end{pmatrix} \tag{5.12}$$

The source vector $\mathbf{S_\tau}(\mathbf{U})$ denotes the momentum dissipation due to the basal resistance

$$\mathbf{S_\tau}(\mathbf{U}) = \begin{pmatrix} 0 \\ -\tau_{bx}/\rho_w \\ -\tau_{by}/\rho_w \\ 0 \end{pmatrix} \tag{5.13}$$

5.2 Finite Volume method for the bedload transport system

System (5.7) is time dependent, non linear and contains source terms. Under the hypothesis of dominant advection it can be classified as belonging to the family of hyperbolic systems. In order to obtain a numerical solution using a Finite Volume (FV) technique, the spatial domain is divided in computational cells using a mesh fixed in time and system (5.7) is integrated in each cell Ω_i using the Gauss theorem. Assuming a piecewise uniform representation of the conserved variables $\mathbf{U}$ at the cells, the integrated system of

equations for the i cell in the global framework $\mathbf{X} = (x, y)$ can be expressed as

$$\frac{\mathrm{d}}{\mathrm{d}t}\int_{\Omega_i} \mathbf{U}\,\mathrm{d}\Omega + \sum_{k=1}^{\mathrm{NE}} (\mathbf{E}\cdot\mathbf{n})_k\, l_k = \int_{\Omega_i} \mathbf{S_b}(\mathbf{U})\,\mathrm{d}\Omega + \int_{\Omega_i} \mathbf{S_\tau}(\mathbf{U})\,\mathrm{d}\Omega \tag{5.14}$$

where the surface integral in the second term has been already replaced by a sum over the cell edges, being NE the number of edges for the i cell. The term $(\mathbf{E}\cdot\mathbf{n})_k$ denotes the value of the normal flux through the kth cell edge, $\mathbf{n} = (n_x,\, n_y)$ the outward unit normal vector to the edge and l_k the length of the edge.

For each kth cell edge, the local framework is defined as $\hat{\mathbf{X}} = \mathbf{R}_k\mathbf{X} = (\hat{x}, \hat{y})$ and the rotation matrix $\mathbf{R}_k$ is

$$\mathbf{R}_k = \begin{pmatrix} 1 & 0 & 0 & 0 \\ 0 & n_x & n_y & 0 \\ 0 & -n_y & n_x & 0 \\ 0 & 0 & 0 & 1 \end{pmatrix}_k \tag{5.15}$$

The rotation invariance property (3.26) of the convective flux matrix $\mathbf{E}(\mathbf{U})$ can be used again to rewrite the normal fluxes through the edge [44, 138] as

$$(\mathbf{E}\cdot\mathbf{n})_k = \big[\mathbf{F}(\mathbf{U})\,n_x + \mathbf{G}(\mathbf{U})\,n_y\big]_k = \mathbf{R}_k^{-1}\,\mathbf{F}(\mathbf{R}_k\mathbf{U}) \tag{5.16}$$

being $\mathbf{R}_k^{-1}$ the inverse of the rotation matrix, and hence the homogeneous left hand side of (5.14) is expressed in the local framework $\hat{\mathbf{X}}$ of the kth cell edge as

$$\frac{\mathrm{d}}{\mathrm{d}t}\int_{\Omega_i} \mathbf{R}_k\mathbf{U}\,\mathrm{d}\Omega + \sum_{k=1}^{\mathrm{NE}} \mathbf{F}(\mathbf{R}_k\mathbf{U})\, l_k \tag{5.17}$$

Therefore, the set of local conserved variables $\hat{\mathbf{U}} \equiv \mathbf{R}_k\mathbf{U}$ is defined as

$$\hat{\mathbf{U}} \equiv \mathbf{R}_k\mathbf{U} = \begin{pmatrix} h, & h\,\hat{u}, & h\,\hat{v}, & z_b \end{pmatrix}^T \tag{5.18}$$

and the local homogeneous convective fluxes $\mathbf{F}(\hat{\mathbf{U}})_k \equiv \mathbf{F}(\mathbf{R}_k\mathbf{U})$

$$\mathbf{F}(\hat{\mathbf{U}})_k \equiv \mathbf{F}(\mathbf{R}_k\mathbf{U}) = \begin{pmatrix} h\hat{u} \\ h\hat{u}^2 + \frac{1}{2}gh^2 \\ h\hat{u}\hat{v} \\ \frac{1}{1-\xi}G|\mathbf{u}|^2\hat{u} \end{pmatrix} \tag{5.19}$$

being $\hat{u} = un_x + vn_y$ and $\hat{v} = -un_y + vn_x$ the normal and tangential flow velocities respectively.

The Jacobian matrix of the local flux vector $\mathbf{F}(\hat{\mathbf{U}})_k$ is

$$\mathbf{J}_k = \frac{\partial\mathbf{F}(\hat{\mathbf{U}})}{\partial\hat{\mathbf{U}}} = \begin{pmatrix} 0 & 1 & 0 & 0 \\ gh - \hat{u}^2 & 2\hat{u} & 0 & 0 \\ -\hat{u}\hat{v} & \hat{v} & \hat{u} & 0 \\ -(\hat{u}a + \hat{v}b) & a & b & 0 \end{pmatrix}_k \tag{5.20}$$

with

$$-(\hat{u}a + \hat{v}b) \equiv \frac{\partial \hat{q}_b}{\partial h} = \frac{-1}{1-\xi} G 3\hat{u}(\hat{u}^2 + \hat{v}^2)\frac{1}{h} \tag{5.21a}$$

$$a \equiv \frac{\partial \hat{q}_b}{\partial (h\hat{u})} = \frac{1}{1-\xi} G(3\hat{u}^2 + \hat{v}^2)\frac{1}{h} \geq 0 \tag{5.21b}$$

$$b \equiv \frac{\partial \hat{q}_b}{\partial (h\hat{v})} = \frac{1}{1-\xi} G(2\hat{u}\hat{v})\frac{1}{h} \tag{5.21c}$$

being $\hat{q}_b = \frac{1}{1-\xi} G|\mathbf{u}|^2\hat{u}$ the bedload solid flux normal to the cell edge expressed in the local framework. It is worth noting that:

- First, the term $a = \partial \hat{q}_b/\partial(h\hat{u})$ (5.21b) is always positive and hence the bed transport rate increases as the normal flow discharge grows;
- Second, when the bedload transport flux $\hat{q}_b$ is computed by means of empirical relationships, these derivatives require a suitable treatment to ensure solid mass conservation across the cell edge, as it is detailed in Section 5.3.
- Third, the Jacobian $\mathbf{J}_k$ (5.20) is a singular matrix since any flux derivative depends on the conserved variable z_b. This might create problems for the numerical resolution of the system based on the Jacobian matrix eigenvalues [52]

The bed-pressure vector $\mathbf{S_b}(\mathbf{U})$ is unconditionally invariant under rotation [21] and, hence, the cell-centered integral of bed-pressure source term can be discretized within edge-contributions using

$$\int_{\Omega_i} \mathbf{S_b}(\mathbf{U})\, \mathrm{d}\Omega = \sum_{k=1}^{\mathrm{NE}} \mathbf{R}_k^{-1}\, \mathbf{H}(\hat{\mathbf{U}})_k\, l_k \tag{5.22}$$

where

$$\mathbf{H}(\hat{\mathbf{U}})_k = \begin{pmatrix} 0 \\ -gh\,\Delta z_b \\ 0 \\ 0 \end{pmatrix}_k \tag{5.23}$$

denotes the bed-pressure flux vector at the kth cell edge [103]. The bed-pressure momentum source vector $(\hat{\mathbf{S}}_\mathbf{b})_k$ along the normal direction to the kth cell edge can be rewritten in the local framework $\hat{\mathbf{X}} = (\hat{x}, \hat{y})$ as

$$(\hat{\mathbf{S}}_\mathbf{b})_k = \frac{\partial \mathbf{H}(\hat{\mathbf{U}})_k}{\partial \hat{x}} = \begin{pmatrix} 0 \\ -gh\,\dfrac{\partial z_b}{\partial \hat{x}} \\ 0 \\ 0 \end{pmatrix}_k = \hat{\mathbf{S}}(\hat{\mathbf{U}})_k \frac{\partial \hat{\mathbf{U}}}{\partial \hat{x}} \tag{5.24}$$

being $\hat{\mathbf{S}}(\hat{\mathbf{U}})_k$ the non-conservative matrix

$$\hat{\mathbf{S}}(\hat{\mathbf{U}})_k = \begin{pmatrix} 0 & 0 & 0 & 0 \\ 0 & 0 & 0 & -gh \\ 0 & 0 & 0 & 0 \\ 0 & 0 & 0 & 0 \end{pmatrix}_k \tag{5.25}$$

The cell-centered basal resistance contribution in (5.14) is edge-discretized using the differential approach (see Section 3.2.1) as

$$\int_{\Omega_i} \mathbf{S}_{\boldsymbol{\tau}}(\mathbf{U})\, \mathrm{d}\Omega = \sum_{k=1}^{\mathrm{NE}} \mathbf{R}_k^{-1}\, \mathbf{T}(\hat{\mathbf{U}})_k\, l_k \tag{5.26}$$

where $\mathbf{T}(\hat{\mathbf{U}})_k$ is the integrated basal resistance at the kth cell edge, expressed in the local framework $\hat{\mathbf{X}}$ as

$$\mathbf{T}(\hat{\mathbf{U}})_k = \begin{pmatrix} 0 \\ -ghC_f|\mathbf{u}|\,(\hat{u}\Delta\hat{x} + \hat{v}\Delta\hat{y}) \\ 0 \\ 0 \end{pmatrix}_k \tag{5.27}$$

being $(\Delta\hat{x}, \Delta\hat{y})$ the integration distances along the local $\hat{x}-$ and $\hat{y}-$coordinates respectively. Hence, the basal resistance vector $(\hat{\mathbf{S}}_{\boldsymbol{\tau}})_k$ along the normal direction of the edge in the local framework reads

$$(\hat{\mathbf{S}}_{\boldsymbol{\tau}})_k = \frac{\partial \mathbf{T}(\hat{\mathbf{U}})_k}{\partial \hat{x}} = \begin{pmatrix} 0 \\ -ghC_f|\mathbf{u}|\,\hat{u} \\ 0 \\ 0 \end{pmatrix}_k \tag{5.28}$$

Using (5.22) and (5.26), the bed-pressure and basal resistance contribution can be included into the locally integrated system (5.17) for the kth cell edge as

$$\frac{\mathrm{d}}{\mathrm{d}t}\int_{\Omega_i} \mathbf{R}_k\mathbf{U}\, \mathrm{d}\Omega + \sum_{k=1}^{\mathrm{NE}} \mathbf{F}(\hat{\mathbf{U}})_k\, l_k = \sum_{k=1}^{\mathrm{NE}} \mathbf{H}(\hat{\mathbf{U}})_k\, l_k + \sum_{k=1}^{\mathrm{NE}} \mathbf{T}(\hat{\mathbf{U}})_k\, l_k \tag{5.29}$$

The local system (4.31) allows to define an augmented numerical flux $\mathbf{F}_k^{\downarrow}$ for the i cell at the kth edge which incorporates the integrated bed-pressure and basal resistance edge-contributions, $\mathbf{H}(\hat{\mathbf{U}})_k$ and $\mathbf{T}(\hat{\mathbf{U}})_k$ respectively, into the homogeneous fluxes $\mathbf{F}(\hat{\mathbf{U}})_k$ at the cell edge

$$\mathbf{F}_k^{\downarrow} = \Big(\mathbf{F}(\hat{\mathbf{U}}) - \mathbf{H}(\hat{\mathbf{U}}) - \mathbf{T}(\hat{\mathbf{U}})\Big)_k \tag{5.30}$$

Restoring the augmented flux (5.30) to the global framework $\mathbf{X} = (x, y)$, the integrated system (5.14) is rewritten as

$$\frac{\mathrm{d}}{\mathrm{d}t}\int_{\Omega_i} \mathbf{U}\, \mathrm{d}\Omega = -\sum_{k=1}^{\mathrm{NE}} \mathbf{R}_k^{-1}\, \mathbf{F}_k^{\downarrow}\, l_k \tag{5.31}$$

Assuming a piecewise uniform representation of the conserved variables $\mathbf{U}$ at the i cell for the time $t = t^n$

$$\mathbf{U}_i^n = \frac{1}{A_i} \int_{\Omega_i} \mathbf{U}(x, y, t^n)\, \mathrm{d}\Omega \tag{5.32}$$

where A_i is the cell area, and using an explicit temporal integration for the mass and momentum source terms, the updating formulation for the conserved variables $\mathbf{U}$ at the each cell is expresed as

$$\mathbf{U}_i^{n+1} = \mathbf{U}_i^n - \frac{\Delta t}{A_i} \sum_{k=1}^{\mathrm{NE}} \mathbf{R}_k^{-1}\, \mathbf{F}_k^{\downarrow}\, l_k \tag{5.33}$$

where $\Delta t = t^{n+1} - t^n$ is the time step.

Hence the resolution procedure needs to compute the numerical fluxes $\mathbf{F}_k^{\downarrow}$ at the cell edges ensuring (5.30). It is worth mentioning that the addition of the source terms to the homogeneous fluxes leads to the losing of the conservative character for the momentum flux but ensures the well-balance property for quiescent and steady states [103, 104]. The upwind computation of the intercell fluxes $\mathbf{F}_k^{\downarrow}$ for the kth cell edge requires to solve the local plane Riemann problem (RP) associated to (5.29), which can be written as

$$\begin{gathered} \frac{\partial \hat{\mathbf{U}}}{\partial t} + \frac{\partial \mathbf{F}(\hat{\mathbf{U}})}{\partial \hat{x}} = \hat{\mathbf{S}}_{\mathbf{b}} + \hat{\mathbf{S}}_{\boldsymbol{\tau}} \\ \hat{\mathbf{U}}(\hat{x}, 0) = \begin{cases} \hat{\mathbf{U}}_i = \mathbf{R}_k \mathbf{U}_i^n & \text{if} \quad \hat{x} < 0 \\ \hat{\mathbf{U}}_j = \mathbf{R}_k \mathbf{U}_j^n & \text{if} \quad \hat{x} > 0 \end{cases} \end{gathered} \tag{5.34}$$

where i and j denote the left and right neighbouring cells to the kth edge respectively.

In this thesis, we propose two new approximated Riemann solvers based on the augmented Roe solver (A-Roe) approach [91, 103, 138] to solve (5.34) and to obtain the intercell numerical flux $\mathbf{F}_k^{\downarrow}$, leading to two different FV methods for coupling flow and bedload transport.

5.2.1 Fully-coupled Riemann solver (FCM)

The fully-coupled strategy approximates the solution of the local plane RP (5.34) at the kth edge, separating the left i cell and the right j cell, using a constant coefficient linear RP [138] written as follows

$$\begin{gathered} \frac{\partial \hat{\mathbf{U}}}{\partial t} + \widetilde{\mathbf{J}}_k \frac{\partial \hat{\mathbf{U}}}{\partial \hat{x}} - \widetilde{\mathbf{S}}_k \frac{\partial \hat{\mathbf{U}}}{\partial \hat{x}} = (\widetilde{\mathbf{S}}_{\boldsymbol{\tau}})_k \\ \hat{\mathbf{U}}(\hat{x}, 0) = \begin{cases} \hat{\mathbf{U}}_i & \text{if} \quad \hat{x} < 0 \\ \hat{\mathbf{U}}_j & \text{if} \quad \hat{x} > 0 \end{cases} \end{gathered} \tag{5.35}$$

where $\widetilde{\mathbf{J}}_k = \mathbf{J}_k(\hat{\mathbf{U}}_i, \hat{\mathbf{U}}_j)$ is a constant coefficient matrix which approximates the Jacobian of the non-linear RP, $\widetilde{\mathbf{S}}_k$ is the edge-averaged non-conservative bed-pressure matrix defined in (5.25) and $(\widetilde{\mathbf{S}}_{\boldsymbol{\tau}})_k$ is the edge-averaged flow resistance momentum term (5.28).

Therefore, a pseudo-Jacobian matrix $\widetilde{\mathbf{M}}_k$ can be defined for the linear RP at the kth cell edge coupling the Jacobian of the convective fluxes and the non-conservative bed pressure variations as

$$\widetilde{\mathbf{M}}_k = (\widetilde{\mathbf{J}} - \widetilde{\mathbf{S}})_k = \begin{pmatrix} 0 & 1 & 0 & 0 \\ g\widetilde{h} - \widetilde{u}^2 & 2\widetilde{u} & 0 & g\widetilde{h} \\ -\widetilde{u}\widetilde{v} & \widetilde{v} & \widetilde{u} & 0 \\ -(\widetilde{u}\widetilde{a} + \widetilde{v}\widetilde{b}) & \widetilde{a} & \widetilde{b} & 0 \end{pmatrix}_k \tag{5.36}$$

Integration of (5.35) over the discrete space $\hat{x} \in [\hat{x}_i, \hat{x}_j]$, corresponding to the kth cell edge, leads to the following constraint involving conservation across discontinuities

$$\boldsymbol{\delta}\mathbf{F}(\hat{\mathbf{U}})_k = \widetilde{\mathbf{M}}_k \, \boldsymbol{\delta}\hat{\mathbf{U}}_k \tag{5.37}$$

where $\boldsymbol{\delta}\hat{\mathbf{U}}_k = \hat{\mathbf{U}}_j - \hat{\mathbf{U}}_i$ is the conserved variables increment, allowing to estimate the constant coefficients of $\widetilde{\mathbf{M}}_k$ as

$$\begin{aligned} \widetilde{h} &= \frac{h_i + h_j}{2} \\ \widetilde{u} &= \frac{\hat{u}_i\sqrt{h_i} + \hat{u}_j\sqrt{h_j}}{\sqrt{h_i} + \sqrt{h_j}} \\ \widetilde{v} &= \frac{\hat{v}_i\sqrt{h_i} + \hat{v}_j\sqrt{h_j}}{\sqrt{h_i} + \sqrt{h_j}} \\ \widetilde{a} &= \frac{1}{1-\xi}\widetilde{G}\left(\frac{\hat{u}_i^2 + \hat{u}_i\hat{u}_j + \hat{u}_j^2}{\sqrt{h_i h_j}} + \frac{\hat{v}_i\hat{v}_j}{\sqrt{h_i h_j}}\right) \\ \widetilde{b} &= \frac{1}{1-\xi}\widetilde{G}\left(\frac{\hat{u}_i\hat{v}_i + \hat{u}_j\hat{v}_j}{\sqrt{h_i h_j}}\right) \end{aligned} \tag{5.38}$$

being $\widetilde{G}$ an averaged Grass-type interaction factor. For the sake of clarity, and following [86, 100], a value $\widetilde{G} = (G_i + G_j)/2$ is adopted in this work, although a more complex estimation of $\widetilde{G}$ is proposed in [87].

The approximate matrix $\widetilde{\mathbf{M}}_k$ (5.36) is diagonalizable with four approximate real eigenvalues, $\widetilde{\lambda}_{m,k}$ for $m = 1, \cdots, 4$, resulting from the resolution of the characteristic polynomial $P_\lambda = \det(\widetilde{\mathbf{M}} - \widetilde{\lambda}\mathbf{I}) = 0$, being $\mathbf{I}$ the 4×4 identity matrix

$$P_\lambda = (\widetilde{u} - \widetilde{\lambda})\left[-\widetilde{\lambda}[(\widetilde{u} - \widetilde{\lambda})^2 - \widetilde{c}^2] + \widetilde{c}^2\widetilde{a}(\widetilde{\lambda} - \widetilde{u})\right] = 0 \tag{5.39}$$

where $\widetilde{c} = \sqrt{g\widetilde{h}}$ is the averaged celerity of the infinitesimal waves. One of the approximate eigenvalues $\widetilde{\lambda}_{m,k}$ takes the value of the edge-averaged normal velocity $\widetilde{u}$, corresponding to the tangential shear wave in the RP structure. The remaining three eigenvalues, referred to as $\mathcal{A}$, $\mathcal{B}$ and $\mathcal{C}$, can be computed exactly applying the Cardano-Vieta formula to solve the roots of the cubic polynomial $R_\lambda = -\widetilde{\lambda}[(\widetilde{u} - \widetilde{\lambda})^2 - \widetilde{c}^2] + \widetilde{c}^2\widetilde{a}(\widetilde{\lambda} - \widetilde{u}) = 0$, which can be rewritten as

$$R_\lambda = \widetilde{\lambda}^3 + c_1\widetilde{\lambda}^2 + c_2\widetilde{\lambda} + c_3 = 0 \tag{5.40}$$

with the coefficients

$$\begin{aligned} c_1 &= -2\widetilde{u} \\ c_2 &= \widetilde{u}^2 - \widetilde{c}^2 - \widetilde{c}^2\widetilde{a} \\ c_3 &= \widetilde{c}^2\widetilde{a}\widetilde{u} \end{aligned} \tag{5.41}$$

Therefore, $\mathcal{A}$, $\mathcal{B}$ and $\mathcal{C}$ can be analytically computed [23] as

$$\begin{aligned} \mathcal{A} &= 2\sqrt{-L}\cos(\phi/3) - c_1/3 \\ \mathcal{B} &= 2\sqrt{-L}\cos(\phi/3 + 2\pi/3) - c_1/3 \\ \mathcal{C} &= 2\sqrt{-L}\cos(\phi/3 + 4\pi/3) - c_1/3 \end{aligned} \tag{5.42}$$

where

$$L = \frac{3c_2 - c_1^2}{9} \qquad \phi = \arccos\left(\frac{R}{\sqrt{-L^3}}\right) \qquad R = \frac{9c_1c_2 - 27c_3 - 2c_1^3}{54} \tag{5.43}$$

Furthermore, the eigenvalues $\mathcal{A}$, $\mathcal{B}$ and $\mathcal{C}$ of the sub-polynomial R_λ can be analysed graphically as intersection of the cubic curve

$$f_1(\widetilde{\lambda}) = \widetilde{\lambda}\left[(\widetilde{u} - \widetilde{\lambda})^2 - \widetilde{c}^2\right] \tag{5.44}$$

representing the hydrodynamical component of the system, with the straight line

$$f_2(\widetilde{\lambda}) = \widetilde{c}^2\widetilde{a}(\widetilde{\lambda} - \widetilde{u}) \tag{5.45}$$

Considering right-going motion $\widetilde{u} > 0$, regardless of subcritical or supercritical flow regime, the eigenvalues $\widetilde{\lambda}_{m,k}$ can be sorted (Figure 5.1) as follows

$$\widetilde{\lambda}_{1,k} = \mathcal{A} < 0 < \widetilde{\lambda}_{2,k} = \mathcal{B} < \widetilde{\lambda}_{3,k} = \widetilde{u}_k < \widetilde{\lambda}_{4,k} = \mathcal{C} \tag{5.46}$$

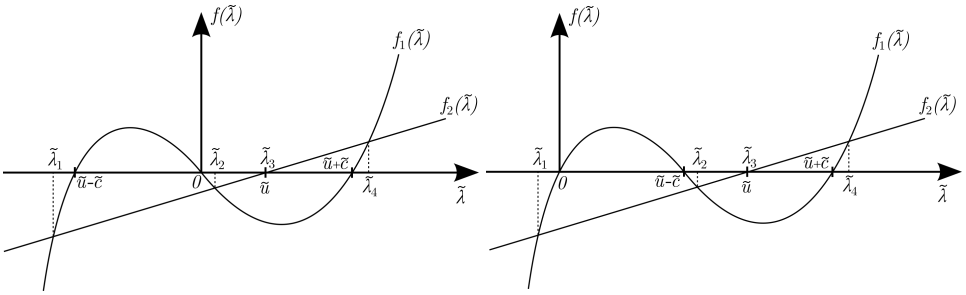

(a) Subcritical regime. (b) Supercritical regime.

Figure 5.1: Graphical representation of the coupled eigenvalues for right-going flow $\widetilde{u} > 0$.

Similarly, for left-going flow $\widetilde{u} < 0$, regardless of subcritical or supercritical flow regime, the coupled eigenvalues are sorted (Figure 5.2) as

$$\widetilde{\lambda}_{1,k} = \mathcal{A} < \widetilde{\lambda}_{2,k} = \widetilde{u}_k < \widetilde{\lambda}_{3,k} = \mathcal{B} < 0 < \widetilde{\lambda}_{4,k} = \mathcal{C} \tag{5.47}$$

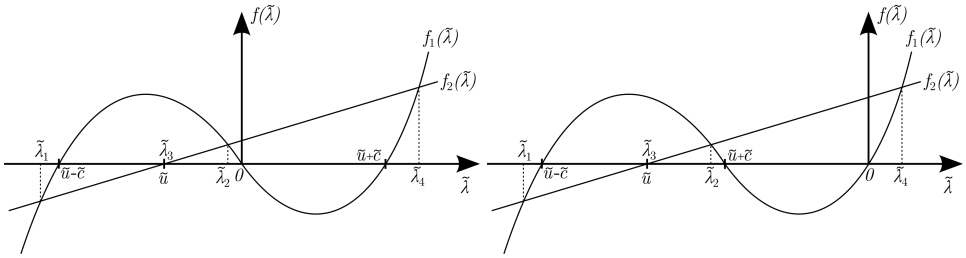

(a) Subcritical regime. (b) Supercritical regime.

Figure 5.2: Graphical representation of the coupled eigenvalues for left-going flow $\widetilde{u} < 0$.

and, in addition, it can be demonstrated that

$$\widetilde{\lambda}_{1,k} < (\widetilde{u} - \widetilde{c})_k \qquad \widetilde{\lambda}_{4,k} > (\widetilde{u} + \widetilde{c})_k \tag{5.48}$$

Therefore, it is possible to conclude that:

i) One of the eigenvalues has always opposite direction to the flow, transporting information upstream, and the remaining three eigenvalues have the same direction as the flow;

ii) The maximum wave celerity in the coupled eigenstructure is higher than the pure hydrodynamic wave celerity, reducing the actual stability region of the local RP.

From now on, we consider right-going flow $\widetilde{u} > 0$ for the sake of clarity but the following results can be straightforwardly derived for left-going flow $\widetilde{u} < 0$. The associated orthogonal basis of eigenvectors $(\widetilde{\mathbf{e}}_m)_k$ of $\widetilde{\mathbf{M}}_k$ is used to built the matrix $\widetilde{\mathbf{P}}_k = (\widetilde{\mathbf{e}}_1, \widetilde{\mathbf{e}}_2, \widetilde{\mathbf{e}}_3, \widetilde{\mathbf{e}}_4)_k$ as

$$\widetilde{\mathbf{P}}_k = \begin{pmatrix} 1 & 1 & \widetilde{c}^2\widetilde{b} & 1 \\ \widetilde{\lambda}_1 & \widetilde{\lambda}_2 & \widetilde{c}^2\widetilde{b}\widetilde{u} & \widetilde{\lambda}_4 \\ \widetilde{v} & \widetilde{v} & \widetilde{c}^2(\widetilde{v}\widetilde{b} - \widetilde{u}) & \widetilde{v} \\ \dfrac{(\widetilde{\lambda}_1 - \widetilde{u})^2 - \widetilde{c}^2}{\widetilde{c}^2} & \dfrac{(\widetilde{\lambda}_2 - \widetilde{u})^2 - \widetilde{c}^2}{\widetilde{c}^2} & -\widetilde{c}^2\widetilde{b} & \dfrac{(\widetilde{\lambda}_4 - \widetilde{u})^2 - \widetilde{c}^2}{\widetilde{c}^2} \end{pmatrix}_k \tag{5.49}$$

which satisfies

$$\widetilde{\mathbf{M}}_k = (\widetilde{\mathbf{P}}\widetilde{\mathbf{\Lambda}}\widetilde{\mathbf{P}}^{-1})_k \qquad \widetilde{\mathbf{\Lambda}}_k = \begin{pmatrix} \widetilde{\lambda}_1 & & 0 \\ & \ddots & \\ 0 & & \widetilde{\lambda}_4 \end{pmatrix}_k \tag{5.50}$$

being $\widetilde{\mathbf{P}}_k^{-1}$ the inverse matrix of $\widetilde{\mathbf{P}}_k$.

One result of Roe's linearization is that the approximate Riemann solution consists of only discontinuities and $\hat{\mathbf{U}}(\hat{x}, t)$ is constructed as a sum of jumps or shocks. The solution for $\hat{\mathbf{U}}(x, t)$ is governed by the celerities in $\widetilde{\mathbf{\Lambda}}_k$ and consists of four regions connected by 5 waves, one of them a contact wave with null celerity accounting for the integrated resistance source term $(\hat{\mathbf{S}}_{\boldsymbol{\tau}})_k$ at $\hat{x} = 0$. The intermediate states (blue regions) of the approximate

solution at the left and right side of the kth edge, $\hat{\mathbf{U}}_i^-$ and $\hat{\mathbf{U}}_j^+$ respectively, are defined as

$$\begin{aligned}\hat{\mathbf{U}}_i^- &= \lim_{\hat{x}\to 0^-} \hat{\mathbf{U}}(\hat{x},t)\\ \hat{\mathbf{U}}_j^+ &= \lim_{\hat{x}\to 0^+} \hat{\mathbf{U}}(\hat{x},t)\end{aligned} \tag{5.51}$$

and the numerical flux at the left and right side of the kth cell edge can be estimated using an approximate flux function $\hat{\mathbf{F}}(\hat{x},t)$ as

$$\mathbf{F}_k^{\downarrow}(\hat{x}\to 0^-) = \lim_{\hat{x}\to 0^-} \hat{\mathbf{F}}(\hat{x},t) \equiv \mathbf{F}_k^{\downarrow -} \tag{5.52a}$$

$$\mathbf{F}_k^{\downarrow}(\hat{x}\to 0^+) = \lim_{\hat{x}\to 0^+} \hat{\mathbf{F}}(\hat{x},t) \equiv \mathbf{F}_k^{\downarrow +} \tag{5.52b}$$

Following [138], the conserved variable differences $\boldsymbol{\delta}\hat{\mathbf{U}}_k$ and the integrated resistance source terms $\widetilde{\mathbf{T}}_k$ (5.27) at the cell edge are projected on the eigenvector basis in order to obtain the wave and source strength vectors, $\widetilde{\mathbf{A}}_k$ and $\widetilde{\mathbf{B}}_k$ respectively leading to

$$\begin{aligned}\widetilde{\mathbf{A}}_k = (\widetilde{\alpha}_1,\,\ldots,\widetilde{\alpha}_4)_k^T = \widetilde{\mathbf{P}}_k^{-\mathbf{1}}\,\boldsymbol{\delta}\hat{\mathbf{U}}_k \quad &\longrightarrow \quad \boldsymbol{\delta}\hat{\mathbf{U}}_k = \sum_{m=1}^{4}(\widetilde{\alpha}_m\widetilde{\mathbf{e}}_m)_k\\ \widetilde{\mathbf{B}}_k = (\widetilde{\beta}_1,\,\ldots,\,\widetilde{\beta}_4)_k^T = \widetilde{\mathbf{P}}_k^{-\mathbf{1}}\,\widetilde{\mathbf{T}}_k \quad &\longrightarrow \quad \widetilde{\mathbf{T}}_k = \sum_{m=1}^{4}(\widetilde{\beta}_m\widetilde{\mathbf{e}}_m)_k\end{aligned} \tag{5.53}$$

The wave strengths $\widetilde{\alpha}_m$ are

$$\widetilde{\mathbf{A}}_k \equiv \begin{cases} \widetilde{\alpha}_m = \dfrac{\mathcal{W}_m^1}{\mathcal{D}_m}\,\delta(h) + \dfrac{\mathcal{W}_m^2}{\mathcal{D}_m}\,\delta(h\hat{u}) + \dfrac{\mathcal{W}_m^3}{\mathcal{D}_m}\,\delta(h\hat{v}) + \dfrac{\mathcal{W}_m^4}{\mathcal{D}_m}\,\delta(z_b) \quad \text{for} \quad m=1,2,4 \\ \widetilde{\alpha}_3 = \dfrac{\widetilde{v}}{\widetilde{c}^2\widetilde{u}}\,\delta(h) - \dfrac{1}{\widetilde{c}^2\widetilde{u}}\,\delta(h\hat{v}) \end{cases} \tag{5.54}$$

being the coefficients $\mathcal{W}_m$ and $\mathcal{D}_m$:

$$\begin{aligned}\mathcal{W}_m^1 &= \widetilde{u}\Big(\widetilde{c}^2 - \widetilde{u}^2 + \prod_{r\neq m}\widetilde{\lambda}_r\Big) - \widetilde{v}\widetilde{b}\Big(\widetilde{u}^2 - \widetilde{u}\sum_{r\neq m}\widetilde{\lambda}_r + \prod_{r\neq m}\widetilde{\lambda}_r\Big)\\ \mathcal{W}_m^2 &= \widetilde{u}\Big(2\widetilde{u} - \sum_{r\neq m}\widetilde{\lambda}_r\Big)\\ \mathcal{W}_m^3 &= \widetilde{b}\Big(\widetilde{u}^2 - \widetilde{u}\sum_{r\neq m}\widetilde{\lambda}_r + \prod_{r\neq m}\widetilde{\lambda}_r\Big)\\ \mathcal{W}_m^4 &= \widetilde{c}^2\widetilde{u}\\ \mathcal{D}_m &= \widetilde{u}\Big(\widetilde{\lambda}_m^2 - \widetilde{\lambda}_m\sum_{r\neq m}\widetilde{\lambda}_r + \prod_{r\neq m}\widetilde{\lambda}_r\Big)\end{aligned} \tag{5.55}$$

The source strengths $\widetilde{\beta}_m$ can be expressed as

$$\widetilde{\mathbf{B}}_k \equiv \begin{cases} \widetilde{\beta}_m = \dfrac{\mathcal{W}_m^2}{\mathcal{D}_m}\widetilde{T} \quad \text{for} \quad m = 1, 2, 4 \\ \\ \widetilde{\beta}_3 = 0 \end{cases} \tag{5.56}$$

where the coefficients $\mathcal{W}_m^2$ and $\mathcal{D}_m$ are defined as in (5.55) and $\widetilde{T}$ is the resistance momentum contribution spatially integrated in the control volume corresponding to the cell edge (5.27).

Using these projections, the reconstruction of the approximated solution at the left and right sides of the cell edge [91], $\hat{\mathbf{U}}_i^-$ and $\hat{\mathbf{U}}_j^+$ respectively, can be expressed as

$$\begin{aligned} \hat{\mathbf{U}}_i^- &= \hat{\mathbf{U}}_i + \sum_{m-} (\widetilde{\gamma}_m \widetilde{\mathbf{e}}_m)_k \\ \hat{\mathbf{U}}_j^+ &= \hat{\mathbf{U}}_j - \sum_{m+} (\widetilde{\gamma}_m \widetilde{\mathbf{e}}_m)_k \end{aligned} \tag{5.57}$$

where $\widetilde{\gamma}_m = \widetilde{\alpha}_m - \widetilde{\beta}_m / \widetilde{\lambda}_m$ and the subscript $m-$ and $m+$ under the sums indicate waves traveling inward and outward the i cell.

Therefore, the approximated solution for the flux function $\mathbf{F}(\hat{x}, t)$ can also be constructed by defining appropriate Rankine-Hugoniot (RH) relations across each moving wave. The solution of the approximate flux function provides the definition of the numerical fluxes at the left and right sides, $\mathbf{F}_k^{\downarrow -}$ and $\mathbf{F}_j^{\downarrow +}$ respectively, of the kth cell edge following

$$\begin{aligned} \mathbf{F}_k^{\downarrow -} &= \mathbf{F}(\hat{\mathbf{U}}_i) + \sum_{m-} (\widetilde{\lambda}_m \widetilde{\gamma}_m \widetilde{\mathbf{e}}_m)_k \\ \mathbf{F}_k^{\downarrow +} &= \mathbf{F}(\hat{\mathbf{U}}_j) - \sum_{m+} (\widetilde{\lambda}_m \widetilde{\gamma}_m \widetilde{\mathbf{e}}_m)_k \end{aligned} \tag{5.58}$$

Note that, when momentum source terms are incorporated into the Riemann solver, it is no longer possible to define a unique value of the numerical flux at both sides of the cell edge [128]. The relation between the approximate fluxes $\mathbf{F}_k^{\downarrow -}$ and $\mathbf{F}_k^{\downarrow +}$ can be analyzed using the Rankine-Hugoniot (RH) relation at $\hat{x} = 0$. The corresponding flux difference is given by

$$\mathbf{F}_k^{\downarrow +} - \mathbf{F}_k^{\downarrow -} = \sum_{m=1}^{4} (\widetilde{\beta}_m \widetilde{\mathbf{e}}_m)_k = \widetilde{\mathbf{T}}_k \tag{5.59}$$

The inward fluxes $\mathbf{F}_k^{\downarrow -}$ provides the four component of the numerical flux vector required in (5.33) for updating the conserved variables in the i cell and hence

$$\mathbf{F}_k^{\downarrow} = \mathbf{F}_k^{\downarrow -} \tag{5.60}$$

Finally, in order to ensure the stability of the explicitly computed numerical solution, the time step should be small enough to avoid the interaction of waves from neighbouring RP's. The dynamical limitation of the time step at the kth edge is addressed here assuming that the fastest wave

celerity corresponds to the absolute maximum of the eigenvalues of $\widetilde{\mathbf{M}}_k$ (5.36)

$$\Delta t_k = \frac{\min(A_i, A_j)}{l_k \max_m(|\widetilde{\lambda}_{m,k}|)} \tag{5.61}$$

and the global time step $\Delta t = t^{n+1} - t^n$ is limited using the Courant-Friedrichs-Lewy (CFL) condition as

$$\Delta t = \text{CFL} \min_k(\Delta t_k) \tag{5.62}$$

with $\text{CFL} < 0.5$ for square orthogonal meshes and $\text{CFL} < 1$ for the triangular mesh topology and 1D-mesh cases.

5.2.2 Approximate-coupled Riemann solver (ACM)

A second approach is addressed in this thesis to solve the numerical fluxes $\mathbf{F}_k^{\downarrow}$ (5.30) at intercell edges. This strategy consists of solving separately the hydrodynamical equations (5.1) and the continuity equation for the bed layer (5.2) at each time step. The mass and momentum numerical fluxes in (5.33) for the hydrodynamical equations, referred to as $\mathbf{F}_k^{\downarrow\{1,2,3\}}$, are computed approximating the local plane RP (5.34) at each kth cell edge by means of a constant-coefficients linear RP defined as

$$\begin{gathered}\frac{\partial \hat{\mathbf{U}}'}{\partial t} + \widetilde{\mathbf{J}'}_k \frac{\partial \hat{\mathbf{U}}'}{\partial \hat{x}} = (\widetilde{\mathbf{S}}_{\mathbf{b}} + \widetilde{\mathbf{S}}_{\boldsymbol{\tau}})_k \\ \hat{\mathbf{U}}'(\hat{x}, 0) = \begin{cases} \hat{\mathbf{U}}'_i = \mathbf{R}_k(\mathbf{U}')_i^n & \text{if} \quad \hat{x} < 0 \\ \hat{\mathbf{U}}'_j = \mathbf{R}_k(\mathbf{U}')_j^n & \text{if} \quad \hat{x} > 0 \end{cases}\end{gathered} \tag{5.63}$$

where $\hat{\mathbf{U}}' = (h, h\hat{u}, h\hat{v})^T$ is the reduced set of hydrodynamical conserved variables, $(\widetilde{\mathbf{S}}_{\mathbf{b}})_k$ and $(\widetilde{\mathbf{S}}_{\boldsymbol{\tau}})_k$ are the edge-averaged bed-pressure and flow resistance momentum term, (5.24) and (5.28) respectively.

Following the above Chapter 4, the matrix $\widetilde{\mathbf{J}}'_k = \mathbf{J}'_k(\hat{\mathbf{U}}'_i, \hat{\mathbf{U}}'_j)$ is the 3×3 constant coefficient Jacobian of the local hydrodynamical RP, defined as

$$\widetilde{\mathbf{J}}'_k = \begin{pmatrix} 0 & 1 & 0 \\ g\widetilde{h} - \widetilde{u}^2 & 2\widetilde{u} & 0 \\ -\widetilde{u}\widetilde{v} & \widetilde{v} & \widetilde{u} \end{pmatrix}_k \tag{5.64}$$

being the constant coefficients defined as in (5.38).

The three eigenvalues of $\widetilde{\mathbf{J}}'_k$ are

$$\widetilde{\lambda}'_{1,k} = (\widetilde{u} - \widetilde{c})_k < \widetilde{\lambda}'_{2,k} = \widetilde{u}_k < \widetilde{\lambda}'_{3,k} = (\widetilde{u} + \widetilde{c})_k \tag{5.65}$$

with the associated eigenvectors $\widetilde{\mathbf{e}}'_{m,k}$ matrix expressed as

$$\widetilde{\mathbf{P}}'_k = (\widetilde{\mathbf{e}}'_1, \widetilde{\mathbf{e}}'_2, \widetilde{\mathbf{e}}'_3)_k = \begin{pmatrix} 1 & 0 & 1 \\ \widetilde{\lambda}'_1 & 0 & \widetilde{\lambda}'_3 \\ \widetilde{v} & \widetilde{c} & \widetilde{v} \end{pmatrix}_k \tag{5.66}$$

Following the procedure detailed above for the fully-coupled Riemann solver, the discrete increments in the hydrodynamical conserved variables

$\boldsymbol{\delta}\hat{\mathbf{U}}'_k$ are projected on the orthogonal basis of eigenvectors to obtain the wave strength vector, $\widetilde{\mathbf{A}}'_k$, as

$$\widetilde{\mathbf{A}}'_k = (\widetilde{\alpha}'_1, \ldots, \widetilde{\alpha}'_3)^T_k = \widetilde{\mathbf{P}}'^{-1}_k \boldsymbol{\delta}\hat{\mathbf{U}}'_k \tag{5.67}$$

where the wave strengths $\widetilde{\alpha}'_m$ are

$$\widetilde{\mathbf{A}}'_k \equiv \begin{cases} \widetilde{\alpha}'_1 = \dfrac{\widetilde{c}-\widetilde{u}}{2\widetilde{c}}\,\delta(h) - \dfrac{1}{2\widetilde{c}}\,\delta(h\hat{u}) \\ \widetilde{\alpha}'_2 = \dfrac{-\widetilde{v}}{\widetilde{c}}\,\delta(h) + \dfrac{1}{\widetilde{c}}\,\delta(h\hat{v}) \\ \widetilde{\alpha}'_3 = \dfrac{\widetilde{c}+\widetilde{u}}{2\widetilde{c}}\,\delta(h) + \dfrac{1}{2\widetilde{c}}\,\delta(h\hat{u}) \end{cases} \tag{5.68}$$

Similarly, the edge-integrated bed-pressure $\widetilde{\mathbf{H}}_k$ (5.23) and basal resistance $\widetilde{\mathbf{T}}_k$ (5.27) contributions are also projected on the orthogonal basis of eigenvectors to obtain the source strength vector $\widetilde{\mathbf{B}}'_k$ as

$$\widetilde{\mathbf{B}}'_k = (\widetilde{\beta}'_1, \ldots, \widetilde{\beta}'_3)^T_k = \widetilde{\mathbf{P}}'^{-1}_k \left(\widetilde{\mathbf{H}}_k + \widetilde{\mathbf{T}}_k\right) \tag{5.69}$$

with

$$\widetilde{\mathbf{B}}'_k \equiv \begin{cases} \widetilde{\beta}'_1 = -\dfrac{1}{2\widetilde{c}}\left(\widetilde{H}+\widetilde{T}\right) \\ \widetilde{\beta}'_2 = 0 \\ \widetilde{\beta}'_3 = \dfrac{1}{2\widetilde{c}}\left(\widetilde{H}+\widetilde{T}\right) \end{cases} \tag{5.70}$$

where $\widetilde{H}$ and $\widetilde{T}$ are the suitable values of the integrated bed-pressure and resistance momentum contributions at the cell edge.

Therefore, the hydrodynamical fluxes at the left side of the kth cell edge $\mathbf{F}_k^{\downarrow\{1,2,3\}}$ are obtained using

$$\mathbf{F}_k^{\downarrow\{1,2,3\}} = \mathbf{F}'^{\downarrow-}_k = \mathbf{F}(\hat{\mathbf{U}}'_i) + \sum_{m-} (\widetilde{\lambda}'_m \widetilde{\gamma}'_m \widetilde{\mathbf{e}}'_m)_k \tag{5.71}$$

where $\widetilde{\gamma}'_m = \widetilde{\alpha}'_m - \widetilde{\beta}'_m/\widetilde{\lambda}'_m$ and the subscript $m-$ under the sums indicates waves travelling inward the i cell. Finally, the hydrodynamical conserved variables (h, hu, hv) in the $(x,\, y)$ framework are updated using (5.33) and the augmented intercell fluxes (5.71).

The numerical flux for the bed layer continuity equation (5.2), referred as $\mathbf{F}_k^{\downarrow\{4\}}$, is computed separately at each time step by solving the following approximated scalar RP [65, 91]

$$\begin{aligned} &\frac{\partial z_b}{\partial t} + \widetilde{\lambda}_{b,k} \frac{\partial z_b}{\partial \hat{x}} = 0 \\ &z_b(\hat{x}, 0) = \begin{cases} (z_b)^n_i & \text{if} \quad \hat{x} < 0 \\ (z_b)^n_j & \text{if} \quad \hat{x} > 0 \end{cases} \end{aligned} \tag{5.72}$$

where a virtual bedload wave celerity $\widetilde{\lambda}_{b,k}$ is defined as:

$$\widetilde{\lambda}_{b,k} = \left(\frac{\delta \hat{q}_b}{\delta z_b}\right)_k \tag{5.73}$$

Note that the scalar RP (5.72) is homogeneous and hence there does not exist a jump between the left and right inner states of the approximate flux function at $\hat{x} = 0$. Therefore, it is possible to compute the bedload numerical flux at the k cell edge as

$$\mathbf{F}_k^{\downarrow\{4\}} = \begin{cases} (\hat{q}_b)_i^n & \text{if} \quad \widetilde{\lambda}_{b,k} > 0 \\ (\hat{q}_b)_j^n & \text{if} \quad \widetilde{\lambda}_{b,k} < 0 \end{cases} \tag{5.74}$$

and the morphodynamical conserved variable z_b is also updated using (5.33) with the intercell solid flux (5.74).

This separate formulation for the hydrodynamical and morphodynamical components of the system, and the corresponding separate numerical resolution, would lead to a decoupled model. It is known that totally decoupled schemes suffer from oscillations and instabilities in many flow conditions [26]. Previous works [24, 65] defined a weakly-coupled strategy by controlling the global numerical stability by means of the most restrictive among the hydrodynamic eigenvalues (5.65) and the virtual bed load celerity (5.73). This approach was useful but imposes an excessive time step restrictions under a wide range of flow configurations [91].

In order to ensure the stability of this decoupled scheme without reducing the computational performance, even for fast bed evolution conditions, a new strategy for the restriction of the time step is also proposed here. This strategy leads to an "approximate-coupling" of the hydrodynamical and morphodynamical components of the system. For each k cell edge, the maximum time step is limited considering the characteristic eigenstructure of the coupled pseudo-Jacobian $\widetilde{\mathbf{M}}_k$ (5.36). Following [26], even without calculating the exact eigenvalues $\widetilde{\lambda}_{m,k}$ from the characteristic equation $P_\lambda = 0$, their minimum and maximum values can be bounded into an approximated range $[\widetilde{\lambda}_1^*, \widetilde{\lambda}_4^*]_k$ using the mathematical properties of the characteristic polynomial P_λ (5.39).

The eigenvalues $\mathcal{A}$, $\mathcal{B}$ and $\mathcal{C}$ of the sub-polynomial R_λ (5.39) can be analyzed graphically as intersection of a cubic curve $f_1(\widetilde{\lambda})$ (5.44) representing the hydrodynamical component of the system, with a straight line $f_2(\widetilde{\lambda})$ (5.45) accounting for the morphodynamic component. This is shown in Figure 5.3 considering right-going subcritical flow $\widetilde{u} > 0$ but the procedure can bed extended to supercritical conditions and left-going flow $\widetilde{u} < 0$ without loss of generality (see Figures 5.1 and 5.2).

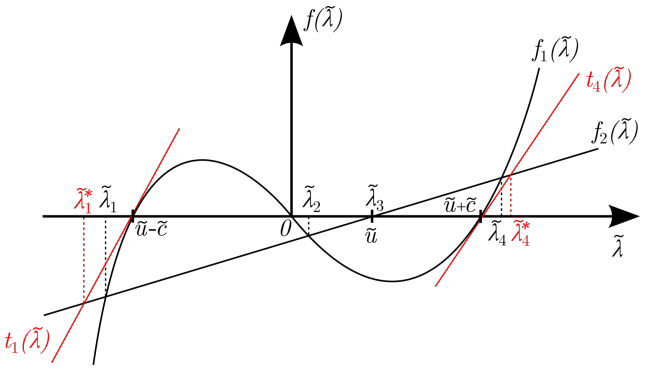

Figure 5.3: Bounds for the time step limitation using AC method, considering right-going flow $\widetilde{u} > 0$ and subcritical regime.

The lower and upper bounds, $\widetilde{\lambda}_1^*$ and $\widetilde{\lambda}_4^*$ respectively, can be estimated as the intersection of the straight line $f_2(\widetilde{\lambda})$ (5.45) with two auxiliary straight lines $t_1(\widetilde{\lambda})$ and $t_4(\widetilde{\lambda})$. These auxiliary straight lines are tangential to the cubic function $f_1(\widetilde{\lambda})$ (5.44) at the points $(\widetilde{u}-\widetilde{c})_k$ and $(\widetilde{u}+\widetilde{c})_k$ respectively. Hence, the upper and lower bounds are computed as

$$\begin{aligned} &\text{Lower bound: } t_1(\widetilde{\lambda}) = f_2(\widetilde{\lambda}) \quad \Rightarrow \quad \widetilde{\lambda}_{1,k}^* = \left(\frac{(\widetilde{u}-\widetilde{c})\,\Theta_1 - \widetilde{c}^2\widetilde{a}\widetilde{u}}{\Theta_1 - \widetilde{c}^2\widetilde{a}} \right)_k \\ &\text{Upper bound: } t_4(\widetilde{\lambda}) = f_2(\widetilde{\lambda}) \quad \Rightarrow \quad \widetilde{\lambda}_{4,k}^* = \left(\frac{(\widetilde{u}+\widetilde{c})\,\Theta_4 - \widetilde{c}^2\widetilde{a}\widetilde{u}}{\Theta_4 - \widetilde{c}^2\widetilde{a}} \right)_k \end{aligned} \tag{5.75}$$

being the parameter

$$\Theta_1 = \left. \frac{\partial f_1}{\partial \widetilde{\lambda}} \right|_{\widetilde{\lambda}=(\widetilde{u}-\widetilde{c})_k} \tag{5.76}$$

the value of the first derivative of the cubic curve $f_1(\widetilde{\lambda})$ (5.44) at $\widetilde{\lambda} = (\widetilde{u}-\widetilde{c})_k$ and, similarly, the parameter

$$\Theta_4 = \left. \frac{\partial f_1}{\partial \widetilde{\lambda}} \right|_{\widetilde{\lambda}=(\widetilde{u}+\widetilde{c})_k} \tag{5.77}$$

the value of the first derivative of $f_1(\widetilde{\lambda})$ (5.44) at $\widetilde{\lambda} = (\widetilde{u}+\widetilde{c})_k$.

Finally, the limiting time step at kth cell edge is computed using

$$\Delta t_k = \frac{\min(A_i, A_j)}{l_k \, \max(|\widetilde{\lambda}_{1,k}^*|, |\widetilde{\lambda}_{4,k}^*|)} \tag{5.78}$$

and the global time step $\Delta t = t^{n+1} - t^n$ is limited using the Courant-Friedrichs-Lewy (CFL) condition as

$$\Delta t = \text{CFL} \min_k(\Delta t_k) \tag{5.79}$$

with $\text{CFL} < 0.5$ for square orthogonal meshes and $\text{CFL} < 1$ for the triangular mesh topology and 1D-mesh cases.

Test 5.2.A: 1D bed evolution with transient exact solution

The goal of this test is to assess the capability of both numerical schemes, FCM and ACM, to converge to the exact solution of a transient bedload transport problem. An exact solution for the 1D shallow water-bedload system was proposed by Berthon *et al.* [6]. Considering a frictionless case with uniform flow discharge $q = hu$ and the Grass formulation for the bedload discharge, $q_b = A_g u^2 u$ with $A_g = \frac{1}{1-\xi} G = const$, the 1D transient

exact solution for system (5.1)–(5.2) can be expressed as:

$$
\begin{aligned}
u &= \left(\frac{\alpha x + \beta}{A_g}\right)^{2/3} \qquad\qquad h = q/u \\
z_b^0 &\equiv z_b(t=0) = -\frac{u^3 + 2gq}{2gu} + \gamma \\
z_b(t) &= z_b^0 - \alpha t
\end{aligned}
\tag{5.80}
$$

being α, β and γ constant parameters, g the gravity acceleration and z_b^0 the initial bed elevation. For this test case, $\alpha = 0.005$, $\beta = 0.005$, $\gamma = 2$, $q = 1\,m^2/s$ and $A_g = 0.01\,s^2/m$ are taken. Considering a 1D spatial domain $x = [0, 10]\,m$, the transient exact solution (5.80) for both the free surface elevation $h + z_b$ and the bed elevation z_b at time $t = 10\,s$ is shown in Figure 5.4.

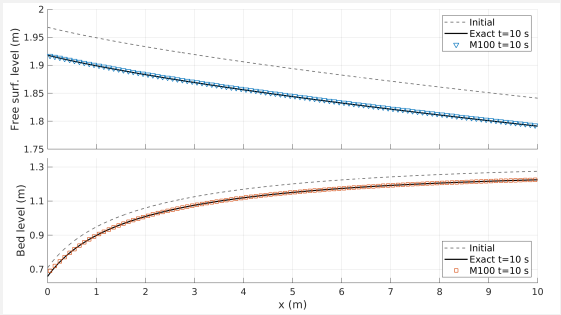

Figure 5.4: Test 5.2.A – Initial conditions and exact solutions for the free surface and bed elevations at $t = 10\,s$. Numerical results with the fully-coupled method (FCM) on the mesh M100 are also plotted.

In order to analyze the convergence of both numerical schemes (FCM and ACM) to the exact solution, six one-dimensional square-cell meshes are considered increasing the number of cells from the coarsest M100, with 100 cells of edge length $\Delta x = 0.1\,m$, to the finest M3200, with 3200 cells of edge length $\Delta x = 0.003125\,m$. Constant flow and bedload solid discharges, $q = 1\,m^2/s$ and $q_b = 0.005\,m^2/s$ respectively, are set as boundary conditions at the inlet section, whereas the normal flow depth $h = 0.5665\,m$ is imposed at the outlet boundary. The CFL is set to 1.0 for all the simulations.

The computed results at $t = 10\,s$ for the free surface and bed elevations using FCM on the mesh M100 have been depicted in Figure 5.4. The convergence of the FCM and ACM method to the exact solution is analyzed using the L_1 and L_∞ error norms. Figure 5.5–(a) shows the L_1 norm for the water depth h and bed elevation z_b with both FCM and ACM, whereas Figure 5.5–(b) shows the L_∞ error norm for h and z_b. The ACM solver obtains a smaller L_1 norm than the FCM method, whereas the values of the L_∞ norm are similar for both numerical schemes.

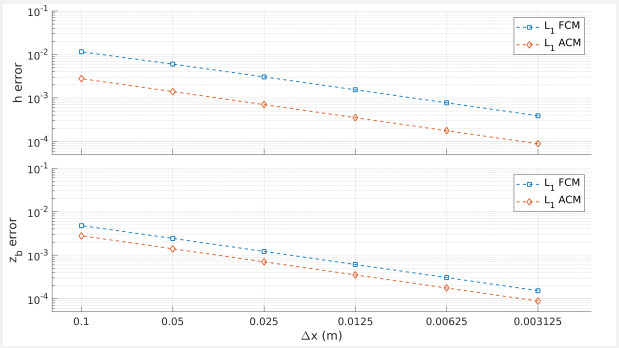

(a) L_1 error norms

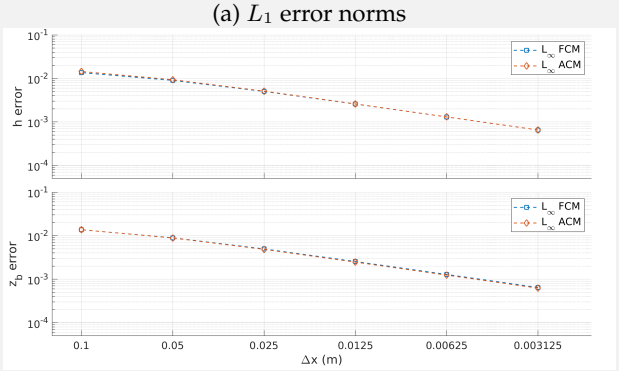

(b) L_∞ error norms

Figure 5.5: Test 5.2.A – Convergence errors for h and z_b with FCM and ACM numerical methods

The values of the L_1 and L_∞ error norms for the water depth h and the bed elevation z_b have been summarized in Tables 5.6 and 5.7 for the FCM and ACM schemes, respectively. The convergence order of both methods between refinement steps has also been computed based on the error norms values. Both the FCM and the ACM Riemann solvers are able to converge to the exact solution with a similar convergence order.

FCM		Water depth h			
Mesh	$\Delta x(m)$	L_1	Order	L_∞	Order
M100	0.1	1.15E-2	-	1.36E-2	-
M200	0.05	5.99E-3	0.942	9.01E-3	0.592
M400	0.025	3.05E-3	0.973	5.02E-3	0.844
M800	0.0125	1.54E-3	0.987	2.58E-3	0.960
M1600	0.00625	7.74E-4	0.992	1.30E-3	0.986
M3200	0.003125	3.88E-4	0.994	6.53E-4	0.995
FCM		Bed level z_b			
Mesh	$\Delta x(m)$	L_1	Order	L_∞	Order
M100	0.1	4.78E-3	-	1.36E-2	-
M200	0.05	2.23E-3	0.979	8.95E-3	0.611
M400	0.025	1.22E-3	0.991	4.97E-3	0.850
M800	0.0125	6.11E-4	0.998	2.55E-3	0.961
M1600	0.00625	3.06E-4	0.999	1.28E-3	0.986
M3200	0.003125	1.53E-4	1.000	6.46E-4	0.994

Figure 5.6: Test 5.2.A – Convergence analysis for FCM method.

ACM		Water depth h			
Mesh	$\Delta x(m)$	L_1	Order	L_∞	Order
M100	0.1	2.78E-3	-	1.44E-2	-
M200	0.05	1.40E-3	0.988	9.33E-3	0.629
M400	0.025	7.03E-4	0.994	5.10E-3	0.870
M800	0.0125	3.52E-4	0.997	2.59E-3	0.975
M1600	0.00625	1.76E-4	0.997	1.31E-3	0.992
M3200	0.003125	8.87E-5	0.991	6.54E-3	0.996
ACM		Bed level z_b			
Mesh	$\Delta x(m)$	L_1	Order	L_∞	Order
M100	0.1	2.79E-3	-	1.37E-2	-
M200	0.05	1.40E-3	0.994	8.87E-3	0.630
M400	0.025	7.03E-4	0.997	4.85E-3	0.870
M800	0.0125	3.52E-4	0.998	2.46E-3	0.975
M1600	0.00625	1.76E-4	1.000	1.24E-3	0.991
M3200	0.003125	8.83E-5	0.997	6.22E-4	0.996

Figure 5.7: Test 5.2.A – Convergence analysis for ACM method.

Test 5.2.B: 1D subcritical symmetric dambreak over erodible bed

This synthetic test aims at assessing the stability of both FCM and ACM as the bedload transport component increases its importance. A frictionless 1D symmetrical dambreak over erodible flat bed is considered with the following initial conditions:

$$\begin{aligned} h(x,0) &= \begin{cases} 1\,m & \text{if } -0.5 \leq x \leq 0.5 \\ 0.2\,m & \text{otherwise} \end{cases} \\ u(x,0) &= 0\,m/s \quad \forall x \\ v(x,0) &= 0\,m/s \quad \forall x \\ z_b(x,0) &= 1\,m \quad \forall x \end{aligned} \tag{5.81}$$

which allow subcritical flow ($Fr = |u|/\sqrt{gh} < 1$) during the whole test. The bedload transport rate is calculated considering one sediment class with porosity $\xi = 0.40$ and three different constant flow-bed interaction factors: $G = 0.001\,s^2/m$ (low interaction), $G = 0.01\,s^2/m$ (medium interaction) and $G = 0.1\,s^2/m$ (high interaction). All the simulations are performed using a one-dimensional square-cell mesh with $\Delta x = 0.01\,m$ edge length and CFL $= 1$.The final time is $t = 1.0\,s$ for all the simulations.
Figure 5.8 shows the free surface and bed elevation profiles at $t = 0.1\,s$, $t = 0.3\,s$ and $t = 0.6\,s$ with both FCM and ACM numerical schemes for the low interaction $G = 0.001\,s^2/m$ case. On both sides of the symmetric dambreak, the solution is characterized by a frontal shock wave which affects the flow and erodible bed layers, followed by a rarefaction wave between the domain center and the front wave which creates a highly eroded region. As the interaction factor G grows, the magnitude of the sediment shock wave and the highly-eroded region increase, affecting greatly the flow structure.

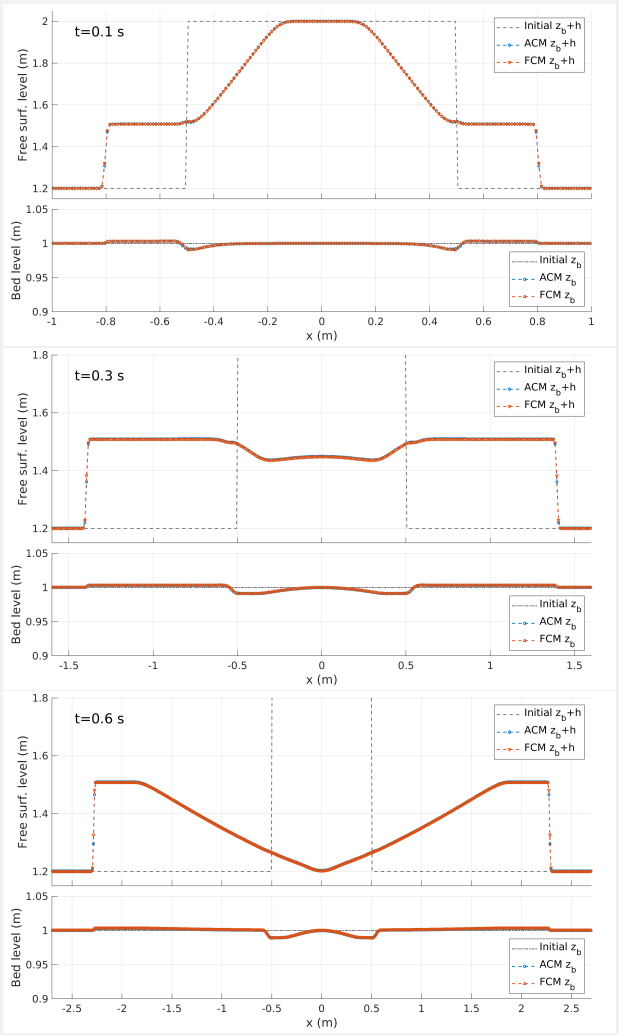

Figure 5.8: Test 5.2.B – Subcritical dambreak evolution with ACM and FCM models for a constant Grass interaction factor $G = 0.001\, s^2/m$. From top to bottom: $t = 0.1\, s$, $t = 0.3\, s$ and $t = 0.6\, s$

For low interaction $G = 0.001\, s^2/m$ (see Figure 5.8), both methods remain stable and show quite similar solutions for the free surface and bed elevation. As G increases, differences between the FCM and the ACM schemes appear. For medium interaction factor $G = 0.01\, s^2/m$ (Figure 5.9, although both schemes offer a stable behaviour, some differences appear at the bed level profile as time progresses, especially at the transition between the shock wave and the rarefaction region.

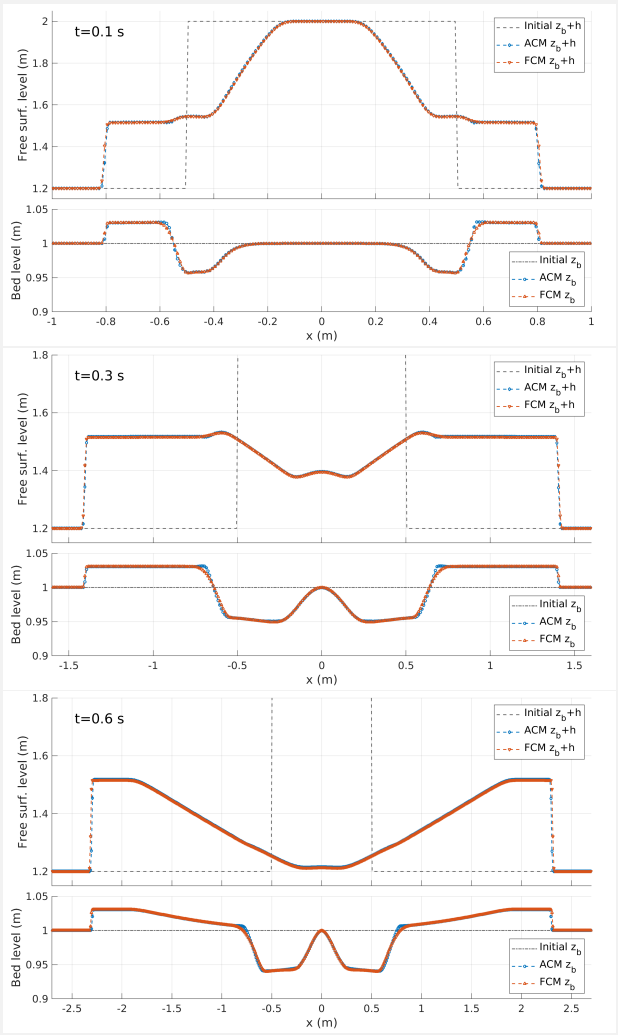

Figure 5.9: Test 5.2.B – Subcritical dambreak evolution with ACM and FCM models for a constant Grass interaction factor $G = 0.01\, s^2/m$. From top to bottom: $t = 0.1\, s$, $t = 0.3\, s$ and $t = 0.6\, s$

When the value of G is increased to $0.1\, s^2/m$, representing a high interaction between the flow and the bedload layer (see Figure 5.10), the ACM scheme becomes oscillatory near the shock-rarefaction transition at the first stages of the dambreak. As time progresses, these spurious oscillations grow and cause the ACM solution to lose its symmetric behaviour. However, the FCM solution remains stable, smooth and symmetrical even for these high interaction factor values. High values of bed-flow interaction can appear locally in real-scale two-dimensional flows when the bed shear stress increases over a certain threshold, leading to the failure of the ACM prediction at these regions.

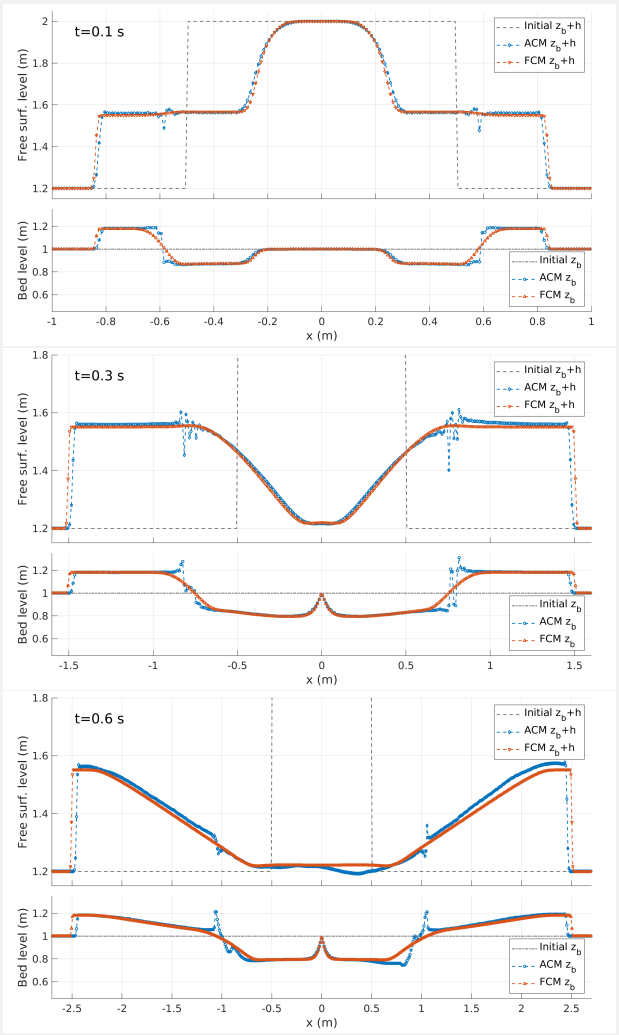

Figure 5.10: Test 5.2.B – Subcritical dambreak evolution with ACM and FCM models for a constant Grass interaction factor $G = 0.1\, s^2/m$. From top to bottom: $t = 0.1\, s$, $t = 0.3\, s$ and $t = 0.6\, s$

Although the solution obtained with the ACM scheme loses symmetry and shows local spurious oscillations for high flow-bed interaction, the proposed approximate-coupled time step limitation applied in the ACM method demonstrates to improve greatly the stability of the scheme. Figure 5.11 shows the bed and flow levels at $t = 0.6\, s$ using the ACM scheme compared with the results obtained if only the flow eigenvalues (5.65) are taken into account for limiting the time step (totally decoupled scheme). Low ($G = 0.1\, s^2/m$), medium ($G = 0.1\, s^2/m$) and high ($G = 0.1\, s^2/m$) values for the Grass interaction factor are analyzed. For low and medium interaction factors the ACM and the totally decoupled methods perform almost similar in this synthetic test. However, if high interaction values are considered, the totally decoupled scheme fails catastrophically and the solution loses the stability whereas the ACM method only shows some local deviations from the FCM solution (see Figure 5.10). Although in this synthetic case, the decoupled method only shows stability loss for Grass factors of order $G > \mathcal{O}(10^{-1})$, the totally decoupled resolution can fail in a wide range of flow conditions which involves medium or even low bed-flow interaction [26].

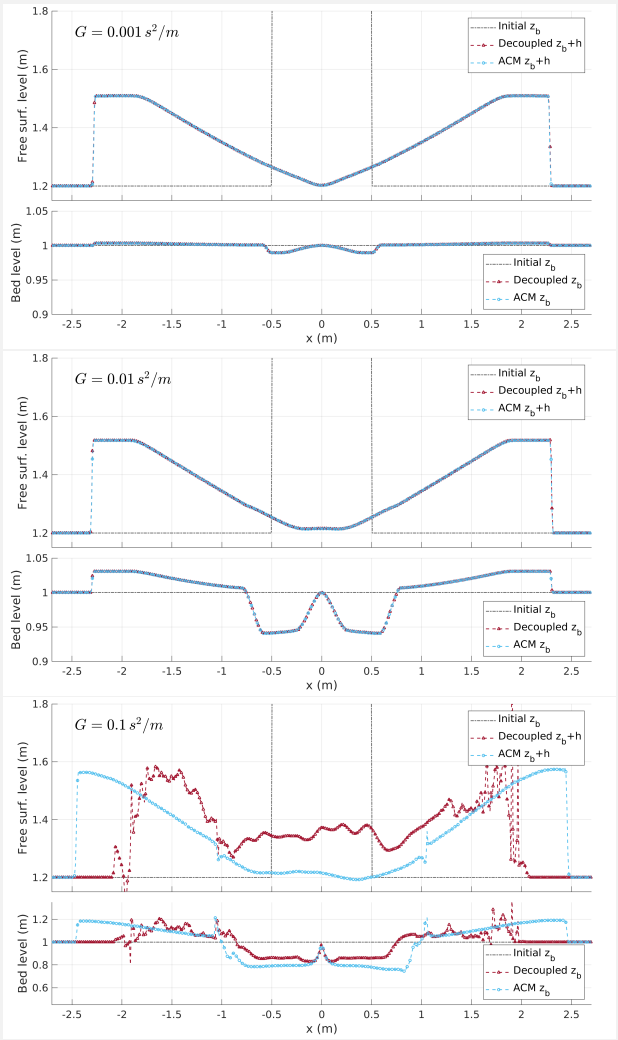

Figure 5.11: Test 5.2.B – Subcritical dambreak at $t = 0.6\,s$ with ACM and totally decoupled models for (top) $G = 0.001\,s^2/m$, (center) $G = 0.01\,s^2/m$ and (bottom) $G = 0.1\,s^2/m$.

Furthermore, Table 5.1 shows the computational time required for both numerical schemes to complete the simulation. The ACM method shows a slightly smaller computational effort for low and medium flow-bed interaction factor, since the FCM scheme requires more algebraical operations to compute the solution. Nevertheless, for high interaction factor, the appearance of spurious oscillations in the ACM solution causes an important loss of efficiency, whereas the FCM solver remains stable and requires a much smaller computational time to perform the simulation. The speed-up of the FCM solver is near 1.5 for high interaction factor $G = 0.1\,s^2/m$ test.

Inter. factor	Comp. time (s)		Speed-up
$G(s^2/m)$	ACM	FCM	ACM/FCM
0.001	0.501	0.513	0.98
0.01	0.522	0.549	0.95
0.1	0.933	0.633	1.47

Table 5.1: Test 5.2.B – Computation times for Test 5.2.B

5.3 Extension to generalized bedload transport

Following Section 2.3.3, the generalized Grass interaction factor G_p for the pth sediment class is calculated as a function of the flow depth h, the dimensionless size-specific Shields stress θ_p at the bed interface and the bedload transport layer thickness η_p as

$$G_p = \Gamma_1(h)\,\Gamma_2(\theta_p)\,\Gamma_3(\eta_p) \tag{5.82}$$

Formulation	$\Gamma_1(h)$	$\Gamma_2(\theta_p)$	$\Gamma_3(\eta_p)$	θ_c
MPM [97]	$\frac{n_p^3\sqrt{g}}{(r_p-1)\sqrt{h}}$	$\frac{8\sqrt{\Delta\theta_p}}{\theta_p^{3/2}}$	$\frac{r_p\,k_D}{k_E}\frac{\eta_p}{d_{s,p}}$	0.047
Smart [132]	$\frac{n_p^2}{(r_p-1)h^{1/3}}$	$\frac{4.2\,S^{0.6}}{\theta_p}$	$\frac{r_p\,k_D}{k_E}\frac{\eta_p}{d_{s,p}}$	0.047
Wu [144]	$\frac{(n_p^3 n_b)^{3/4}\sqrt{g}}{(r_p-1)\sqrt{h}}$	$\frac{0.0053\sqrt{\Delta\theta_p}}{\theta_{c,p}^{2.2}\,\theta_p^{3/2}}$	$\frac{r_p\,k_D}{k_E}\frac{\eta_p}{d_{s,p}}$	0.030

Table 5.2: Generalized Grass-type interaction factor G_p for transport rate formulations.

Expressions for functions Γ_1, Γ_2 and Γ_3 have been included in Table 5.2 for the empirical relations used in this chapter, but an extended list can be found in Table 2.2 of the Section 2.3.3. Here, $n_p = 1/21\,d_{s,p}^{1/6}$ is the Manning roughness parameter corresponding to the grain resistance of the pth sediment class, $r_p = \rho_{s,p}/\rho_w$ is the specific solid/liquid density ratio for the sediment particles, k_D and k_E are two positive constants associated to the detention and entrainment exchange rates between the bedload transport (moving) layer and the underlying static bed stratum, and θ_c is the global threshold of the Shields stress for the incipient motion. In the Smart [132] relation, the parameter S accounts for the bed slope along the sediment transport direction whereas n_b denotes the bulk Manning roughness parameter for the non-uniform bed layer in the Wu [144] relationship.

The Shields stress excess $\Delta\theta_p$ for the pth sediment class is calculated as

$$\Delta\theta_p = \begin{cases} \theta_p - \theta_{c,p} & \text{if} \quad \theta_p > \theta_{c,p} \\ 0 & \text{if} \quad \theta_p \leq \theta_{c,p} \end{cases} \tag{5.83}$$

being θ_p the specific dimensionless Shields stress, calculated using the ratio between the turbulent shear force exerted by the flow on the sediment grains at the top of the bed layer and the gravitational force as

$$\theta_p = \frac{n_p^2\,|\mathbf{u}|^2}{(r_p-1)\,d_{s,p}\,h^{1/3}} \tag{5.84}$$

and $\theta_{c,p}$ is the critical Shields threshold for the incipient motion of the pth sediment class, which here is graded from the global threshold θ_c including the hiding/exposure mechanism in non-uniform beds using the Egiazaroff [32] relation.

This generalized Grass-type model (5.82) for the bedload transport has two important advantages compared with classical capacity models:

- First, it allows the possibility to consider capacity or non-capacity hypothesis for the bedload solid transport by only changing the expression to calculate the moving layer thickness η_p of each sediment class. Assuming the capacity approach leads to an instantaneous adaptation of the bedload transport rate to its capacity value and the specific equilibrium transport thickness η_p^* can be estimated as

$$\eta_p \equiv \eta_p^* = \frac{k_E}{r_p\, k_D}\, \Delta\theta_p\, d_{s,p} \tag{5.85}$$

The non-capacity assumption requires to estimate the temporal evolution of the bedload layer thickness by solving the transport equation (2.125) for each pth sediment class as

$$\frac{\partial \eta_p}{\partial t} + \frac{1}{1-\xi}\frac{\partial}{\partial x}(G_p|\mathbf{u}|^2\, u) + \frac{1}{1-\xi}\frac{\partial}{\partial y}(G_p|\mathbf{u}|^2\, v) = - (\dot{\eta}_D - \dot{\eta}_E)_p \tag{5.86}$$

where $\dot{\eta}_{D,p}$ and $\dot{\eta}_{E,p}$ are the detention and entrainment exchange rates, respectively, between the bedload transport layer and the underlying static stratum for the pth sediment size class. This equation is added to the system 5.7 and solved separately at each time step, regardless of using FCM or ACM Riemann solver for the computation of the intercell numerical flux. The bed porosity effect is assumed similar for all the sediment fractions composing the non-uniform bed layer. Following (2.135) and (2.143), the detention and entrainment rates can be expressed as

$$\dot{\eta}_{D,p} = k_D \frac{\eta_p}{d_{s,p}} \frac{\sqrt{(r_p-1) g d_{s,p}^3}}{d_{s,p}} \tag{5.87a}$$

$$\dot{\eta}_{E,p} = k_E \frac{\Delta\theta_p}{r_p} \frac{\sqrt{(r_p-1) g d_{s,p}^3}}{d_{s,p}} \tag{5.87b}$$

- Second, using (5.3) and (5.82), the bulk thickness of the bedload transport layer in non-uniform beds can be assumed as

$$\eta = \sum_{p=1}^{\mathrm{N}} F_{b,p}\eta_p \tag{5.88}$$

When an underlying non-erodible stratum, i.e. a bedrock layer, is reached during the erosion process, the unavailability of sediment creates a special situation which is not considered by the classical bedload models but can be easily addressed with the proposed model. Considering an erodible layer depth $\epsilon_b = z_b - z_R$, being z_R the non-erodible layer elevation, if the transport (moving) layer thickness is higher than the available erodible depth, i.e. $\eta > \epsilon_b$, a non-capacity state in the bedload transport appears. This leads to a reduction of the actual solid discharge respect to its value for infinitely erodible layer

conditions. This non-equilibrium state is addressed by means of the reduction of the specific transport thickness η_p following

$$\eta_p' = \beta_R\, \eta_p \tag{5.89}$$

being $\beta_R = \epsilon_b/\eta$ a linear reduction coefficient and η_p' the actual bedload layer thickness over the non-erodible stratum. Note that, using (5.82), the reduction of the bedload thickness straightforwardly limits the specific bed-flow Grass interaction factor G_p for the pth sediment class. Hence, for a sediment unavailability situation ($\epsilon_b = 0$), the generalized bedload model adapts to null solid discharge ($G_p = 0$) regardless of considering capacity or non-capacity formulation.

5.3.1 Bedload updating with capacity and non-capacity approaches

Regardless of using FCM or ACM Riemann solver for the computation of the intercell numerical flux, the updating procedure for transport layer thickness depends on the assumption made for the bedload transport. Assuming the capacity hypothesis, the cell-centered value of the transport thickness for the pth sediment class at the next time step t^{n+1} is directly computed using (5.85) as

$$\eta_{p,i}^{n+1} = \frac{k_E}{r_p\, k_D}\, (\Delta\theta_p)_i^{n+1}\, d_{s,p} \tag{5.90}$$

where $(\Delta\theta_p)_i^{n+1}$ is the non-dimensional Shields excess (5.83) at the i cell computed with the conserved variables updated to time t^{n+1}. From now on, when the capacity formulation is used, the resulting model is referred to as R-Cap.

On the other hand, the assumption of the non-capacity approach requires to solve (5.86) for each sediment class at each time step using the updating formula

$$\eta_{p,i}^{n+1} = \eta_{p,i}^{n} - \frac{\Delta t}{A_i} \sum_{k=1}^{\mathrm{NE}} (F_p^{\eta})_k^{\downarrow}\, l_k - \Delta t\, (\dot\eta_D - \dot\eta_E)_{p,i}^{n} \tag{5.91}$$

being $(F_p^{\eta})_k^{\downarrow}$ the numerical flux at the kth intercell edge for the homogeneous transport equation of the pth sediment class and $(\dot\eta_D - \dot\eta_E)_{p,i}^{n}$ denotes the cell-centered balance between the specific detention and entrainment rates (5.87) at time t^n.

To compute the numerical flux $(F_p^{\eta})_k^{\downarrow}$ for the pth sediment class at the kth cell edge, the left hand side of the transport equation (5.86) is integrated along the normal direction to the edge and the numerical flux at the intercell interface is approximated using the linearized homogeneous RP [88]

$$\begin{aligned} &\frac{\partial \eta_p}{\partial t} + \widetilde{\lambda}_{\eta,k} \frac{\partial \eta_p}{\partial \hat{x}} = 0 \\ &\eta_p(\hat{x}, 0) = \begin{cases} \eta_{p,i}^{n} & \text{if} \quad \hat{x} < 0 \\ \eta_{p,j}^{n} & \text{if} \quad \hat{x} > 0 \end{cases} \end{aligned} \tag{5.92}$$

where the virtual bedload wave celerity $\widetilde{\lambda}_{\eta,k}$ is defined as

$$\widetilde{\lambda}_{\eta,k} = \frac{\Delta\left[G_p(\hat{u}^2+\hat{v}^2)\,\hat{u}\right]_k}{(1-\xi)\,\Delta(\eta_p)_k} \tag{5.93}$$

being $\Delta(\cdot)_k = (\cdot)_j^n - (\cdot)_i^n$ and $(\hat{u},\hat{v})$ the normal and tangential velocity to the cell edge, respectively. Therefore, the intercell numerical flux for the transport thickness of the pth sediment class is computed as

$$(F_p^{\eta})_k^{\downarrow} = \begin{cases} \frac{1}{1-\xi}\left[G_p(\hat{u}^2+\hat{v}^2)\,\hat{u}\right]_i^n & \text{if} \quad \widetilde{\lambda}_{\eta,k} > 0 \\ \frac{1}{1-\xi}\left[G_p(\hat{u}^2+\hat{v}^2)\,\hat{u}\right]_j^n & \text{if} \quad \widetilde{\lambda}_{\eta,k} < 0 \end{cases} \tag{5.94}$$

Regardless of considering capacity or non-capacity formulation, the updated value of the bedload thickness for the pth sediment class $\eta_{p,i}^{n+1}$ is limited following (5.89) to ensure the adaptation of the bedload transport rate to sediment unavailability conditions. Finally, the cell-centered value of the bed-flow Grass interaction factor G_p for the pth sediment class at the next time step t^{n+1} is computed using (5.82) as

$$G_{p,i}^{n+1} = \Gamma_1(h_i^{n+1})\,\Gamma_2(\theta_{p,i}^{n+1})\,\Gamma_3(\eta_{p,i}^{n+1}) \tag{5.95}$$

with Γ_1, Γ_2 and Γ_3 as in Table 5.2.

Therefore, the bulk Grass-type interaction factor G used to compute the bedload transport rate $\hat{q}_b$ normal to the kth cell edge in (5.19) varies spatially as a function of the local flow features at the left and right cells. Following [86, 87, 100], the discrete increment of the bedload solid flux throughout the intercell edges can be split as

$$(\delta\hat{q}_b)_k = \delta\hat{q}_b^{-}(G_i,\widetilde{G},\hat{\mathbf{U}}_i) + \delta\widetilde{q}_b(\widetilde{G},\hat{\mathbf{U}}_i,\hat{\mathbf{U}}_j) + \delta\hat{q}_b^{+}(\widetilde{G},G_j,\hat{\mathbf{U}}_j) \tag{5.96}$$

where

$$\begin{aligned} \delta\hat{q}_b^{-}(G_i,\widetilde{G},\hat{\mathbf{U}}_i) &= \hat{q}_b(\widetilde{G},\hat{\mathbf{U}}_i) - \hat{q}_b(G_i,\hat{\mathbf{U}}_i) \\ \delta\widetilde{q}_b(\widetilde{G},\hat{\mathbf{U}}_i,\hat{\mathbf{U}}_j) &= \hat{q}_b(\widetilde{G},\hat{\mathbf{U}}_j) - \hat{q}_b(\widetilde{G},\hat{\mathbf{U}}_i) \\ \delta\hat{q}_b^{+}(\widetilde{G},G_j,\hat{\mathbf{U}}_j) &= \hat{q}_b(G_j,\hat{\mathbf{U}}_j) - \hat{q}_b(\widetilde{G},\hat{\mathbf{U}}_j) \end{aligned} \tag{5.97}$$

$\widetilde{G}$ being the averaged bulk interaction factor at the kth cell edge.

Incorporating a non-uniform Grass interaction factor G into both the fully- and approximate-coupled Riemann solvers requires to consider this discrete solid flux splitting. Therefore, both corrector terms must be added to the computation of the numerical intercell bedload flux at the left and right sides of the cell edge, called $\boldsymbol{\delta}\mathbf{F}_i^{\Delta}$ and $\boldsymbol{\delta}\mathbf{F}_j^{\Delta}$ respectively. These corrector terms account for the variation of the bulk Grass interaction factor between the cell center value, G_i and G_j, and the averaged value $\widetilde{G}$ used at the edge [100]. The extended numerical fluxes at the left and right side of the kth cell edge are therefore defined as

$$\begin{aligned} \mathbf{F}_k^{\Rightarrow} &= \mathbf{F}_k^{\downarrow -} + \boldsymbol{\delta}\mathbf{F}_i^{\Delta} \\ \mathbf{F}_k^{\Leftarrow} &= \mathbf{F}_k^{\downarrow +} - \boldsymbol{\delta}\mathbf{F}_j^{\Delta} \end{aligned} \tag{5.98}$$

where $\mathbf{F}_k^{\downarrow -}$ and $\mathbf{F}_k^{\downarrow +}$ are calculated using (5.58) in the FCM solver and (5.71) plus (5.74) in the ACM solver, and the corrector term at the left $\boldsymbol{\delta}\mathbf{F}_i^{\Delta}$ and right $\boldsymbol{\delta}\mathbf{F}_j^{\Delta}$ sides of the edge are computed as

$$\begin{aligned}
\boldsymbol{\delta}\mathbf{F}_i^{\Delta} &= \begin{pmatrix} 0 \\ 0 \\ 0 \\ \frac{1}{1-\xi}(\widetilde{G} - G_i)(\hat{u}_i^2 + \hat{v}_i^2)\,\hat{u}_i \end{pmatrix}_k \\
\boldsymbol{\delta}\mathbf{F}_j^{\Delta} &= \begin{pmatrix} 0 \\ 0 \\ 0 \\ \frac{1}{1-\xi}(G_j - \widetilde{G})(\hat{u}_j^2 + \hat{v}_j^2)\,\hat{u}_j \end{pmatrix}_k
\end{aligned} \tag{5.99}$$

This splitting of the bedload solid flux is directly controlled by the value of the Grass interaction parameter $\widetilde{G}_k$ at the intercell edge an hence it is directly linked to the Jacobian matrix eigenstructure. The corrector flux at the left cell $\boldsymbol{\delta}\mathbf{F}_i^{\Delta}$ can be associated to the fastest wave travelling with negative velocity, whereas the corrector flux at the right cell $\boldsymbol{\delta}\mathbf{F}_j^{\Delta}$ can be associated to the fastest wave travelling with positive velocity. The Rankine-Hugoniot conditions for the split corrector fluxes lead to

$$\begin{aligned}
\boldsymbol{\delta}\mathbf{F}_i^{\Delta} &= \widetilde{\lambda}_1\,\boldsymbol{\delta}\hat{\mathbf{U}}_i^{\Delta} \\
\boldsymbol{\delta}\mathbf{F}_j^{\Delta} &= \widetilde{\lambda}_4\,\boldsymbol{\delta}\hat{\mathbf{U}}_j^{\Delta}
\end{aligned} \tag{5.100}$$

being $\boldsymbol{\delta}\hat{\mathbf{U}}_i^{\Delta}$ and $\boldsymbol{\delta}\hat{\mathbf{U}}_j^{\Delta}$ the contribution to the inner state of the approximate solution associated to the corrector fluxes.

Regardless of using FCM or ACM approaches, the final updating formula for the conserved variables $\mathbf{U}$ can be expressed as

$$\mathbf{U}_i^{n+1} = \mathbf{U}_i^n - \frac{\Delta t}{A_i}\sum_{k=1}^{\mathrm{NE}} \mathbf{R}_k^{-\mathbf{1}}\,\mathbf{F}_k^{\Rightarrow}\,l_k \tag{5.101}$$

Test 5.3.A: 1D transport of a finite-depth rectangular dune

The aim of this original test case is to study the influence of the non-capacity assumption on the transport of a non-cohesive rectangular dune over a non-erodible layer with a 0.1% positive slope. The effects of both the deposition constant value and the relation between erosion and deposition constants will be analyzed in detail using this erosive numerical test. The non-erodible layer with constant slope of $0.1\,\%$ is considered. The rectangular dune is placed at $20\,m < x < 40\,m$ and its initial thickness is set to $1\,m$. A constant inlet water discharge of $q_{in} = 5m^2/s$ is considered and the water depth at the outlet is set to the exact normal depth $h_{out} = 1.99526\,m$. The Manning's roughness coefficient is $n_b = 0.02\,sm^{-1/3}$ for both the sediment material and the non-erodible layer. A unique sediment class is considered with the following features: density $\rho_s = 2650\,kg/m^3$, particle diameter $d_s = 1\,mm$, internal friction angle $\delta_b = 35°$, porosity $\xi = 0.4$. The spatial domain is $100\,m$ long and

is discretized using one-row square-cell mesh with $\Delta x = 1\,m$. The FCM solver is used for the computation of the intercell flux and CFL=1 is set. The initial state for the sediment transport simulation was calculated developing the flow for static-bed conditions until steady state was reached (Fig. 5.12). The initial flow regime was subcritical in the whole domain except at $x = 40\,m$, where a supercritical point was reached due to the chute. To compute the bed-load solid transport rate, the Meyer-Peter & Müller [97] formulation was chosen (see Table 5.2). The deposition constant was initially set to $k_E = 0.3$ with a relation $k_E/k_D = 10$ according to literature values [10, 38]. The initial value for active layer thickness η was set to its value under equilibrium state η^*.

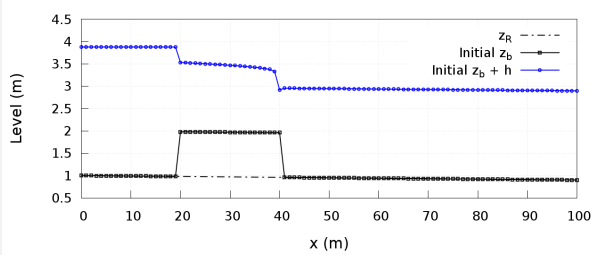

Figure 5.12: Test 5.3.A – Initial bed and steady-state free surface level for the erosive simulations.

The temporal bed level evolution has been depicted in Fig. 5.13 considering capacity and non-capacity approaches. A visual comparison of the bed profiles at different time shows the most noticeable differences between both approaches at the tail of the dune, where the Shields stress excess $\Delta\theta$ had the highest initial values and hence the adaptation length was longer. As the dune moves downstream, the erosion and deposition rates are high enough to allow a fast transition to equilibrium transport conditions on the bedload layer and hence the capacity and non-capacity solutions tended to approximate.

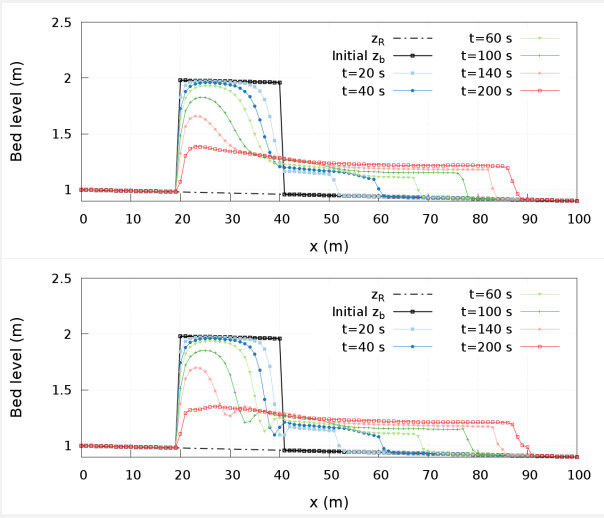

Figure 5.13: Test 5.3.A – Bed level evolution with $k_E = 0.3$ and $k_E/k_D = 10$: (top) capacity approach and (bottom) non-capacity approach.

Calibration of the erosion and deposition rates, i.e. the net exchange flux through the static-moving bed layers interface, is a key point in non-capacity bed-load models and it has a huge influence on the numerical results. A wide range of values for the erosion and deposition constants can be found in literature [10, 25, 37, 73], leading to high uncertainty in the numerical results obtained with non-capacity models. Usually, values for the erosion constant are of the order $k_E \sim \mathcal{O}(10^{-2}, 10^{1})$, whereas the relation k_E/k_D varies from 2 to 30. Fig. 5.14 shows the bed level profile at different times with the non-capacity approach, increasing k_E from 0.3 to 1.0 and maintaining the ratio $k_E/k_D = 10$. Reduction of the erosion constant k_E leads to an increment of the equivalent bedload adaptation length and hence to a transport rate more different from the equilibrium value at the dune downward slope. This non-equilibrium state reduced the solid transport rate at the head of the downward slope and increased the transport rates at the toe with respect to the corresponding capacity transport rates. This fact causes a high erosion effect downstream the bed dune, where the flow regime changes from subcritical to supercritical.

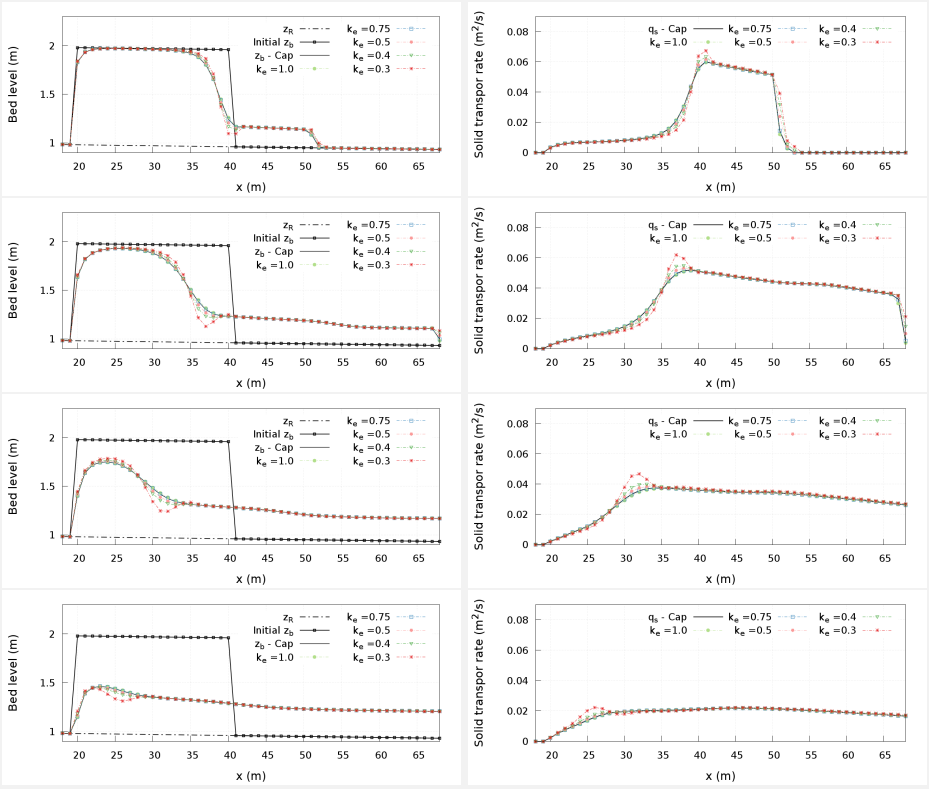

Figure 5.14: Test 5.3.A – Influence of the deposition constant k_E value: (left) bed level and (right) solid transport rate at time (first row) $t_1 = 20\,s$, (second row) $t_2 = 60\,s$, (third row) $t_3 = 120\,s$ and (fourth row) $t_4 = 180\,s$.

Comparison of the erosion-deposition net exchange flux (see Fig. 5.15–right) along the dune domain shows the highest non-equilibrium zones at the upward and downward slopes of the rectangular dune for the first stages of the bed movement. Negative values of $\dot{\eta}_D - \dot{\eta}_E$ imply erosion of the static layer taking place whereas positive values lead to aggradation

of static bed layer. An important erosive net flux appears at the downward slope of the dune associated to a strong shear-stress change (the flow is changing from subcritical to supercritical regime) and to lower values of the moving layer thickness (see Fig. 5.15–left).

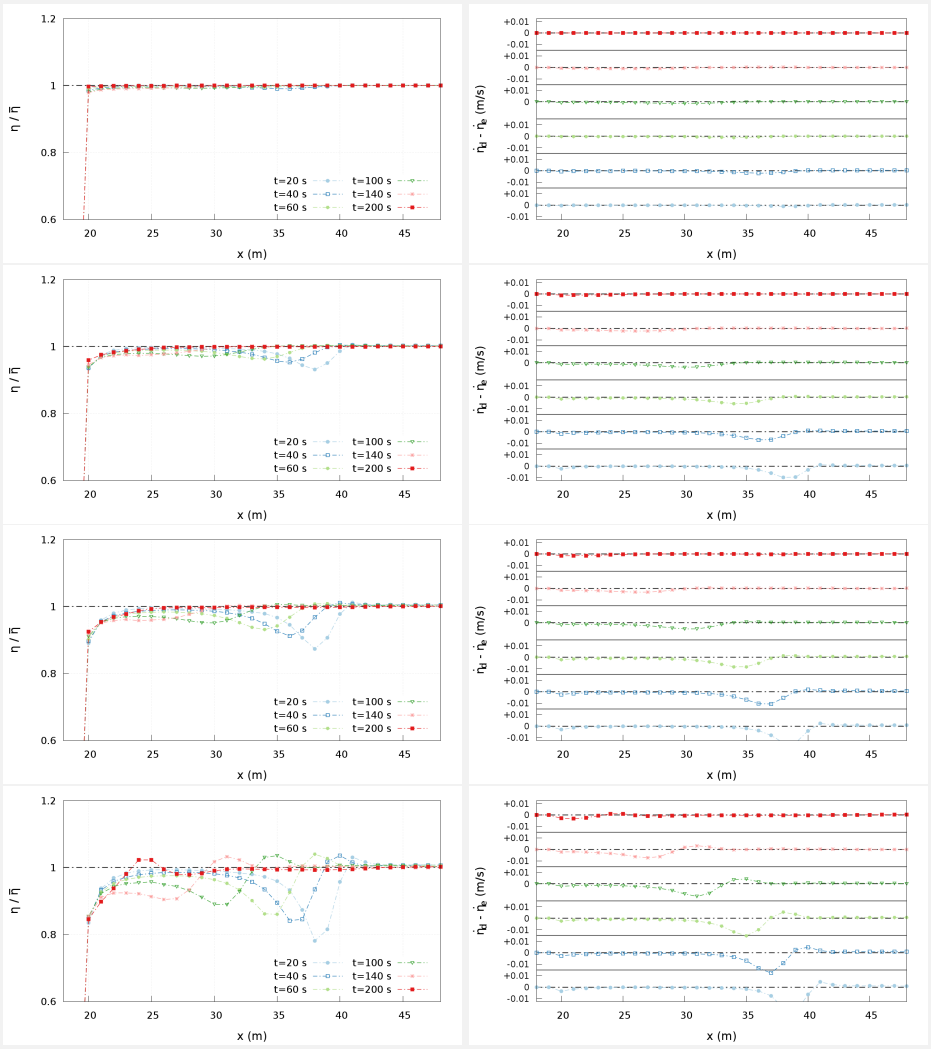

Figure 5.15: Test 5.3.A –Influence of the deposition constant k_E value: (left) normalized moving layer thickness η/η^* and (right) net exchange flux through the static-moving layers interface with (first row) $k_E = 0.75$, (second row) $k_E = 0.5$, (third row) $k_E = 0.4$ and (fourth row) $k_E = 0.3$.

Furthermore, two important points should be noted: first, as the bed movement progresses with time, the imbalance between erosion and deposition rates tends to disappear, which is in agreement with the non-equilibrium assumption. Second, as the erosion constant k_E decreases, the imbalance between erosion and deposition rates at the downward slope of the dune tends to become more marked and to extend in time, demonstrating an agreement between the erosion-deposition formulation proposed in this work and the classical approach for the net exchange flux adopted by other authors [114, 144].
Finally, Fig. 5.16 shows the transport layer thickness η computed with the non-capacity formulation at different times along the dune profile. It

is worth noting that the reduction of the relation k_E/k_D leads to a reduction of the moving layer thickness. However, as k_E/k_D decreases, the non-equilibrium in the bedload transport state does not show noticeable modifications.

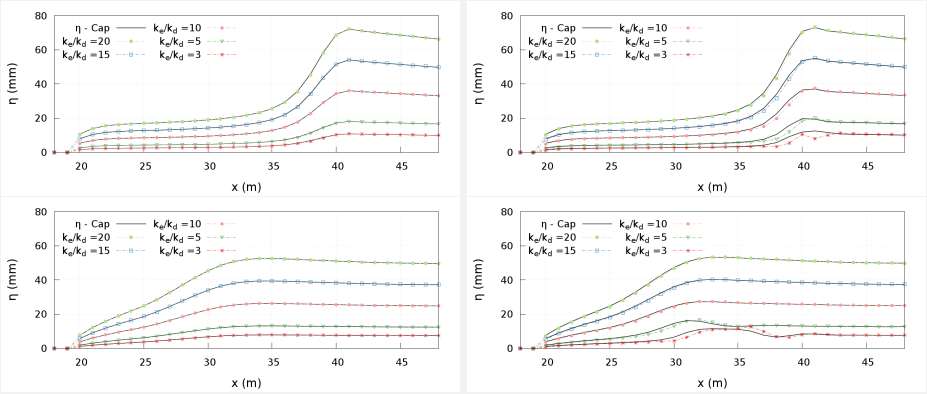

Figure 5.16: Test 5.3.A – Influence of the erosion-deposition constants ratio k_E/k_D: (first row) $t_1 = 20\,s$ and (second row) $t_2 = 120\,s$ with (left column) $k_E = 0.75$ and (right column) $k_E = 0.4$.

5.4 Bed evolution control with finite-depth erodible layers

This is a common issue in sediment transport numerical schemes dealing with finite-depth sediment layers [24, 30, 37, 110, 130, 136], which requires to control the numerical solution in order to ensure non-negative values of the sediment mass, i.e. avoiding unphysical over-eroded cells where sediment mass is numerically created leading to accuracy, conservation and stability issues. A widely extended strategy [24, 110, 136] to deal with this situation is to reduce the time step, ensuring in this way the positivity of the cell averaged sediment thickness ϵ_b values but leading to an important increase of the computational effort. In this thesis, in the framework of the fully-coupled FCM scheme (see Section 5.2.1), a new reconstruction strategy based on enforcing sediment thickness ϵ_b positivity on the inner states of the approximate RP solution at the intercell edges is proposed. This method, referred to as *Active Control of the Sediment Thickness Positivity* (AC-STP) from now on, intents to avoid unphysical negative values of the cell-averaged sediment mass and to preserve the time step obtained from the Jacobian $\widetilde{\mathbf{M}}_k$ (5.36).

The available sediment thickness ϵ_b at time t^n in the i cell is defined as

$$\epsilon_{b,i}^n = z_{b,i}^n - z_{R,i} \tag{5.102}$$

where $z_{R,i}$ is the level of the underlying non-erodible rigid layer at the i cell, which does not change in time. Considering right–direction flow $\widetilde{u}_k > 0$ at

the cell edge and (5.102), the cell-averaged solution at the next time in the left i cell $\epsilon_{b,i}^{n+1}$ (Fig. 5.17) can be evaluated as

$$\epsilon_{b,i}^{n+1} = \epsilon_{b,i}^{n} + |\widetilde{\lambda}_1| \frac{l_k}{A_i} \Delta t (\epsilon_{b,i}^{-} - \epsilon_{b,i}^{n}) \geq 0 \tag{5.103}$$

being $\epsilon_{b,i}^{-}$ the inner state of the approximate solution for the sediment thickness at the left cell of the kth cell edge (5.57), computed as

$$\epsilon_{b,i}^{-} = \epsilon_{b,i}^{n} + \widetilde{\gamma}_1 \widetilde{\mathrm{e}}_1^{\{4\}} + \delta\epsilon_{b,i}^{\Delta} \tag{5.104}$$

being $\widetilde{\mathrm{e}}_1^{\{4\}}$ the fourth component of the first eigenvector $\widetilde{\mathbf{e}}_1$ (5.49) and $\delta\epsilon_{b,i}^{\Delta}$ the sediment thickness increment due to the variation of the Grass factor between cell-center i and the kth edge (5.100).

For the right j cell, the updated cell-averaged value of the sediment thickness can be expressed as

$$\begin{aligned} \epsilon_{b,j}^{n+1} = \epsilon_{b,j}^{n} &+ \widetilde{\lambda}_4 \frac{l_k}{A_j} \Delta t (\epsilon_{b,j}^{+++} - \epsilon_{b,j}^{n}) \\ &+ \widetilde{\lambda}_3 \frac{l_k}{A_j} \Delta t (\epsilon_{b,j}^{++} - \epsilon_{b,j}^{+++}) + \widetilde{\lambda}_2 \frac{l_k}{A_j} \Delta t (\epsilon_{b,j}^{+} - \epsilon_{b,j}^{++}) \geq 0 \end{aligned} \tag{5.105}$$

being $\epsilon_{b,j}^{+}$, $\epsilon_{b,j}^{++}$ and $\epsilon_{b,j}^{+++}$ the inner states of the approximate solution for the sediment thickness at the right cell of the kth cell edge (5.57), computed as

$$\begin{aligned} \epsilon_{b,j}^{+} &= \epsilon_{b,j}^{++} - \widetilde{\gamma}_2 \widetilde{\mathrm{e}}_2^{\{4\}} \\ \epsilon_{b,j}^{++} &= \epsilon_{b,j}^{+++} - \widetilde{\gamma}_3 \widetilde{\mathrm{e}}_3^{\{4\}} \\ \epsilon_{b,j}^{+++} &= \epsilon_{b,j}^{n} - \widetilde{\gamma}_4 \widetilde{\mathrm{e}}_4^{\{4\}} - \delta\epsilon_{b,j}^{\Delta} \end{aligned} \tag{5.106}$$

being $\widetilde{\mathrm{e}}_m^{\{4\}}$ the fourth component of the eigenvector $\widetilde{\mathbf{e}}_m$ (5.49) and $\delta\epsilon_{b,j}^{\Delta}$ the sediment thickness increment due to the variation of the Grass factor between cell-center j and the kth edge (5.100).

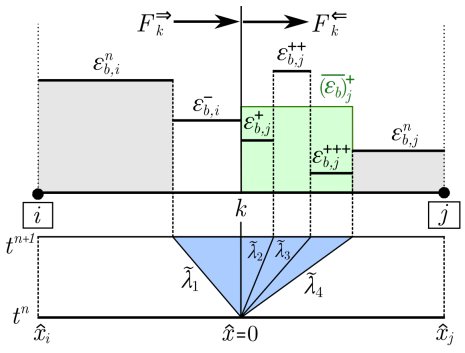

Figure 5.17: Inner states for the sediment thickness ϵ_b at the kth intercell edge.

The right cell-averaged approximate solution for the sediment thickness (5.105) can be rewritten by defining an averaged inner state $(\overline{\epsilon_b})_j^{+}$ at the right side of the edge as

$$(\overline{\epsilon_b})_j^{+} = \epsilon_{b,j}^{+++} - \frac{\widetilde{\lambda}_3}{\widetilde{\lambda}_4} \widetilde{\gamma}_3 \widetilde{\mathrm{e}}_3^{\{4\}} - \frac{\widetilde{\lambda}_2}{\widetilde{\lambda}_4} \widetilde{\gamma}_2 \widetilde{\mathrm{e}}_2^{\{4\}} \tag{5.107}$$

and hence

$$\epsilon_{b,j}^{n+1} = \epsilon_{b,j}^{n} + \widetilde{\lambda}_4 \frac{l_k}{A_j} \Delta t \left((\overline{\epsilon_b})_j^{+} - \epsilon_{b,j}^{n} \right) \geq 0 \tag{5.108}$$

The stability condition in (5.61)–(5.62) requires both $|\widetilde{\lambda}_1| \frac{l_k}{A_i} \Delta t \leq 1$ and $\widetilde{\lambda}_4 \frac{l_k}{A_j} \Delta t \leq 1$. Hence, from (5.103) and (5.107), it is possible to derive the conditions $\epsilon_{b,i}^{-} \geq 0$ (5.104) and $(\overline{\epsilon_b})_j^{+} \geq 0$ (5.107) to ensure positive averaged solutions of the sediment mass at the left and right cells of the kth edge, respectively.

Since the presence of a finite-depth erodible layer and its influence in the bedload transport rate is mainly contained in the specific Grass interaction factor G_p for each sediment class, the following limits are proposed for the corrector sediment thickness increment $\delta\epsilon_{b,i}^{\Delta}$ at the left side of the kth cell edge

$$\delta\epsilon_{b,i}^{\Delta} \geq \left[\delta\epsilon_{b,i}^{\Delta} \right]^{\mathrm{MIN}} = -(\epsilon_{b,i}^{n} + \widetilde{\gamma}_1 \widetilde{\mathrm{e}}_1^{\{4\}}) \tag{5.109}$$

and, similarly, for the corrector sediment thickness increment $\delta\epsilon_{b,j}^{\Delta}$ at the right side of the kth cell edge

$$\begin{aligned} \delta\epsilon_{b,j}^{\Delta} \leq \left[\delta\epsilon_{b,j}^{\Delta} \right]^{\mathrm{MAX}} = \epsilon_{b,j}^{n} - \frac{1}{\widetilde{\lambda}_4} \Big(& \widetilde{\lambda}_4 \widetilde{\gamma}_4 \widetilde{\mathrm{e}}_4^{\{4\}} \\ & + \widetilde{\lambda}_3 \widetilde{\gamma}_3 \widetilde{\mathrm{e}}_3^{\{4\}} + \widetilde{\lambda}_2 \widetilde{\gamma}_2 \widetilde{\mathrm{e}}_2^{\{4\}} \Big) \end{aligned} \tag{5.110}$$

The following strategy is suggested:

a) If $\epsilon_{b,i}^{-} < 0$ and $(\overline{\epsilon_b})_j^{+} > 0$

1. $\delta\epsilon_{b,i}^{\Delta} = \left[\delta\epsilon_{b,i}^{\Delta} \right]^{\mathrm{MIN}}$
2. $\boldsymbol{\delta \mathbf{F}}_i^{\Delta} = \begin{pmatrix} 0 \\ 0 \\ 0 \\ \widetilde{\lambda}_1 \, \delta\epsilon_{b,i}^{\Delta} \end{pmatrix}$
3. $\boldsymbol{\delta \mathbf{F}}_j^{\Delta} = \begin{pmatrix} 0 \\ 0 \\ 0 \\ (\delta \hat{q}_b)_k - \sum_{m=1}^{4} \left(\widetilde{\lambda}_m \widetilde{\alpha}_m \widetilde{\mathrm{e}}_m^{\{4\}} \right)_k - \widetilde{\lambda}_1 \, \delta\epsilon_{b,i}^{\Delta} \end{pmatrix}$
4. $\delta\epsilon_{b,j}^{\Delta} = \delta F_j^{\Delta\{4\}} / \widetilde{\lambda}_4$
5. If $\delta\epsilon_{b,j}^{\Delta} > \left[\delta\epsilon_{b,j}^{\Delta} \right]^{\mathrm{MAX}}$, reduce Δt until (5.108) becomes true.

(5.111)

b) If $\epsilon^{-}_{b,i} > 0$ and $(\overline{\epsilon_b})^{+}_{j} < 0$

1. $\delta\epsilon^{\Delta}_{b,j} = \left[\delta\epsilon^{\Delta}_{b,j}\right]^{\mathrm{MAX}}$
2. $\boldsymbol{\delta}\mathbf{F}^{\Delta}_{j} = \begin{pmatrix} 0 \\ 0 \\ 0 \\ \widetilde{\lambda}_4\,\delta\epsilon^{\Delta}_{b,j} \end{pmatrix}$
3. $\boldsymbol{\delta}\mathbf{F}^{\Delta}_{i} = \begin{pmatrix} 0 \\ 0 \\ 0 \\ (\delta\hat{q}_b)_k - \sum_{m=1}^{4}\left(\widetilde{\lambda}_m\widetilde{\alpha}_m\widetilde{\mathbf{e}}^{\{4\}}_m\right)_k - \widetilde{\lambda}_4\,\delta\epsilon^{\Delta}_{b,j} \end{pmatrix}$ (5.112)
4. $\delta\epsilon^{\Delta}_{b,i} = \delta F_i^{\Delta\{4\}}/\widetilde{\lambda}_1$
5. If $\delta\epsilon^{\Delta}_{b,i} < \left[\delta\epsilon^{\Delta}_{b,i}\right]^{\mathrm{MIN}}$, reduce Δt until (5.103) becomes true.

It is worth noting that the specific Grass interaction factor G_p for each sediment class has already been reduced at cells by limiting the actual moving layer thickness η when a non-erodible stratum is reached. Therefore, the step 5 of the above strategy is a guarantee for extreme cases and is rarely needed. The above procedure is derived for edges with right-direction flow $\widetilde{u}_k \geq 0$ but it can be easily extended to left-direction $\widetilde{u}_k < 0$ edges.

5.5 Benchmark and application cases

5.5.1 Synthetic case BL1: 1D supercritical symmetric dambreak over erodible bed

The goal of this synthetic test is to demonstrate the capability of both the FCM and ACM schemes to deal with regime changes in the flow and to asses their stability in these configurations. A frictionless 1D symmetrical dambreak over erodible flat bed is considered with the following initial conditions:

$$\begin{aligned} h(x,0) &= \begin{cases} 50\,m & \text{if } -5 \leq x \leq 5 \\ 0.2\,m & \text{otherwise} \end{cases} \\ u(x,0) &= 0\,m/s \quad \forall x \\ v(x,0) &= 0\,m/s \quad \forall x \\ z_b(x,0) &= 10\,m \quad \forall x \end{aligned} \tag{5.113}$$

which allow the flow to change from subcritical ($Fr = |u|/\sqrt{gh} < 1$) at the center of the domain to supercritical ($Fr = |u|/\sqrt{gh} > 1$) at the dambreak wave fronts. The bedload transport rate is calculated considering one sediment class with porosity $\xi = 0.40$ and a constant flow-bed iteration factor $G = 0.01\,s^2/m$. The final time is $t = 1.0\,s$ for all the simulations. All the simulations are performed using a one-dimensional square-cell mesh with $\Delta x = 0.1\,m$ edge length and CFL $= 1$.

Figure 5.18–left shows the free surface and bed elevation profiles at $t = 0.1\,s$, $t = 0.3\,s$ and $t = 0.6\,s$ for both FCM and ACM numerical schemes, whereas the Froude number of the flow throughout the right side of the

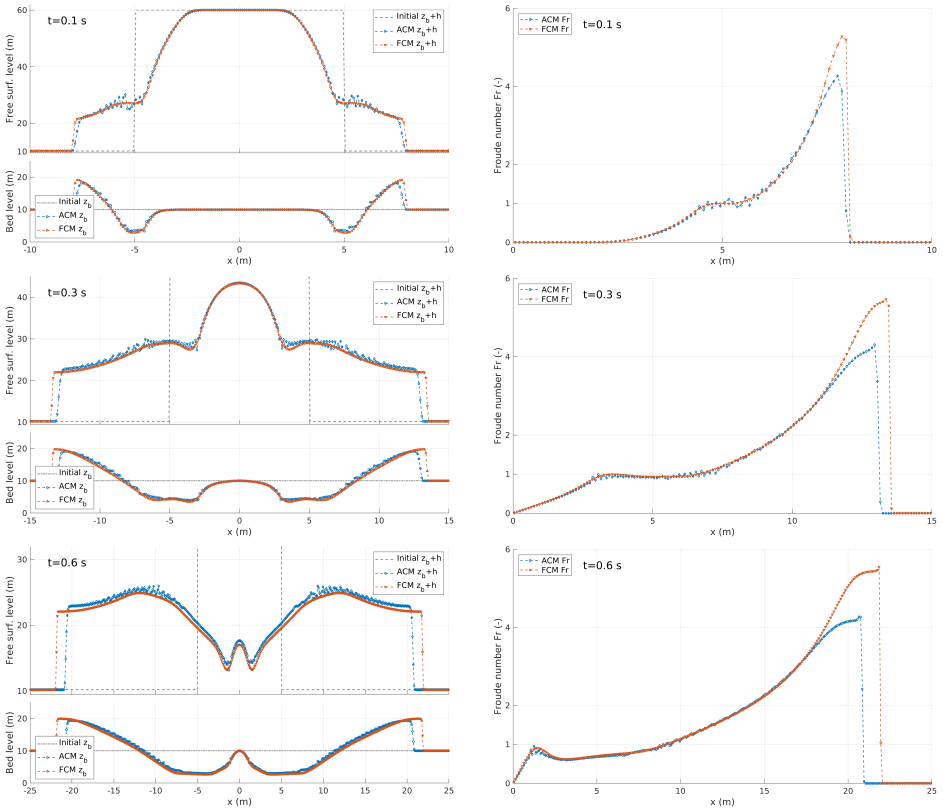

Figure 5.18: Synthetic case BL1 – Dambreak evolution with ACM and FCM models for $G = 0.01\, s^2/m$: (left) bed and free surface levels and (right) Froude number. From top to bottom: $t = 0.1\, s$, $t = 0.3\, s$ and $t = 0.6\, s$.

symmetric dambreak is depicted in Figure 5.18–right for both schemes at the same times. At $t = 0.1\, s$, the flow structure is characterized by a supercritical shock wave which strongly affects the erodible bed layer, followed by a transcritical rarefaction wave where the flow changes from subcritical to supercritical at $x \approx 5\, m$. At $t = 0.3\, s$, the transcritical region behind the supercritical wave front increases and two critical points can be distinguished at $x \approx 3.5\, m$ and $x \approx 6.5\, m$ respectively, with a slightly subcritical region between them. The appearance of two critical points in the flow structure is a direct consequence of the high interaction between the flow and the movable bed. As the dambreak progresses, this double critical-point structure disappears and only one regime change is observed separating the supercritical wave front and the rarefaction wave ($x \approx 9\, m$) at $t = 0.6\, s$.

Both numerical methods demonstrate to be stable when dealing with flow regime changes. However, the ACM shows spurious oscillations in the water depth h and the bed level z_b generated around the critical points. Furthermore, the ACM scheme predicts a slower advance of the dambreak wave front than that of the FCM scheme. This difference could be related to a slower characteristic wave celerity for the flow motion, since the decoupled approach does not take into account the influence of the bed changes in the Jacobian eigenvalues, contrarily to the FCM method. It is worth noting that the predicted Froude numbers at the dambreak wave front are also smaller for the ACM simulation ($Fr \approx 4$) than that computed using the FCM scheme ($Fr \approx 5$).

As in the previous subcritical dambreak case for high flow-bed interaction, although the solution obtained with the ACM scheme shows local spurious oscillations, the ACM time step estimation improves greatly the stability of the scheme. Figure 5.19 shows the bed and flow levels at $t = 0.6\,s$ using the ACM scheme compared with the results obtained by the totally decoupled strategy. Also in this test, involving a medium flow-bed interaction factor ($G = 0.01\,s^2/m$), the totally decoupled scheme fails and loses the stability, whereas the ACM method only shows local oscillation and does not loss the solution symmetry.

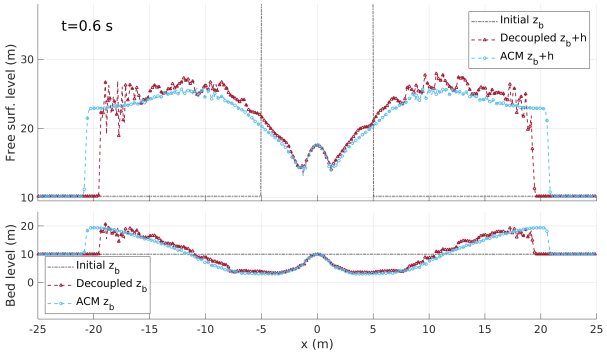

Figure 5.19: Synthetic case BL1 – Dambreak at $t = 0.6\,s$ with ACM and totally decoupled models for $G = 0.01\,s^2/m$.

Inter. factor $G(s^2/m)$	Comp. time (s) ACM	FCM	Speed-up ACM/FCM
0.01	0.737	0.540	1.36

Table 5.3: Synthetic case BL1 – Computational times.

Furthermore, the high interaction between the flow and the movable bed leads to a slower computational time for the fully-coupled method compared with the ACM scheme, even though the FCM method requires more algebraical operations to compute numerical fluxes at the intercell edges. The speed-up of the FCM solver against the ACM approach is near 1.4 for this test (see Table 5.3).

5.5.2 Synthetic case BL2: 2D supercritical symmetric dambreak over erodible bed

The aim of this synthetic test is to assess the capability of both schemes to deal with structured and unstructured meshes, regardless of the number of edges of the cells. The idealized supercritical symmetric dambreak reported above for synthetic test B (see 5.113) is considered here but over a two-dimensional $50 \times 10\,m$ domain discretized using three different kind of mesh: an orthogonal square-cell mesh (SQ), a structured triangle-cell mesh (TS) and an unstructured triangle-cell mesh (TU). Details of the the three mesh topologies are shown in Figure 5.20 and their geometrical characteristics have been reported in Table 5.4:

All the simulations are performed considering one sediment class with porosity $\xi = 0.40$ and a constant flow-bed interaction factor $G = 0.01\,s^2/m$,

Mesh	Topology	Cell type	Number of cells	Edge length (m)
SQ	Orthogonal	Square	50000	0.1
TS	Structured	Triangle	100000	≈0.1
TU	Unstructured	Triangle	96561	≈0.1

Table 5.4: Synthetic case BL2 – Mesh characteristics.

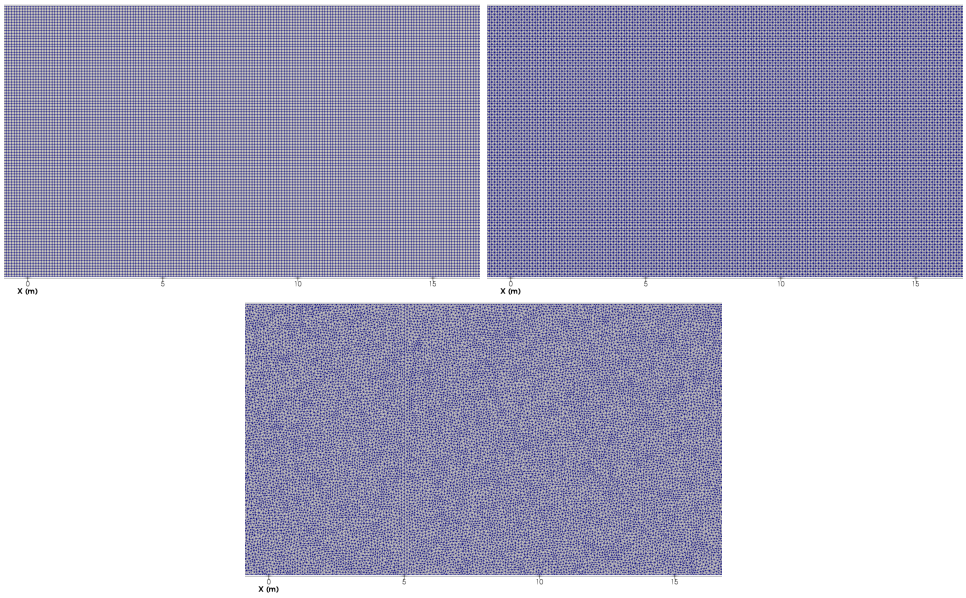

Figure 5.20: Synthetic case BL2 – Mesh topology: (top left) orthogonal square mesh SQ, (top right) triangular structured mesh TS and (bottom) triangular unstructured mesh TU.

as in the above synthetic test B. The final time is $t = 1.0\,s$ and the CFL is set to 0.5 for the three meshes, in order to compare computational times.

Figure 5.21 shows a view of the free surface and bed elevation at $t = 0.3\,s$ using the FCM scheme on the three meshes. The color scale denotes the free surface level and the bed changes magnitude respectively. Regardless of the kind of mesh, the scheme is able to compute correctly the evolution of the symmetric dambreak, with the same flow structure as in the above one-dimensional Synthetic case BL1 5.5.1.

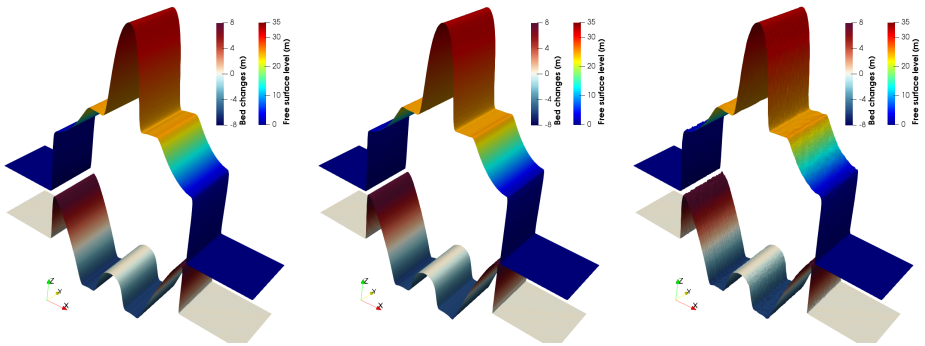

Figure 5.21: Synthetic case BL2 – View of the free surface and elevation and bed changes with FCM at $t = 0.3\,s$ for (left) square mesh SQ, (center) triangular structured mesh TS and (right) triangular unstructured mesh TU.

Furthermore, the longitudinal free surface and bed level profiles along the right side of the symmetric dambreak ($x > 0\,m$) have been plotted in Figure 5.22 as computed on the three meshes at $t = 0.1\,s$, $t = 0.3\,s$ and $t = 0.6\,s$. The left column depicts the results obtained with the FCM scheme, whereas the right column shows those predicted by the ACM approach. Regarding the FCM results, small differences appear in the free surface and bed level depending on the mesh selected but these can be considered negligible and mainly related to the differences in the numerical diffusion between the three mesh topologies. Contrarily, the ACM scheme shows a more marked dependence on the mesh topology since the spurious oscillations observed in the above one-dimensional test B also appear for the orthogonal square mesh SQ, whereas the higher numerical diffusion associated to the triangular meshes (especially in the unstructured topology TU) reduces this spurious oscillations. Therefore, differences in the solution depending on the mesh topology arise with the ACM method, although they can be considered small.

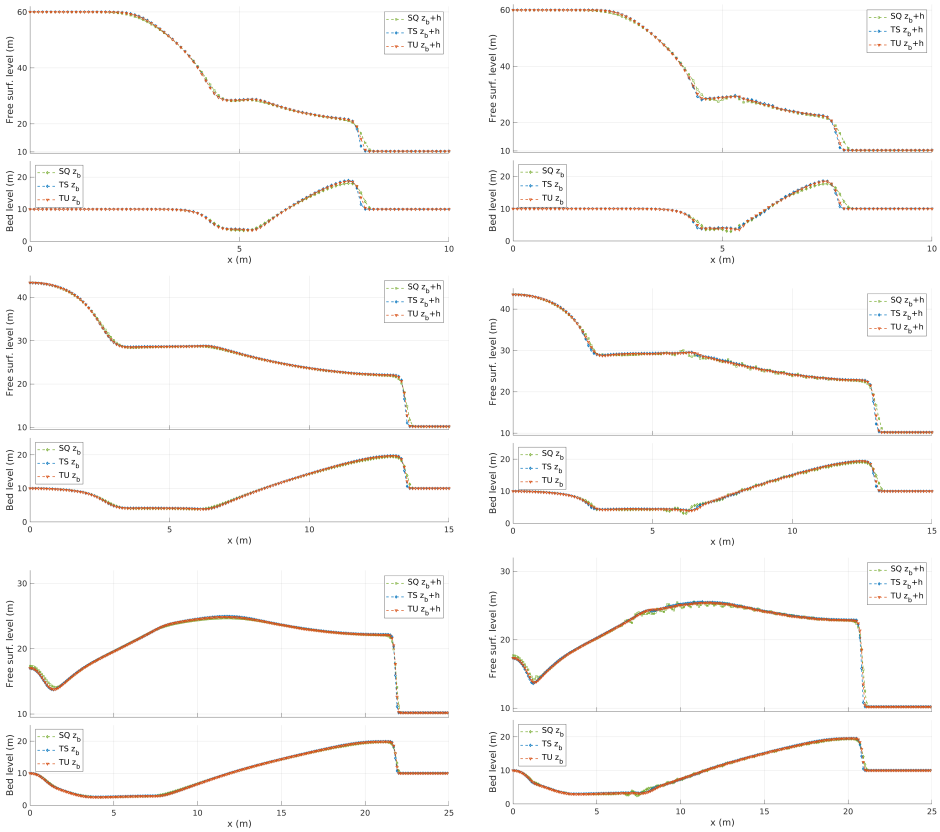

Figure 5.22: Synthetic case BL2 – Dambreak evolution with (left) FCM and (right) ACM models for $G = 0.01\,s^2/m$ considering square (SQ), triangular structured (TS) and triangular unstructured (TU) meshes. From top to bottom: (top row) $t = 0.1\,s$, (center row) $t = 0.3\,s$ and (bottom row) $t = 0.6\,s$.

Table 5.5 shows the computational times required to complete the simulation with each mesh for both FV methods. The computational effort increases for the triangular meshes TS and TU, especially for the unstructured topology, with respect to the orthogonal square mesh SQ. This increment is mainly caused by the larger number of cells for the triangular meshes TS

and TU. Interestingly, despite the ACM scheme does not show important spurious oscillations in the solution, its efficiency is lower than that of the FCM method for all the mesh topologies tested. The speed-up of the FCM is about 1.5 times that of the decoupled scheme.

Mesh Topology	Comp. time (s) ACM	FCM	Speed-up ACM/FCM
SQ	59.946	39.824	1.51
TS	236.939	159.088	1.49
TU	484.030	332.594	1.46

Table 5.5: Synthetic case BL2 – Computational times.

This loss of efficiency of the ACM is related to more restricted stability conditions. Figure 5.23 shows the time step size for the FCM and ACM schemes along the simulated time with the three meshes considered (SQ, TS and TU). Moreover, for the approximate-coupled simulations, the global time step limitations associated to both the hydrodynamical eigenvalues $\widetilde{\lambda}'_{m,k}$ (5.65) and the virtual bed celerity $\widetilde{\lambda}_{b,k}$ (5.73) at the cell edges are also depicted.

On the one hand, regardless of the mesh topology, the maximum time steps allowed for the FCM method are slightly smaller than those obtained considering only the hydrodynamical component of the flow because of the influence of the movable bed in the local RP eigenstructure. On the other hand, the ACM strategy leads to a more restricted time step limitation than the FCM approach since, as the flow-bed interaction increases, the approximated bounds $(\widetilde{\lambda}^*_{1,k}, \widetilde{\lambda}^*_{4,k})$ (5.75) move away from the exact eigenvalues (see Figure 5.3).

Nevertheless, the maximum time step associated to these approximated bounds is several orders of magnitude higher than the time step limitation derived from considering the virtual bed celerity $\widetilde{\lambda}_{b,k}$. Therefore, the usage of the ACM strategy to limit the maximum time step ensures the stability of the decoupled numerical scheme even for high flow-bed interaction problems and avoids unsuitable time step limitations associated to including the virtual bed celerity $\widetilde{\lambda}_{b,k}$ in the stability determination [65].

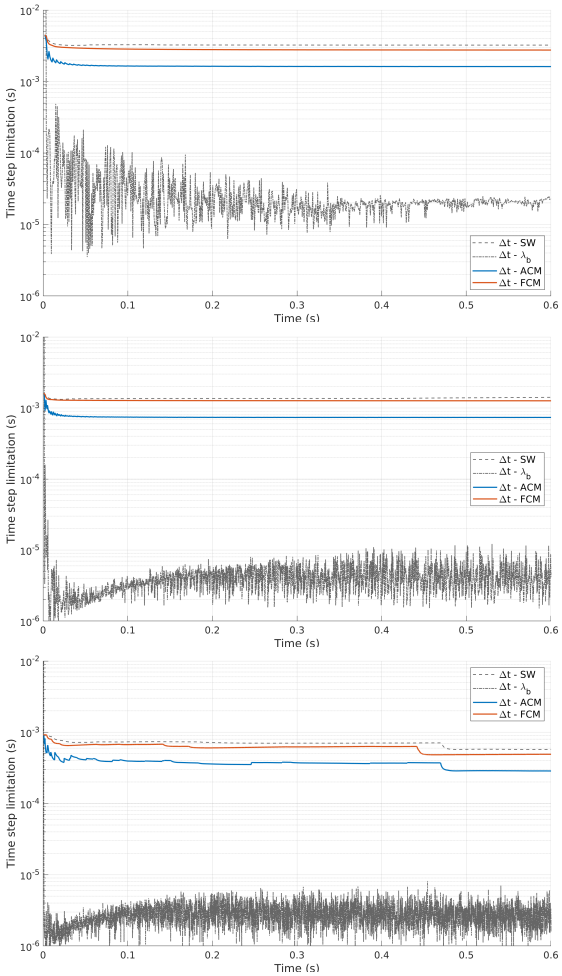

Figure 5.23: Synthetic case BL2 – Time step restrictions during the supercritical symmetric dambreak evolution for $G = 0.01\, s^2/m$ considering (top) orthogonal SQ, (center) triangle-structured TS and (bottom) triangle-unstructured TU meshes.

5.5.3 Experimental case BL3: Dambreak over light-weight sediment flat bed

The aim of this benchmark test is to analyze the behavior of the capacity (R-Cap) and non-capacity (R-NCap) bedload formulations in presence of highly erosive unsteady flows. This experimental test [135] consists of an idealized dam-break flow over a light-weight sediment flat bed made of cylindrical PVC pellets, with equivalent diameter $d_s = 3.9\, mm$, density $\rho_s = 1580\, kg/m^3$, internal friction angle $\delta_b = 30°$ and porosity $p = 0.42$. The experiment was carried out in a 6 m long and 0.25 m width. The flume was uniformly filled to a height of 0.1 m over the flume floor with the light-weight sediment. Breaking of the dam was reproduced by the downward movement of a pneumatically actuated thin gate placed at the middle of the flume. The initial water level was 0.35 m upstream the gate and nil downstream. Once the gate was open and the dam-break wave progressed downstream, an intense sediment transport process started instantaneously caused by the high fluid velocity and the low sediment density. The temporal evolutions of the free water surface, bed surface and static-moving

bed layer interface were reported experimentally until 1.5 sec after the gate opening each 0.25 sec.

For this case, the Manning roughness coefficient is estimated as $n_b = 0.028\, s/m^3$. A deposition constant $k_D = 0.03$ and a erosion constant $k_E = 0.2$ are set. The actual transport rate has been estimated using a modified version of the MPM model with the coefficient $c = 16$ in order to correctly capture the influence of the low density of the erodible layer particles [150]. The simulations have been performed using the FCM method on a single-row square-cell mesh with cell size $\Delta x = 0.01\, m$ and CFL = 0.95.

Fig. 5.24 shows the numerical results for the temporal evolution of the free water surface, bed level and static-moving bed layers interface with the equilibrium approach (left column) and the non-capacity approach (right column). In general, a good agreement with measured data can be found with both assumptions, especially at times greater than $t = 0.50\, s$. For the first stages after the gate opening ($0\, s < t \leq 0.75\, s$) both models underestimate the thickness of the moving bed layer η (see Table 5.6 and Figure 5.25). This discrepancy can be generated by the marked vertical velocities that appear at the first instants of the fluid movement [36] that can not be captured by the depth-averaged model. However, the free water surface and the bed level are well predicted (Table 5.6) and the propagation velocity of the dam-break wave is accurately captured (see Fig. 5.24).

Some differences between numerical results and observed data appear at the gate region. This region is the most affected by vertical fluid velocities at the first stages of the dam-break flow and suffers an intense erosion process during the whole experiment. It is worth mentioning that the R-NCap formulation is not able to improve the agreement of the computed static-moving interface level z_f and bed level z_b with those observed experimentally, over the results obtained using the R-Cap formulation. Nevertheless, the prediction of the free water surface level (WSL) computed with the R-NCap bedload transport formulation shows lower deviations respect to the experimental data than the capacity results for all the dam-break stages.

	RMSE			
Formulation	$z_f\,(m)$	$z_b\,(m)$	$WSL\,(m)$	$\eta\,(m)$
Early stages: $0\, s < t \leq 0.75\, s$				
Cap.	0.01668	0.01276	0.02032	0.02594
Non-Cap.	0.01961	0.01363	0.01472	0.02957
Later stages: $0.75\, s < t \leq 1.5\, s$				
Cap.	0.00776	0.01689	0.01819	0.01692
Non-Cap.	0.00792	0.01782	0.01623	0.01469

Table 5.6: Experimental case BL3 – RMSE for the static bed layer elevation z_f, bed level z_b, water surface level (WSL) and active bed layer thickness η with R-Cap and R-NCap formulations.

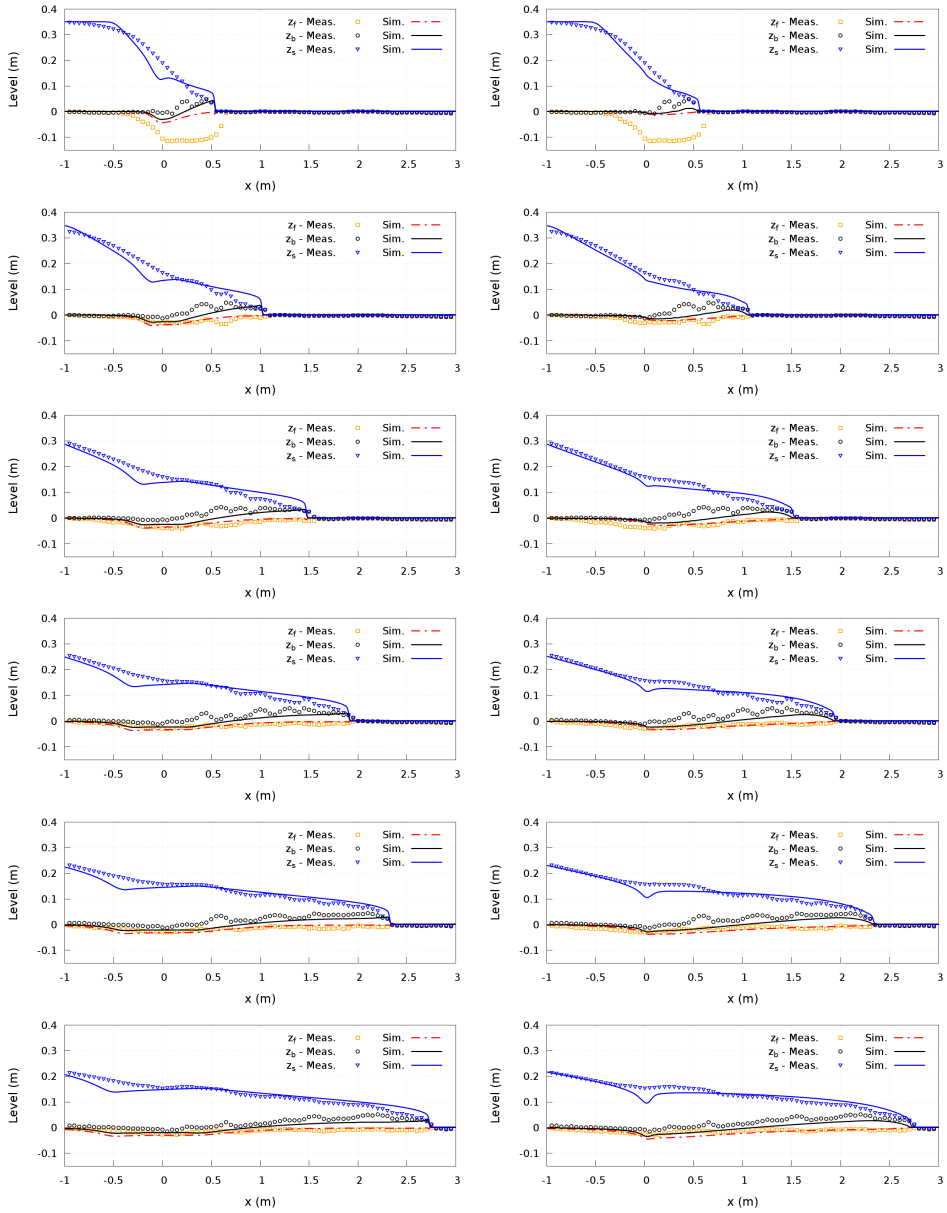

Figure 5.24: Experimental case BL3 – Free water surface, bed level and static-moving bed layers interface for (left column) equilibrium approach and (right column) non-capacity approach at times $t = 0.25\,s$, $0.5\,s$, $0.75\,s$, $1.0\,s$, $1.25\,s$ and $1.5\,s$ after the gate opening.

Fig. 5.25 shows the moving bed layer thickness distribution at three different times during the dam-break wave propagation. Both approaches underestimated η but the results can be considered reasonable, specially for the later stages (Table 5.6). For the first stages, the sediment thickness computed using the equilibrium model offer a better approximation to those observed in laboratory than the result obtained with non-capacity model. However, as time progresses and the fluid moves downstream, the non-capacity model predicts better the active thickness distribution, with lower RMSE for times larger than 0.75 s.

The net exchange flux $\dot{\eta}_D - \dot{\eta}_E$ through the static-moving bed layers interface shows a marked erosive non-equilibrium for the first stages of

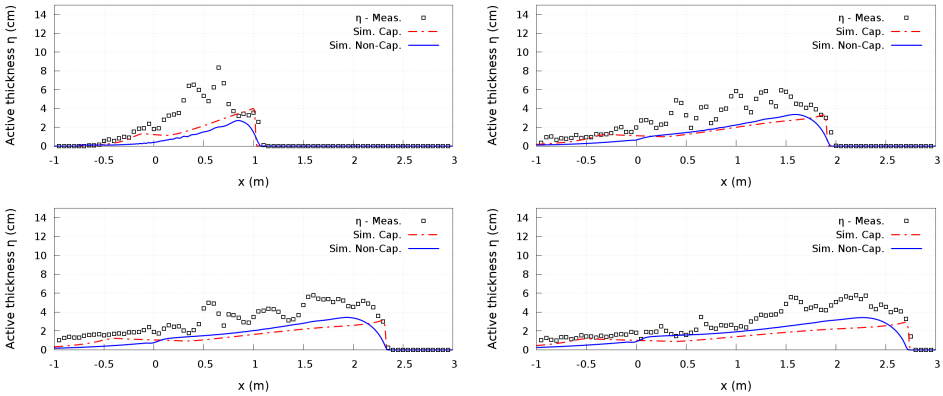

Figure 5.25: Experimental case BL3 – Moving bed layer thickness η with both equilibrium and non-capacity approaches at times (top left) $t = 0.5\,s$, (top right) $t = 1.0\,s$, (bottom left) $t = 1.25\,s$ and (bottom right) $t = 1.5\,s$.

the wave advance ($0 < t \leq 0.75\,s$) at the whole dam-break wave domain (see Fig. 5.26-top). Nevertheless, as the flow moves downstream, this net exchange flux tends to reduce generally, approaching progressively the equilibrium state at $t = 1.5\,s$. From that time there is null net exchange flux along the dambreak wave, except at both the wave-front and the gate region, where flow changes from subcritical to supercritical conditions. In these two regions marked erosive net exchange fluxes are maintained through the static-moving bed layers interface during the whole simulation time.

Note that in the region between the gate and the wave front, a quasi-uniform net exchange flux appears for the later stages ($0.75\,s < t \leq 1.5\,s$). In this region, the relationship between the dimensionless bedload layer thickness $\eta\, d_s^{-1}$ and the excess of Shields stress $\Delta\theta$ also tends progressively to near-equilibrium conditions, signaled by the fact that the slope of the $\eta d_s^{-1}/\Delta\theta$ curve is reducing as the dambreak wave progresses (see Fig. 5.26-bottom). Therefore, the slope of the $\eta\, d_s^{-1}/\Delta\theta$ curve tends to be nil as near-equilibrium states are progressively reached during the dam break wave advance. It is worth mentioning that the capacity state is a particular case of the generalized non-capacity formulation where the relation $\eta^*\, d_s^{-1}/\Delta\theta = const = k_E/(\rho_s/\rho_w\, k_D)$ can be derived from (5.85).

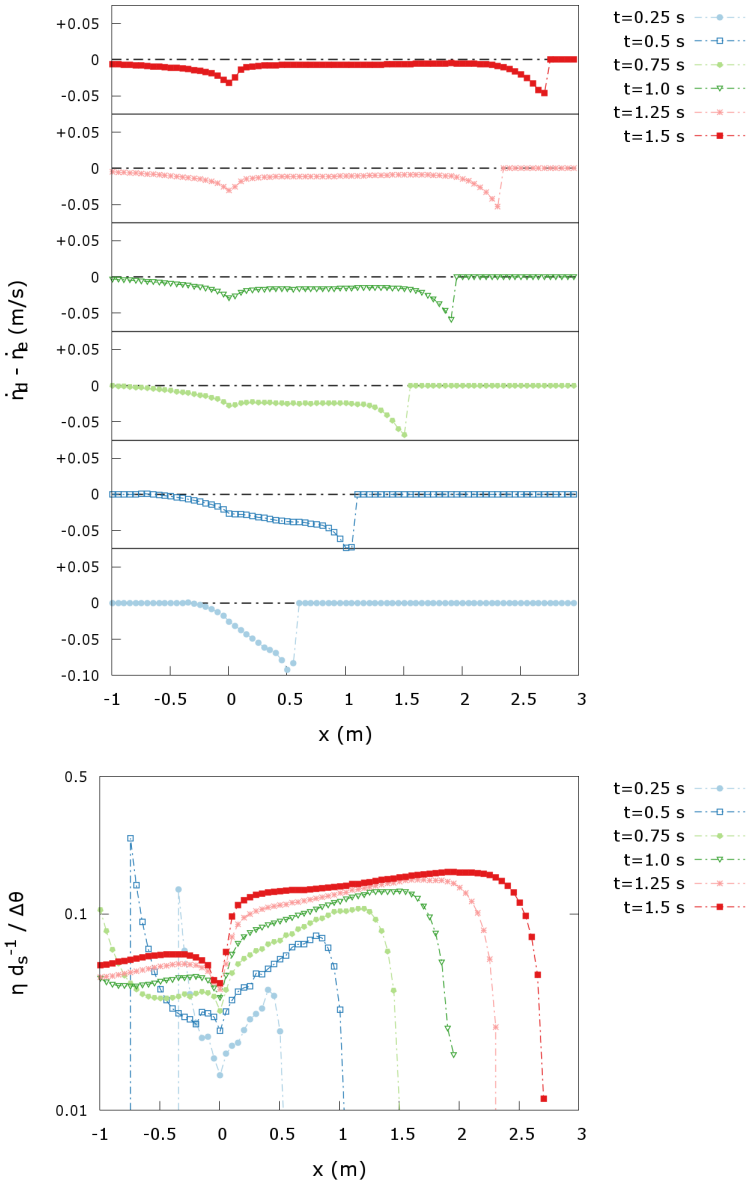

Figure 5.26: Experimental case BL3 – (Top) Net exchange flux through the static-moving bed layers interface and (bottom) relationship between the dimensionless active layer thickness $\eta\, d_s^{-1}$ and the excess of Shields stress $\Delta\theta$ at times $t = 0.25\,s$, $0.5\,s$, $0.75\,s$, $1.0\,s$, $1.25\,s$ and $1.5\,s$.

5.5.4 Experimental case BL4: Dike-breaking by overtopping flow

This experimental test case was carried out [137] in a straight rectangular cross-section flume $35\,m$ long and $1m$ wide. A trapezoidal dyke was constructed in the middle of the flume with a non-cohesive sand of characteristic diameter $d_s = 1.13\,mm$ ($d_{30} = 0.52\,mm$, $d_{50} = 0.86\,mm$, $d_{90} = 3.80\,mm$), density $\rho_s = 2650\,kg/m^3$, internal stability angle $\delta_b = 30°$ and porosity $\xi = 0.22$. The height over the non-erodible flume bed and crest width of the dyke were 0.80 m and 0.30 m, respectively. A vertical plate was placed at the middle of the crest in order to achieve horizontal water surface elevations upstream the dyke. In a first step, a constant discharge q_{inlet} was set at the flume inlet and the upstream reach was filled to a height of 3 cm over

the dyke crest. Then, the plate was suddenly lifted up to allow overflow to start, maintaining the constant inlet discharge.

The dyke surface evolution was recorded by photography. Temporal bed elevation data were provided at $P1 = 15\,cm$, $P2 = 65\,cm$ and $P3 = 115\,cm$ with distances measured from the midpoint of the dyke crest. The temporal evolution of the discharge at the dyke crest and the upstream reservoir level were also reported. Two different experiments, here referred to as BL4.A and BL4.B respectively, have been used to test the proposed model capabilities. The inlet discharge and the dyke upstream and downstream slopes, S_u and S_d respectively, have been summarized in Table 5.7. The Manning's roughness coefficient was calibrated as $n_b = 0.15 sm^{-1/3}$ [65]. The erosion and deposition constants, k_E and k_D respectively, used in simulations for each benchmarking test are summarized in Table 5.7. The FCM model is used here with both the capacity (R-Cap) and non-capacity (R-NCap) formulations for the bedload transport rate. The mesh used is again a single-row quadrilateral grid with cell size $\Delta x = 0.01m$ and the CFL was set to 0.95.

Case	$q_{inlet}\,(l/s)$	S_u	S_d	k_E	k_D
BL4.A	1.05	1V:3H	1V:5H	0.4	0.02
BL4.B	1.23	1V:3H	1V:3H	0.3	0.01

Table 5.7: Experimental case BL4 – Geometrical features and erosion-deposition constants used in the simulations.

Case BL4.A

Figure 5.27 shows the numerical results, considering the capacity transport assumption (R-Cap), for the temporal evolutions of both the reservoir level and the discharge at the dyke crest with different empirical formulations for the bedload transport rate. Measured data have also been plotted for comparison. The Smart formulation offers the best results, especially for the discharge at the dyke crest, but overestimates the erosion of the dyke at the first stages after the overflow starting. On the other hand, both MPM and Wu closure relations underestimate the bedload transport rate, resulting in a slower evolution of the dyke surface and leading to a lower peak in the discharge hydrograph.

The Smart closure relation has been chosen to study the influence of the non-capacity approach (R-NCap) on the computed dyke surface evolution. Figure 5.28 shows the numerical results considering both capacity and non-capacity approaches for the temporal evolutions of the reservoir water level and discharge at the crest. The obtained results have been plotted against the measured data. The numerical results reported by Juez *et al.* [65] with a weakly-coupled capacity model (WCM) have also been plotted for comparison. Although the predicted peak in the discharge with R-NCap formulation is lower than those observed in the laboratory, in general the numerical results agree better with the measured data than those obtained with both the R-Cap model and the WCM model reported by [65], improving the reservoir level and discharge predictions (Table 5.8).

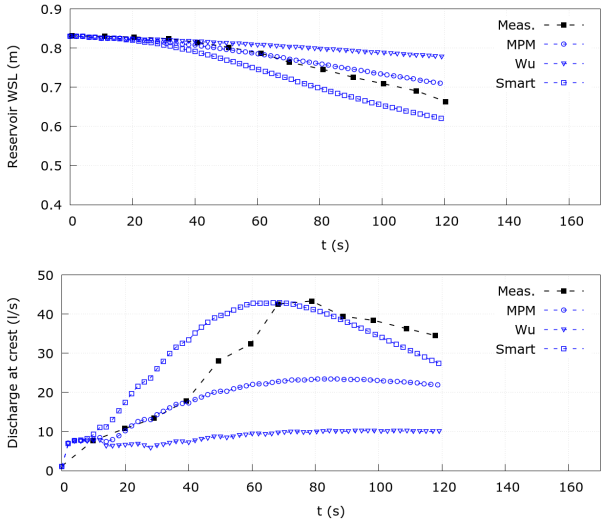

Figure 5.27: Experimental case BL4.A – Temporal evolution of the (top) reservoir water surface level and (bottom) discharge at the dyke crest: measured data compared to numerical results with R-Cap model.

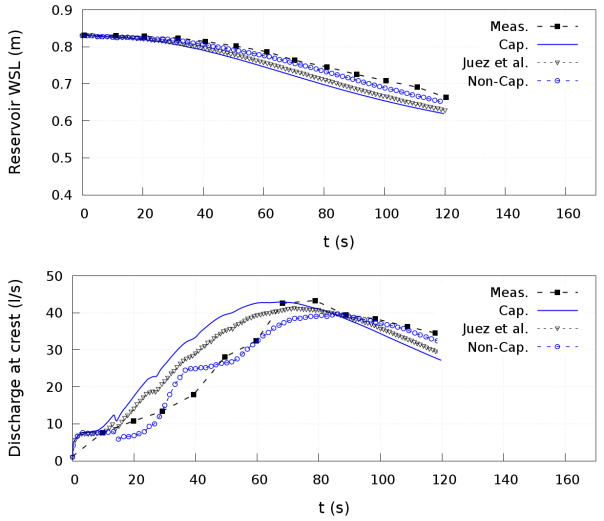

Figure 5.28: Experimental case BL4.A – Temporal evolution of the (top) reservoir water surface level and (bottom) discharge at the dyke crest with the Smart bedload formula.

	RMSE		
Variable	Capacity	Non-Capacity	Juez *et al.* [65]
WSL_{reserv} (m)	0.03865	0.01279	0.02967
Q_{crest} (m^3/s)	0.00755	0.00304	0.00499
z_{b1} (m)	0.04191	0.02543	0.03437
z_{b2} (m)	0.03573	0.01370	0.03275
z_{b3} (m)	0.01998	0.01583	0.01959

Table 5.8: Experimental case BL4.A – RMSE (case C1) for the reservoir level WSL_{reserv}, discharge at the dam crest Q_{crest}, and bed level at the probes P1 z_{b1}, P2 z_{b2} and P3 z_{b3}, with capacity and non-capacity formulations. Also RMSE for the results obtained with the WCM model Juez *et al.* [65] has been reported.

Furthermore, the dyke bed surface evolution has been plotted in Figure 5.29 at probes P1, P2 and P3, considering the modified Smart-CBFS formulation under capacity and non capacity conditions. The non-equilibrium hypothesis is able to improve the agreement with bed evolution measured data at all the probes (see Table 5.8). At the first stages after the overflow starts, marked non-equilibrium states are obtained by the active layer thickness η. Nevertheless, as time progresses, the bedload transport tends to reach the equilibrium state and the active layer thickness approximates its value under capacity conditions.

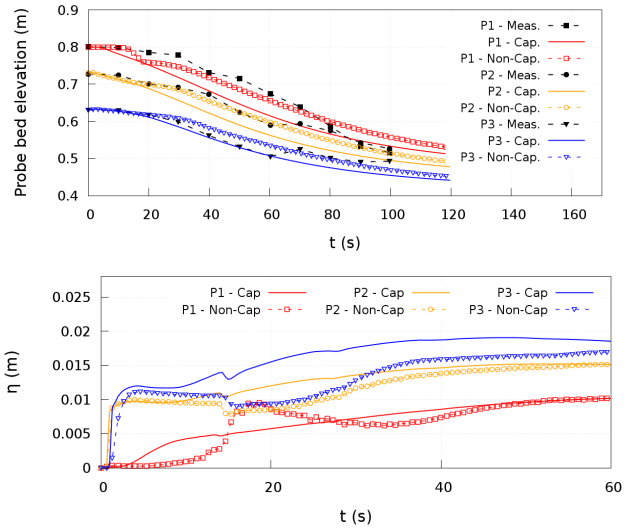

Figure 5.29: Experimental case BL4.A – Temporal evolution of the (top) dyke surface elevation and (bottom) active bed layer thickness η at probes P1, P2 and P3. The moving layer thickness has only been plotted for the first 60 sec of simulation.

Case BL4.B

Case BL4.B represents a more challenging benchmark for numerical models. The steeper dyke downward slope leads to a more energetic overtopping flow with elevated erosion rates and also involving stability failures. As in the previous case BL4.A, the best agreement with observed data is achieved with the bedload transport rate computed with the Smart closure relation. Figure 5.30 shows the dyke surface at times $t = 30\,s$ and $t = 60\,s$ after the overflow starts, whereas Figure 5.31 depicts the temporal evolutions of the reservoir water level and discharge at the crest. Numerical results considering both equilibrium and non-capacity approaches have been plotted against measured data. The equilibrium condition largely overestimates the erosion of the dyke surface at the first stages after the flow starts, leading to a rapid decrease in the reservoir level and reaching the peak of the discharge hydrograph faster than observed in laboratory (Figure 5.31).

On the other hand, in general considering non-equilibrium conditions improves the agreement between numerical results and measured data, especially at the first stages after the gate opening. Despite the stability failures observed at the downward dyke slope during the experiment, the measured and computed dyke surfaces considering the non-equilibrium hypothesis show a good agreement. The root-mean-square error for the

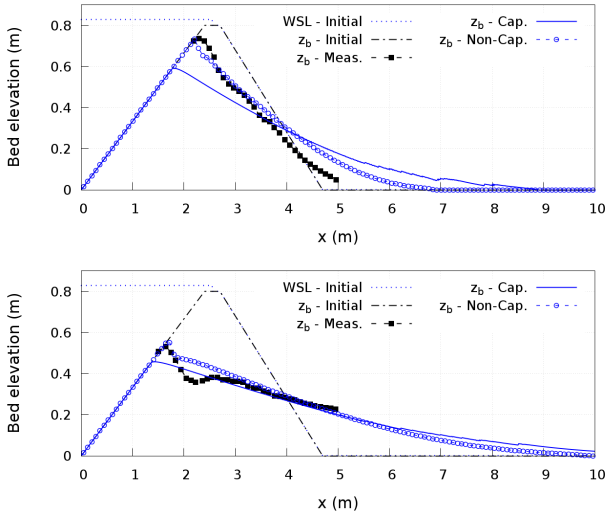

Figure 5.30: Experimental case BL4.B – Measured and numerical dyke surfaces at times (top) $t = 30\,s$ and (bottom) $t = 60\,s$ using Smart formulation, with R-Cap and W-NCap models.

	RMSE	
Variable	Capacity	Non-Capacity
WSL_{reserv} (m)	0.11240	0.03808
Q_{crest} (m^3/s)	0.04469	0.01546
z_{b30} (m)	0.10873	0.06024
z_{b60} (m)	0.02792	0.03050

Table 5.9: Experimental case BL4.B – RMSE (case C2) for the reservoir level WSL_{reserv}, discharge at the dam crest Q_{crest}, and bed level profiles at times $t = 30\,s$ (z_{b30}) and $t = 60\,s$ (z_{b60}), with R-Cap and W-NCap models.

non-capacity results are lower for the dyke profile at time $t = 30\,s$ and slightly higher for the time $t = 60\,s$ than those obtained with the capacity bedload transport formulation (Table 5.9). Furthermore, the R-NCap model improves both the reservoir level and the discharge at the dike crest predictions. The root-mean-square error for the reservoir level prediction and the discharge at the dyke crest are much lower with the R-NCap model than those obtained considering the equilibrium hypothesis. However, the numerical model considering non-capacity solid transport formulation is not able to properly predict the magnitude of the hydrograph peak observed in laboratory (Fig. 5.31).

Finally, Table 5.10 shows the CPU computational times for tests C1 and C2 using both capacity and non-capacity approaches and the modified Smart-CBFS formula for the determination of the solid transport rate. Differences in computational effort associated to the assumption of capacity or non-capacity formulation can be considered negligible in both benchmark tests.

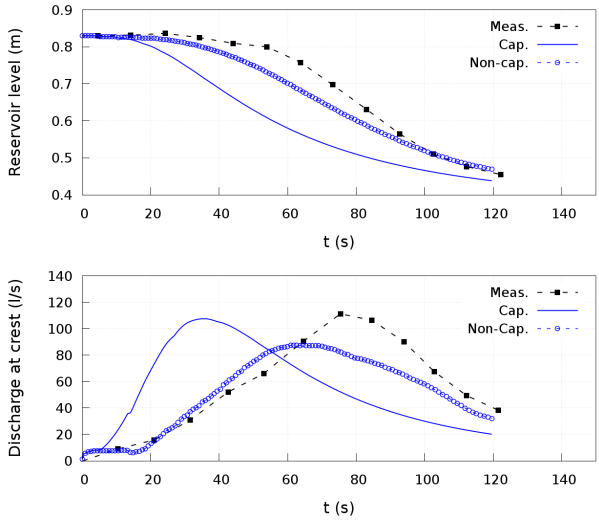

Figure 5.31: Experimental case BL4.B – Temporal evolution of the (top) reservoir water surface level and (bottom) discharge at the dyke crest using Smart formulation, with R-Cap and W-NCap models.

	Comp. time (s)	
Formulation	Case BL4.A	Case BL4.B
R-Cap	49.400	41.199
R-NCap	48.288	40.687

Table 5.10: Experimental case BL4.B – CPU computational times for cases BL4.A and BL4.B with capacity and non-capacity formulations using the Smart bedload rate.

5.5.5 Experimental case BL5: Evolution of a trench over non-erodible stratum

This experimental benchmark test aims to demonstrate the effectivity of the proposed active control of the sediment thickness positivity method (AC-STP) compared with the classical time step reduction method (TSR) to avoid unphysical over-eroded regions without increasing the required computational cost. The experiments were carried out by Struiksma [136], consisting in the propagation of a trench excavated in a uniform sand bed over a 3 m long non-erodible layer made of a medium gravel (8-16 mm). The experiments were performed in a straight rectangular cross-section flume with an effective length of $11.5\,m$ and a width of $0.20\,m$. The flume was filled with uniform sand ($d_s = 0.45\,mm$, $\rho_s = 2650 kg/m^3$, $\delta_b = 32°$ and $\xi = 0.38$) to a height of 0.15 m above the flume concrete floor, covering also the non-erodible layer. In a first step, a constant discharge was set at the flume inlet and both water and sand were recirculated until uniform bed slope was achieved. The water level was controlled by an adjustable tailgate at the flume outlet. Once a steady bed slope was reached, a 2 m long and 0.04 m deep trench was excavated upstream the gravel layer. The flow was restarted and this bed perturbation propagated downstream, disappearing over the non-erodible layer exposing the gravel stratum and reappearing downstream later. Struiksma [136] proposed a solid transport rate formula $q_b = \kappa\, u^5$ to reproduce the advance velocity of the trench, with κ being a

tuning parameter which should be calibrated. Therefore an adapted expression to adjust $G = \kappa\, u^2$ has been derived for the proposed scheme. This case has previously been used for benchmarking by Caviedes-Voullième *et al.* [24], Dewals *et al.* [30], Ortiz *et al.* [110], and Struiksma [136] since it reproduces a process of great interest and measured bed elevation data are available.

Two different experimental tests are reproduced in this work, BL5.A and BL5.B. The main difference between both experiments is that, in BL5.B, the initial sand thickness over the non-erodible layer is lower than in the case BL5.A and hence the gravel stratum is exposed longer. The erosion and deposition constant are initially set to $k_E = 2 \cdot 10^{-3}$ and $k_D = 1 \cdot 10^{-5}$ respectively. The flow and sediment transport features used in simulations for both tests have been reported in Table 5.11 whereas the initial profiles for both the gravel and the erodible layers, as well as the water surface elevation, are shown in Figure 5.32. The FCM model is used here with both the capacity (R-Cap) and non-capacity (R-NCap) formulations for the bedload transport rate. The mesh used is again a single-row quadrilateral grid with cell size $\Delta x = 0.05\, m$ and the CFL was set to 0.95.

Case	$q_{inlet}\,(l/s)$	$q_{b,inlet}\,(l/h)$	$n_b\,(s/m^3)$	$h_{out}\,(m)$	$\kappa\,(s^4/m^3)$
BL5.A	9.2	7.0	0.019	0.338	0.00020
BL5.B	9.2	4.2	0.019	0.323	0.00022

Table 5.11: Experimental case BL5 – Main parameters used in the simulations for each benchmarking case.

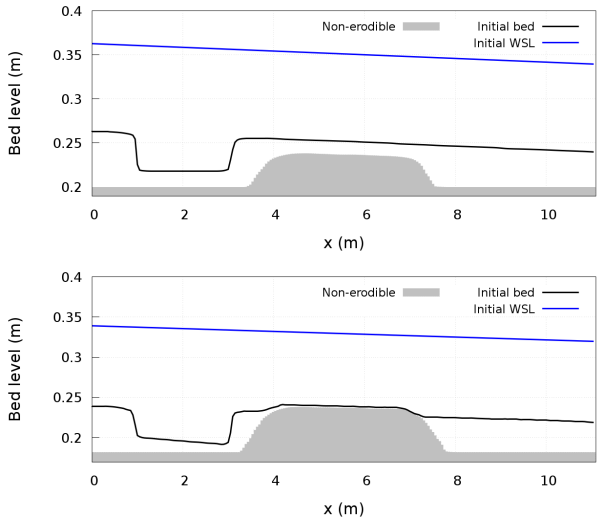

Figure 5.32: Experimental case BL5 – Initial bed and water surface elevations for cases (top) BL5.A and (bottom) BL5.B.

Figure 5.33 depicts the temporal bed evolution for both cases and compares the measured data (black points) with the numerical results obtained considering non-capacity (point-dashed blue lines) and equilibrium (solid blue lines) approaches. Numerical results obtained with the coupled scheme reported by Martínez-Aranda *et al.* [86] are also shown (dashed red

lines). This model uses the capacity approach for the transport rate determination and the over-erosion problems are controlled by reducing the dynamic time step to avoid cells with negative sediment thickness values (TSR strategy). The time step reduction is limited to 10% of the value determined by the original CFL condition hence solid mass conservation problems can appear at cells where this reduction is not enough.

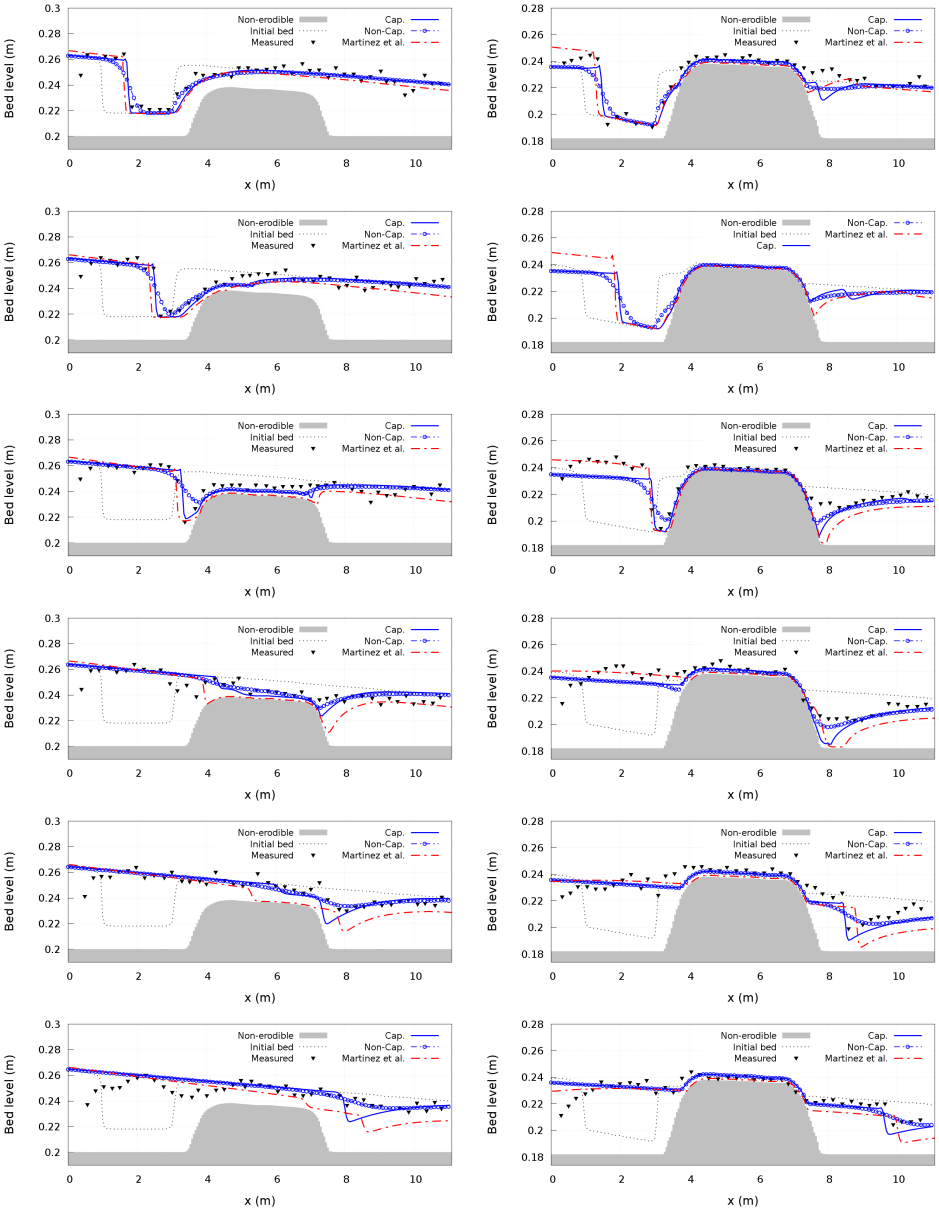

Figure 5.33: Experimental case BL5 – Bed level for (left column) case BL5.A at times $t = 1\,h, 2\,h, 3\,h, 4\,h, 5\,h, 6\,h$ and (right column) case BL5.B at times $t = 1\,h, 2\,h, 4\,h, 6\,h, 8\,h, 10\,h$.

The AC-STP method is able to reproduce the trench propagation process over the non-erodible gravel stratum, considering both equilibrium and non-capacity conditions. The non-capacity approach with $k_E = 2 \cdot 10^{-3}$

seems to introduce an extra-diffusion term on the numerical solution comparing with the equilibrium approach, although the trench propagation velocity is similar and agrees with the observed data for both tests. The AC-STP method avoids unphysical over-erosion and improves largely the prediction of the trench propagation obtained with the scheme reported in [86] using the TSR strategy (see Table 5.12).

	RMSE z_b (m)	
Formulation	Case BL5.A	Case BL5.B
Capacity	0.00651	0.00685
Non-Capacity	0.00621	0.00654
Martínez-Aranda *et al.* [86]	0.00911	0.00847

Table 5.12: Experimental case BL5 – RMSE (cases BL5.A y BL5.B) for the bed level evolution z_b, with capacity and non-capacity formulations. Also RMSE for the results obtained with the Martínez-Aranda *et al.* [86] model has been reported.

Furthermore, most numerical models dealing with these cases [24, 30, 110] predict an excavated region downstream the gravel stratum which was not observed in experiments. That excavated zone is also reproduced here using the equilibrium model proposed by Martínez-Aranda *et al.* [86] with the classical time-reduction (TSR) treatment for the non-erodible layer. The present non-capacity formulation ($k_E = 2 \cdot 10^{-3}$) is able to eliminate totally this excavation for case BL5.A and to reduce it significantly for case BL5.B. The solid transport q_b over the gravel stratum is reduced as an effect of the sediment unavailability using (5.89). This reduction interferes with the equivalent non-equilibrium adaptation length, leading to a solid transport rate smaller than the flow transport capacity downstream the gravel stratum. Therefore, the solid transport rate at the downstream region is lower with non-capacity formulation than that considering the equilibrium hypothesis, therefore reducing the excavation.

Figure 5.34 shows the effects of the erosion constant k_E on the evolution of the excavated region downstream the gravel stratum. Lower erosion constant k_E values lead to an increment of the equivalent adaptation length L_b. The reduction of the physical solid transport rate applied in cells where the theoretical moving layer thickness η is greater than the available sediment thickness ϵ_b leads to a more stable propagation of the trench over the gravel stratum and reduces the excavated region downstream. As the erosion constant k_E increases, the equivalent adaptation length decreases and the non-equilibrium solid transport states caused by the appearance of the non-erodible layer are also reduced. Hence, the non-capacity solution tends to approximate the equilibrium bed evolution profile (see Figure 5.34). With $k_E = 2 \cdot 10^{-2}$ the non-capacity results practically agree with the equilibrium prediction, demonstrating the sensitivity of the model to the erosion-deposition constants calibration.

Finally, the positivity control mechanism for the sediment thickness is triggered many times during simulations as the gravel stratum is successively exposed and recovered during the trench advance. In order to

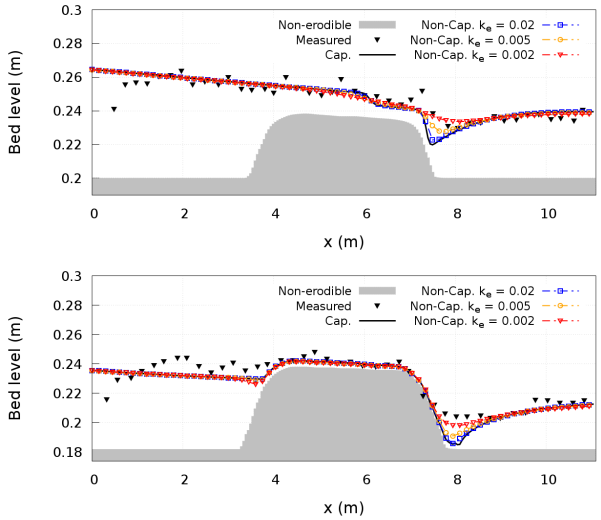

Figure 5.34: Experimental case BL5 – Bed level for (top) case BL5.A at time $t = 5\,h$ and (bottom) case BL5.B at time $t = 6\,h$ with non-capacity formulation.

demonstrate the effectiveness of the AC-STP method, additional simulations were carried out considering the proposed model but using the classical TSR strategy to avoid unphysical over-eroded cells, using both equilibrium and non-equilibrium hypothesis. Figure 5.35 shows the bed profiles for case BL5.A at $t = 3\,h$ and case BL5.B at $t = 4\,h$. At these times, the whole gravel stratum was exposed. The bed level predictions computed with capacity AC-STP and capacity TSR methods show small variations caused by the different treatment of the non-erodible stratum. Similar small variations are found comparing non-capacity AC-STP and non-capacity TSR methods. However, using the AC-STP method the numerical solution remains stable and it is not necessary to reduce the time step to ensure the sediment mass conservation or numerical stability (Figure 5.36), unlike using the TSR method [24]. Furthermore, the time step reduction strategy demonstrates not to be able to avoid completely the over-erosion problems without a marked reduction of the time step, leading to a higher computational effort for the simulations (Table 5.13). Moreover, as the time step reduction is limited to avoid an excessive computational effort, solid mass conservation errors appear in cells which require higher limitations to ensure positive sediment thickness values.

	Comp. time (s)	
Formulation	Case BL5.A	Case BL5.B
Capacity AC-STP	134.144	225.748
Capacity TSR	253.478	757.296
Non-Capacity AC-STP	133.528	232.663
Non-Capacity TSR	202.018	448.121
Martínez et al. TSR	463.105	921.838

Table 5.13: Experimental case BL5 – CPU computational times (cases BL5.A y BL5.B) for capacity AC-STP, capacity TSR, non-capacity AC-STP and non-capacity TSR models. Also the computational time for Martínez et al. TSR model [86] has been reported.

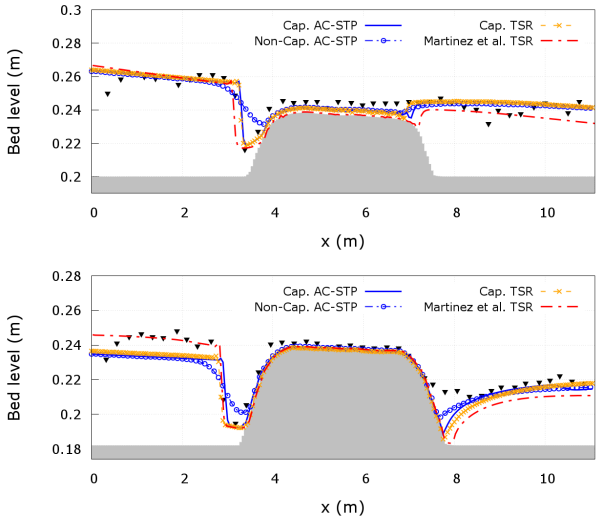

Figure 5.35: Experimental case BL5 – Bed level for (left) case BL5.A at time $t = 3\,h$ and (right) case BL5.B at time $t = 4\,h$ using non-capacity AC-STP, non-capacity TSR, capacity TSR and Martínez et al. TSR models.

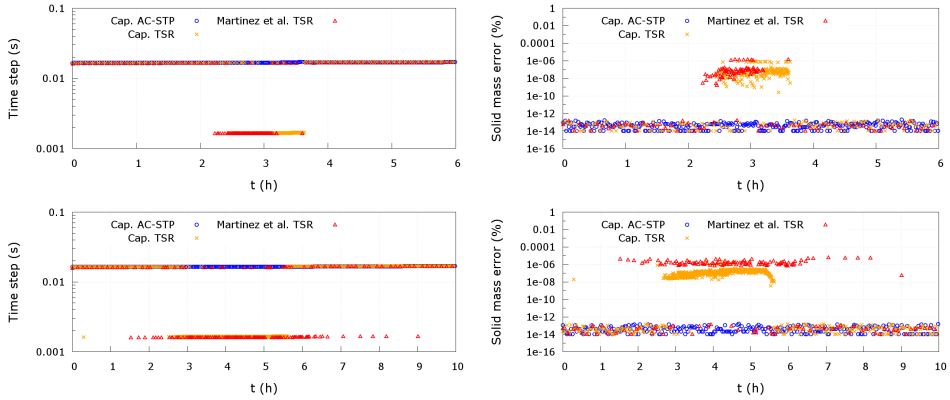

Figure 5.36: Experimental case BL5 – Dynamic time step (left column) and solid mass conservation errors (right column) for cases (top) BL5.A and (bottom) BL5.B. Note that results are shown for every 20 time steps. For the sake of clarity only results using capacity formulation have been depicted.

5.5.6 Experimental cases BL6: Flood wave over an erodible bed narrowing

In this experimental benchmark case, both the FCM and ACM numerical schemes, using different capacity formulations, are faced to two-dimensional highly erosive flow experiments. These new experiments were carried out during the PhD period at the Laboratory of Fluid Mechanics of the University of Zaragoza [92].

The experiments consist of a dambreak wave moving along a $3.25\,m$ long and $24\,cm$ wide flume over a $5\,cm$ depth erodible flat bed made of non-cohesive sand. The cross-section of the flume was modified by creating a $11\,cm$ long and $13\,cm$ wide narrowing using both $11\,cm$ diameter semi-circular (Case BL6.A) and $11 \times 5.5\,cm$ rectangular (Case BL6.B) pieces, centered at $150\,cm$ from the flume beginning, allowing the generation of two-dimensional flow at the measurement region. The dambreak wave

was triggered by lifting a pneumatic gate which separates the flume from a $157\,cm$ long and $81\,cm$ wide upstream reservoir where the initial height of the water was $8\,cm$ over the dry flume floor. Downstream the flume, a $275\,cm$ long sediment trap stored the eroded material before a recovery tank. A RGB-D sensor (Kinect, Microsoft, 2010) was used to perform instantaneous measurements of the 2D transient water surface height during the wave propagation throughout the narrowing. This device records the distance to the water free-surface using an infrared light projection technique with 30 Hz acquisition rate, 1.4 mm spatial resolution and 1-2 mm precision approximately. After the dambreak wave, the 2D bed surface elevation was also recorded using the same RGB-D sensor in order to determine the morphodynamical changes generated by the flow. A skecth of the experiments setup is shown in Figure 5.37.

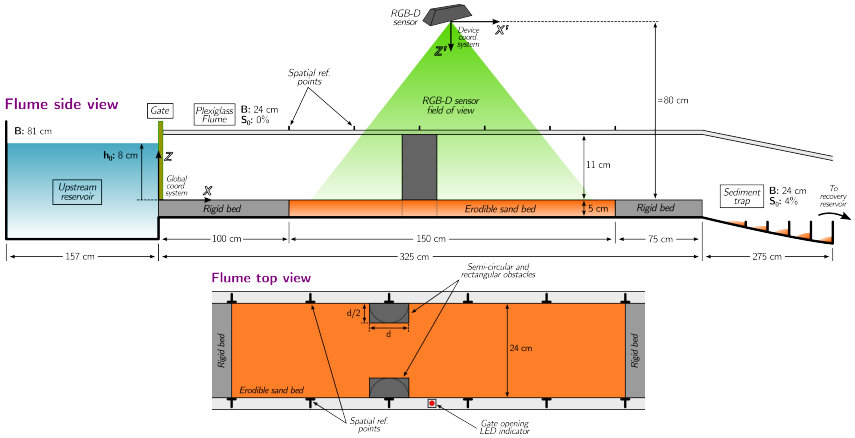

Figure 5.37: Experimental cases BL6 – Experimental setup and initial conditions.

The erodible bed consisted of a mix of two uniform sand size-classes with characteristic parameters shown in Table 5.14. The global bed porosity was estimated as $\xi = 0.34$, the deposition and erosion constants are set to $k_D = 0.02$ and $k_E = 0.3$ respectively, and the Manning resistance factor is calibrated to $n_r = 0.012$ at the fixed bed regions and $n_b = 0.026$ throughout the movable bed region.

	Diameter $d_s(mm)$	Density $\rho_s(kg/m^3)$	Bed fraction $F_{b,p}(-)$	Manning coeff. $n_p(sm^{-1/3})$
Coarse sand	1.3	2650	0.5	0.0157
Fine sand	0.7	2650	0.5	0.0141

Table 5.14: Experimental cases BL6 – Erodible bed composition.

Mesh refinement calibration

In order to determine the mesh refinement level required to reduce the associated error maximizing the computational efficiency, a previous blind study is performed using the semicircular narrowing geometry and five different unstructured triangular meshes with different refinement levels throughout the erodible bed region. Table 5.15 shows the geometrical characteristics of the five meshes considered. It is worth noting that the base

mesh MB is maintained unchanged at the upstream reservoir and the fixed bed regions regardless of the refinement level at the movable bed region.

Mesh	Base mesh	Cell refinement features		
		Edge (cm)	Area (cm^2)	Number of cells
MB	-	≈ 4	≈ 6.93	-
M1	MB	≈ 4.00	≈ 6.93	5354
M2	MB	≈ 2.00	≈ 1.73	8102
M3	MB	≈ 1.00	≈ 0.533	16634
M4	MB	≈ 0.50	≈ 0.108	64611
MR	MB	≈ 0.25	≈ 0.0271	224397

Table 5.15: Experimental cases BL6 – Geometrical features of the meshes considered in the refinement study.

The simulations are performed using the FCM scheme, CFL=0.95 and the capacity Meyer-Peter-Müller formulation to estimate the bedload solid rate (see Table 5.2). The numerical results obtained with the different meshes at $t = 10\,s$ are compared in terms of bed change error and computational efficiency in order to determine the optimal refinement level, taking the finest mesh MR results as reference.

Figure 5.38–left shows the root mean square error (RMSE) for the bed level z_b obtained with the meshes M1, M2, M3 and M4 respect to the those obtained with the reference mesh MR. Furthermore, Figure 5.38–right depicts the efficiency ratio between the RMSE for z_b and the computational time required by the model. The RMSE shows a uniform decrease with the mesh refinement whereas the ratio tends to an asymptotic behavior. Based on these results, the mesh M4 is selected for the simulation of the experimental cases.

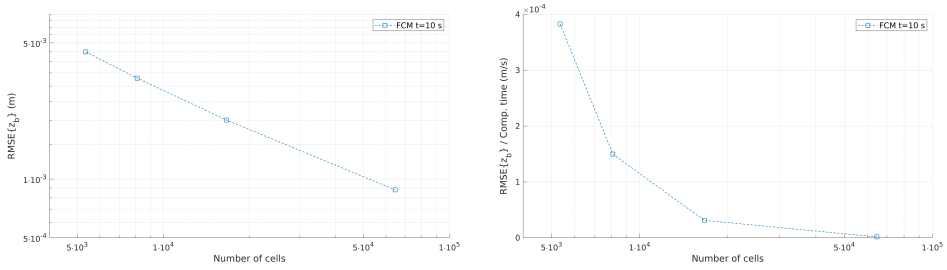

Figure 5.38: Experimental cases BL6 – Mesh refinement tests: (left) RMSE for the bed level z_b and (right) efficiency ratio RMSE/Computational time.

Case BL6.A: Semicircular narrowing

BL6.A considers the dambreak propagation along the flume with the semicircular narrowing geometry. The simulations are performed using both the FCM and the ACM models. The Meyer-Peter-Müller and the Wu relationships are considered to estimate the bedload solid rate. The simulations run until a time $t = 25\,s$ so that the bedload transport totally stops.

Figure 5.39 shows the two-dimensional water depth h fields measured with the Kinect sensor at different times after the gate opening. The water depth h is expressed in cm referred to the original flat bed. The dambreak

wave front reaches the narrowing $1.6\,s$ after the gate opening approximately. Initially, two water columns rise up near the narrowing walls (see $t = 1.8351\,s$ image) caused by the impact of the wave front on the semicircular walls. This violent impact leads to marked vertical accelerations in the flow near the semicircular walls at the first stages after the wave arrival. Then, these water columns disappear progressively (images $t = 2.0355\,s$ and $t = 2.3354\,s$) as the wave front moves downstream. A triangle-shaped hydraulic jump appears upstream the narrowing and moves toward the flume beginning, whereas the characteristic diamond structure is created downstream the narrowing region (see $t = 2.7695\,s$ and $t = 3.2035\,s$ images).

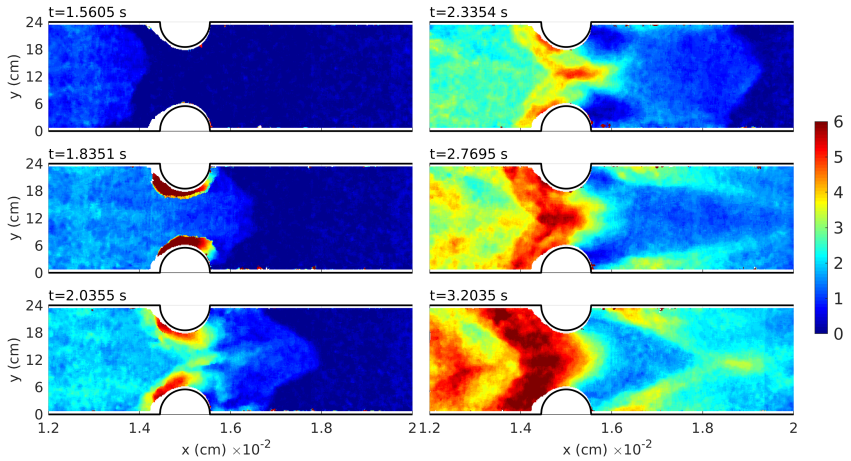

Figure 5.39: Experimental cases BL6.A – Measured water depth h (in cm) over the initial flat bed at different times after the gate opening.

The temporal evolution of the water depth over the initial flat bed computed with the FCM is shown in Figure 5.40 using the MPM (left column) and Wu (right column) relationships for the bedload transport rate estimation. Results obtained with the ACM show a quite similar water depth evolution. Both numerical models are able to predict the arrival time of the wave front to the narrowing, as well as the appearance and evolution of both the upstream hydraulic jump and the diamond structure downstream the narrowing region. Nevertheless, the appearance of marked vertical acceleration during the first stages after the wave front arrival to the narrowing region shows the limitations of both models (hydrostatic pressure assumption), since they can not correctly predict the growth of the water columns near the semicircular narrowing walls after the wave front impact. Furthermore, the triangular shape of the upstream hydraulic jump observed in the laboratory is not fully captured by the numerical models.

With respect to the influence of the bedload transport rate formulation in the water depth temporal evolution, the simulation performed using the Wu relationship shows a slightly slower wave front progression than that performed using the MPM formula, as well as thinner diamond structures downstream the narrowing. Furthermore, the triangular shape of the upstream hydraulic jump is also slightly better predicted using the Wu formula than with the MPM relationship.

The temporal evolution of the water depth h over the initial flat bed is extracted from the 2D water-surface Kinect measurements at different

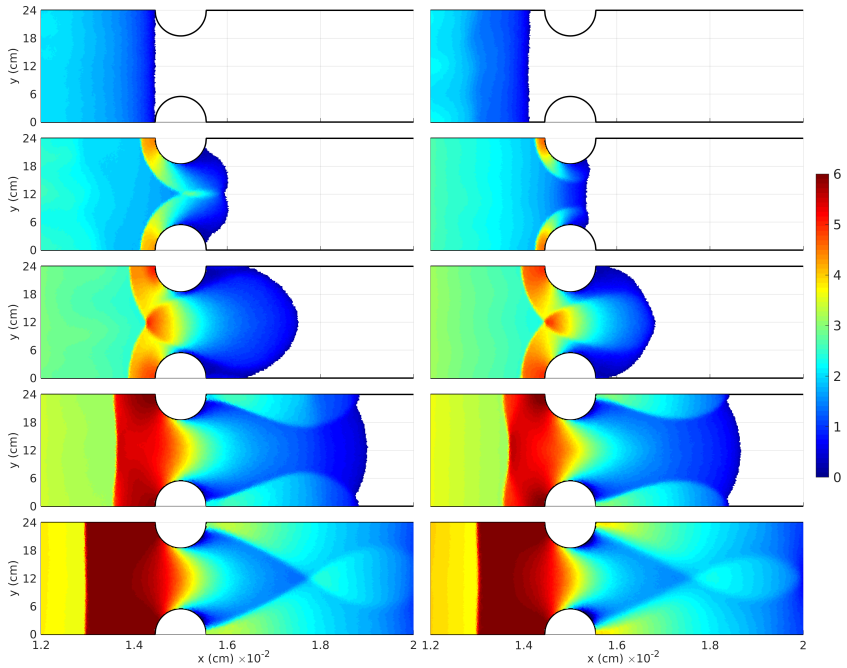

Figure 5.40: Experimental cases BL6.A – Computed water depth h (in cm) over the initial flat bed with FCM solver, using (left column) MPM and (right column) Wu bedload solid rate formulations. From top to bottom: $t = 1.6\,s$, $t = 1.8\,s$, $t = 2.0\,s$, $t = 2.3\,s$ and $t = 2.6\,s$.

gauge points: upstream the narrowing P1 ($x = 140\,cm, y = 12\,cm$), at the center of the narrowing P2 ($x = 150\,cm, y = 12\,cm$), downstream the narrowing P3 ($x = 165\,cm, y = 12\,cm$), and near the semicircular walls P4–right ($x = 144.5\,cm, y = 6.5\,cm$) and P4–left ($x = 144.5\,cm, y = 17.5\,cm$). Figure 5.41 shows the measured water depth evolution at the considered gauge points and the comparison with the data obtained from the numerical simulations using the FCM scheme. The numerical results obtained with the ACM model are rather similar. In general, both the FCM and the ACM schemes predict well the water depth tendency at all the gauge points considered, regardless of the empirical relationship used for the bedload rate estimation, but some differences appear and should be commented. Upstream the narrowing (P1), both models predict a water depth increment sharper than was measured in the laboratory. At the center of the narrowing (P2), the numerical water depth evolution obtained with the MPM formula for the bedload transport rate shows a sharp increment at $t \approx 8\,s$ which is not shown in the experimental data, whereas the numerical results with the Wu relationship show a more acceptable behaviour. However, the maximum water depth obtained with the Wu formula at this gauge point is lower in the numerical simulations than in the experiments. Downstream the narrowing (P3), both numerical schemes show again a sharper water depth increase than in the experimental data. Near the narrowing walls (P4–right and P4–left) the numerical results are in agreement with the measured water depth regardless of the formulation used for the bedload rate computation.

Figure 5.42 depicts the bed changes measured in laboratory after the bed layer was totally dry and the comparison with the numerical results obtained at the end of the simulations. The bathymetry after the dambreak

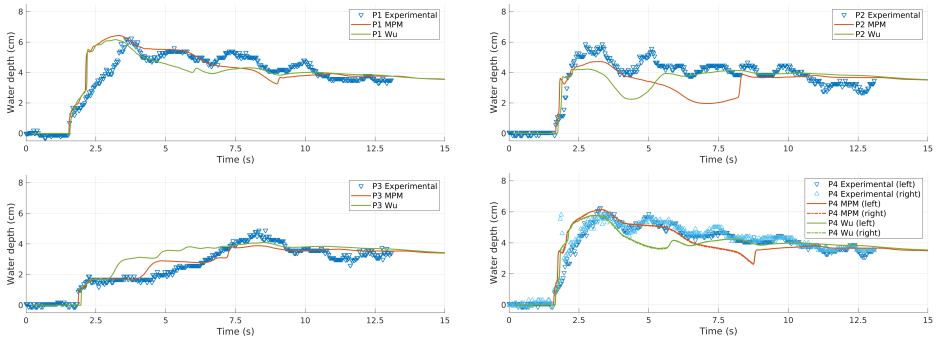

Figure 5.41: Experimental cases BL6.A – Experimental and numerical (FCM) water depth evolution at (top–left) P1, (top–right) P2, (bottom–left) P3 and (bottom–right) P4.

wave observed in the experiments is characterized by high erosion at the center of the narrowing, especially near the semicircular walls, and by the appearance of a marked diamond-shape deposition bar downstream the narrowing. Both the fully-coupled and the approximate coupled models are able to predict these characteristic structures in the bed layer level, regardless of the empirical formulation selected for the bedload transport. However, the length of the erosion region and the diamond-shape deposition bar are better predicted with the Wu formula than using the MPM relation, leading to lower RMSE for the global z_b with the Wu expression (see Table 5.16). Furthermore, the FCM scheme shows lower RMSE for z_b than the approximate–coupled method whereas, regarding the computational effort, the FCM method is slightly more expensive than the ACM scheme (Table 5.16), although those differences are practically negligible.

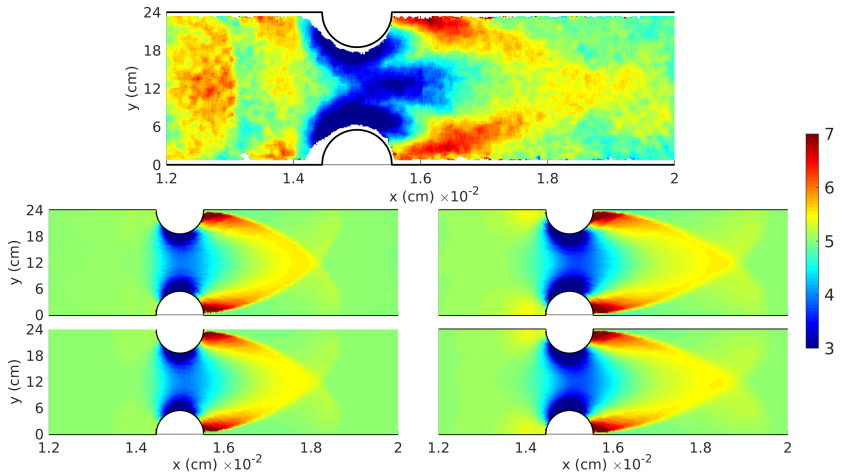

Figure 5.42: Experimental cases BL6.A – (top row) Experimental bed elevation z_b in cm after the dambreak wave and numerical results: (center–left) FCM with MPM bedload, (center–right) FCM with Wu bedload, (bottom–left) ACM with MPM bedload and (bottom–right) ACM with Wu bedload.

Solid transport formulation	RMSE z_b (cm)		Comp. time (s)	
	ACM	FCM	ACM	FCM
Meyer-Peter-Müller	0.5542	0.5407	1019.464	1068.815
Wu	0.4666	0.4517	1068.152	1109.912

Table 5.16: Experimental cases BL6.A – Root mean square error (RMSE) for the bed elevation z_b respect to the experimental data and computational effort of the FCM and ACM methods.

Case BL6.B: Rectangular narrowing

Case BL6.B considers the dambreak propagation along the flume with the rectangular narrowing geometry. The simulations are performed following the same procedure and using the same parameters as in Case 1. Figure 5.43 shows the two-dimensional water depth h fields measured with the Kinect sensor at different times after the gate opening. As in the previous case, the wave reaches the narrowing $1.6\,s$ after the gate opening and two marked water columns rise up near the narrowing walls (see $t = 1.8661\,s$ image) caused by the impact of the wave front, leading to marked vertical accelerations in the flow near the narrowing walls at the first stages after the front arrival. Then, these water columns evolve progressively (image $t = 2.0364\,s$) and create a hydraulic jump upstream the narrowing which moves to the flume beginning (see $t = 2.3364\,s$, $t = 2.7705\,s$ and $t = 3.3699\,s$ images). For this case, the hydraulic jump is perpendicular to the flume axis almost from the first stages. Also the characteristic diamond structure appears downstream the narrowing region (image $t = 3.3699\,s$) although less noticeable than in Case 1.

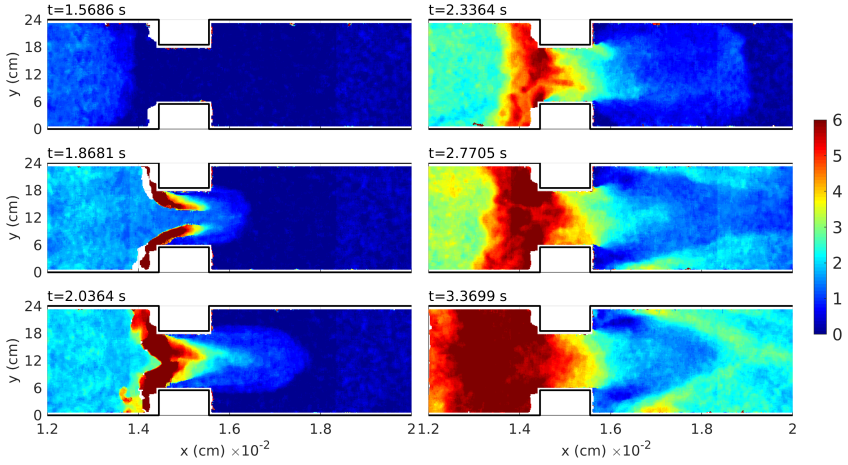

Figure 5.43: Experimental cases BL6.B – Measured water depth h (in cm) over the initial flat bed at different times after the gate opening.

The two-dimensional water depth h fields over the initial flat bed computed with the FCM scheme at times $t = 1.6\,s$, $t = 1.8\,s$, $t = 2.0\,s$, $t = 2.3\,s$ and $t = 2.6\,s$ are shown in Figure 5.44, using the MPM (left column) and Wu (right column) formulations for the bedload transport rate estimation. The results obtained with the ACM shows a quite similar water depth evolution hence they are not shown. Both schemes are again able to predict the arrival time of the wave front to the narrowing, as well as the appearance and

evolution of both the upstream hydraulic jump and the diamond structure downstream the narrowing region. With respect to the influence of the bedload transport rate formulation in the water depth temporal evolution, the simulation performed using the Wu relationship shows a slightly slower wave front progression than that performed using the MPM formula, as in previous Case 1.

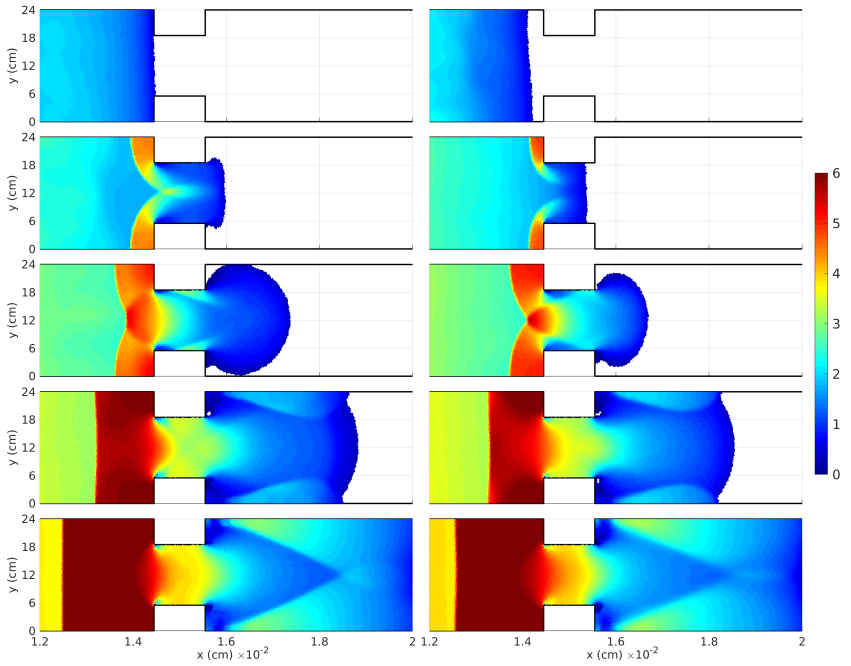

Figure 5.44: Experimental cases BL6.B – Computed water depth h (in cm) over the initial flat bed with FCM solver, using (left column) MPM and (right column) Wu bedload solid rate formulations. From top to bottom: $t = 1.6\,s$, $t = 1.8\,s$, $t = 2.0\,s$, $t = 2.3\,s$ and $t = 2.6\,s$.

Figure 5.45 depicts the temporal evolution of the water depth h extracted from the two-dimensional Kinect measurements at the same gauge points as in Case BL6.A: upstream the narrowing P1, at the center of the narrowing P2, downstream the narrowing P3, and near the upstream corner of the rectangular narrowing pieces P4–right and P4–left. Data obtained from the numerical simulations using the FCM scheme are also plotted for comparison. Regardless of the empirical formulation chosen for the bedload transport rate estimation, the proposed numerical schemes predict well the water depth h at all the gauge points considered, with the exception of the first stages after the wave front arrival at the gauge points P4 where the vertical accelerations are again huge and hence the hydrostatic hypothesis is not fully valid.

Figure 5.46 depicts the bed changes measured in laboratory after the bed layer was totally dry and the comparison with the numerical results obtained at the end of the simulations. The bathymetry after the dambreak wave observed in the experiments is again characterized by high erosion at the center of the narrowing, especially near to the upstream corner of the narrowing walls, and by the appearance of a diffused diamond-shape deposition bar downstream. Both the FCM and the ACM schemes are able to predict these characteristic structures in the bed layer, regardless of the empirical formulation selected for the bedload transport. Nevertheless, the

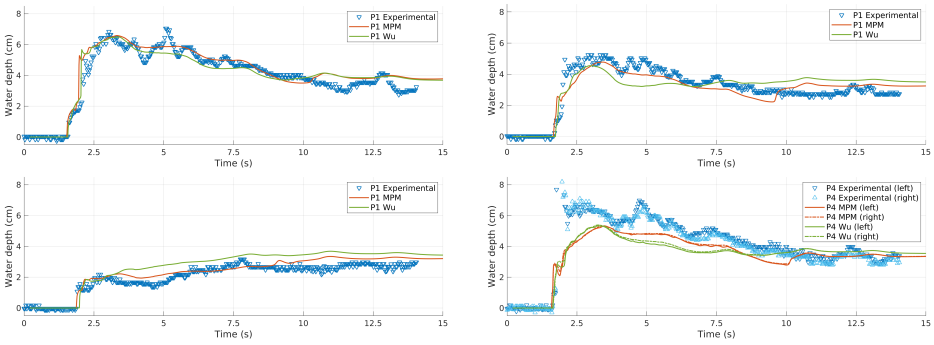

Figure 5.45: Experimental cases BL6.B – Experimental and numerical (FCM) water depth evolution at (top–left) P1, (top–right) P2, (bottom–left) P3 and (bottom–right) P4.

erosion region is much more pronounced with the Wu bedload rate formulation and also the length and shape of the deposition bar is better predicted. This leads to much lower RMSE for the numerical bed elevation z_b with the Wu expression compared with those obtained with the MPM formula (see Table 5.17). Furthermore, the FCM scheme shows lower RMSE for z_b and computational times than the approximate–coupled method for this experimental case.

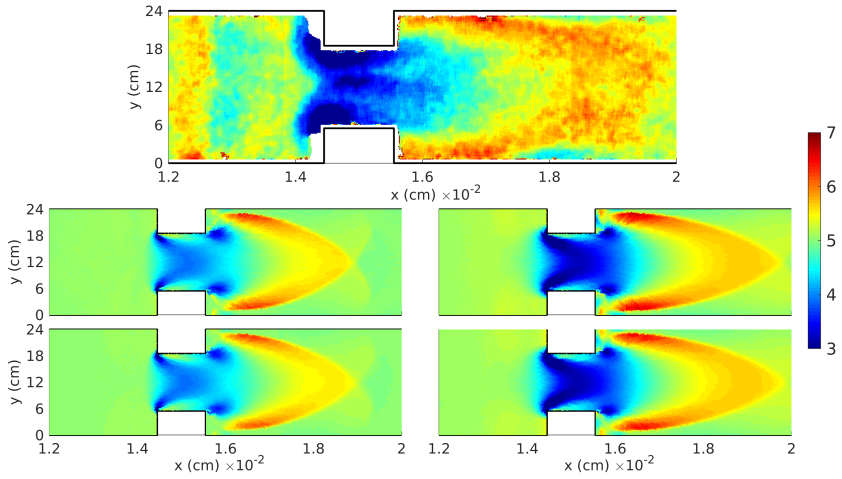

Figure 5.46: Experimental cases BL6.B – (top row) Experimental bed elevation z_b in cm after the dambreak wave and numerical results: (center–left) FCM with MPM bedload, (center–right) FCM with Wu bedload, (bottom–left) ACM with MPM bedload and (bottom–right) ACM with Wu bedload.

Solid transport formulation	RMSE z_b (cm)		Comp. time (s)	
	ACM	FCM	ACM	FCM
Meyer-Peter-Müller	0.5597	0.5566	1099.344	1094.036
Wu	0.4457	0.4462	1158.093	1148.897

Table 5.17: Experimental cases BL6.B – Root mean square error (RMSE) for the bed elevation z_b respect to the experimental data and computational effort of the FCM and ACM methods.

5.5.7 Experimental case BL7: Dambreak over erodible bed in a channel with a 90° bend

This experimental test was carried out at the UCL laboratory during the PhD period and designed to benchmark transient bedload transport models. The experiment consists of a two-dimensional dambreak occurring in a flume with a 90° bend and with an initial finite erodible $7.5\,cm$ thick layer. The experimental technique and the main results were published in Meurice *et al.* [96]. Both the water free surface and the bed level were measured with different data-retrieval techniques. This data set is used to assess the capabilities and limits of the capacity and non-capacity approaches for bedload transport. The FCM model was used here for all the simulations.

The geometry of the flume and the position of the gauges used to record the evolution of the water level are illustrated in Figure 5.47. The erodible layer was made of a uniform $d_s = 1.7\,mm$ non-cohesive sand Initially, the water level of the reservoir was $26\,cm$ above the non-erodible bed of the flume (reference level). An aluminium gate separates the reservoir from the upstream-reach of the flume and can be raised manually to simulate a quasi-instantaneous dambreak which progresses downstream over the erodible flat bed. After $3.92\,m$, the water wave-front will enter the downstream-reach of the flume that is perpendicular (90° bend) to the first one. This will lead the flow to show 2D and even 3D features. At the outlet section of this downstream-reach, the water flows freely in a dissipation reservoir.

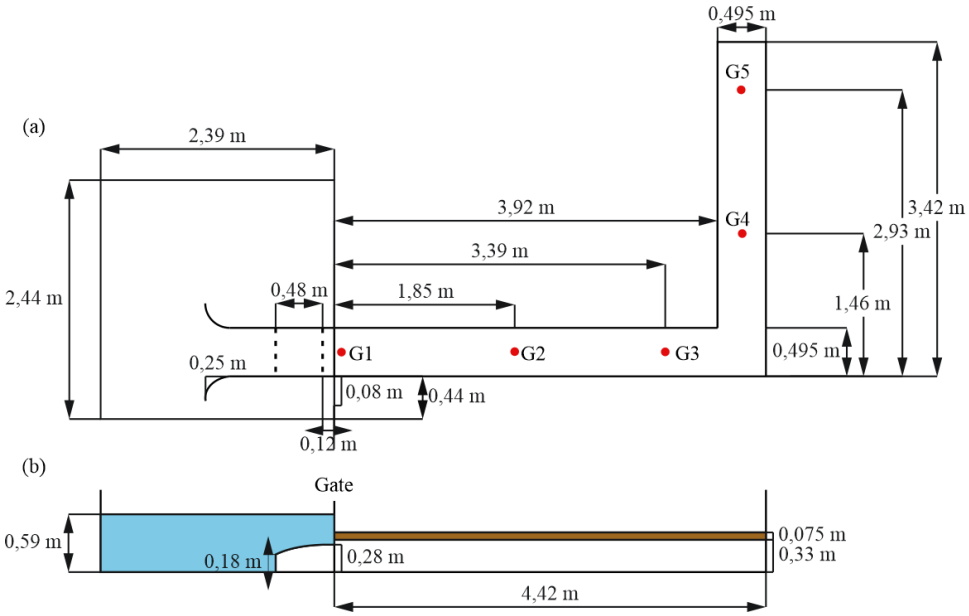

Figure 5.47: Experimental case BL7 – (a) Plane view of the experimental flume and position of the gauges G1 to G5 ; (b) Vertical cut taken along the longitudinal axis of the first part of the flume.

Water levels were recorded continuously at five different points with ultrasonic gauges and no less than thirty-four different runs were made. Hereafter, the numerical results for the water surface elevation will be compared with the aggregated experimental results at each gauge point. Bed levels were recorded with two different techniques. The temporal evolution of the bed level at different cross-sections were recorded using laser

profilometry, while photogrammetry techniques were applied to capture the final topography after drainage of the channel. Hereafter, only the photogrammetric results will be used to compare the experiments with the simulations because of their total spatial coverage of the flume. This last technique was used to reconstruct the topography consecutive to three different experimental runs. The average topography was then calculated and is represented in Figure 5.48. This is the dataset that will be compared with the numerical results as far as the bed level surface is concerned.

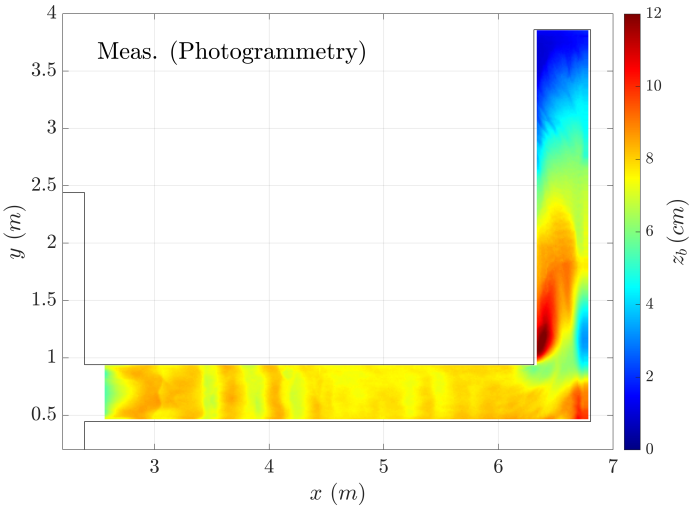

Figure 5.48: Experimental case BL7 – Final topography obtained after the channel drainage using photogrammetry and averaged over the three experimental runs available.

On the one hand, large accumulation regions appeared downstream the inner corner, with a final bed elevation locally larger than $12\,cm$, and at the outer corner stagnation zone. On the other hand, noticeable local erosion was detected downstream the outer corner stagnation zone, as well as at downstream-reach outlet where the rigid floor of the channel was practically reached, if not completely. Furthermore, marked one-directional dunes were found at the beginning of the flume upstream-reach. These bed forms were created during the fist stages of dambreak wave advance and progressively disappeared as they got closer to the corner region. It is worth mentioning that a slightly eroded zone appeared close to the inner corner, with a maximum erosion lower than $2\,cm$ with respect to the original bed level.

Water density ρ_w	$1000\,kg/m^3$
Solid density ρ_s	$2650\,kg/m^3$
Solid particles diameter d_s	$1.7\,mm$
Manning's roughness coeff. n_b	$0.0165\ sm^{-1/3}$
Bed porosity ξ	0.44

Table 5.18: Experimental case BL7 – Setup of the simulations.

Assessment of the capacity model

In order to assess the suitability of the capacity closure formulation for predicting the experimental observations, the simulations were performed using the FCM schmee with capcity formulation for the bedload rate, referred to as R-Cap model from now on. The parameters summarized in Table 5.18 were set in all the simulations. Three diffierent capacity relationships were used: MPM [97], Wu [144] and Smart[132] (see Table 5.2). A triangular unstructured mesh with 36212 cells was used. The resolution varied across the mesh. It was fixed at $50\,cm$ and $5\,cm$ in the reservoir and in the channel respectively, but was increased to $0.5\,cm$ in the corner region in order to capture the local transient structures of the flow. All the simulations lasted $180\,s$, even though the bed evolution occurred mainly during the first $20\,s$ and practically stopped after $120\,s$ from the dam-break initiation. CFL=0.95 is set in all the simulations.

Figure 5.49 shows the temporal evolution of the water surface level (wsl) at the gauge points measured during the experiment. The arrival time of the dambreak wave-front is well predicted by the R-Cap model at the gauge points placed at the upstream-reach of the flume ($G1$, $G2$ and $G3$, located upstream the bend) and the three capacity formulations considered show quite similar water surface evolutions. However, at the gauge points placed downstream the bend ($G4$ and $G5$) the R-Cap model predicts a shorter arrival time of the wave-front than those observed in laboratory. Furthermore, the temporal evolution of the water surface at these downstream-reach gauge points shows differences depending on the capacity bedload rate formulation, specially at the gauge point $G5$. Nevertheless, the transient flow structure is reasonably well predicted by all the numerical models.

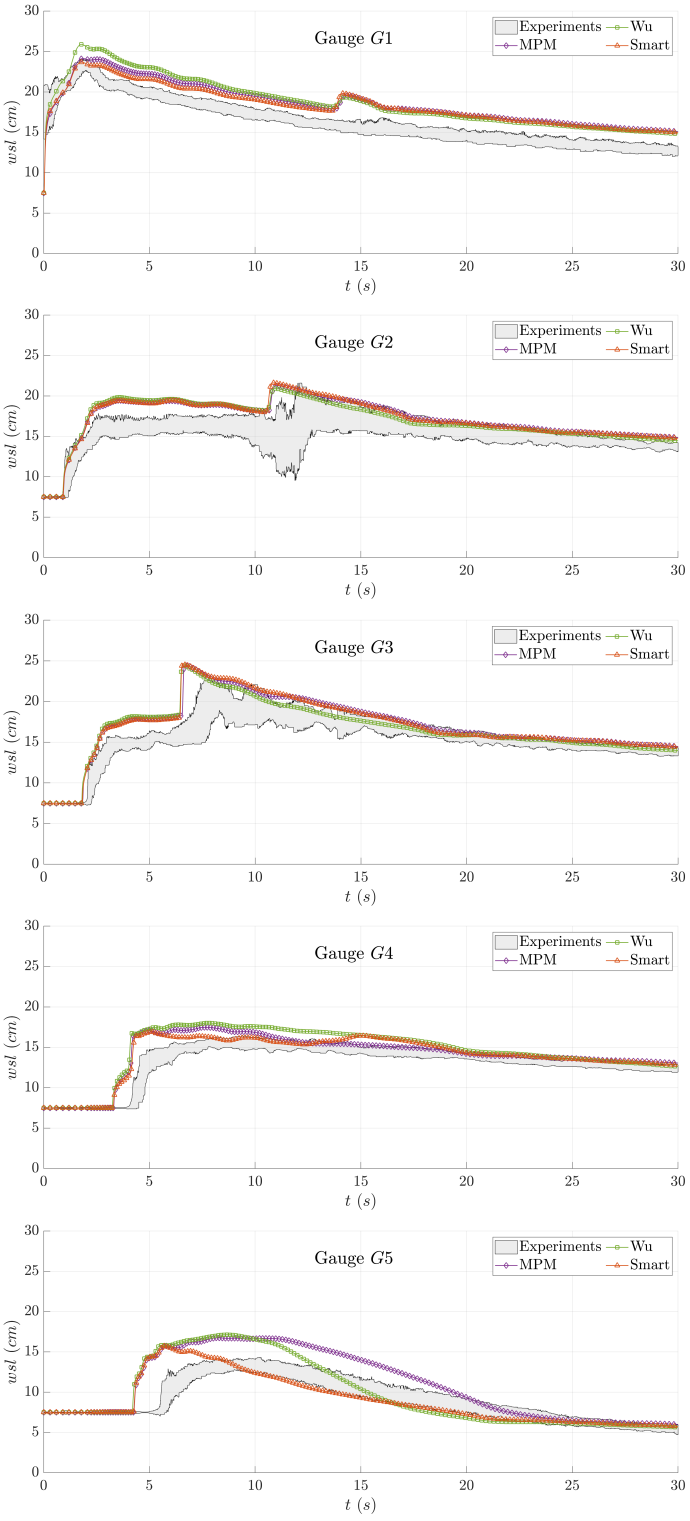

Figure 5.49: Experimental case BL7 – Water surface elevation $wsl\ (cm)$ at the gauge points $G1$, $G2$, $G3$, $G4$ and $G5$.

In order to assess the performance of the different capacity closure relations to predict the bed changes caused by the dambreak wave, the final bed elevation obtained at the time $t = 180\,s$ are compared against the photogrammetry measurements. Figure 5.50 shows 2D-maps of the bed elevation z_b obtained with R-Cap and the different bedload rate closures at the final time $t = 180\,s$. Several common aspects should be pointed out:

- First, the three bedload capacity formulations are able to predict reasonably well the bed degradation close to the outlet boundary. Contrarily, none of them are able to obtain the bed forms observed in the experimental measurements at the upstream-reach of the flume.
- Second, generally, the MPM and the Smart relationships reproduce well the main structures observed in the experiments for the final bed elevation. However, the Wu formula leads to an overestimation of the bedload transport rate and distorts the main features observed in the measured topography (see Figure 5.48). The global RMSE error for the final bd elevation z_b is summarized in Table 5.19.

	MPM	Wu	Smart
z_b RMSE (cm)	1.02	1.46	1.05

Table 5.19: Experimental case BL7 – Global bed level z_b RMSE with R-Cap model and MPM, Wu and Smart formulations.

  However, none of the capacity formulations are able to predict accurately the absolute accumulation of bed material observed in the experiments downstream of the inner corner, nor the depth of the opposite eroded region.

- Third, the three considered capacity formulations show a noticeable eroded zone close to the inner corner. Although slight erosion was observed at the region in the laboratory, all the bedload formulations overestimate the bed degradation in this zone as a consequence of the formation and development of a vortex downstream of the inner corner.

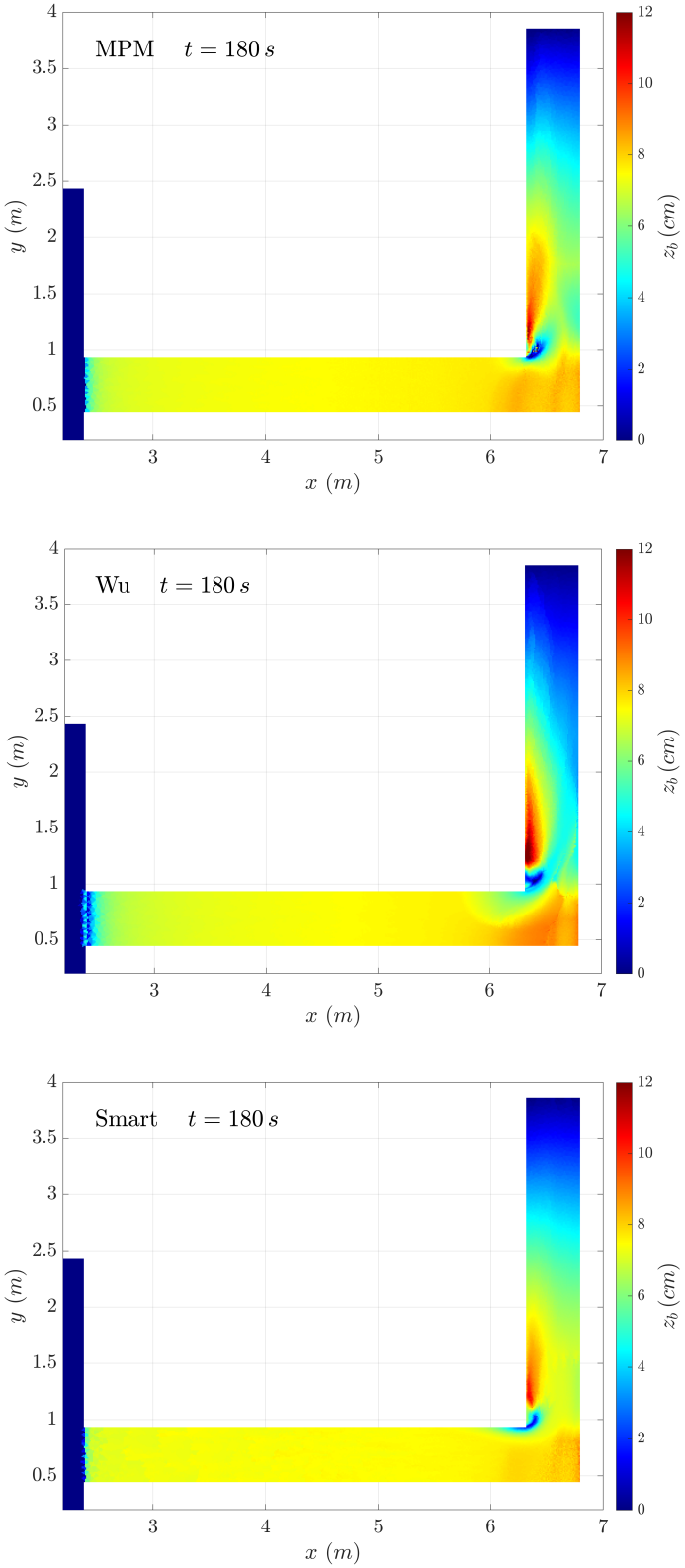

Figure 5.50: Experimental case BL7 – Bed elevation z_b 2D-maps at $t = 180\,s$ obtained with R-Cap model and the MPM, Wu and Smart closures.

In order to identify quantitatively the performance of the capacity closures, numerical bed profiles taken along $x = 6.34\,m$ (A), $x = 6.77\,m$ (B)

and $y = 0.60\,m$ (C) were obtained for $t = 180\,s$ and compared against the photogrammetry data in Figure 5.51.

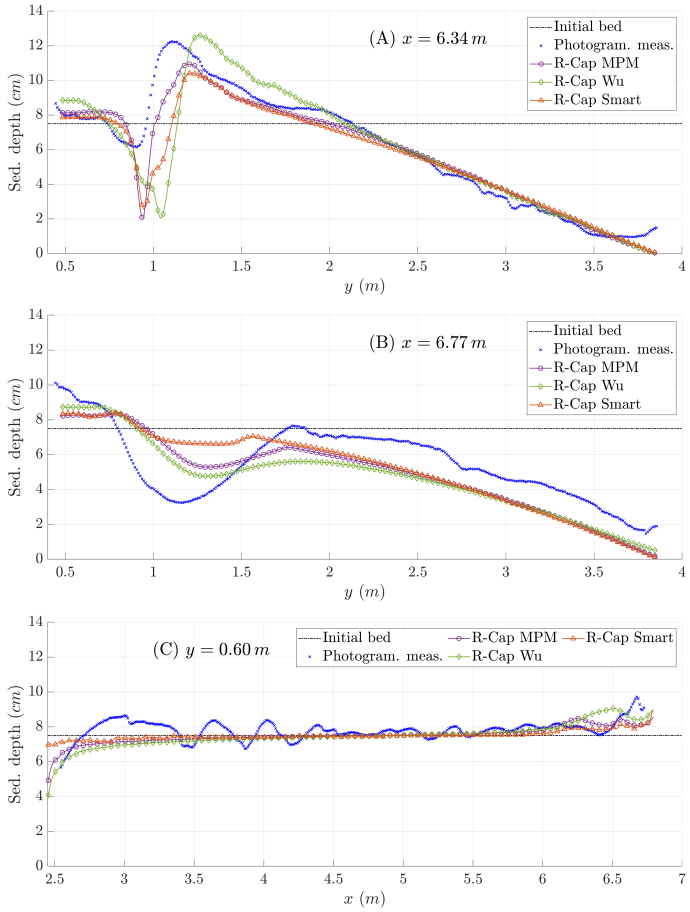

Figure 5.51: Experimental case BL7 – Final bed level profiles along $x = 6.34\,m$, $x = 6.77\,m$ and $y = 0.60\,m$ with R-Cap model and the MPM, Wu and Smart closures.

Regarding the (A) profile, the MPM closure approximates better the accumulation region downstream the inner corner than the Wu and Smart formulations. However, the depth of the over-eroded region at the inner corner is similar for the three relationships. Eventually, the MPM closure shows the lowest RMSE for the bed level z_b along this profile ($RMSE = 0.95\,cm$) whereas the Wu and Smart formulations show higher errors (see Table 5.20).

The Wu closure performs slightly better than the MPM relation along profile (B) (see Figure 5.51), with RMS errors of $1.43\,cm$ and $1.45\,cm$ respectively. However, both formulations under-predicts the eroded depth downstream the outer corner. The Smart relation performs worse than the others (RMSE=$1.60\,cm$), especially at the erosion zone downstream the outer corner.

Finally, the three closures perform quite similarly along profile (C), with an RMSE below $0.55\,cm$, and are able to predict the general trend of the bed change, as it is shown in Figure 5.51. However, none of them are able to approximate the formation of dunes in the inlet reach of the channel. The formation of this kind of bed form is directly related to the vertical structure of the flow near the bed surface [144] and is hence difficult to mimic using depth-averaged bedload transport models.

Profile	z_b RMSE (cm)		
	MPM	Wu	Smart
(A) $x = 6.34\,m$	0.95	1.74	1.34
(B) $x = 6.77\,m$	1.45	1.43	1.60
(C) $y = 0.60\,m$	0.46	0.54	0.44

Table 5.20: Experimental case BL7 – Bed level z_b RMSE for the profiles (A) $x = 6.34\,m$, (B) $x = 6.77\,m$ and (C) $y = 0.60\,m$ with R-Cap model and the MPM, Wu and Smart closures.

Application of the non-capacity model

The main feature of the R-NCap model is the progressive adaptation of the bedload transport rate $\mathbf{q_b}$ to the local flow conditions until the equilibrium transport state is reached, contrarily to the capacity models that assume instantaneous adaptation. The celerity of this adaptation is controlled by the entrainment and detention constants k_E and k_D respectively, but also depends directly on the dimensionless Shields stress excess $\Delta\theta$ at the bed interface [87]. This is one of the main differences between the proposed R-NCap scheme and other non-equilibrium bedload models which assume a constant value for the adaption length L_b [17, 115, 144] and computes the entrainment rate as:

$$\dot{\eta}_E = \frac{|\mathbf{q_b^*}|}{L_b} \tag{5.114}$$

where $|\mathbf{q_b^*}|$ is the modulus of the equilibrium bedload rate (2.144).

Comparing both non-capacity approaches, it can be easily derived that, for the Meyer-Peter & Müller [97] formulation, the equivalent adaptation length applied by the R-NCap models scales with:

$$L_b = \frac{8\,r_s\,d_s}{1-\xi}\frac{\sqrt{\Delta\theta}}{k_E} \tag{5.115}$$

and hence the equivalent adaptation length increases at regions where the boundary Shields stress excess is high. Furthermore, the smaller the entrainment constant k_E, the larger the adaptation length L_b.

This property of the R-NCap model is used to improve the numerical prediction at the inner corner region. One of the main flaws in the numerical results obtained with the capacity R-Cap model is the appearance of a marked over-eroded region near the inner corner. This over-eroded zone was not observed in the experimental measurements. The simulation shows that the marked erosion happens at the first stages of the dam-break progress throughout the corner region, when a vortex was formed downstream of the inner corner. The right panel of Figure 5.52 shows the velocity vectors at the corner region for the R-Cap simulation at $t = 15\,s$. The formation of the vortex is clearly associated to the appearance of the over-eroded zone.

Moreover, the changes on the flow direction at the inner corner region lead to high bed Shields stresses which contribute to increase the erosion within this region. The left panel of Figure 5.52 is a 2D-map of the maximum values of bed Shields stress excess $\Delta\theta$ as computed by the R-Cap model. The maximum $\Delta\theta$ is around 1.0 in most of the channel but increases

at the inner corner region until reaching a maximum value greater than 2.5, leading to a high erosion in this zone.

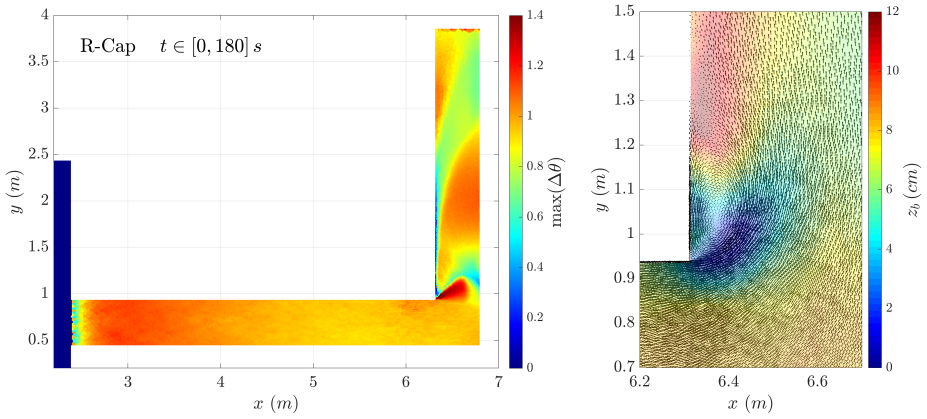

Figure 5.52: Experimental case BL7 – Flow structure with the R-Cap model: (left) 2D map of the maximum $\Delta\theta$; (right) zoom on the inner corner region. The velocity vectors are superimposed with the bed elevation.

Considering the 2D-map of the maximum $\Delta\theta$ recorded for the R-Cap model and the features of the sediment used in this experiment, we analyzed the sensitivity of the R-NCap model by setting the entrainment and detention constants, k_E and k_D respectively, to the values summarized in Table 5.21. Therefore, four simulations using the R-NCap model were carried out, varying entrainment constant from $k_E = 1.60$ to $k_E = 0.05$, but maintaining the k_E/k_D ratio equal to 20. Note that, for all the simulations T0 to T4, the relation between the characteristic thickness of the bedload transport layer under equilibrium conditions and the sediment diameter remains $\eta^*/d_s \approx 9$ since, according to (5.85), it only depends on both the k_E/k_D ratio and the characteristic maximum value of the bed Shields stress excess $\Delta\theta$.

Therefore, as k_E decreases, the characteristic value of the equivalent adaptation length increases from $L_b \approx 5\,cm$ for case T1 to $L_b \approx 150\,cm$ for case T4. The increment on the adaptation length means that the spatial and temporal delay between the actual bedload transport rate and its capacity value becomes larger and hence, the non-equilibrium states are activated. Note that these values for the η^*/d_s ratio and the adaptation length L_b only correspond to the inner corner region, where the bed Shields stress is higher during the first stages of the dambreak wave. At other regions of the channel, the equivalent L_b would be shorter and the η^*/d_s ratio smaller.

Figure 5.53 shows the final topography at time $t = 180\,s$. When R-NCap model is applied, the adaption of the actual bedload solid rate to the flow capacity at the inner corner region becomes non-instantaneous. Hence, the appearance of the over-eroded zone is not only delayed in time but also moves further downstream the inner corner. As k_E decreases, the non-capacity state at that region is enabled, until the formation of the over-eroded zone is avoided. The other main features of the topography observed in the laboratory are maintained, even if alterations in the bed level z_b results also occur at other regions of the channel.

Table 5.22 shows the global RMSE for the numerical topographies computed with the R-NCap model with respect to the photogrammetric data

Test	Model	k_E/K_D (-)	K_E (-)	$\Delta\theta$ (-)	η^*/d_s (5.85) (-)	L_b (5.115) (cm)
T0	R-Cap	20	1.6	1.4	9.4	-
T1	R-NCap	20	1.60	1.4	9.4	4.8
T2	R-NCap	20	0.20	1.4	9.4	38.1
T3	R-NCap	20	0.10	1.4	9.4	76.1
T4	R-NCap	20	0.05	1.4	9.4	152.3

Table 5.21: Experimental case BL7 – Non-capacity setup for the analysis of the R-NCap model behavior.

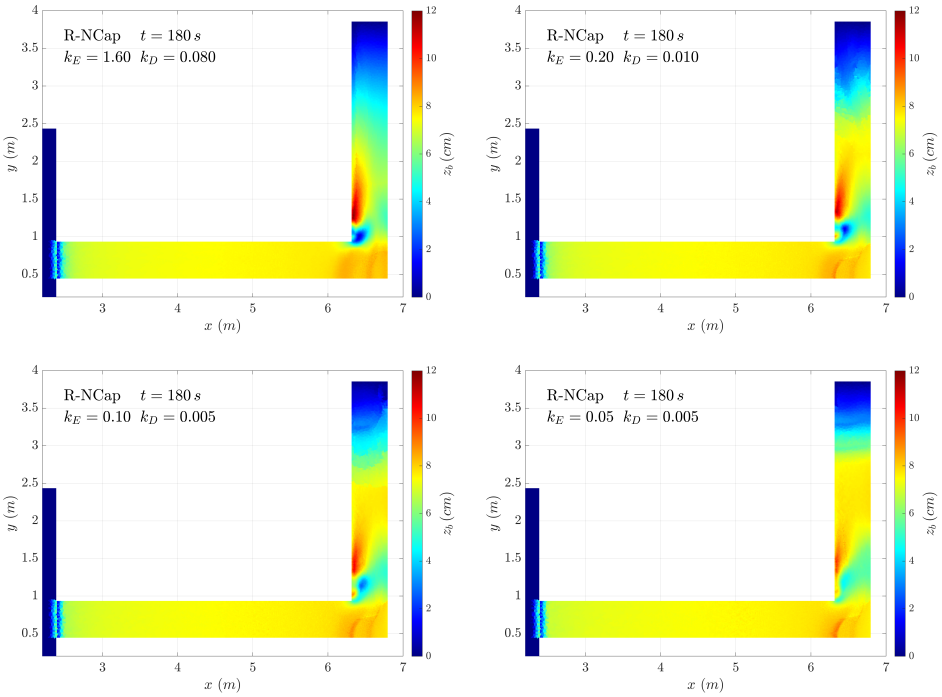

Figure 5.53: Experimental case BL7 – Bed elevation z_b 2D-maps obtained with R-NCap model at $t = 180\,s$.

(Figure 5.48). The improvement of the global performance using the R-NCap model is not marked but an optimal value for the entrainment constant $k_E = 0.20$ can be found, corresponding to test T2. Once again, the difference between the models may look limited regarding this indicator, because of the close results that they show before the bend (Figure 5.51(C)).

Test	Global RMSE for z_b (cm)
T0: R-Cap	1.02
T1: R-NCap $k_E = 1.60$	1.01
T2: R-NCap $k_E = 0.20$	0.98
T3: R-NCap $k_E = 0.10$	1.02
T4: R-NCap $k_E = 0.05$	1.15

Table 5.22: Experimental case BL7 – Global RMSE for the bed level z_b with R-Cap and R-NCap models.

The final bed level z_b computed with the R-NCap model was plotted along profiles (A) and (B) in Figure 5.54. The results from the R-Cap model and the photogrammetric data were also depicted for comparison purposes. For the (A) profile, the activation of the non-equilibrium states led to the avoidance of the over-eroded zone, but a spatial delay of the accumulation zone was also predicted, as well as a reduction of the accumulation height. Furthermore, the prediction of the bed slope at the outlet reach of the channel is increasingly worse as k_E decreases. Despite the gain of accuracy allowed by the non-capacity feature near the inner corner, these worse and worse slope predictions lead to higher RMSE values for the R-NCap model than for the R-Cap one along that profile (see Table 5.23).

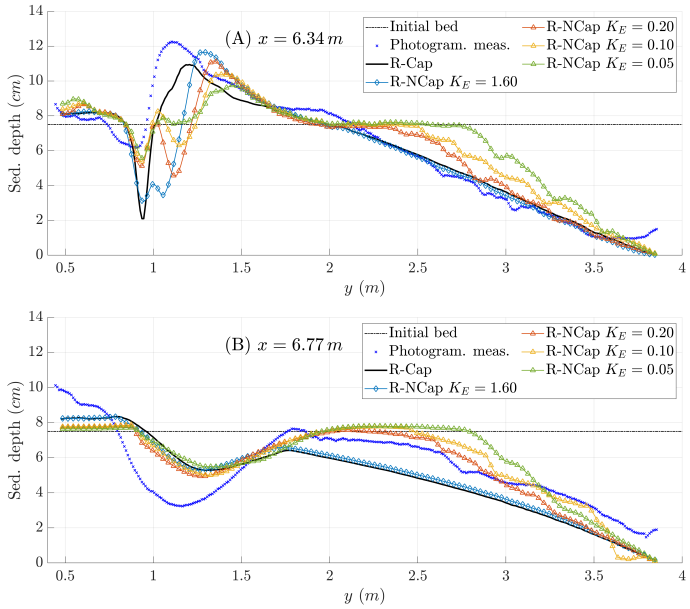

Figure 5.54: Experimental case BL7 – Final bed level profiles along (A) $x = 6.34\,m$ and (B) $x = 6.77\,m$ with R-NCap model. Experimental photogrammetric data and results from the R-Cap model are also plotted.

For the (B) profile, the R-NCap model improves the prediction of the bed slope in the channel outlet reach without affecting significantly other regions (see Figure 5.54). This also improves the RMSE of the bed level z_b with respect to the photogrammetric data along this profile, in comparison with the R-Cap model, as highlighted by Table 5.23. The best agreement is given for $k_E \in [0.10, 0.20]$ with a ratio $k_E/k_D = 20$.

Test	z_b RMS error (cm)	
	(A) $x = 6.34\,m$	(B) $x = 6.77\,m$
T0: R-Cap	0.95	1.45
T1: R-NCap $k_E = 1.60$	1.70	1.32
T2: R-NCap $k_E = 0.20$	1.61	1.05
T3: R-NCap $k_E = 0.10$	1.51	1.13
T4: R-NCap $k_E = 0.05$	1.69	1.34

Table 5.23: Experimental case BL7 – Bed level z_b RMS error for the profiles (A) $x = 6.34\,m$ and (B) $x = 6.77\,m$ with R-Cap and R-NCap models.

5.6 In Closing

The numerical resolution of the bedload sediment transport system in non-uniform beds, composed by the two-dimensional shallow water equations and the mass conservation for the bed layer, have been implemented using two different coupling strategies between the hydrodynamical and morphodynamical components of the system. Both strategies for transient simulations are based on the Finite Volume Method (FVM) using the Roe's approach for the computation of the numerical fluxes between neighbouring cells. Both resolution strategies have been implemented into the same CPU-based computational kernel and hence a realistic comparison of the range of applicability and efficiency of both method can be performed without the influence of external factors.

The main novelties in this chapter are summarized as:

1. The first strategy, called FCM, is based on the full coupling of the 2D shallow water and bedload transport equations, leading to a new formulation for the intercell numerical fluxes which includes the bed elevation z_b into the resolution of the approximated local Riemann problem (RP) at the edges. New explicit expressions have been provided for the wave and source strengths. The stability region of this method is controlled by the eigenvalues of the approximate Jacobian matrix at each intercell edge.

2. An alternative approximate-coupled strategy, called ACM, is proposed based on solving independently the shallow water and the bed transport equations at each time step but controlling the maximum time step allowed by means of an approximation of the bounds of the coupled Jacobian matrix eigenvalues. This method allows simpler expressions for the numerical fluxes at the edges than those of the FCM and the approximate-coupled time step limitation improves the stability of the scheme.

3. Furthermore, the non-equilibrium bedload transport concepts developed in Section 2.3 Chapter 2 have been used to propose a new 2D numerical model able to deal with highly unsteady flows and partially non-erodible bed layers. Based on a generalized non-capacity bedload transport model, the proposed transport rate formulation allows to limit the physical solid flux at cells in regions where the total sediment thickness ϵ_b hinders the development of equilibrium tates in the solid transport.

The capability of both FCM and ACM schemes to deal with structured and unstructured meshes, regardless of the number of edges of the cells, has been demonstrated using a idealized and experimental benchmark tests. Both schemes were able to predict with an acceptable accuracy the bed changes and the flow structures. Both model have shown a almost similar performance in terms of efficiency, robustness and accuracy. It is worthy to state that decoupled or weakly-coupled strategies (such as ACM scheme) for the bedload transport system of equations, which are widespread because of their simple implementation, can only guarantee non-oscillatory results when the bed-flow interaction is very small. Otherwise, the ACM

scheme loses its accuracy and robustness. Furthermore, for highly erosive flows the FCM scheme demonstrated to be more efficient in terms of computational effort than the approximate-couple strategy, one of the key points for realistic bedload transport application.

Finally, when non-capacity model is applied, the adaptation of the actual bedload solid rate to the flow carrying capacity becomes non-instantaneous and the appearance of bed changes is delayed in time and space. As the equivalent adaptation length is increased, the non-capacity states are promoted. In general, better predictions can be obtained with moderate values of the non-equilibrium parameters. Even though the non-capacity approach can improve the model performance in regions with complex transient processes, it requires a careful calibration of the non-equilibrium parameters.

Chapter 6

Conclusions and relevant contributions

In this thesis, the numerical modeling of geophysical surface flows involving sediment transport is addressed using a comprehensive strategy: beginning with the derivation of proper shallow-type mathematical models, following by the development of robust and accurate numerical schemes within the Finite Volume (FV) framework and ending with the implementation of efficient HPC algorithms. This integrated approach is required to the development of Efficient Simulation Tools (EST) for environmental processes involving sediment transport with realistic temporal and spatial scales.

Concerning the mathematical modelling, the generalized 2D system of depth-averaged conservation laws for environmental surface flows of water-sediment mixtures over movable bed conditions have been derived, starting from the general 3D Navier-Stokes equations. This is a fundamental step to understand the physical consequences of the mathematical shallow-type simplification. From the mathematical modelling approach, the fluidized material in motion is contained in a flow layer consisting of a mixture of water and multiple solid phases. This flow layer usually moves rapidly downstream steep channels and involves complex topography. The liquid-solid material can be exchanged throughout the bottom interface with the underlying static bed layer, hence involving also a transient bottom boundary for the flow layer. These features lead to an increasing complexity for the mathematical simplification of sediment transport surface flows, which can not be entirely understood without a careful treatment. Furthermore, this derivation stage allows to obtain essential relationships for the closure of the shallow-type system, as the depth-averaged non-Newtonian basal resistance (see Section 2.1.3).

All these processes involve multiple relations between the variables but, probably, the most challenging and unknown is the development of pore-fluid pressure. When the solid particles are transported throughout the entire flow column, the liquid and solid phases in the flow column might have different velocities and hence might lead to the solid phase segregation and the development of non-hydrostatic pressures in the pore-fluid. For the first time, a closure relation for the shear-induced pore-fluid pressure distribution during the movement of dense-packed solid-liquid mixtures has been obtained and analyzed in Section 2.2.2. This pore pressure affects the effective normal stress along the flow column, leading to a modification of the frictional shear stress between solid particles respect to the hydrostatic

condition and changing the basal resistance, hence affecting the flow mobility. Moreover, using this new pore pressure distribution, the effects of the sediment particles dilation have been included into the depth-averaged solid transport equation, leading to a novel formulation for the advective solid fluxes which accounts for the shear-induced separation of the solid a liquid phases (Section 2.2.3).

When the solid particles are transported only in a thin layer near the bed interface, the bedload transport is the dominant process. The mathematical model for the bedload transport has been reformulated. A new closure relation for the mass exchange between the flow and the underlying static stratum has been proposed from a grain-scale inertial analysis (Section 2.3.2). Additionally, a novel generalized non-capacity model for the bedload transport rate has been proposed and compared with the classical capacity/equilibrium assumption (Section 2.3.3). This new generalized model for the non-capacity bedload transport requires to compute the bedload transport thickness, but it is able to account for the temporal and spatial delay of the actual sediment transport rate with respect to its potential capacity in highly unsteady flows.

The 2D shallow-type system of equations for variable-density multigrain water-sediment flows have been solved using a Finite Volume (FV) method supplemented with an upwind resolution of the intercell numerical fluxes based on the augmented Roe's approach (see Section 3.2.2). This approach maintains coupled the flow depth and density in the conservative variables and fluxes, allowing the bulk sediment concentration to participate in the eigenstructure of the local Riemann problem at the cell edges. Also, the bed-pressure momentum source term has been included into the numerical fluxes at the cell edges by their projections into the RP eigenstructure. The main consequence is a robust and accurate computation of the intercell fluxes even involving highly transient density interfaces, as well as the well-balanced character of the solution is ensured in quiescent and steady states. Moreover, an adaptive numerical fix for the correct treatment of the wet-dry front has been reported in Section 3.3.1. This model for variable-density mud/debris flows over non-uniform erodible bed has been referred to as vdMD model.

Two new strategies for the discretization of the 2D basal resistance force into local plane Riemann problem at the intercell edges have been derived in Section 3.2.1. These new methods, called respectively integral and differential approaches, allow to separate the cell-centered non-Newtonian shear stress force into edge-contributions to the local numerical fluxes at the cell edges ensuring the rotation invariant property of the integrated basal resistance term. Based on the previous results, the non-Newtonian basal resistance momentum source term has been also projected into the RP eigenstructure at the cell edges. Corresponding explicit integration procedures for the upwind basal resistance contribution at the cell edges have been derived in Section 3.3.3). These procedures allow not only to compute the explicit edge-value of the shear resistance contribution but also to limit its value in order to avoid numerical oscillations and ensuring the non-dependence of the solution on the mesh topology.

The effects of the shear-induced solid phase dilation on the pore-fluid pressure have been also included into the EST for variable-density mud/debris flows. Two important differences arise here in comparison

with previous models available in literature: first, the shear-induced segregation of the solid material within the flow is caused by a deviatoric contribution to the solid flux at the edges which ensures the continuity equations of the system maintain their conservative character; second, it is possible to estimate a local value for the basal pore-pressure excess depending on the mixture packed state. Therefore, under the same flow conditions, dense packed mixtures are associated to a lower flow mobility whereas liquefied slurries are related to larger runout distances (see Section 3.4).

Finite Volume (FV) models have also been developed for the resolution of passive suspended transport of multiple sediment classes. Two different robust and efficient numerical models have been proposed for the resolution of the suspended sediment transport system. Both of them are based on the artificial decoupling of the flow depth and density in order to allows the use of widespread solvers designed for shallow clear-water problems. The first one, referred to as udPST model, accounts for the mass and momentum exchange between the bed layer and the flow, but does not include the effects of the sediment concentration in the flow dynamics. The the second one, referred to as vdPST model, also includes the contribution of the flow density gradients to the momentum equations as a new source term which is upwind discretized. The intercell fluxes for the hydrodynamical component of the system have been built using the augmented Roe's approach, whereas the passive transport of the different suspended sediment classes is computed using a reduced formulation in both models. Important differences have been found between the results provided by udPST and the vdPST models in different idealized benchmark tests. These results indicate that, when high solid concentrations are expected in the flow, it is required to include the density-gradients momentum contribution in order to obtain reliable results. Often, the vdPST formulation is used for the simulation of variable-density mud/debris flows. However, for transient problems with noticeable density gradients, the results obtained with vdPST model show differences respect to those obtained with the variable-density vdMD model described in the Chapter 3.

The numerical resolution of the bedload sediment transport system in non-uniform beds has been implemented using two different coupling strategies between the hydrodynamical and morphodynamical components of the system. Both strategies for transient simulations are based on the FV framework and use the Roe's approach for the computation of the numerical fluxes between neighbouring cells (see Section 5.2). The first strategy, called FCM, is based on the full coupling of the 2D shallow water and bedload transport equations, leading to a new formulation for the numerical fluxes which includes the bed elevation into the resolution of the local RP at the edges. An alternative approximate-coupled strategy, called ACM, is proposed based on solving independently the shallow water and the bed transport equations at each time step but controlling the maximum time step allowed by means of the coupled Jacobian eigenvalues. This method allows simpler expressions for the numerical fluxes at the edges than those of the FCM and the approximate-coupled time step limitation improves the stability of the scheme. The capability of both FCM and ACM schemes to deal with structured and unstructured meshes has been demonstrated, predicting with an acceptable accuracy bed changes and flow structures in benchmark tests. It is worth to state that decoupled

or weakly-coupled strategies (such as ACM scheme) for the bedload transport system, which are widespread because of their simple implementation, can only guarantee non-oscillatory results when the bed-flow interaction is very small. Otherwise, the ACM scheme loses its accuracy and robustness. Furthermore, for highly erosive flows the FCM scheme demonstrated to be more efficient in terms of computational effort than the approximate-couple strategy, one of the key points for realistic bedload transport application.

Finally, the non-equilibrium bedload transport concepts have been used to propose a new 2D numerical model able to deal with highly unsteady flows and partially non-erodible bed layers. Based on a generalized non-capacity bedload transport model, the proposed transport rate formulation allows to limit the physical solid flux at cells in regions where the total sediment thickness hinders the development of equilibrium states in the solid transport. When non-capacity model is applied, the adaptation of the actual bedload solid rate to the flow carrying capacity becomes non-instantaneous and the appearance of bed changes is delayed in time and space. As the equivalent adaptation length is increased, the non-capacity states are promoted. In general, better predictions can be obtained with moderate values of the non-equilibrium parameters. Even though the non-capacity approach can improve the model performance in regions with complex transient processes, it requires a careful calibration of the non-equilibrium parameters.

Capítulo 6

Conclusiones y contribuciones destacadas

En esta tesis, el modelado numérico de los flujos superficiales geofísicos que involucran transporte de sedimentos se aborda utilizando una estrategia integral: comenzando con la derivación de modelos matemáticos de tipo superficial adecuados, seguido por el desarrollo de esquemas numéricos robustos y precisos dentro del marco de los métodos de Volúmenes Finitos (FV) y terminando con la implementación de algoritmos de computación de alto rendimiento (HPC) eficientes. Este enfoque integrado es necesario para el desarrollo de Herramientas Eficientes de Simulación (HES) para procesos ambientales que involucran transporte de sedimentos con escalas temporales y espaciales realistas.

En cuanto a la modelización matemática, se ha derivado el sistema bidimensional generalizado de leyes de conservación promediadas en profundidad para los flujos superficiales ambientales de mezclas de agua y sedimentos en condiciones de lecho móvil, a partir de las ecuaciones generales 3D de Navier-Stokes. Este es un paso fundamental para comprender las consecuencias físicas de la simplificación matemática de tipo superficial ('shallow-type'). Desde el enfoque de modelado matemático, el material fluidificado en movimiento está contenido en una capa de flujo que consiste en una mezcla de agua y múltiples fases sólidas. Esta capa de flujo generalmente se mueve rápidamente aguas-abajo a lo largo de canales empinados e involucra una topografía compleja. El material líquido-sólido se puede intercambiar a través de la interfaz inferior con la capa del lecho estático subyacente, lo que implica también un frontera inferior transitoria para la capa de flujo. Estas características conducen a una complejidad creciente para la simplificación matemática de los flujos superficiales con transporte de sedimentos, que no pueden entenderse por completo sin un tratamiento cuidadoso. Además, esta etapa de derivación permite obtener relaciones esenciales para el cierre del sistema de ecuaciones, como la resistencia basal no-Newtoniana promediada en profundidad (ver Sección 2.1.3).

Todos estos procesos involucran múltiples relaciones entre las variables pero, probablemente, el más desafiante y desconocido es el desarrollo de la presión del fluido intersticial. Cuando las partículas sólidas se transportan a través de toda la columna de flujo, las fases líquida y sólida en la columna de flujo pueden tener diferentes velocidades y, por lo tanto, pueden conducir a la segregación de la fase sólida y al desarrollo de presiones no hidrostáticas en el fluido poroso. Por primera vez, una relación de cierre para la distribución de presión de fluido intersticial inducida por cizallamiento durante el movimiento de mezclas sólido-líquidas densamente

empaquetadas ha sido obtenida y analizada en la Sección 2.2.2. Esta presión de poro afecta la tensión normal efectiva a lo largo de la columna de flujo, lo que lleva a una modificación del esfuerzo cortante por fricción entre las partículas sólidas con respecto a la condición hidrostática y cambia la resistencia basal, afectando así la movilidad del flujo. Además, utilizando esta nueva distribución de presión de poro, los efectos de la dilatación de las partículas de sedimento se han incluido en la ecuación de transporte de sólidos promediados en profundidad, lo que lleva a una formulación novedosa para los flujos sólidos advectivos que explica la segregación de la fase sólida inducida por cizallamiento (Sección 2.2.3).

Cuando las partículas sólidas se transportan solo en una capa delgada cerca de la interfaz del lecho, el transporte de carga de fondo es el proceso dominante. Se ha reformulado el modelo matemático para el transporte de carga de fondo. Se ha propuesto una nueva relación de cierre para el intercambio de masa entre el flujo y el estrato estático subyacente a partir de un análisis inercial a escala de grano (Sección 2.3.2). Además, se ha propuesto un nuevo modelo generalizado para la tasa de transporte de fondo en condiciones de no-capacidad y se ha comparado con el supuesto clásico de capacidad/equilibrio (Sección 2.3.3). Este nuevo modelo generalizado para el transporte de carga de fondo en condiciones de no-capacidad requiere calcular el espesor de la capa de carga de fondo, pero es capaz de tener en cuenta el retraso temporal y espacial de la tasa de transporte de sedimentos real con respecto a la capacidad potencial en flujos muy transitorios.

El sistema de ecuaciones 2D de tipo superficial para flujos de densidad variable con múltiples clases de sedimentos se ha resuelto utilizando un método de Volúmenes Finitos (VF) complementado con una resolución 'upwind' de los flujos numéricos entre celdas basado en el enfoque aumentado de Roe (ver Sección 3.2.2). Este enfoque mantiene acoplada la profundidad y la densidad del flujo en las variables y flujos conservativos, lo que permite que la concentración de sedimentos participe en la estructura de valores/vectores propios del problema de Riemann (PR) local en los bordes de la celda. Además, el término fuente de presión de lecho se ha incluido en los flujos numéricos en los bordes de la celda mediante su proyección en la base de vectores propios del PR. La consecuencia principal es un cálculo robusto y preciso de los flujos entre celdas, incluso cuando interfaces de densidad altamente transitorias están involucradas, así como asegurar el carácter bien-equilibrado de la solución en estados de reposo y estacionarios. Además, en la Sección 3.3.1 se presenta de una corrección numérica adaptativa para el correcto tratamiento de frentes seco-mojado. Este modelo para flujos de lodo/detritos de densidad variable sobre lecho erosionable no-uniforme se ha denominado modelo vdMD.

En la Sección 3.2.1 se han derivado dos nuevas estrategias para la discretización de la fuerza de resistencia basal 2D en el problema de Riemann (PR) local en los bordes entre celdas. Estos nuevos métodos, denominados enfoques integrales y diferenciales respectivamente, permiten separar la fuerza de esfuerzo cortante no-Newtoniano centrada en la celda en contribuciones de borde que se añaden a los flujos numéricos locales en los bordes de la celda, lo que garantiza la propiedad de invarianza ante rotación del término de resistencia basal integrado. Con base en los resultados anteriores, el término de fuente de resistencia basal no-Newtoniana también se ha proyectado en la estructura de vectores propios del PR en los bordes

de la celda. Los correspondientes procedimientos de integración explícitos para la contribución de la resistencia basal 'upwind' en los bordes de la celda se han derivado en la Sección 3.3.3). Estos procedimientos permiten no solo calcular el valor de la resistencia en los bordes de las celdas de forma explícita, sino también limitar su valor para evitar oscilaciones numéricas y garantizar la no dependencia de la solución con la topología de la malla computacional.

Los efectos de la dilatación de la fase sólida inducida por el cizallamiento sobre la presión del fluido intersticial también se han incluido en la HES para flujos de lodo/detritos de densidad variable. Aquí surgen dos diferencias importantes en comparación con los modelos anteriores disponibles en la literatura: primero, la segregación inducida por cizallamiento del material sólido dentro del flujo es causada por una contribución desviadora al flujo sólido en los bordes que asegura que las ecuaciones de continuidad del sistema mantienen su carácter conservativo; en segundo lugar, es posible estimar un valor local para el exceso de presión de poro basal dependiendo del estado de empaquetamiento de la mezcla. Por lo tanto, bajo las mismas condiciones de flujo, las mezclas densamente empaquetadas se asocian a una menor movilidad de flujo mientras que las lechadas licuadas se relacionan con mayores distancias recorridas (ver Sección 3.4).

Se han desarrollado también modelos de Volúmenes Finitos (VF) para la resolución del transporte pasivo en suspensión de múltiples clases de sedimentos. Se han propuesto dos modelos numéricos diferentes, robustos y eficientes para la resolución del sistema de transporte de sedimentos en suspensión. Ambos se basan en el desacoplamiento artificial de la profundidad y densidad del flujo para permitir el uso de esquemas numéricos generalistas diseñados para problemas de aguas claras poco profundas. El primero, denominado modelo udPST, tiene en cuenta el intercambio de masa y momento entre la capa del lecho y el flujo pero no incluye los efectos de la concentración de sedimentos en la dinámica del flujo. El segundo, denominado modelo vdPST, también incluye la contribución de los gradientes de densidad de flujo a las ecuaciones de cantidad de movimiento como un nuevo término fuente discretizado 'upwind'. Los flujos en el borde las celdas para las componentes hidrodinámicas del sistema se han construido utilizando el método de Roe aumentado (ARoe), mientras que el transporte pasivo de las diferentes clases de sedimentos en suspensión se calcula utilizando una formulación reducida en ambos modelos. Se han encontrado diferencias importantes entre los resultados proporcionados por los modelos udPST y vdPST en diferentes tests de referencia. Estos resultados indican que, cuando se esperan altas concentraciones de sólidos en el flujo, se requiere incluir la contribución de los gradientes de densidad en las ecuaciones de cantidad de movimiento para obtener resultados confiables. A menudo, la formulación vdPST se usa para la simulación de flujos de lodo/detritos de densidad variable. Sin embargo, para problemas transitorios con gradientes de densidad importantes, los resultados obtenidos con el modelo vdPST muestran diferencias con respecto a los obtenidos con el modelo vdMD de densidad variable descrito en el Capítulo 3.

La resolución numérica del sistema de transporte de sedimentos por carga de fondo en lechos no-uniformes se ha implementado utilizando dos

estrategias de acoplamiento diferentes entre las componentes hidrodinámicas y morfodinámicas del sistema. Ambas estrategias para simulaciones transitorias se basan en el marco FV y utilizan el enfoque de Roe para el cálculo de los flujos numéricos entre celdas vecinas (consulte la Sección 5.2). La primera estrategia, denominada FCM, se basa en el acoplamiento completo de las ecuaciones 2D de transporte de carga de lecho y aguas poco profundas, lo que lleva a una nueva formulación para los flujos numéricos que incluye la elevación del lecho en la resolución del RP local en los bordes. Se propone una estrategia alternativa de acoplamiento aproximado, denominada ACM, basada en resolver de forma independiente las ecuaciones de aguas someras y transporte de lecho en cada paso de tiempo, pero controlando el paso de tiempo máximo permitido mediante los valores propios propios del Jacobiano acoplado. Este método permite expresiones más simples para los flujos numéricos en los bordes que los del FCM y la limitación del paso de tiempo acoplado aproximado mejora la estabilidad del esquema. Se ha demostrado la capacidad de los esquemas FCM y ACM para lidiar con mallas estructuradas y no estructuradas, prediciendo con una precisión aceptable cambios de lecho y estructuras de flujo en pruebas de referencia. Cabe señalar que las estrategias desacopladas o débilmente acopladas (como el esquema ACM) para el sistema de transporte de carga de lecho, que están muy extendidas por su simple implementación, solo pueden garantizar resultados no oscilatorios cuando la interacción lecho-flujo es muy pequeña. De lo contrario, el esquema ACM pierde su precisión y solidez. Además, para flujos altamente erosivos, el esquema FCM demostró ser más eficiente en términos de esfuerzo computacional que la estrategia de par aproximado, uno de los puntos clave para una aplicación realista de transporte de carga de fondo.

Finalmente, los conceptos de tasa de transporte de fondo en condiciones de no-equilibrio se han utilizado para proponer un nuevo modelo numérico 2D capaz de lidiar con flujos altamente transitorios y capas de lecho parcialmente no erosionables. Basado en el generalizado modelo de transporte de carga de fondo en no-capacidad, la formulación de la tasa de transporte propuesta permite limitar el flujo de sólidos físicos en las celdas en regiones donde el espesor total del sedimento dificulta el desarrollo de estados de equilibrio en el transporte de sólidos. Cuando se aplica el modelo de no-capacidad, la adaptación de la tasa de sólidos de carga de lecho real a la capacidad de transporte de flujo se vuelve no instantánea y la aparición de cambios de lecho se retrasa en el tiempo y el espacio. A medida que aumenta la longitud de adaptación equivalente, se promueve la aparición los estados de no-capacidad. En general, se pueden obtener mejores predicciones con valores moderados de los parámetros de no-equilibrio. Aunque el enfoque de no-capacidad puede mejorar el rendimiento del modelo en regiones con procesos transitorios complejos, requiere una calibración cuidadosa de los parámetros de desequilibrio.

Bibliography

1. Armanini, A. & Di Silvio, G. A one-dimensional model for the transport of a sediment mixture in non-equilibrium conditions. *Journal of Hydraulic Research* **26,** 275–292 (1988).
2. Armanini, A., Fraccarollo, L. & Rosatti, G. Two-dimensional simulation of debris flows in erodible channels. *Computers & Geosciences* **35,** 993 –1006 (2009).
3. Bagnold, R. The nature of saltation and of bed-load transport in water. *Proceedings of the Royal Society of London. A. Mathematical and Physical Sciences* **332,** 473–504 (1973).
4. Benkhaldoun, F., Sari, S. & Seaid, M. A flux-limiter method for dambreak flows over erodible sediment beds. *Applied Mathematical Modelling* **36,** 4847 –4861 (2012).
5. Berger, C., McArdell, B. W. & Schlunegger, F. Direct measurement of channel erosion by debris flows, Illgraben, Switzerland. *Journal of Geophysical Research: Earth Surface* **116,** 93 –104 (2011).
6. Berthon, C., Cordier, S., Le, M. & Delestre, O. An analytical solution of Shallow Water system coupled to Exner equation. *Comptes Rendus Mathematique, Elsevier Masson* **350,** 183–186 (2012).
7. Berti, M. & Simoni, A. Experimental evidences and numerical modeling of debris flow initiated by channel runoff. *Landslides* (2005).
8. Berti, M., Genevois, R., Simoni, A. & Tecca, P. R. Field observations of a debris flow event in the Dolomites. *Geomorphology* **29,** 265–274 (1999).
9. Board, O. A. R. *OpenMP Application Programming Interface* (High-Performance Computing Center Stuttgart, 2015).
10. Bohorquez, P. & Ancey, C. Particle diffusion in non-equilibrium bedload transport simulations. *Applied Mathematical Modelling* **40,** 7474 – 7492 (2016).
11. Brooks, G. & Lawrence, D. The drainage of the Lake Ha!Ha! reservoir and downstream geomorphic impacts along Ha!Ha! River, Saguenay area, Quebec, Canada. *Geomorphology* **28,** 141 –167 (1999).
12. Brufau, P., Garcia-Navarro, P., Ghilardi, P., Natale, L. & Savi, F. 1D Mathematical modelling of debris flow. *Journal of Hydraulic Research* **38,** 435–446 (2000).
13. Burguete, J., García-Navarro, P. & Murillo, J. Friction term discretization and limitation to preserve stability and conservation in the 1D shallow-water model: Application to unsteady irrigation and river flow. *Int. J. Numer. Meth. Fluids* **54,** 403–425 (2008).

14. Calhoun, N. C. & Clague, J. J. Distinguishing between debris flows and hyperconcentrated flows: an example from the eastern Swiss Alps. *Earth Surface Processes and Landforms* **43,** 1280–1294 (2018).

15. Cao, Z., Day, R. & Egashira, S. Coupled and Decoupled Numerical Modeling of Flow and Morphological Evolution in Alluvial Rivers. *Journal of Hydraulic Engineering* **128,** 306–321 (2002).

16. Cao, Z., Li, Z., Pender, G. & Hu, P. Non-capacity or capacity model for fluvial sediment transport. *Proceedings of the Institution of Civil Engineers - Water Management* **165,** 193–211 (2012).

17. Cao, Z., Hu, P. & Pender G. Liu, H.-H. Non-capacity transport of non-uniform bed load sediment in alluvial rivers. *Journal of Mountain Science* **13,** 377–396 (2016).

18. Cao, Z., Pender, G., Wallis, S. & Carling, P. Computational Dam-Break Hydraulics over Erodible Sediment Bed. *Journal of Hydraulic Engineering* **130,** 689–703 (2004).

19. Cao, Z., Hu, P. & Pender, G. Multiple Time Scales of Fluvial Processes with Bed Load Sediment and Implications for Mathematical Modeling. *Journal of Hydraulic Engineering* **137,** 267–276 (2011).

20. Cao, Z., Xia, C., Pender, G. & Liu, Q. Shallow Water Hydrosediment-Morphodynamic Equations for Fluvial Processes. *Journal of Hydraulic Engineering* **143,** 02517001 (2017).

21. Castro, M., Fernández-Nieto, E., Ferreiro, A., García-Rodríguez, J. & Parés, C. High Order Extensions of Roe Schemes for Two-Dimensional Nonconservative Hyperbolic Systems. *Journal of Scientific Computing* **39,** 67–114 (2009).

22. Castro-Díaz, M., Fernández-Nieto, E. & Ferreiro, A. Sediment transport models in Shallow Water equations and numerical approach by high order finite volume methods. *Computers & Fluids* **37,** 299 –316 (2008).

23. Castro-Díaz, M., Fernández-Nieto, E. & Ferreiro, A. Sediment transport models in Shallow Water equations and numerical approach by high order finite volume methods. *Computers & Fluids* **37,** 299 –316 (2008).

24. Caviedes-Voullième, D., Morales-Hernández, M., Juez, C., Lacasta, A. & García-Navarro, P. Two-Dimensional Numerical Simulation of Bed-Load Transport of a Finite-Depth Sediment Layer: Applications to Channel Flushing. *Journal of Hydraulic Engineering* **143,** 04017034 (2017).

25. Charru, F. Selection of the ripple length on a granular bed sheared by a liquid flow. *Physics of Fluids* **18,** 121508 (2006).

26. Cordier, S., Le, M. & Morales de Luna, T. Bedload transport in shallow water models: Why splitting (may) fail, how hyperbolicity (can) help. *Advances in Water Resources* **34,** 980 –989 (2011).

27. Cunge, J., Holly, F. & Verwey, A. *Practical aspects of computational river hydraulics* (Pitman Advanced Publishing Program, 1980).

28. [de la Asunción], M. & Castro, M. Simulation of tsunamis generated by landslides using adaptive mesh refinement on GPU. *Journal of Computational Physics* **345,** 91 –110 (2017).

29. Denlinger, R. P. & Iverson, R. M. Flow of variably fluidized granular masses across three-dimensional terrain: 2. Numerical predictions and experimental tests. *Journal of Geophysical Research: Solid Earth* **106,** 553–566 (2001).

30. Dewals, B., Rulot, F., Erpicum, S., Archambeau, P. & Pirotton, M. in *Sediment Transport* (ed Ginsberg, S. S.) chap. 1 (IntechOpen, Rijeka, Croatia, 2011).

31. Egashira, S., Honda, N. & Itoh, T. Experimental study on the entrainment of bed material into debris flow. *Physics and Chemistry of the Earth, Part C: Solar, Terrestrial & Planetary Science* **26,** 645 –650 (2001).

32. Egiazaroff, I. Calculation of nonuniform sediment concentrations. *Proc. ASCE* **91,** 225–247 (1965).

33. El Kadi Abderrezzak, K. & Paquier, A. One-dimensional numerical modeling of sediment transport and bed deformation in open channels. *Water Resources Research* **45** (2009).

34. El Kadi Abderrezzak, K., Paquier, A. & Gay, B. One-dimensional numerical modelling of dam-break waves over movable beds: application to experimental and field cases. *Environmental Fluid Mechanics* **8,** 169–198 (2008).

35. Exner, F. *Über die Wechselwirkung zwischen Wasser und Geschiebe in Flüssen: Gedr. mit Unterstütz g aus d. Jerome u. Margaret Stonborough-Fonds* (Akademie der Wissenschaften, Wien, 1925).

36. Fent, I., Zech, Y. & Soares-Frazão, S. Dam-break flow experiments over mobile bed: velocity profile. *Journal of Hydraulic Research* **57,** 131–138 (2019).

37. Fernández-Nieto, E., Lucas, C., Morales-de Luna, T. & Cordier, S. On the influence of the thickness of the sediment moving layer in the definition of the bedload transport formula in Exner systems. *Computers & Fluids* **91,** 87 –106 (2014).

38. Fernández-Nieto, E. D., Luna, T. M. d., Narbona-Reina, G. & Zabsonré, J. d. D. Formal deduction of the Saint-Venant-Exner model including arbitrarily sloping sediment beds and associated energy. *Mathematical Modelling and Numerical Analysis* **51,** 115–145 (2017).

39. Ferreira, R. M. L., Franca, M. J., Leal, J. G.A. B. & Cardoso, A. H. Mathematical modelling of shallow flows: Closure models drawn from grain-scale mechanics of sediment transport and flow hydrodynamics. **36,** 1605–1621 (2009).

40. Forterre, Y. & Pouliquen, O. Flows of Dense Granular Media. *Annual Review of Fluid Mechanics* **40,** 1–24 (2008).

41. Fraccarollo, L., Capart, H. & Zech, Y. A Godunov method for the computation of erosional shallow water transients. *International Journal for Numerical Methods in Fluids* **41,** 951–976 (2003).

42. George, D. L. & Iverson, R. M. A depth-averaged debris-flow model that includes the effects of evolving dilatancy. II. Numerical predictions and experimental tests. *Proceedings of the Royal Society A: Mathematical, Physical and Engineering Sciences* **470,** 20130820 (2014).

43. George, L. & Iverson, M. *A two-phase debris-flow model that includes coupled evolution of volume fractions, granular dilatancy and pore-fluid pressure* in *5th International Conference on Debris-Flow Hazards: Mitigation, Mechanics, Prediction and Assessment"* (2011), 10.

44. Godlewski, E. & Raviart, P.-A. *Numerical Approximation of Hyperbolic Systems of Conservation Laws* (Springer-Verlag, New York, 1996).

45. Goutière, L., Soares-Frazão, S., Savary, C., Laraichi, T. & Zech, Y. One-Dimensional Model for Transient Flows Involving Bed-Load Sediment Transport and Changes in Flow Regimes. *Journal of Hydraulic Engineering* **134,** 726–735 (2008).

46. Greco, M., Di Cristo, C., Iervolino, M. & Vacca, A. Numerical simulation of mud-flows impacting structures. *Journal of Mountain Science* **16,** 364–382 (2019).

47. Gualtieri, C., Ianniruberto, M. & Filizola, N. On the mixing of rivers with a difference in density: The case of the Negro/Solimões confluence, Brazil. *Journal of Hydrology* **578,** 124029 (2019).

48. Gunawan, P. & Lhébrard, X. Hydrostatic relaxation scheme for the 1D shallow water - Exner equations in bedload transport. *Computers & Fluids* **121,** 44 –50 (2015).

49. Hager, G. & Wellein, G. *Introduction to High Performance Computing for Scientists and Engineers* (CRC Press, Taylor & Francis Group, 2011).

50. Heng Zhao, J., Özgen, I., fang Liang, D. & Hinkelmann, R. Comparison of depth-averaged concentration and bed load flux sediment transport models of dam-break flow. *Water Science and Engineering* **10,** 287–294 (2017).

51. Hess, J., Tai, Y.-C. & Wang, Y. Debris flows with pore pressure and intergranular friction on rugged topography. *Computers & Fluids* **190,** 139 –155 (2019).

52. Hudson, J. & Sweby, P. K. Formulations for Numerically Approximating Hyperbolic Systems Governing Sediment Transport. *Journal of Scientific Computing* **19,** 225–252 (2003).

53. Hungr, O. A model for the runout analysis of rapid flow slides, debris flows, and avalanches. *Canadian Geotechnical Journal* **32,** 610–623 (1995).

54. Hungr, O., Evans, S. G., Bovis, M. J. & Hutchinson, J. N. A review of the classification of landslides of the flow type. *Environmental and Engineering Geoscience* **7,** 221–238 (2001).

55. Iverson, R. M. The physics of debris flows. *Reviews of Geophysics* **35,** 245–296 (1997).

56. Iverson, R. M. & Denlinger, R. P. Flow of variably fluidized granular masses across three-dimensional terrain: 1. Coulomb mixture theory. *Journal of Geophysical Research: Solid Earth* **106,** 537–552 (2001).

57. Iverson, R. M. & George, D. L. A depth-averaged debris-flow model that includes the effects of evolving dilatancy. I. Physical basis. *Proceedings of the Royal Society A: Mathematical, Physical and Engineering Sciences* **470,** 20130819 (2014).
58. Iverson, R. M. & Ouyang, C. Entrainment of bed material by Earth-surface mass flows: Review and reformulation of depth-integrated theory. *Reviews of Geophysics* **53,** 27–58 (2015).
59. Iverson, R. M. & Vallance, J. W. New views of granular mass flows. *Geology* **29,** 115–118 (2001).
60. Iverson, R. M. *et al.* Positive feedback and momentum growth during debris-flow entrainment of wet bed sediment. *Nature Geoscience* **4,** 116–121 (2011).
61. Iverson, R. M., Logan, M., LaHusen, R. G. & Berti, M. The perfect debris flow? Aggregated results from 28 large-scale experiments. *Journal of Geophysical Research: Earth Surface* **115,** F03005 (2010).
62. J., K. *Two-phase modeling of debris flows* PhD thesis (ETH Zurich, Switzerland, 2008).
63. Jakob, M. & Hungr, O. *Debris-flow Hazards and Related Phenomena* (Springer Berlin Heidelberg, 2005).
64. Juez, C., Murillo, J. & García-Navarro, P. 2D simulation of granular flow over irregular steep slopes using global and local coordinates. *J. Comput. Phys* **255,** 166–204 (2013).
65. Juez, C., Murillo, J. & García-Navarro, P. A 2D weakly-coupled and efficient numerical model for transient shallow flow and movable bed. *Advances in Water Resources* **71,** 93 –109 (2014).
66. Juez, C., Murillo, J. & Garcia-Navarro, P. Numerical assessment of bed-load discharge formulations for transient flow in 1D and 2D situations. *Journal of Hydroinformatics* **15,** 1234–1257 (2013).
67. Juez, C., Lacasta, A., Murillo, J. & García-Navarro, P. An efficient GPU implementation for a faster simulation of unsteady bed-load transport. *Journal of Hydraulic Research* **54,** 275–288 (2016).
68. Julien, P. Y. & Lan, Y. Rheology of Hyperconcentrations. *Journal of Hydraulic Engineering* **117,** 346–353 (1991).
69. Kowalski, J. & McElwaine, J. N. Shallow two-component gravity-driven flows with vertical variation. *Journal of Fluid Mechanics* **714,** 434–462 (2013).
70. Lacasta, A., Juez, C., Murillo, J. & García-Navarro, P. An efficient solution for hazardous geophysical flows simulation using GPUs. *Computers & Geosciences* **78,** 63 –72 (2015).
71. Lacasta, A., Morales-Hernández, M., Murillo, J. & García-Navarro, P. An optimized GPU implementation of a 2D free surface simulation model on unstructured meshes. *Advances in Engineering Software* **78,** 1 –15 (2014).
72. Lacasta, A., Morales-Hernández, M., Murillo, J. & García-Navarro, P. GPU implementation of the 2D shallow water equations for the simulation of rainfall/runoff events. *Environmental Earth Sciences* **74,** 7295–7305 (2015).

73. Lajeunesse, E., Malverti, L. & Charru, F. Bed load transport in turbulent flow at the grain scale: Experiments and modeling. *Journal of Geophysical Research: Earth Surface* **115,** F04001 (2010).

74. Lancaster, S. T., Hayes, S. K. & Grant, G. E. Effects of wood on debris flow runout in small mountain watersheds. *Water Resources Research* **39,** 21 (2003).

75. Lane, S. N. *et al.* Causes of rapid mixing at a junction of two large rivers: Río Paraná and Río Paraguay, Argentina. *Journal of Geophysical Research: Earth Surface* **113,** F02024 (2008).

76. Lee, H. & Hsu, I. Investigation of Saltating Particle Motions. *Journal of Hydraulic Engineering* **120,** 831–845 (1994).

77. Leighton, F. Z., Borthwick, A. G. L. & Taylor, P. H. 1-D numerical modelling of shallow flows with variable horizontal density. *International Journal for Numerical Methods in Fluids* **62,** 1209–1231 (2010).

78. Li, J. & Chen, G. The generalized Riemann problem method for the shallow water equations with bottom topography. *Int J. Numer. Meth. Eng* **65,** 834–862 (2006).

79. Li, J., Cao, Z., Hu, K., Pender, G. & Liu, Q. A depth-averaged two-phase model for debris flows over erodible beds. *Earth Surface Processes and Landforms* **43,** 817–839 (2018).

80. Liu, X., Mohammadian, A., Kurganov, A. & Infante-Sedano, J. Well-balanced central-upwind scheme for a fully coupled shallow water system modeling flows over erodible bed. *Journal of Computational Physics* **300,** 202 –218 (2015).

81. Luna, B. Q., Remaître, A., [van Asch], T., Malet, J.-P. & [van Westen], C. Analysis of debris flow behavior with a one dimensional run-out model incorporating entrainment. *Engineering Geology* **128,** 63 – 75 (2012).

82. Luque, R. F. & Beek, R. V. Erosion And Transport Of Bed-Load Sediment. *Journal of Hydraulic Research* **14,** 127–144 (1976).

83. Lyn, D. & Altinakar, M. St. Venant-Exner Equations for Near-Critical and Transcritical Flows. *Journal of Hydraulic Engineering* **128,** 579–587 (2002).

84. Macías, J., Castro, M. J., Ortega, S., Escalante, C. & González-Vida, J. M. Performance Benchmarking of Tsunami-HySEA Model for NTHMPs Inundation Mapping Activities. *Pure Appl. Geophys.* **174,** 3147–3183 (2017).

85. Major, J. J. & Iverson, R. M. Debris-flow deposition: Effects of pore-fluid pressure and friction concentrated at flow margins. *GSA Bulletin* **111,** 1424–1434 (1999).

86. Martínez-Aranda, S., Murillo, J. & García-Navarro, P. A 1D numerical model for the simulation of unsteady and highly erosive flows in rivers. *Computers & Fluids* **181,** 8–34 (2019).

87. Martínez-Aranda, S., Murillo, J. & García-Navarro, P. A comparative analysis of capacity and non-capacity formulations for the simulation of unsteady flows over finite-depth erodible beds. *Advances in Water Resources* **(in print)** (2019).

88. Martínez-Aranda, S., Murillo, J. & García-Navarro, P. *A new 2D bedload transport model based on non-capacity approach to overcome the problems associated to finite-depth sediment layers* in *In proceedings of the 10th International Conference on Fluvial Hydraulics (River Flow 2020), July 7-10, Delft, Netherlands* (2020).

89. Martínez-Aranda, S. *et al.* in. Chap. Finite Volume models and Efficient Simulation Tools (EST) for Shallow Flows (Springer (In print), 2021).

90. Martínez-Aranda, S., Murillo, J. & García-Navarro, P. A robust two-dimensional model for highly sediment-laden unsteady flows of variable density over movable beds. *Journal of Hydroinformatics* **22,** 1138–1160 (2020).

91. Martínez-Aranda, S., Murillo, J. & García-Navarro, P. Comparison of new efficient 2D models for the simulation of bedload transport using the augmented Roe approach. *Advances in Water Resources* **xxx,** 103931 (2021).

92. Martínez Aranda, S., Navas-Montilla, A., Lozano, A. & García-Navarro, P. *Experimental study of resonant shallow flows past a lateral cavity: a benchmark test for high-resolution numerical models* in *EGU General Assembly, Online 4-8 May* (2020).

93. McArdell, B. W., Bartelt, P. & Kowalski, J. Field observations of basal forces and fluid pore pressure in a debris flow. *Geophysical Research Letters* **34,** L07406 (2007).

94. McCoy, S. W. *et al.* Sediment entrainment by debris flows: In situ measurements from the headwaters of a steep catchment. *Journal of Geophysical Research: Earth Surface* **117,** F03016 (2012).

95. Meng, X. & Wang, Y. Modelling and numerical simulation of two-phase debris flows. *Acta Geotechnica* **11,** 1027–1045 (2016).

96. Meurice, R., Martínez-Aranda, S., Ebrahimi, M., García-Navarro, P. & Soares-Frazão, S. Laser Profilometry to measure the bed evolution in a dam-break flow. *submitted* **xxx,** xxx (2021).

97. Meyer-Peter, E. & Müller, R. *Formulas for Bed-Load Transport* in *Report on 2nd meeting on international association on hydraulic structures research* (Stockholm, Sweden, 1948), 39–64.

98. Ming, X., Liang, Q., Xia, X., Li, D. & Fowler, H. J. Real-time flood forecasting based on a high-performance 2D hydrodynamic model and numerical weather predictions. *Water Resources Research* **56,** e2019WR025583 (2020).

99. Multiple time scales of alluvial rivers carrying suspended sediment and their implications for mathematical modeling. *Advances in Water Resources* **30,** 715 –729 (2007).

100. Murillo, J. & García-Navarro, P. An Exner-based coupled model for two-dimensional transient flow over erodible bed. *J. Comput. Phys* **229,** 8704–8732 (2010).

101. Murillo, J. & García-Navarro, P. Energy balance numerical schemes for shallow water equations with discontinuous topography. *J. Comput. Phys* **236,** 119–142 (2012).

102. Murillo, J. & García-Navarro, P. Wave Riemann description of friction terms in unsteady shallow flows: application to water and mud/debris floods. *J. Comput. Phys* **231,** 1963–2001 (2012).

103. Murillo, J. & García-Navarro, P. Weak solutions for partial differential equations with source terms: application to the shallow water equations. *J. Comput. Phys* **229,** 4327–4368 (2010).

104. Murillo, J. & Navas-Montilla, A. A comprehensive explanation and exercise of the source terms in hyperbolic systems using Roe type solutions. Application to the 1D-2D shallow water equations. *Advances in Water Resources* **98,** 70 –96 (2016).

105. Murillo, J., Latorre, B., García-Navarro, P. & Riemann, A. A Riemann solver for unsteady computation of 2D shallow flows with variable density. *J. Comput. Phys* **231,** 4775–4807 (2012).

106. Murillo, J., García-Navarro, P. & Burguete, J. Time step restrictions for well balanced shallow water solutions in non-zero velocity steady states. *Int. J. Numer. Meth. Fluids* **56,** 661–686 (2008).

107. Naef, D., Rickenmann, D., Rutschmann, P. & Mcardell, B. W. Comparison of flow resistance relations for debris flows using a one-dimensional finite element simulation model. *Natural Hazards and Earth System Science* **6,** 155–165 (2006).

108. Nielsen, P. *Coastal Bottom Boundary Layers and Sediment Transport* (World Scientific, 1992).

109. O'Brien, J. S., Julien, P. Y. & Fullerton, W. T. Two‐Dimensional Water Flood and Mudflow Simulation. *Journal of Hydraulic Engineering* **119,** 244–261 (1993).

110. Ortiz, P., Anguita, J. & Riveiro, M. Free surface flows over partially erodible beds by a continuous finite element method. *Environmental Earth Sciences* **74,** 7357–7370 (2015).

111. Ouyang, C., He, S. & Xu, Q. MacCormack-TVD Finite Difference Solution for Dam Break Hydraulics over Erodible Sediment Beds. *Journal of Hydraulic Engineering* **141,** 06014026 (2015).

112. Ouyang, C., He, S. & Tang, C. Numerical analysis of dynamics of debris flow over erodible beds in Wenchuan earthquake-induced area. *Engineering Geology* **194,** 62 –72 (2015).

113. Pailha, M. & Pouliquen, O. A two-phase flow description of the initiation of underwater granular avalanches. *Journal of Fluid Mechanics* **633,** 115–135 (2009).

114. Paquier, A. & El Kadi, K. *A Model for Bed-Load Transport and Morphological Evolution in Rivers: Description and Pertinence* in *Hyperbolic Problems: Theory, Numerics, Applications* (eds Benzoni-Gavage, S. & Serre, D.) (Springer Berlin Heidelberg, Berlin, Heidelberg, 2008), 285–296.

115. Paquier, A. & Goutal, N. Dam and levee failures: an overview of flood wave propagation modeling. *La Houille Blanche - Revue internationale de l'eau*, 5–12 (2016).

116. Pastor, M. *et al.* Depth Averaged Models for Fast Landslide Propagation: Mathematical, Rheological and Numerical Aspects. *Archives of Computational Methods in Engineering* **22,** 67–104 (2015).

117. Pelanti, M., Bouchut, F. & Mangeney, A. A Roe-type scheme for two-phase shallow granular flows over variable topography. *ESAIM Mathematical Modelling and Numerical Analysis* **42,** 851–885 (2008).

118. Pierson, T. *Hyperconcentrated flow – transitional process between water flow and debris flow. Debris-flow Hazards and Related Phenomena* (Springer Berlin Heidelberg, Berlin, Germany, 2005).

119. Pirulli, M., Bristeau, M.-O., Mangeney, A. & Scavia, C. The effect of the earth pressure coefficients on the runout of granular material. *Environmental Modelling & Software* **22,** 1437–1454 (2007).

120. Pitlick, J. & Cress, R. Downstream changes in channel geometry of a large gravel bed river. *Water Resources Research* **38,** 34–1 (2002).

121. Pitman, E. B. & Le, L. A two-fluid model for avalanche and debris flows. *Philosophical Transactions of the Royal Society A: Mathematical, Physical and Engineering Sciences* **363,** 1573–1601 (2005).

122. Quecedo, M., Pastor, M., Herreros, M. I. & Fernández Merodo, J. A. Numerical modelling of the propagation of fast landslides using the finite element method. *International Journal for Numerical Methods in Engineering* **59,** 755–794 (2004).

123. Ramon, C. L., Armengol, J., Dolz, J., Prats, J. & Rueda, F. J. Mixing dynamics at the confluence of two large rivers undergoing weak density variations. *Journal of Geophysical Research: Oceans* **119,** 2386–2402 (2014).

124. Richardson, J. & Zaki, W. Sedimentation and fluidisation: Part I. *Chemical Engineering Research and Design* **75,** 82–100 (1997).

125. Rickenmann, D., Weber, D. & Stepanov, B. *Erosion by debris flows in field and laboratory experiments* in *3rd International Conference on Debris-Flow Hazards: Mitigation, Mechanics, Prediction and Assessment"* (Rotterdam, Millpress, 2003), 883–894.

126. Robertson, P., de Melo, L., Williams, D. & Wilson, G. W. *Report of the Expert Panel on the Technical Causes of the Failure of Feijão Dam I* tech. rep. (Vale S.A., 2019).

127. Roe, P. L. Approximate Riemann solvers, parameter vectors, and difference schemes. *J. Comput. Phys* **43,** 357–372 (1981).

128. Rosatti, G. & Begnudelli, L. The Riemann problem for the one-dimensional, free-surface Shallow Water Equations with a bed step: theoretical analysis and numerical simulations. *J. Comput. Phys* **229,** 760–787 (2010).

129. Rotta], L. H. S. *et al.* The 2019 Brumadinho tailings dam collapse: Possible cause and impacts of the worst human and environmental disaster in Brazil. *International Journal of Applied Earth Observation and Geoinformation* **90,** 102119 (2020).

130. Rulot, F., Dewals, B., Erpicum, S., Archambeau, P. & Pirotton, M. Modelling sediment transport over partially non-erodible bottoms. *International Journal for Numerical Methods in Fluids* **70,** 186–199 (2012).

131. Saint-Venant, A.-J.-C. Théorie du mouvement non permanent des eaux, avec application aux crues des rivières et à l'introduction des marées dans leur lit. *Comptes rendus hebdomadaires des séances de l'Académie des sciences, France* **73,** 11 (1871).

132. Smart, G. Sediment transport formula for steep channels. *Journal of Hydraulic Engineering* **3,** 267–276 (1984).

133. Soares-Frazão, S., LeGrelle, N., Spinewine, B. & Zech, Y. Dam-break induced morphological changes in a channel with uniform sediments: measurements by a laser-sheet imaging technique. *Journal of Hydraulic Research* **45,** 87–95 (2007).

134. Soliman, M. R. & Ushijima, S. Equilibrium and Non-equilibrium Sediment Transport Modeling Based On Parallel MACS Algorithm. *Journal of Japan Society of Civil Engineers* **69,** 79–86 (2013).

135. Spinewine, B. & Zech, Y. Small-scale laboratory dam-break waves on movable beds. *Journal of Hydraulic Research* **45,** 73–86 (2007).

136. Struiksma, N. *Mathematical modelling of bedload transport over non-erodible layers* in *IAHR symposium on River, Coastal amd Estuarine Morphodynamics* (Genova, Italy, 1999), 89–98.

137. Tingsanchali, T. & Chinnarasri, C. Numerical modelling of dam failure due to flow overtopping. *Hydrological Sciences Journal* **46,** 113–130 (2001).

138. Toro, E. *Riemann Solvers and Numerical Methods for Fluid Dynamics: A Practical Introduction* (Springer-Verlag, Berlin, Germany, 1997).

139. Van Rijn, L. Sediment Transport, Part I: Bed Load Transport. *Journal of Hydraulic Engineering* **110,** 1431–1456 (1984).

140. Van-Rijn, L. in. Chap. 10, Bed material transport, erosion and deposition in non-steady and non-uniform flow (Aqua Publications, Amsterdam, 1993).

141. Vergilio, C. d. S. *et al.* Metal concentrations and biological effects from one of the largest mining disasters in the world (Brumadinho, Minas Gerais, Brazil). *Scientific Reports* **10,** 5936 (2020).

142. Wang, G., Sassa, K. & Fukuoka, H. Downslope volume enlargement of a debris slide–debris flow in the 1999 Hiroshima, Japan, rainstorm. *Engineering Geology* **69,** 309 –330 (2003).

143. Wong, M. & Parker, G. Reanalysis and Correction of Bed-Load Relation of Meyer-Peter and Müller Using Their Own Database. *Journal of Hydraulic Engineering* **132,** 1159–1168 (2006).

144. Wu, W. *Computational River Dynamics* (CRC Press, 2007).

145. Wu, W. & Wang, S. One-Dimensional Modeling of Dam-Break Flow over Movable Beds. *Journal of Hydraulic Engineering* **133,** 48–58 (2007).

146. Wu, W., Vieira, D. & Wang, S. One-Dimensional Numerical Model for Nonuniform Sediment Transport under Unsteady Flows in Channel Networks. *Journal of Hydraulic Engineering* **130,** 914–923 (2004).

147. Xia, C.-c., Li, J., Cao, Z.-x., Liu, Q.-q. & Hu, K.-h. A quasi single-phase model for debris flows and its comparison with a two-phase model. *Journal of Mountain Science* **15,** 1071–1089 (2018).

148. Xia, X. & Liang, Q. A new efficient implicit scheme for discretising the stiff friction terms in the shallow water equations. *Advances in Water Resources* **117,** 87–97 (2018).

149. Yang, C. *Sediment Transport: Theory and Practice* (McGraw-Hill Inc., New York, 1996).

150. Zech, Y., Soares-Frazão, S., Spinewine, B. & Grelle, N. L. Dam-break induced sediment movement: Experimental approaches and numerical modelling. *Journal of Hydraulic Research* **46,** 176–190 (2008).

151. Zhang, R. & Xie, J. *Sedimentation Research in China: Systematic Selections* (China Water and Power Press, 1993).

152. Zhang, S. & Duan, J. 1D finite volume model of unsteady flow over mobile bed. *Journal of Hydrology* **405,** 57 –68 (2011).

Appendix A

High-performance computational algorithms

In this thesis, GPU-based algorithms have been implemented for the different numerical schemes detailed in the previous sections, using the NVIDIA CUDA Toolkit and the C++ language. Figure A.1 shows a scheme of the general GPU-based algorithm used for the 2D sediment-laden numerical algorithms. The preprocess step and CPU-GPU memory transfer are implemented to run on one CPU core, whereas the time loop computation is accelerated using GPU. However, some tasks inside the time loop are controlled yet by the CPU, such as the time advance control, the boundary conditions application and the output data dump. Therefore, it is necessary to transfer information from/to the GPU at each time-step. While the computational effort required for the time and boundaries transference is considerably smaller than that of each kernel function, in order to dump the intermediate output information, all the variables in the domain must be transferred from GPU device to CPU host.

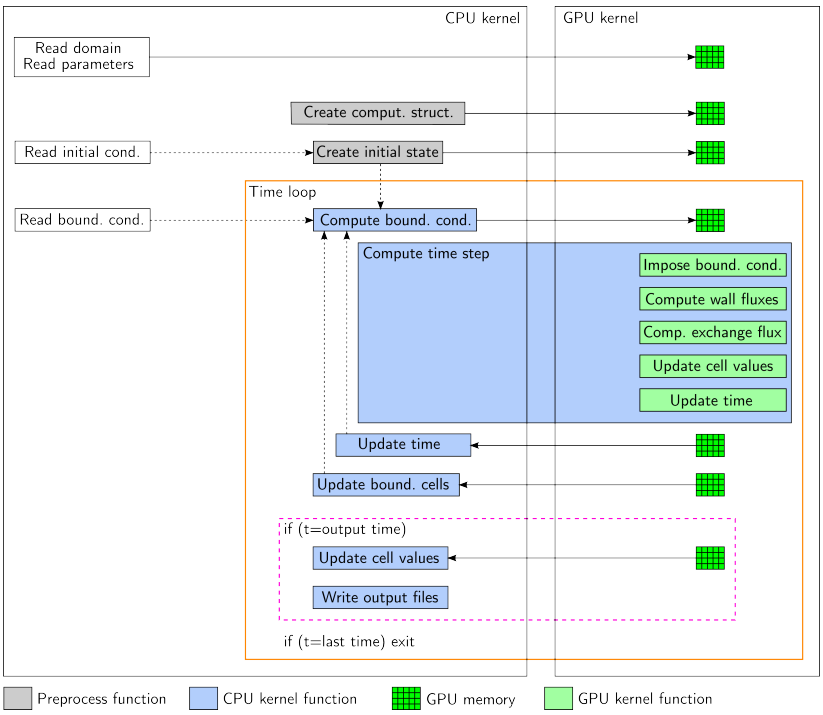

Figure A.1: Scheme of the GPU-accelerated algorithm.

In order to obtain efficient GPU-accelerated codes dealing with unstructured meshes, some of the strategies proposed by [70, 71] have been implemented. The CUDA toolkit allows that all the processed elements can be distributed by threads and blocks of threads. Each thread uses its own thread index to identify the element to be processed, launching several execution threads at the same time (parallel computation). As computing GPU devices are well designed to work efficiently with ordered information, the variables needed for computation are stored in the GPU memory as structures of arrays (SoA), improving the spatial locality for memory accesses. Only the kernel functions, which require a higher computational effort, have been implemented to run on the GPU device. Some tasks in the GPU kernel are optimized using the CUBLAS library included in CUDA. The memory transfer between the CPU host and the GPU device has been reduced as much as possible for each time step.

Furthermore, a CPU-based version of the numerical algorithms has also been implemented using the shared-memory parallelization in C++. In this strategy, a number of CPUs work on the same physical address space [49]. Although transparent to the user, the translation of the different numerical schemes detailed in the previous sections into efficient algorithms is not an easy task. These algorithms consist of some sequential/dependent parts, which can not be parallelized, and some others that can be run independently one each other and which are included into *parallel regions*. To determine parallel regions some directives for the compiler must be declared at the code. In this thesis OpenMP (Open Multi-Processing) [9] is used for shared-memory directives. Figure A.2 shows a scheme of the general GPU-based algorithm used for the 2D sediment-laden numerical schemes.

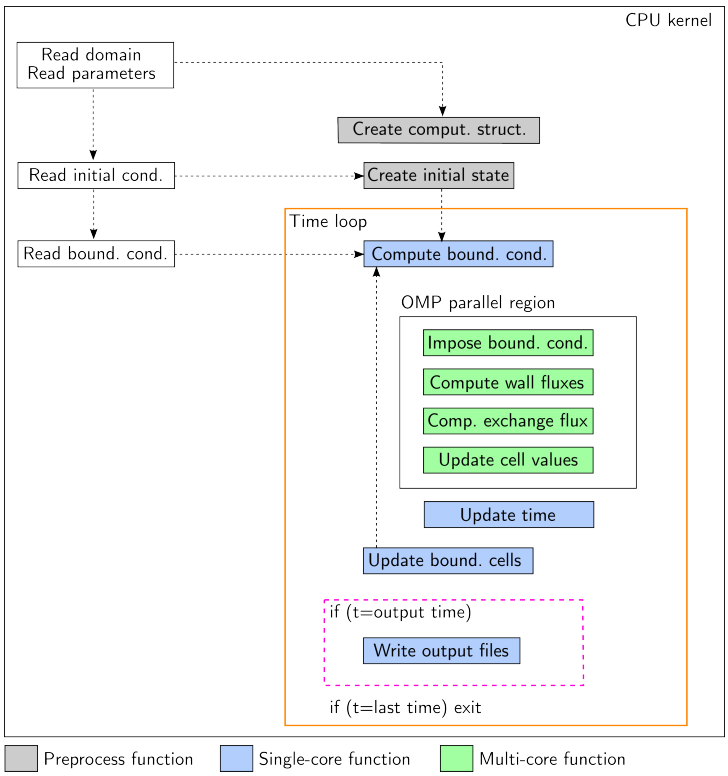

Figure A.2: Scheme of the CPU-based algorithm.

Finally, for all the tests presented in this thesis, the CPU-based version of the code were run on a Intel(R) Core(TM) i7-3820 @3.60GHz and a last generation Intel(R) Core(TM) i7-7700K @4.50GHz, whereas the GPU-based code was tested using two devices: a medium-grade NVIDIA Tesla K40c and a NVIDIA GeForce GTX 1080 Ti. GPU's technology is continuously growing and the devices are fastly improving regarding the number of computation cores, speed on the data transfer and efficiency of the CUDA Toolkit. Therefore, it is expected that the performance of the GPU-accelerated algorithms may increase markedly running in last generation NVIDIA GPUs.

Appendix B

Relevant publications and communications

Chapters in book

[1] Martínez-Aranda, S., Fernández-Pato, J., Echeverribar, I.,Navas-Montilla, A., Morales-Hernández, M., Brufau, P., Murillo, J. & García-Navarro, P., 2021. Finite Volume models and Efficient Simulation Tools (EST) for Shallow Flows. Chapter in *Current Trends in Fluid Dynamics*, Springer (In print)

Articles in international peer-review journals

[2] Martínez-Aranda, S., Fernández-Pato, J., Caviedes-Voullième, D., García-Palacín, I. & García-Navarro, P., 2018. Towards transient experimental water surfaces: a new benchmark dataset for 2D shallow water solvers. *Advances in water resources* 121:130-149. https://doi.org/10.1016/j.advwatres.2018.08.013

[3] Martínez-Aranda, S., Murillo, J. & García-Navarro, P., 2019. A 1D numerical model for the simulation of unsteady and highly erosive flows in rivers. *Computers & Fluids* 181:8-34 https://doi.org/10.1016/j.compfluid.2019.01.011

[4] Martínez-Aranda, S., Murillo, J. & García-Navarro, P., 2019. A comparative analysis of capacity and non-capacity formulations for the simulation of unsteady flows over finite-depth erodible beds. *Advances in water resources* 130:91-112 https://doi.org/10.1016/j.advwatres.2019.06.001

[5] Murillo, J., Martínez-Aranda, S., Navas-Montilla, A. & García-Navarro, P., 2020. Adaptation of flux-based solvers to 2D two-layer shallow flows with variable density including numerical treatment of the loss of hyperbolicity and drying/wetting fronts. *Journal of Hydroinformatics* 22(5):972–1014 https://doi.org/10.2166/hydro.2020.207

[6] Fernández-Pato, J., Martínez-Aranda, S. & García-Navarro, P., 2020. A 2D finite volume simulation tool to enable the assessment of combined hydrological and morphodynamical processes in mountain catchments. *Advances in water resources* 141:103617 https://doi.org/10.1016/j.advwatres.2020.103617

[7] Martínez-Aranda, S., Murillo, J. & García-Navarro, P., 2020. A robust two-dimensional model for highly sediment-laden unsteady flows of variable density over movable beds. *Journal of Hydroinformatics* 22(5):1138-1160 https://doi.org/10.2166/hydro.2020.027

[8] Martínez-Aranda, S., Ramos-Pérez, A. & García-Navarro, P., 2020. A 1D shallow-flow model for two-layer flows based on FORCE scheme with wet-dry treatment. *Journal of Hydroinformatics* 22(5):1015-1037 https://doi.org/10.2166/hydro.2020.002

[9] Fernández-Pato, J., Martínez-Aranda, S., Morales-Hernández, M. & García-Navarro, P., 2020. Analysis of the performance of different culvert boundary conditions in 2D shallow flow models. *Journal of Hydroinformatics* 22(5):1093–1121 https://doi.org/10.2166/hydro.2020.025

[10] Navas-Montilla, A., Martínez-Aranda, S., Lozano, A., García-Palacín, I. & García-Navarro, P., 2021. 2D experiments and numerical simulation of the oscillatory shallow flow in an open channel lateral cavity. *Advances in Water Resources* 148:103836 https://doi.org/10.1016/j.advwatres.2020.103836

[11] Martínez-Aranda, S., Murillo, J. & García-Navarro, P., 2021. Comparison of new efficient 2D models for the simulation of bedload transport using the augmented Roe approach. *Advances in Water Resources* 153:103931 https://doi.org/10.1016/j.advwatres.2021.103931

[12] Martínez-Aranda, S., Meurice, R., Soares-Frazão, S. & García-Navarro, P., 2021. Comparative analysis of HLLC- and Roe-based models for the simulation of a dambreak flow in an erodible channel with a 90° bend. *Water* (In print)

[13] Martínez-Aranda, S., Murillo, J. & García-Navarro, P. Efficient Simulation Tool (EST) for 2D variable-density mud/debris flows over non-uniform erodible beds. *Geology Engineering* (Under review)

[14] Meurice, R., Martínez-Aranda, S., Ebrahimi, M., García-Navarro, P. & Soares-Frazão, S. Laser Profilometry to measure the bed evolution in a dam-break flow. *Journal of Hydraulic Research* (Under review)

Articles in proceedings of international conferences

[15] Martínez-Aranda, S., Fernández-Pato, J., Caviedes-Voullième, D., García-Palacín, I. & García-Navarro, P., 2018. Towards transient experimental water surfaces: strengthening two-dimensional SW model validation. In *Proceedings of 13th International Conference on Hydroinformatics (HIC 2018)*, Palermo (Italy). EPiC Series in Engineering 3, pp. 1324–1331 https://doi.org/10.29007/qpmx

[16] Martínez-Aranda, S., Murillo, J. & García-Navarro, P., 2018. Coupled method for the numerical simulation of 1D shallow water and Exner transport equations in channels with variable cross-section. In

Proceedings of 9th International Conference on Fluvial Hydraulics (River-Flow 2018), Lyon (France). E3S Web Conf. 40, pp. 05012 https://doi.org/10.1051/e3sconf/20184005012

[17] Martínez-Aranda, S., Murillo, J. & García-Navarro, P., 2020. A new 2D bedload transport model based on non-capacity approach to overcome the problems associated to finite-depth sediment layers. In *Proceedings of the 10th Conference on Fluvial Hydraulics (RiverFlow 2020)*, Delft (Netherlands). CRC Press. https://doi.org/10.1201/b22619

Oral communications in international/national conferences

[18] Caviedes-Voullième, D., Martínez-Aranda, S., Fernández-Pato, J., García-Palacín, I. & García-Navarro, P., 2018. Measuring 2D transient shallow water surfaces: raising the benchmark challenges for 2D shallow water solvers. *Tag der Hydrologie*, Dresden (Germany)

[19] Martínez-Aranda, S., Murillo, J. & García-Navarro, P., 2018. Equilibrium and non-equilibrium models applied to unsteady sediment transport. *15th Intern. Conf. Zaragoza-Pau on Mathematics and its Applications*, Jaca (Spain).

[20] Murillo, J., Martínez-Aranda, S., Navas-Montilla, A. & García-Navarro, P., 2019. Energy balanced solvers for 2D two layer shallow flows with variable density: Application to loss of hyperbolicity and exact mass conservation in drying/wetting fronts. *Modeling Hydrodynamics for Water Resources (MODWATER 2019)*, Zaragoza (Spain)

[21] Martínez-Aranda, S., Murillo, J. & García-Navarro, P. A two-dimensional model for hyperconcentrated shallow flows with variable density and non-uniform bedload transport. *Modeling Hydrodynamics for Water Resources (MODWATER 2019)*, Zaragoza (Spain)

[22] Martínez-Aranda, S., Echeverribar, I., Fernández-Pato, J., Murillo, J. & García-Navarro, P., 2019. Avances y retos en la aplicación de modelos numéricos 2D para la predicción de eventos hidráulicos extremos asociados al cambio climático. *IV Jornadas de Investigadores en Formación (JIFFI 2019)*, Granada (Spain)

[23] Martínez-Aranda, S., Vericat, D., Batalla, R.J. & García-Navarro, P., 2019. Modelado morfodinámico de un cauce aluvial frente a eventos de crecida: combinación de datos topográficos de alta resolución y computación GPU para la mejora de los modelos predictivos. *VI Jornadas de Ingeniería del Agua (JIA 2019)*, Toledo (Spain).

[24] Echeverribar, I., Martínez-Aranda, S., Fernández-Pato, J., Murillo, J. & García-Navarro, P., 2019. Use of Riemann Solvers and High Performance Computing for 2D hydraulic and morphodynamic numerical simulations. *American Geophysical Union Fall Meeting (AGU 2019)*, San Francisco (EEUU)

Posters and short communications in international/national conferences

[25] Martínez-Aranda, S., Caviedes-Voullième, D., Fernández-Pato, J., García-Palacín, I., Gordillo G. & García-Navarro, P., 2017. 2D free surface steady and unsteady flows: 3D-sensing device measurements and finite volume simulation. *Workshop on Fluid Mechanics*, Tarragona (Spain)

[26] Martínez-Aranda, S., Murillo, J. & García-Navarro, P., 2018. Coupled method for bed load transport in 1D open channels with arbitrary geometry. *European Geophysical Union General Assembly (EGU 2018)*, Vienna (Austria).

[27] Martínez-Aranda, S., Navas-Montilla, A., García-Palacín, I. & García-Navarro, P., 2019. 2D non-intrusive measurements of dam-break waves in channels with movable bed and width variations. *European Geophysical Union General Assembly (EGU 2019)*, Vienna (Austria)

[28] Navas-Montilla, A., Martínez-Aranda, S., Lozano, A. & García-Navarro, P., 2020. Numerical study of resonant shallow flows past a lateral cavity: benchmarking the model with a new experimental data set. *European Geophysical Union General Assembly (EGU 2020)*, Vienna (Austria)

[29] Martínez-Aranda, S., Navas-Montilla, A., Lozano, A. & García-Navarro, P., 2020. Experimental study of resonant shallow flows past a lateral cavity: a benchmark test for high-resolution numerical models. *European Geophysical Union General Assembly (EGU 2020)*, Vienna (Austria)

Patents and copyrighted software

[30] Fernández-Pato, J., Morales-Hernández, M., García-Navarro, P., Echeverribar, I., Martíez-Aranda S., Murillo, J. & Brufau, P., 2019. PEKA2D.2 – New Software Developments for PEKA2D.1

[31] Fernández-Pato, J., Morales-Hernández, M., Echeverribar, I., García-Navarro, P., Murillo, J., Martíez-Aranda S. & Brufau, P., 2019. OIL2D.2 – New Software Developments for OIL2D.1

[32] Fernández-Pato, J., Martíez-Aranda S., García-Navarro, P., Echeverribar, I., Morales-Hernández, M., Murillo, J. & Brufau, P., 2021. PEKA2D.3 – New Software Developments for PEKA2D.1 and PEKA2D.2

[33] Fernández-Pato, J., Martíez-Aranda S., Echeverribar, I., Morales-Hernández, M., García-Navarro, P., Murillo, J. & Brufau, P., 2021. OIL2D.3 – New Software Developments for OIL2D.1 and OIL2D.2

Universidad Zaragoza

1542